Contribution of quantitative imaging to the mechanical, thermal and calorific characterization of rubber

Sylvain Charles

DOCTORAT MATIERE BRETAGNE MOLECULES LOIRE ET MATERIAUX

UNIVERSITÉ DE RENNES 1

THÈSE DE DOCTORAT DE

L'UNIVERSITÉ DE RENNES 1

ÉCOLE DOCTORALE N° 596
Matière, Molécules, Matériaux
Spécialité : *Science des matériaux*

Par

Sylvain CHARLÈS

Contribution of quantitative imaging to the mechanical, thermal and calorific characterization of rubber

Unité de recherche : Institut de Physique de Rennes (IPR)

Rapporteurs avant soutenance :

Sylvie CASTAGNET — Directrice de rcherche CNRS, ISAE ENSMAE
Xavier BALANDRAUD — Professeur des universités, Sigma-Clermont

Composition du Jury :

Attention, en cas d'absence d'un des membres du Jury le jour de la soutenance, la composition du jury doit être revue pour s'assurer qu'elle est conforme et devra être répercutée sur la couverture de thèse

Examinateurs :	Pierre-Antoine ALBOUY	Directeur de recherche CNRS, Laboratoire de Mécanique des Solides
	Sylvie CASTAGNET	Directrice de recherche CNRS, ISAE ENSMAE
	Xavier BALANDRAUD	Professeur des Universités, Sigma-Clermont
Dir. de thèse :	Jean-Benoît LE CAM	Professeur des Universités, Institut de Physique de Rennes

Invité(s) :

Eric ROBIN — Maitre de conférence, Institut de Physique de Rennes

Remerciements

Je tiens à remercier Monsieur Jean-Benoît LE CAM, Professeur des universités à l'Institut de Physique de Rennes, qui m'a encadré tout au long de cette thèse. Qu'il soit aussi remercié pour sa disponibilité et pour les nombreux conseils qu'il m'a prodiguée.
J'adresse tous mes remerciements à Madame Sylvie CASTAGNET, Directrice de recherche au CNRS à l'Université de Poitiers-ISAE ENSMA, ainsi qu'à Monsieur Xavier BALANDRAUD, Professeur des universités à l'Université de Clermont Auvergne, de l'honneur qu'ils m'ont fait en acceptant d'être rapporteurs de cette thèse.
J'exprime ma gratitude à Monsieur Pierre-Antoine ALBOUY qui a bien voulu être examinateur.
Enfin, je tiens à remercier ma famille, sans qui rien n'aurait été possible.
Un grand merci aussi à tous les membres de l'équipe IQ2M de m'avoir accueilli avec bienveillance.

Table of Contents

Abstract (in French)

L'objectif de cette thèse est de développer et d'étendre des méthodes d'imagerie quantitative relevant, à la fois du visible et de l'infrarouge, dans le cadre de l'étude thermomécanique de matériaux en grandes déformations. Plusieurs aspects ont été successivement abordés, liés à la fois au formalisme des grandes déformations et à la métrologie associée à la mesure couplée de champs de températures et de déplacements.

Dans un premier temps, un travail a été mené afin de mettre en place la technique de mesure calorimétrique de surface sous chargement homogène. Cette étude s'est faite dans le cadre de la validation de mesures de cristallinité sous déformation du caoutchouc naturel à partir de mesures calorimétriques. La cristallisation sous tension d'un caoutchouc est classiquement étudiée par la méthode de diffraction des rayons X. Bien que cette méthode apporte de nombreuses informations, elle a pour inconvénient de ne donner qu'une information ponctuelle, ce qui limite son utilisation pour la cartographie d'un champ de cristallinités. Comme la cristallisation sous tension est un phénomène exothermique, la cristallinité peut être déterminée à partir de la chaleur produite par le matériau [56]. La Figure 1 résume les différentes étapes de la méthode, qui a fait l'objet d'un article dans *Review of Scientific Instruments* [57]. L'étape 1 consiste à mesurer les sources de chaleur produites par le matériau en utilisant l'équation de la chaleur et une mesure de la température. Pour le caoutchouc naturel, une forte production de chaleur est associée au phénomène de cristallisation [38, 96]. L'étape 2 consiste à déterminer les sources de chaleur provenant des phénomènes autres que la cristallisation. Pour les caoutchoucs, celles-ci sont principalement dues aux dissipations intrinsèques et aux couplages thermoélastiques. Ces derniers peuvent être modélisés avec une forme polynomiale : $S_{el} = \sum_{i=1}^{n} C_i(I_1 - 3)^i$. La chaleur due à la cristallisation est identifiée en soustrayant cette quantité à celle mesurée au total. L'étape 3 consiste à calculer la variation de température équivalente qui est due à la cristallisation. Celle-ci est obtenue par l'intégration sur le temps des sources de chaleur dues à la cristallisation, en considérant que cette variation de température est nulle avant que la cristallisation commence. L'étape 4 consiste à déduire la cristallinité de la variation de température équivalente.

Cette méthode est ensuite validée en comparant les résultats obtenus avec ceux obtenus

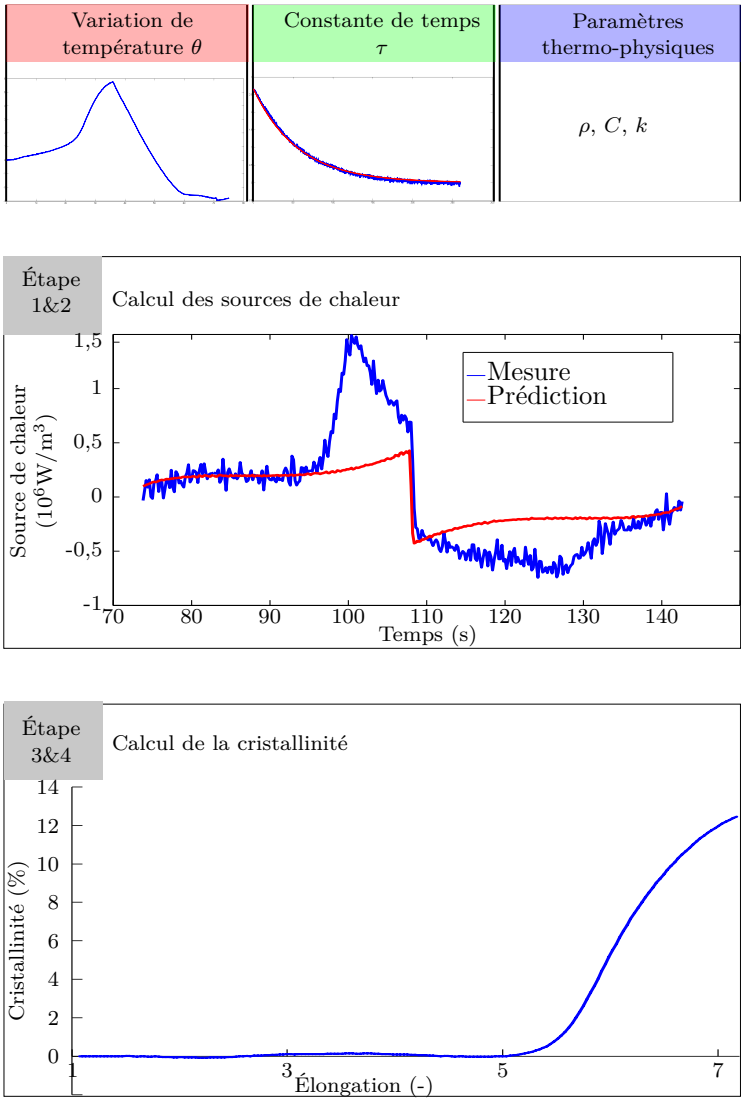

Figure 1 – Mesure de la cristallinité par calorimétrie de surface

par la technique de diffraction des rayons X, sur des éprouvettes de caoutchoucs naturels non chargés de mêmes compositions, à deux vitesses de sollicitation différentes, comme le montre la Figure 2.

La cristallisation sous tension est généralement étudiée en traction uniaxiale et très peu d'études traitent de l'influence de la multiaxialité sur ce phénomène. Une étude récente montre que la biaxialité limite la cristallisation, et qu'aucun cristal n'apparait si l'on a un ratio entre l'élongation maximale et minimale inférieur à 1.6 [21]. Nous avons donc appliqué cette méthode de mesure de cristallinité à un cas de chargement biaxial. Les résultats présentés à la Figure 3 montrent que la multiaxialité réduit bien la cristallinité,

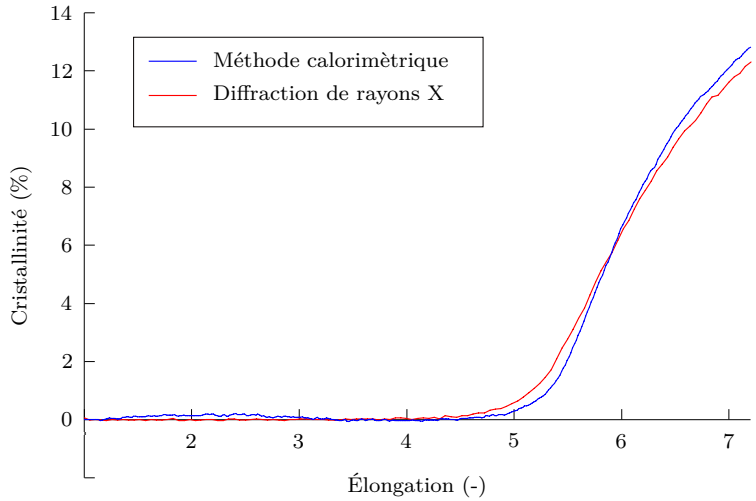

(a) Test à 100 mm/min

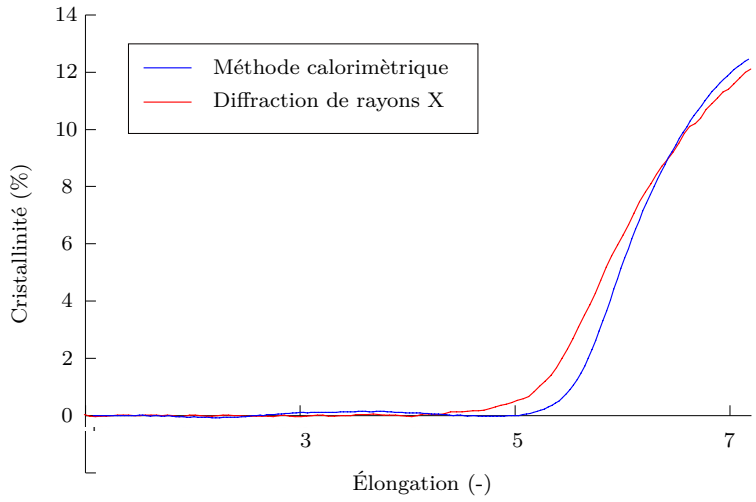

(b) Test à 200 mm/min

Figure 2 – Comparaison de la cristallinité obtenue par DRX et par calorimétrie de surface en traction uniaxiale

cependant la cristallisation apparait même lors d'un cas de chargement quasiment equibiaxial.

Comme mentionné précedemment, l'intérêt d'utiliser une méthode calorimétrique basée sur une mesure de champ est de pouvoir obtenir la cristallinité non pas en un seul point, mais en différents points simultanément, c'est l'objet des travaux suivants. La méthode est dans un premier temps appliquée en 1D à un cas de chargement homogène. Étant donné les grandes déformations subies par le matériau, une méthode de compensation du mouvement a été implémentée. Les résultats sont présentés à la Figure 4. Ils montrent

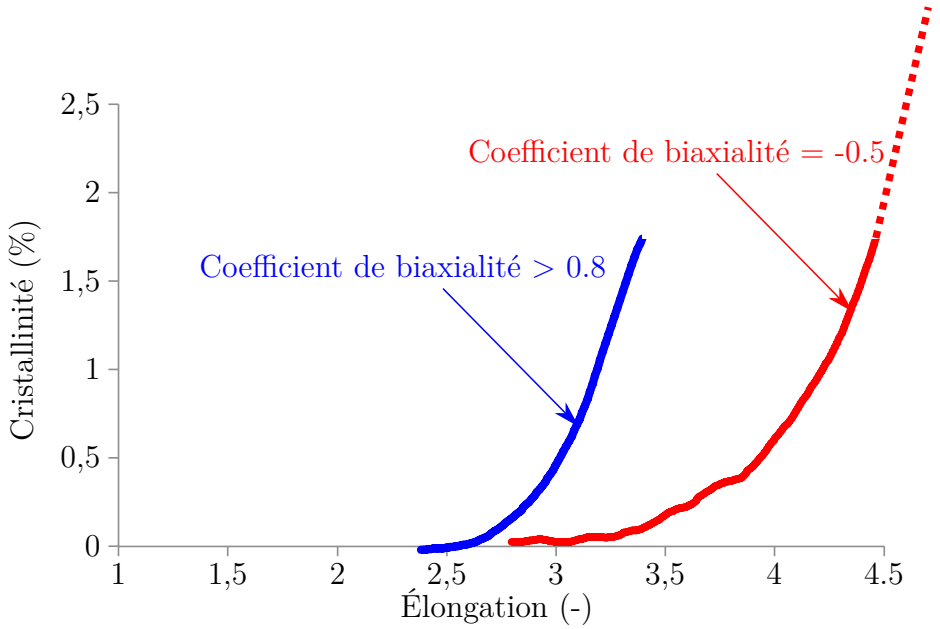

Figure 3 – Cristallinité en fonction de l'élongation et du coefficient de biaxialité

qu'un chargement macroscopique homogène peut conduire à une cristallisation hétérogène à l'échelle macroscopique.

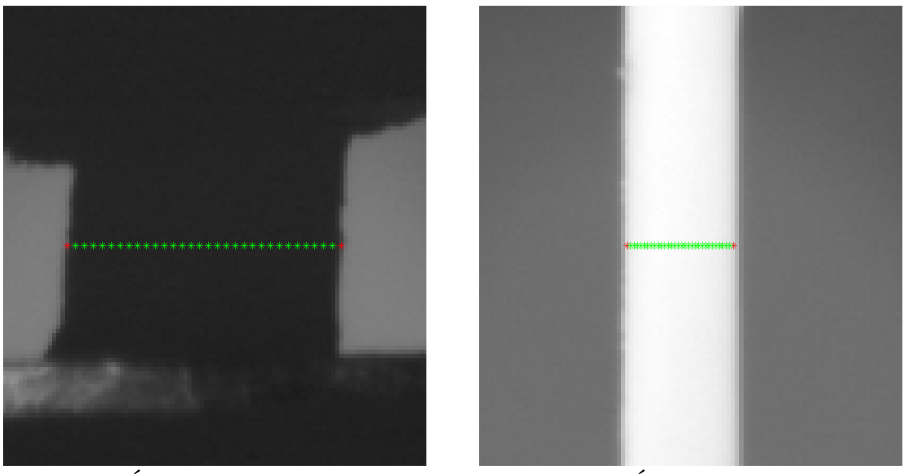

(a) État non déformé (b) État déformé

Figure 4 – Résultat de la compensation du mouvement

Du fait de la forte influence de la multiaxialité sur le comportement mécanique des caoutchoucs, l'utilisation de techniques de champs combinées à des essais mécaniques hétérogènes peut apporter beaucoup d'informations sur le comportement mécanique des caoutchoucs. Cette méthode a d'ailleurs déjà été utilisée par Promma et al. [86] et Guélon

et al. [39]. L'utilisation d'une éprouvette en croix permet d'obtenir de la traction uniaxiale dans les branches, de la traction équibiaxiale au centre et du cisaillement entre les deux autres zones, comme le montre la Figure 5. Il serait donc intéressant de coupler la thermographie infrarouge à des techniques de mesure de champs cinématiques, afin de pouvoir cartographier les sources de chaleur à la surface de matériaux subissant de grandes déformatios hétérogènes.

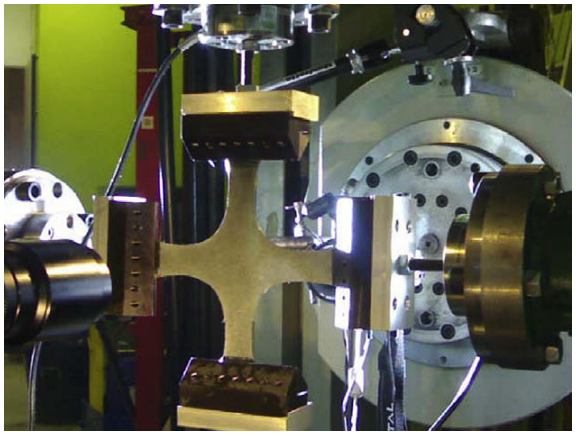

(a) Essai biaxial fait sur une éprouvette en croix [86]

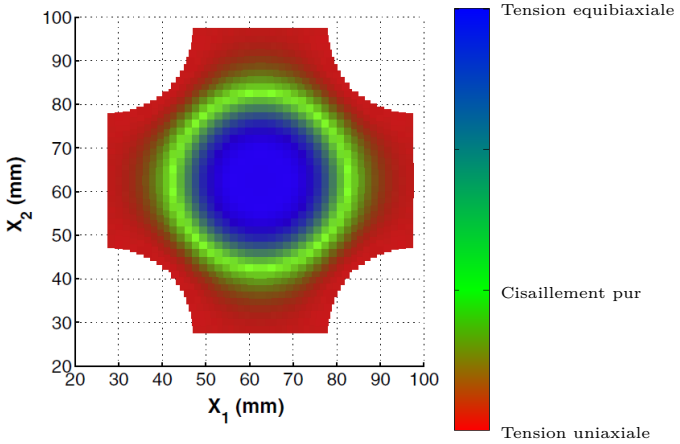

(b) Cas de chargement obtenu par simulation par éléments finis [86]

Figure 5 – Exemple d'essai hétérogène fait sur une éprouvette en croix [86]

Une problématique rencontrée pour faire de la thermograhie infrarouge en grandes déformations est que les points matériels observés sur les images infrarouges ne sont pas fixent, mais se déplacent de pixels en pixels, comme le montre la Figure 6, ce qui nécessite d'utiliser une technique de compensation du mouvement. Différentes techniques ont déjà été proposées, n'utilisant que les images infrarouges [85], ou bien couplant la thermographie infrarouge à une mesure de champs de déplacements [71, 72].

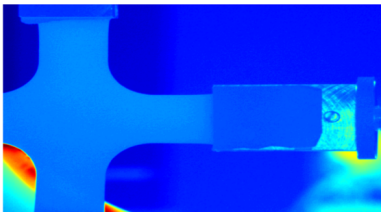

(a) Image IR avant déformation

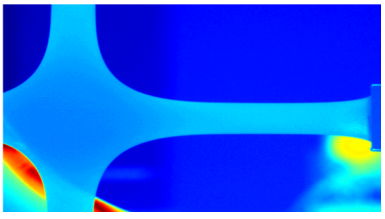

(b) Image IR après déformation

Figure 6 – Images IR pendant un essai en croix

Dans le cas présent, la corrélation d'image numérique (CIN) a été utilisée pour déter-

miner le déplacement des points dans les images thermiques. La Figure 7 montre un exemple de résultat obtenu avec cette méthode. Une analyse métrologique de la méthode a été effectuée afin de caractériser l'influence de différents paramètres sur les résultats, que ce soit en terme d'élongation, de température ou de source de chaleur.

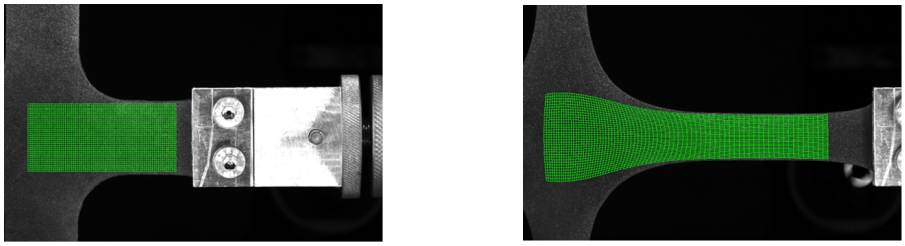

(a) Résultat de la corrélation d'image numérique

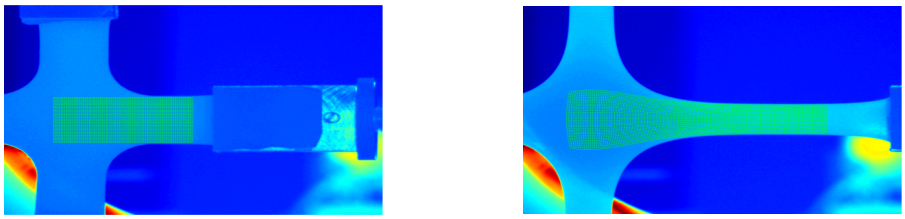

(b) Grille de corrélation numérique superposée sur l'image thermique

Figure 7 – Résultat de la compensation du mouvement

Cette technique de compensation du mouvement a été utilisée dans un premier temps pour l'identification inverse de modèles hyperélastiques. En effet, la forte influence de la multiaxialité sur les paramètres hyperélastiques fait que classiquement ces paramètres sont identifiés à partir de 3 essais différents : un en traction uniaxiale, un en traction équibiaxiale et un en cisaillement pur. Cette méthode présente beaucoup d'inconvénients, notamment le fait de devoir faire plusieurs essais de natures différentes oblige d'avoir différentes machines et différents moules pour fabriquer les éprouvettes, en plus de prendre du temps. Afin de palier à cela, une méthode se basant sur un unique essai hétérogène regroupant les trois cas de chargement a déjà été proposée dans la littérature [39, 86]. Différentes stratégies d'identification ont été mises en place à partir de cet essai hétérogène, principalement la méthode des éléments finis et la méthode des champs virtuels. Dans les deux cas, la connaissance des conditions aux limites est nécessaire, mais ces derniers peuvent dans certains cas être complexes à mesurer expérimentalement. Une méthode, se basant sur la chaleur produite par le matériau pendant sa déformation, a été développée

et fait l'objet d'un article dans *Strain* [20]. Cette méthode a été appliqueé pour déterminer le paramètre Néo-Hookéen d'un nitrile lors d'un essai biaxial sur une éprouvette en croix. L'intérêt de cette méthode est qu'elle permet non pas de déterminer un unique jeu de paramètres, mais un champ complet de paramètres hyperélastiques, comme montré sur la Figure 8. Cela signifie qu'une mesure locale peut suffire pour identifier les paramètres et qu'il n'est pas nécessaire de connaître les conditions aux limites. Les aspects métrologiques sont également abordés dans cette étude.

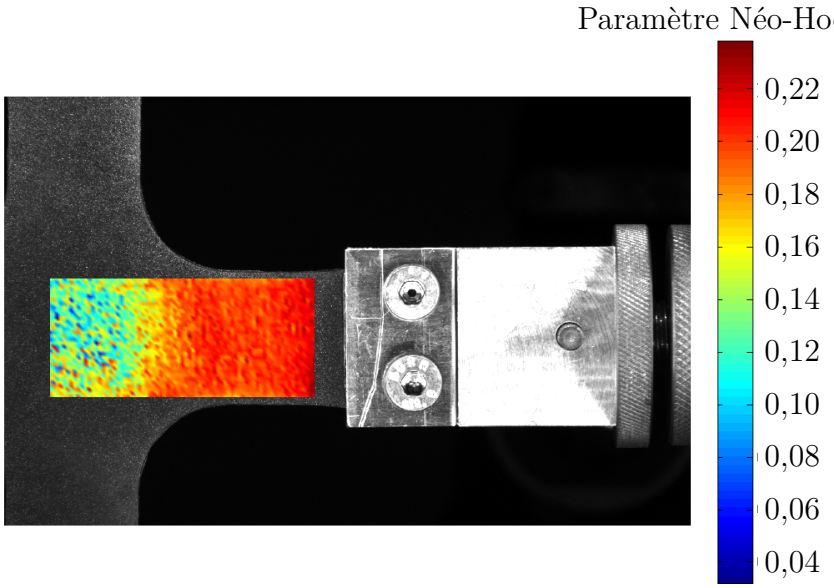

Figure 8 – Cartographie du paramètre Néo-Hookéen identifié (matériaux fourni par PCM Technologies S.A.S)

La technique de compensation du mouvement a également été utilisée sur une éprouvette composée de deux thermoplastiques différents obtenus par surmoulage, comme le montre la Figure 9. L'intérêt de l'utilisation de cette méthode est qu'elle permet d'une part d'isoler le comportement thermo-mécanique de chacun des matériaux, et d'autres part d'investiguer les phénomènes qui se déroulent au niveau de l'interface.

Pour finir, la technique de compensation de mouvement est combinée à la méthode calorimétrique de mesure de la cristallinité pour cartographier le niveau de cristallisation dans des cas complexes, comme en pointe de fissure. En effet, l'inconvénient majeur de la méthode de diffraction des rayons X est qu'elle ne donne qu'une information ponctuelle. L'obtention d'un champ de cristallinité n'est alors possible que par balayage [92], elle n'est donc pas simultanée. Ceci peut être problématique étant donné que la cristallisation dans le caoutchouc est un phénomène qui dépend de l'élongation certes, mais également

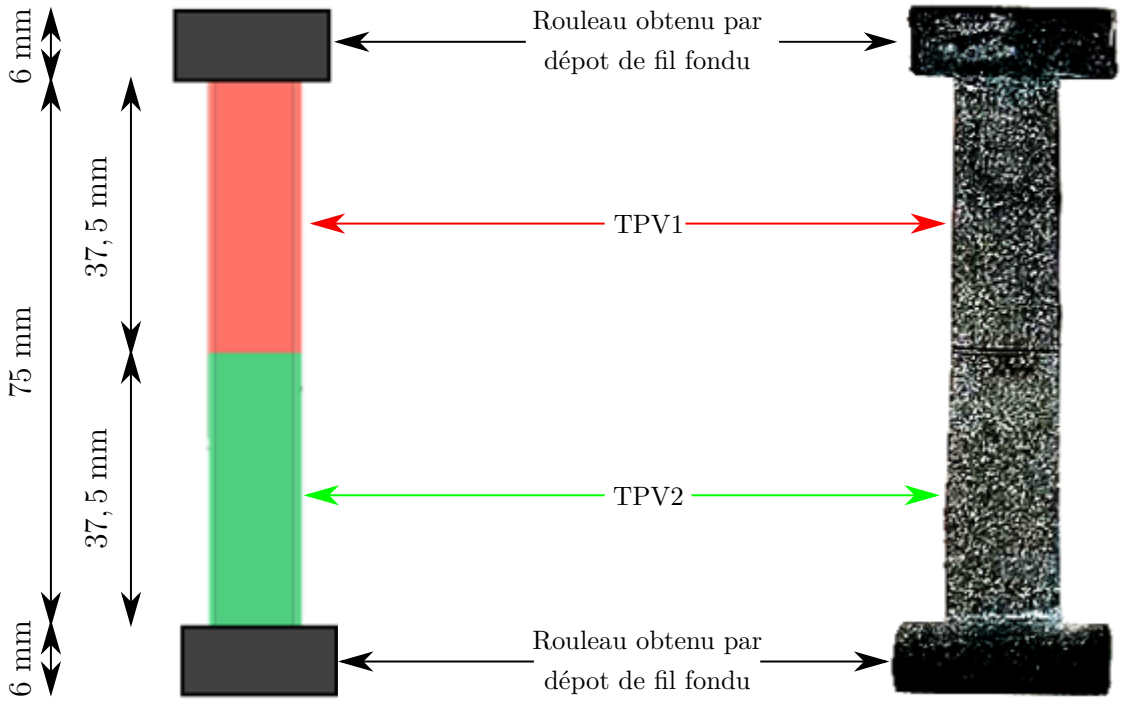

Figure 9 – Éprouvette surmoulée (matériaux fournis par Cooper Standard, dans le cadre de la thèse de doctorat de Pierre Le Mouellic en cours à l'Université de Nantes)

du temps, ce qui n'est pas le cas de la calorimétrie de surface par mesure de champs thermique. Pour des raisons de confidentialité, les résultats ne seront pas présentés ici.

INTRODUCTION

Context of the study

Since Europeans discovered the natural rubber, used for thousands of years by Central America civilizations, it takes a more and more important in the industry, because of its unique mechanical properties. First studies on the mechanical behavior on rubbers take place at the beginning of the 20^{th} century. Since then, a large number of physical phenomena as been highlighted, such as the Mullins efffect [78], the strain-induced crystallization [51], cavitation and Payne effect, non-exhaustively.

Despite all these studies, purely mechanical analyses appears as not sufficient enough to fully understand these phenomena. As all of these physical phenomena presents a calorimetric signature, the thermomechanical analysis of the rubber deformation could be seen as a promising way to enhance knowledge on these different phenomena.

In addition to its thermosensitivity, the mechanical behavior of rubber is also strongly influenced by the multiaxiality. This is the reason why rubbers are classically characterized through three different tests: one in uniaxial tension, one in pure shear and one in equibiaxial tension. This method presents many disadvantages, such as the need to make different geometries for the specimen. Recently, a new characterization method based on a single heterogeneous test including the three previously mentioned loading cases has been developed. This type of method is possible since the advent of full-field measurement techniques and will be used in the present study.

The combined use of infrared thermography and full-field measurement techniques appears to be promising for bringing new knowledge about the physical phenomena involved in the deformation of rubbers. This method has already been used for thermomechanical studies on others materials [24]. However, this approach has rarely been applied to elastomers (see for instance Toussaint et al. [108]). It could be explained by the difficulty to measure thermal field caused by the high deformations undergone by the material, which needs to go further on both metrological aspects and the implementation of the measurement technique.

The main objective of the present study is to implement quantitative imaging tools

for characterizing the calorimetric response of materials submitted to large deformations, homogeneous and heterogeneous ones. A special attention is paid on investigating the metrology associated with the calorimetric measurements performed. The tools implemented are used in order to characterize the mechanisms involved in the deformation of elastomers, especially the strain-induced crystallization.

Layout of the thesis

This manuscript is composed of four chapters. Chapter 1 is dedicated to a literature survey. After presenting some generalities, physical phenomena involved in the mechanical deformation of elastomers are described. A focus is performed on the strain-induced crystallization. Then, the state of art of calorimetric measurements is given, and focuses on the application to a stretched materials . Once the interest and limitations of the method are presented, surface calorimetry is introduced . Based on the temperature measurement and the heat equation, the method was first introduced by Chrysochoos in the 80's. This method enables us to obtain the calorimetric response of a material in several dimensions, from 0-D for the measure at one point to 2-D for full-field measurements. The technique has recently been extended to the case of large deformations. The chapter finishes on the presentation of the rare studies dedicated to large heterogeneous deformations.

Chapter 2 presents the development of a method to measure the crystallinity level within a rubber-like material. The results obtained with this method is then compared to those obtained with the X-ray diffraction technique, which is the most used method to determine the crystallinity level. Then, the calorimetric method is used to study the influence of the multiaxiality on the strain-induced crystallization phenomenon. Last, the calorimetric method is used to investigate the heterogeneity of the strain-induced crystallization phenomenon.

Chapter 3 presents a methodology to perform coupled kinematic and calorimetric full-field measurement, by coupling the digital image correlation technique with the infrared thermography. After metrological investigations in order to characterize the performance and limitations of the method, the method is applied to different cases: to identify hyperelastic models at the local scale and the thermomechanical study of an assembly of two thermoplastic elastomers by overmoulding.

Chapter 4 applies the calorimetric method for the evaluation of the strain-induced crystallinity field around a crack tip. While the strain-induced crystallinity is often evoked to

explained the high crack growth resistance of natural rubber compared to non-crystallizing rubbers, only a few studies have mapped the crystallinity around a crack tip [92], mainly due to the fact the the main measurement method to measure the crystallinity, which is the X-ray diffraction, only provides the information at a single spot. Therefore, a scan of the crack tip zone has to be carried out.

Finally, a general conclusion underlines the main results obtained, and gives perspectives for future studies.

Chapter 1

Bibliography

Contents

1.1 Generalities on elastomers

1.1.1 History

Rubber comes from South America, used by the successive civilizations that took place. One of the very first usage of this material was to make ball for a ritual sort called *pok-ta-pok* or *tlachtli*. However, these civilizations found others more practical usages for this material. For instance, they made boots by molding the rubber directly on their feet.

Europeans only discovered rubber when explorers took rubber back to Europe. More specifically, De La Condamine and de La Gataudière discovered rubber during an expedition in Peru, Ecuador and Guyana. However, natural rubber was not used industrially during a long time, mainly because rubber becomes too brittle when cooled, and sticky warmed. Moreover, the long travel time between America and Europe solidifies the material, which make it unworkable. The first usage found by the Europeans is to made erasers. In 1790, Peal patented a method to waterproof tissues by mixing resin with rubber. In 1834, Goodyear discovered that adding sulfur in rubber stabilizes it. Nevertheless, while this discovery allowed us more usages of the rubber, it does not provide a homogeneous material. In 1839, he incidentally dropped sulfured rubber in a stove, which homogenizes the material. This is the invention of the vulcanization process. However, the first patent for this process was registered by Hancock in 1843. The principles, shown in Figure 1.1, is to bound the macromolecules (in black) by using chemical bounds (here sulfur bounds in blue).

In 1845, Thomson registered a patent for car tires using rubber, but the invention was not successful. In 1888, Dunlop took up the idea of rubber tires and created the first bicycle tires. After that, Michelin brothers designed the first removable tires, at first for cycles, then for cars. Michelin company continued to enhance tires, for instance with the radial tire in 1946, and continues to do so nowadays. The structure of the natural rubber, which is shown is Figure 1.2, is found at the end of the 19^{th} century, which leads to a patent to make synthetic rubbers. But most of the researches on synthetic rubber was performed during the First World War due to the lack of access to the natural rubber. After the Second World War, synthetic rubbers are seen as an alternative to the natural rubber. Even while natural rubber is still used because of its intrinsic properties ideal for pneumatic, synthetic rubbers presents industrial advantages, since its production does not depend on climatic issues. The boom of synthetic rubbers used could also be due to some ethics issues, since the harvest of the gum have a negative image. The artificial

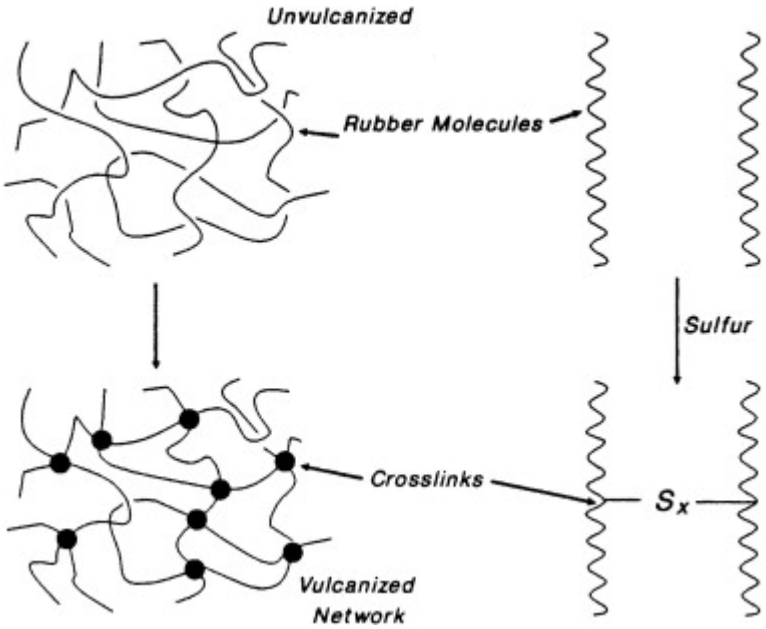

Figure 1.1 – Vulcanization using sulfur [70]

production also enables us a higher freedom in the chemical composition, which leads to an higher increases of the properties.

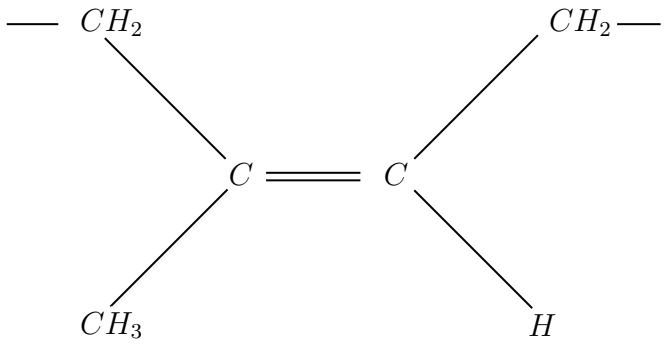

Figure 1.2 – Macromolecule of natural rubber

Rubber industry emits lot of pollution, and rubbers are not biodegradable and pollutes during and after their use. Moreover, only few recycling are developed in Europe. In addition, pneumatic emits particulates by abrasion with the road. These particulates participate to a bad air quality, which is responsible of about 3,7 millions death each year. Recycling rubber is very difficult since the vulcanization process is irreversible. Actually

several processes to devulcanizate rubbers has been found using controlled oxidation [17], micro-waves [97] or by using specific bacteria [99], but these methods could only be applied to synthetic rubber. Moreover, this operation releases toxic additives. For these reasons, used rubber parts are mostly pounds into powder to make modified asphalt, more flexible at cold temperatures and solid at high temperatures than the classical asphalt. Rubber parts can also been used as combustible in some thermal power plants.

1.1.2 Manufacturing a rubber component

Elastomers used in the industry are made using a mix between rubber (which can be natural or synthetic), and some additive products.

1.1.2.1 Gum obtention

Natural rubber requires several operations before being used in the industry. First of all, the Hevea sap is harvested by incising the bark every morning, when the temperature is low enough to make the latex liquid. After being filtered and diluted with water, the latex is treated with an acid in order to coagulate, then the mix must stand to solidify. Last, the rubber must dry. Two techniques exist, the first use a rolling mill to compress and washed the rubber and then cut into thin slices before being drained. Finally, slices are smoked to protect the rubber from oxidation and putrefaction. The second technique consists in draining the solidifed rubber in a special spin dryer where the rubber is washed, stretched and then marked with deep streaks. Synthethic rubbers are obtained by using a polymerisation process.

1.1.2.2 Mixing of different components

The mixing process can be performed by two different ways, either the normal procedure or the inverse one. The gum is inserted before the other components during the normal procedure, and after during the inverse one. Aside the gum, additives to make a rubber are a vulcanization agent, some activating and accelerating agents, plasticizers and protecting agents. The mixing process is made by mechanical milling without any solvent. This process produces heat, which can be detrimental since the vulcanization may start before the mixing process is complete. To avoid that, machines are equipped with a cooling system, and the temperature controle is a critical parameter to monitor.

1.1.2.3 Shaping process of a rubber component

Several shaping techniques are used depending on the part to be manufactured:

— The most used is the injection molding. This technique allows us to obtain any kind of geometry, using a mold and a injection molding machine, as long as it is small enough,

— Another technique used is the extrusion. This techniques provide objects with a fixed cross-sectional profile,

— The last technique is the calendering process. This method provides thin rubber sheets (maximum 3 mm), which are mainly used to cover textiles and wires.

1.1.2.4 Vulcanization

Raw rubbers have only poor mechanical properties, since their macromolecules can easily slip in relation to each others. The vulcanization process consists in creating covalent bonds between chains to avoid any slippage. Vulcanization process requires:

1. energy, often thermal (between 150 and 300 °C), but can also come from radiation or hyperfrequency,
2. the existence of reactive sites, where the chemical bounds will be created,
3. a vulcanization agent. Different agents exist and are chosen depending on the elastomer and the mechanical properties desired. The most used is the sulfur, since it is suitable to natural rubber, but others can be used, such as organic peroxides and metallic oxides,
4. time and high pressure.

1.1.2.5 Additives

As aforementioned, during the mixing process, many other components are added in order to meet industrial needs, whether it is for mechanical properties or the production. One can cite:

— accelerating agents, which speed up the vulcanization process and control sulfur bounds length,

— activating agents. Different on exist, but the main one is the zinc oxide. Since it is not solvable naturally, zinc oxide is most of the time combined with a fatty acid. Sulfur bound length can be controlled with the concentration of activating agents

in the mixture. The higher the concentration of activating agents with respect to the sulfur concentration, the shorter the sulfur bounds. Natural rubber is often vulcanized in a way to have long sulfur chains, since it increases elastic properties, at the cost of a lower heat and aging resistance,

— plasticizers spreads macromolecules, which make it easier to insert other additives. Moreover, it facilitates the shaping process and lower the heat produces during the mixing process,

— many different protecting agents can be included in order to protect the material from oxidation, chemical aggression of ozone, photosensibility or aging, non-exhaustively.

1.1.2.6 Fillers

Fillers may be added in the mixing in order to modify mechanical, chemical and thermal properties. They are gathered into three categories:

— reinforcing fillers increase the elastic modulus of the rubber, as well as modify other properties such as crack growth resistance. Main reinforcing fillers are carbon black and silica. The smaller the fillers are, the more the material is reinforced since their specific surface increases,

— inert fillers do not modify the elastic modulus, but can increase some properties that reinforcing ones do not, such as opacity to X-ray, impermeability and heat resistance,

— semi-reinforcing fillers offer a trade-off between the two previous categories.

1.2 Mechanical behavior of elastomers

1.2.1 Several complex phenomena involved

In a mechanical point of view, elastomers are well known for their ability to undergo high strains reversibly. Figure 1.3 represents a typical mechanical response of a NR specimen uniaxially stretched for multiple increasing stretches. Several complex behavior of elastomers can be observed in this curve.

1.2.1.0.1 Non-linear elasticity As shown in Figure 1.3, uniaxially stretched elastomers presents a non-linear elasticity, which can be separated in 3 distincts areas:

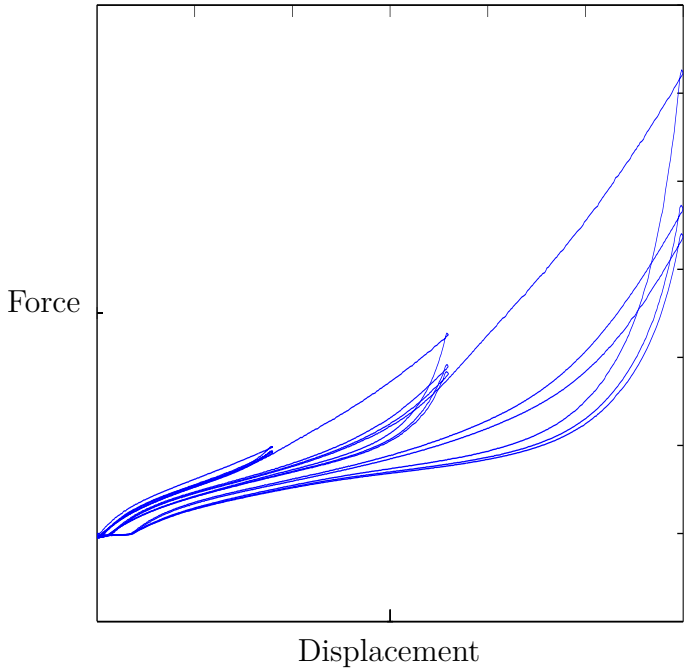

Figure 1.3 – Mechanical behavior of NR sample

— for small deformations (between 10% and 25%), the mechanical work is used to break weak bounds between molecular chains (Van der Waals bounds for instance),
— for medium deformations (from 25% to 400%), the mechanical work is used to untangle macromolecular chains between each others,
— for large deformations (superior to 400%), the mechanical work is used to extend untangled chains, which results in a higher stiffness of the materials. This increase of stiffness is all the more important that the sample crystallizes under stretch, such as the NR. This point will be addressed in the next part.

1.2.1.0.2 Mechanical hysteresis As clearly shown in the Figure 1.3, the stress-strain presents a mechanical hysteresis: at a given strain, the stress is higher during the loading curve than during the unloading curve. This hysteresis appears whatever the strain level applied, but is all the more important when the maximal strain is higher [61].

Even if several phenomena is implied in the mechanical hysteresis, the strain-induced crystallization (SIC) seems to have an major purpose in the hysteresis of NR [55].

1.2.1.0.3 Mullins effect Another phenomenon highlighted in Figure 1.3 is the stress softening for multiple cyclic loadings. Although the stress continues to shrink after several mechanical cycles, the main decrease appears between the first and the second cycle, and one can consider a stabilized behavior after three cycles. This phenomenon, referred to as the Mullins effect, was highlighted for the first time by Bouasse and Carrière [11], and deeply studied then by Mullins [78, 79]. For Mullins, this phenomenon is characterized by 4 features:

— the material stiffness decreases after the first cycle for strains inferior to the maximal strain applied in the first cycle. The more the material is stretched during the first cycle, the more the stiffness decreases,
— for strains superior to the maximal strain applied in the first loading, the stiffness is not affected. After a first cycle, the stress curve for strain superior of the maximal strain of the first cycle is equal to the stress curve of a virgin material,
— the maximal stiffness decrease is obtain between the first and the second cycle. After 3 cycles, one can assume the material to have a stabilized behavior,
— after a first mechanical cycle, near the maximal strain applied, the transition between an accommodate and virgin behavior is not instantaneous, which means that the increase of stiffness does not appear exactly at the maximal strain of the first cycle, but for a bit smaller strain

1.2.1.0.4 Viscoelasticity Even though mechanical behavior of elastomers is mostly reversible, this reversibility is not instantaneous. Actually, elastomers have a viscoelastic behavior. Viscosity can also explain the decrease of stiffness after several cycles, such as the Mullins effect, even though these two phenomena are distinct. Both Mullins effect and viscoelasticity appear to be induced by adding fillers the rubber compound.

1.2.1.0.5 Temperature effect NR stiffness highly depends on the temperature. Figure 1.4 represents a typical stiffness versus temperature curve for a rubber.

At low temperature, the stiffness highly increases, and the material behavior is getting close to a viscoelastic solid. Elastomers are almost never used at these temperatures, because they loose their special mechanical behavior. Also, elastomers can not undergo high temperatures. They are generally used between -50 °C and 100 °C approximatively.

At room temperature, an elastomer is in its rubbery state. In this state, stiffness is relatively lowly affected by temperature. However, some other mechanical properties are

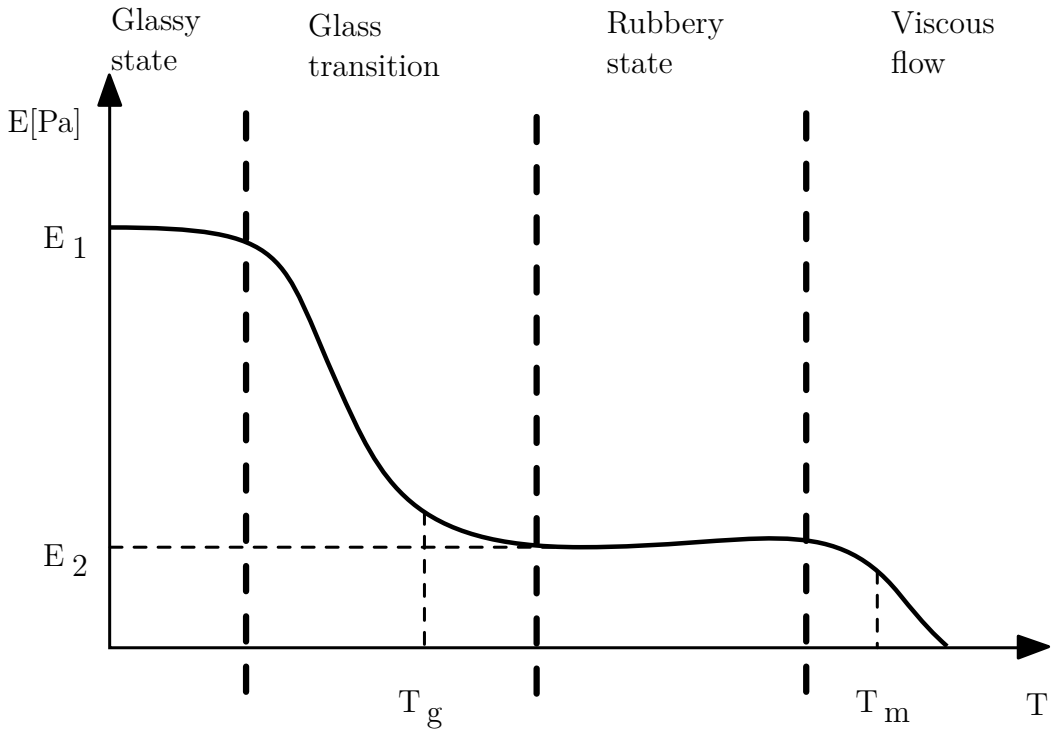

Figure 1.4 – Stiffness versus temperature curve of a polymer

still highly affected by the temperature. First, it appears that the mechanical hysteresis highly decreases with the temperature, while the residual strain after a mechanical cycle highly increases [61]. Moreover, temperature accelerates the Mullins effect recovery time. Last, temperature influence can be observed on fracture surfaces citelecamTHESIS,ruellanTHESIS. The higher the temperature, the more irregular the fracture surface. It seems to be linked to the strain-induced crystallization, since it is not observed for non-crystallizable rubbers [58].

1.2.2 Modeling of rubbers mechanical behavior

In order to predict the mechanical behavior of rubber, different models has been proposed. In the previous section, several aspects of the behavior of rubber has been highlighted. Since the different aspects seems to be independent, they can be modeled separately.

Here, we only considered the case of hyperelastic models.These models has been reviewed and compared in Marckmann and Verron [67], they are briefly recalled in the

following. First, a hyperelastic constitutive model is a model that links the current stress state with the current strain state only. In the following, hyperelasticity will characterized a strain energy W depending on the strain-state $\mathbf{F}$, as:

$$W = W(\mathbf{F}) \tag{1.1}$$

Since models considered the isotropic and incompressibility of the materials, W can be expressed as a functions of the two first invariants of the Cauchy-Green tensor $\mathbf{B}$, or a function of the three principal strain:

$$W = W(I_1, I_2) = W(\lambda_1, \lambda_2, \lambda_3) \tag{1.2}$$

1.2.2.1 Neo-Hookean model

The simplest physically-based model is the Neo-Hookean model [114], which contains only one material parameter n, which correspond to the chain density per unit volume. This model is obtained from the statistical thermodynamics of cross-linked chains. Actually, rubber can be described in a microscopic scale as a network of long flexible chains randomly oriented, connected to eachothers by chemicals bounds. The elasticity of this network is mainly due to entropic changes during the stretching. Using a Gaussian statistical distribution, Treloar obtained the following strain-energy:

$$W = \frac{1}{2} nkT(I_1 - 3) \tag{1.3}$$

with k the Boltzmann constant and T the absolute temperature. This model provides accurate results for low deformation (lower than 50%) whether it is for uniaxial tensile, simple shear or equibiaxial tensile tests.

1.2.2.2 Mooney model

Mooney [76] observed that rubber response is linear under simple shear loading condition, which lead to the following model:

$$W = C_1(I_1 - 3) + C_2(I_2 - 3) \tag{1.4}$$

with C_1 and C_2 the two materials parameters. This model is widely used for moderate deformation (lower than 200%).

1.2.2.2.1 Rivlin Series Rivlin [89] developed the strain energy W as a polynomial series of $(I_1 - 3)$ and $(I_2 - 3)$:

$$W = \sum_{i=0,j=0}^{\infty} C_{ij}(I_1 - 3)^i(I_2 - 3)^j \tag{1.5}$$

with C_{ij} the materials parameters, and $C_{00} = 0$. Actually, this model is often truncated to the second or third order, which lead to the identification of 5 or 9 parameters.

Some models are issued from the Rivlin Series, such as the Biderman [8] model, which retained the 4 following parameters: C_{10}, C_{01}, C_{20} and C_{30}, or the Haines-Wilson [49] model, expressed according to 6 parameters: C_{10}, C_{01}, C_{11}, C_{20}, C_{02} and C_{30}.

1.2.2.3 Ogden model

In 1972, Ogden [81] proposed a model that expresses the strain density as a series of real power of the principal stretches:

$$W = \sum_{n=0}^{\infty} \frac{\eta_n}{\alpha_n}(\lambda_1^{\alpha_n} + \lambda_2^{\alpha_n} + \lambda_3^{\alpha_n} - 3) \tag{1.6}$$

with η_n and α_n the material parameters. These parameters have to fulfill a stability condition:

$$\forall n, \frac{\eta_n}{\alpha_n} > 0 \tag{1.7}$$

By comparing results found using this model and experimental data, authors found that truncated this model to the third order (which leads to a 6 parameter model) give results in good agreement, either for uniaxial tension, pure shear or equibiaxial tension. This model is one of the most used model for large strains.

1.2.2.4 Rivlin and Saunders model

Rivlin and Saunders [90] tried to observed experimentally the evolution of $\partial W/\partial I_1$ and $\partial W/\partial I_2$. They observed that $\partial W/\partial I_1$ is constant, and $\partial W/\partial I_2$ only depends on the second invariant I_2. According to this, they proposed the following form for W:

$$W = C(I_1 - 3) + f(I_2) \tag{1.8}$$

with C a material parameter, and f a function that has to be determined experimentally.

This leads to many proposals for $f(I_2)$.

1.2.2.5 Gent and Thomas model

Considering the Rivlin and Saunders model, Gent and Thomas [33] proposed the following empirical model:

$$W = C_1(I_1 - 3) + C_2 ln\left(\frac{I_2}{3}\right) \tag{1.9}$$

However, this model appears being not more efficient that the Mooney model, using the same number of parameters.

1.2.2.6 Gent model

More recently, Gent [35] used for the first time the concept of limiting chain extensibility. This concept states that the first invariant I_1 admits a maximum value, and proposed the followed model:

$$W = -\frac{E}{6}(I_m - 3)ln(1 - R) \text{ with } R = \frac{I_1 - 3}{I_m - 3} \tag{1.10}$$

This model use only two material parameters, E and I_m which corresponds to a limiting value for the first invariant I_1.

1.2.2.7 Yeoh and Fleming model

As well as Rivlin and Saunders before, Yeoh and Fleming [119] performed and compared results from uniaxial tensile, equibiaxial tensile, simple shear and compression, and showed that, just like Rivlin and Saunders, that $\partial W/\partial I_1$ is more important that $\partial W/\partial I_2$, and proposed to neglect the term depending on the second invariant. They also observed that for larger strain ($I_1 > 8$), the stress tends to a constant value. Considering this, they modified the Gent model previously described to propose a new strain energy model that involves 4 parameters A, B, C_{10} and I_m:

$$W = \frac{A}{B}(I_m - 3)(1 - e^{-BR}) - C_{10}(I_m - 3) \text{ with } R = \frac{I_1 - 3}{I_m - 3} \tag{1.11}$$

1.3 The strain-induced crystallization in natural rubber

Strain-induced crystallization (SIC) is a phenomenon that turns an amorphous solid material into an ordered solid material due to the application of strain. This molecular reorganization highly affects the mechanical properties of the material, such as the crack growth resistance or the durability of the material. SIC occurs in some elastomers such as natural rubber, and is often evoked to explain its remarkable mechanical properties compared to others elastomers [41, 54].

1.3.1 Characterizing SIC

SIC of NR was discovered in 1925 by Katz [51], who achieved to obtain an X-ray diffraction pattern of an uniaxially stretched NR sample. After that, and especially during the 1930s and 1940s, many experimental techniques were used to explore more deeply SIC, such as stress relaxation [34], Raman spectroscopy [45], birefringence [113] or nuclear magnetic resonance [103]. However, X-ray diffraction is one of the most used methods, and is still used today for investigating SIC in deep.

1.3.1.1 The X-ray diffraction technique

X-ray diffraction is an experimental method to investigate the crystalline structure of powder or a thin plate samples. It consists in obtaining a diffraction pattern of an incident X-ray beam from specific directions, as shown in Figure 1.5. By measuring the angles and the intensities from the diffraction pattern, some information on the crystalline structure, such as the crystallite size, orientation, and crystallinity level, can be deduced.

1.3.1.2 X-ray diffraction pattern of NR

Figure 1.6 represents a typical diffraction pattern obtained for a uniaxially stretched NR sample. Actually, some corrections has to be made before studying the diffraction pattern. First, an air pattern, without any sample in the machine, has to be made in order to get rid of pattern due to air. Then, the variation of the sample's thickness has to be considered.

Actually, these diffraction patterns are translated into two different profiles: a first one by integrating the intensity over the azimutal direction (called X-ray spectra), and a

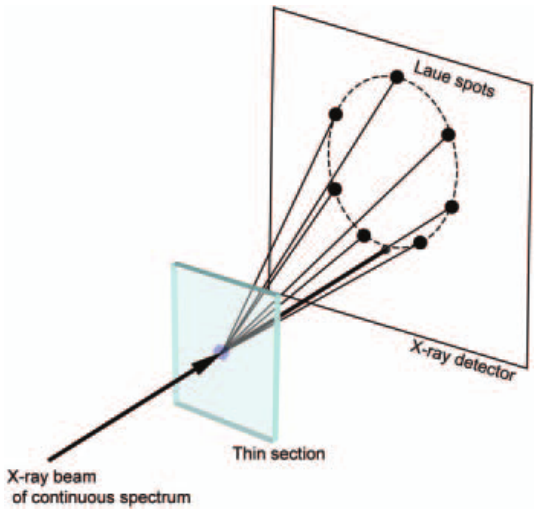

Figure 1.5 – Scheme of the X-ray diffraction technique

second one by integrating the intensity over the Braggs angle (called azimuthal profile). Figure 1.7 represents a typical spectra obtained from the diffraction pattern of a crystallized NR. In order to study these profile, they are fitted by several peaks (using for instance a Pearson or Gaussian function). Each peak corresponds to the oriented amorphous phase or a crystalline component.

1.3.1.2.1 Crystalline structure of NR From the different peaks associated with crystalline phase, several crystallographic data can be obtained.

First, from peak positions in the spectra, the crystal structure and their parameters can be deduced. Actually, the distance between two similar planes can be obtained by using the Bragg law:

$$d_{hkl} = \frac{n\lambda}{\theta} \tag{1.12}$$

with d_{hkl} the distance between two (hkl) planes, n a strictly positive integer, λ the wavelength of the X-ray used and θ the diffraction angle. Various authors proposed a crystallographic structure, with associated parameters. Even though the debate is not close yet, the orthorombic structure, shown in Figure 1.8 seems to emerge among others [69].

While the peak positions are associated with the crystal structure, their width is associated with the crystallite size and orientation. Actually, one can deduced from the diffraction pattern the size of the crystallites l_{hkl} perpendicular to the (hkl) plane by using

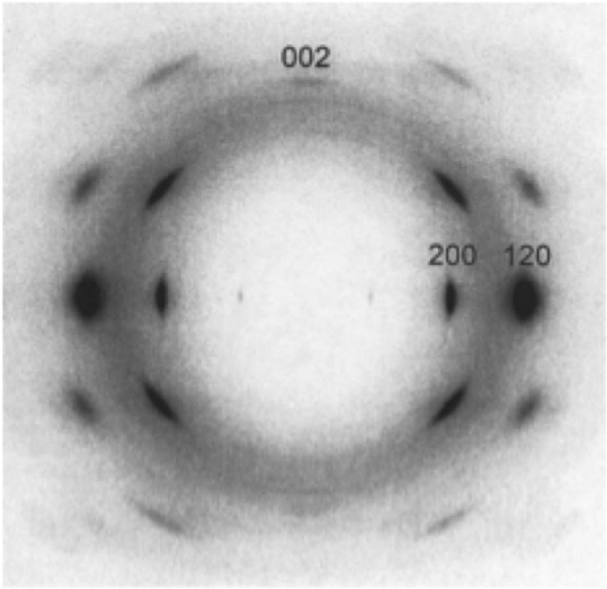

Figure 1.6 – Diffraction pattern obtained from an uniaxially stretched NR sample upon the vertical direction [106]

the Scherrer law:

$$l_{hkl} = \frac{K\lambda}{FWMHcos\theta} \tag{1.13}$$

with K a constant that depends on the crystallite shape and $FWMH$ the full width at half maximum for the considered peak.

Whereas the width in the spectra gives the size of crystallites, the width in the azimuthal profile gives the disorientation around the mean orientation. When calculated for the (002) spot of NR, it gives the crystallites disorientation relative to the stretching direction.

The last parameter that can be measured is the crystallinity of the material, defined as the material part that has crystallized. It can be obtained from spectra peak intensity. Actually, the crystallinity is measured using the following formulation:

$$\chi = \frac{I_{cryst}}{I_{tot}} \tag{1.14}$$

with χ the crystallinity, I_{cryst} the area of peaks due to crystalline phase and I_{tot} the total area of the spectra.

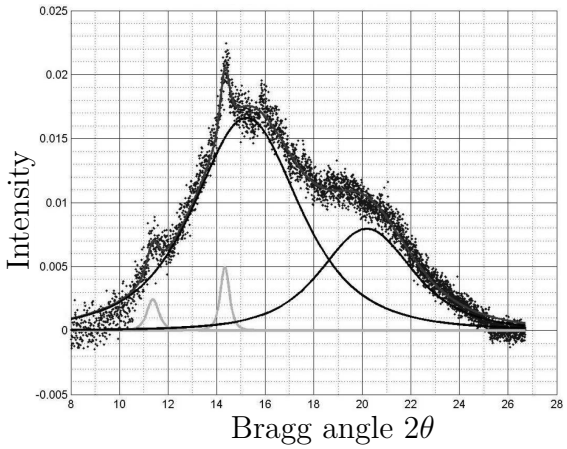

Figure 1.7 – Example of spectra extracted from the diffraction pattern, and fitted peaks using the Pearson function

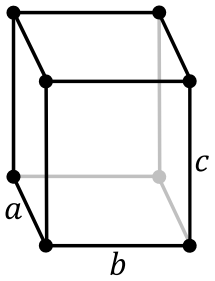

Figure 1.8 – Orthorombic structure

1.3.2 Crystallization evolution during static loadings

Since X-ray diffraction requires some acquisition time, first studies made on SIC were made at constant deformation, and aimed to obtain the time evolution of the crystalllinity at a constant strain.

1.3.2.1 Strain influence on SIC

By measuring the crystallinity at different stretch ratios, the crystallinity versus stretch curve, shown in Figure 1.9, can be obtained. In this figure, two specificity appear.

— first, the crystallization does not occur until a specific stretch ratio. This onset is located around a stretch of 4,

— then, after the onset of crystallization, the crystallinity increases almost linearly with the stretch.

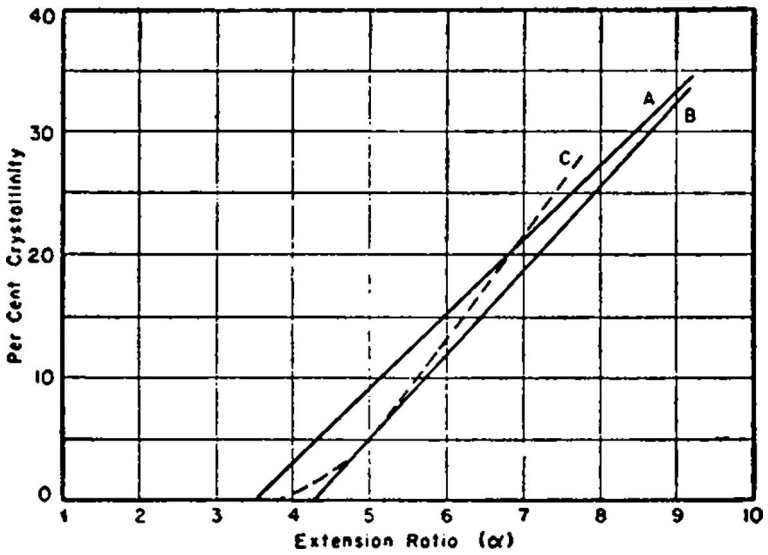

Figure 1.9 – Crystallinity versus stretch ratio at room temperature measure by Alexander, Ohlberg, and Taylor [2] (curve A), Goppel and Arlman [37] (curve B) and Nyburg [80] (curve C)

Later, some studies were devoted to the influence of the strain on the crystallite size and orientation. As expected, the more the material is stretched, the more the crystallites are oriented [31]. However, the crystallite size appears to remain approximately constant [30]. This last point highlights the fact that the increase in crystallinity is explained by an increase in the number of crystallites rather than the increase of crystallites size [44].

1.3.2.2 Crystallinity evolution at a constant strain

Some authors were interested in studying the crystallinity evolution for a static stretch [29, 107], and in all of these studies, the same conclusion was made: the equilibrium of the system is never reached. Actually, even after one full day, the crystallinity keeps growing, which means that every crystallinity measurement have to be made at a specific time in order to be compared, which can explain discrepancies observed in Figure 1.9.

Other authors studied the beginning of the crystallization, and face a major issue: the long time required to perform a X-ray diffraction pattern. This issue has been bypassed by combining multiple cycles and a stroboscopic technique, to accumulate the diffraction pattern intensity. Using this method, they suggested that the SIC phenomenon is not instantaneous, but requires a certain amount of time to take place [88]. This delay strongly depends on the stretch (1 s for $\lambda = 4$ and 50 ms for $\lambda = 5$) [29].

1.3.3 Crystallization during uniaxial tensile loading

1.3.3.1 Influence of the SIC on the mechanical hysteresis

The stress-strain curve of NR is well known to present a hysteretic behavior, and the hysteresis loop is generally more important for crystallizing rubbers, which suggests that SIC has a role in the hysteresis seen in the mechanical behavior. However, due to the long acquisition time needed to make X-ray measurement, this method was not used to study the link between SIC and the mechanical hysteresis, until the use of synchrotron radiation [110], which allows us to make real-time diffraction pattern. Figure 1.10 represents a stress-strain curve, with the corresponding crystallinity evolution.

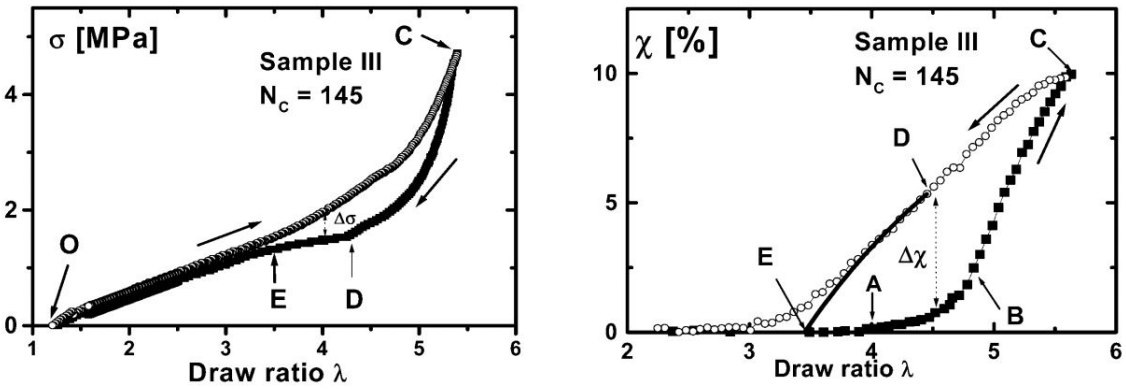

Figure 1.10 – Stress-strain curve (in the left) and corresponding crystallinity (in the right) during a mechanical cycle [110]

Several points are highlighted by this figure:

— first, the crystallization starts around $\lambda = 4$. The crystallization seems to harden the materials,

— second, during the retraction phase, the crystallinity is higher than during the tension phase [26]. This difference is attributed to the "super cooling effect" [**trablesi03a**],

— third, once all the crystallites have completely melt at the end of the cycle, the stress curve is almost superimposed to the stress curve during the tension phase.

The major conclusion is that the mechanical hysteresis is mainly due to SIC, and not to the viscoelasticity of rubber.

1.3.3.2 Crystallites size and orientation

Other studies focused on the microscopic structure of crystallites, and their evolution during the mechanical loading. Before SIC starts, the macromolecules become more and

more aligned, which makes sense since they need to be aligned before crystallizing [88]. Then, the orientation does not change until the beginning of the retraction phase, in which the crystallites seem to be more and more disoriented, until the melting [110]. It can be explained by the fact that during the retraction phase, crystallites are less constrained in space, and can move more easily.

For the crystallite size, while all studies confirmed the fact that the crystallite size in the stretching direction does not evolve during the tension-retraction cycle [110], the evolution in the two other directions is not so clear. Whatever, even though the crystallites volume increases, it does not completely explain the increase in crystallinity, which confirmed that the increase of crystallinity is mainly due to an increase of the number of crystallites rather than an increase of their volume.

1.3.3.3 Influencing factors on the crystallization

The knowledge of the influence of experimental parameters could provide some keys to better explain the SIC phenomenon. Here, the influence of 3 key parameters is described.

It is well known that the addition of fillers, and more especially carbon black fillers, stiffens NR [111]. By comparing the crystallinity during a tension-retraction loading, some points can be deduced:

— first, the crystallization starts at a lower stretch ratio ($\lambda = 2$ instead of $\lambda = 4$) [32]. Actually, the local strain is higher than the macroscopic strain. In fact, only the elastomeric part is supposed to deform, while the fillers remain undeformed [84]. Using this assumption, the local strain for the onset of filled rubber is close to the macroscopic strain for the onset of unfilled rubber,

— second, the "super cooling effect" is less important with fillers,

— third, the maximal crystallinity reached is lower, mainly due to the reduction of matter that can crystallize.

Moreover, crystallite size seems to be lower [84], and they are less orientated, which is consistent with the reduction of the macromolecular chain mobility due to the addition of fillers.

Since SIC is a highly thermosensitive phenomenon, it seems logical that temperature changes affects SIC. All studies show that the crystallinity is reduced when the temperature increases, and becomes almost null when the temperature is equal to 80 °C [1]. These studies also show that the crystallization appears for higher stretch ratios with a higher temperature. While studying the effect of temperature on SIC is easy for temperatures

higher than room temperature, it is more complex for lower temperatures, since it involves another phenomenon, the temperature-induced crystallization or "cold crystallization" [5].

As seen previously, SIC is never in a equilibrium state, even after a long time during a static test. Nevertheless, SIC appears very quickly with the stretch, but not instantaneously. This time lag can explain the shift on the onset crystallization from $\lambda = 5$ to $\lambda = 6$ when the strain rate is increased by 4 order of magnitude [75]. With a higher strain rate, the stress also increases for the same mechanical loading. This can be explained by the antagonist effect of SIC and macromolecular chain relaxation. With an higher strain rate, the chains have not enough time to relax, which leads to an increase of the stress, while with a lower strain rate, the chains can relax more, which leads to a decrease of the stress. Moreover, the fatigue response has been studied using multiple mechanical cycles and results show that SIC totally disappears when the loading frequency is too high [109]. This can be explained by two different effects. On the first hand, the temperature increases with the frequency, due to mechanical dissipation, which leads to a reduction of the crystallinity. On the other hand, the time lag required for the crystallization to occur can be higher that the time available during the mechanical loading.

1.3.3.4 Crack propagation and SIC

The reinforcement of SIC on crack growth resistance can be demonstrated through fatigue test. Actually, two differences occur between crystallizable rubbers and non-crystallizable ones:

— on the one hand, one can observe a higher fatigue life for crystallizable rubbers than for non-crystallizable ones, which seems to indicate that SIC can be at the origin of this reinforcement,

— on the second hand, the observation of the failure surface of crystallizable rubbers reveals striation patterns that do not appear on failure surface of non-crystallizable rubbers. This seems to indicate that striation pattern is due to SIC phenomenon.

In order to find out the link between SIC, striations and fatigue life reinforcement, Ruellan et al. [93] performed several fatigue tests on diabolo-shape specimens under a wide range of loading ratios and loading levels, at different temperatures. For each set of parameters, the lifetime before fracture and the type of failure surface is recorded and analyzed. Three types of failure surface were observed:

— Regime 1 corresponds to small striations with wrenchings, and seems to corresponds to a transition between full wrenchings and full striation zones,

— Regime 2 corresponds to the full striation zone, and is always preceded by the regime 1,
— Regime 3 corresponds to failure surface without any striations, which corresponds to the failure surface of a non-crystallizable rubber.

The fatigue life and failure surface examination for several loading ratios, loading levels and temperatures [94] leads to multiple conclusions:

— striations appears whatever the loading ratio, but are more numerous for non-relaxing loading conditions, in which SIC is promoted. This seems to indicate that striations are a signature of SIC,
— at room temperature, a fatigue life reinforcement is observed for non-relaxing loading conditions, which seems to indicate that SIC improves the crack growth resistance,
— at 90 °C, striations does not appear anymore. As seen before, SIC is highly dependent on the temperature and is almost inexistent for this temperature level. It denotes that striations require a minimum level of crystallinity to take place,
— at 90 °C, fatigue life reinforcement still exists, but is lower than at room temperature. This seems to indicate that a small crystallinity level increases the crack growth resistance,
— at 110 °C, neither striations nor fatigue life reinforcement is observed. The materials behaves as a non-crystallizable rubber.

To better understand the influence SIC in crack growth resistance, a study was made to obtain the spatial distribution of crystallinity around a crack tip, by comparing X-ray diffraction and DIC results [92]. The tests are performed on pure shear sample, in which a crack is made before the test, for a crystallizable rubber and a non-crystallizable one.

First, the multiaxiality and thickness changes are measured from both DIC and X-ray diffraction techniques, and are in good agreement. Then, using X-ray diffraction results, the distribution of crystallinity around the crack tip is obtained for different global stretches. Results are shown in Figure 1.11.

It shows that the closer to the crack tip, the higher the crystallinity, which matches well with the fact that the closer to the vicinity of the crack, the higher the strain.

Then, the tearing energy is measured for different global stretch levels, in order to compare the evolution of the tearing energy with the crystallinity level. This measurement is based on the energy balance approach of Rivlin and Thomas, which is an extension of the energy release concept of Griffith to hyperelasticity. In the case of pure shear samples,

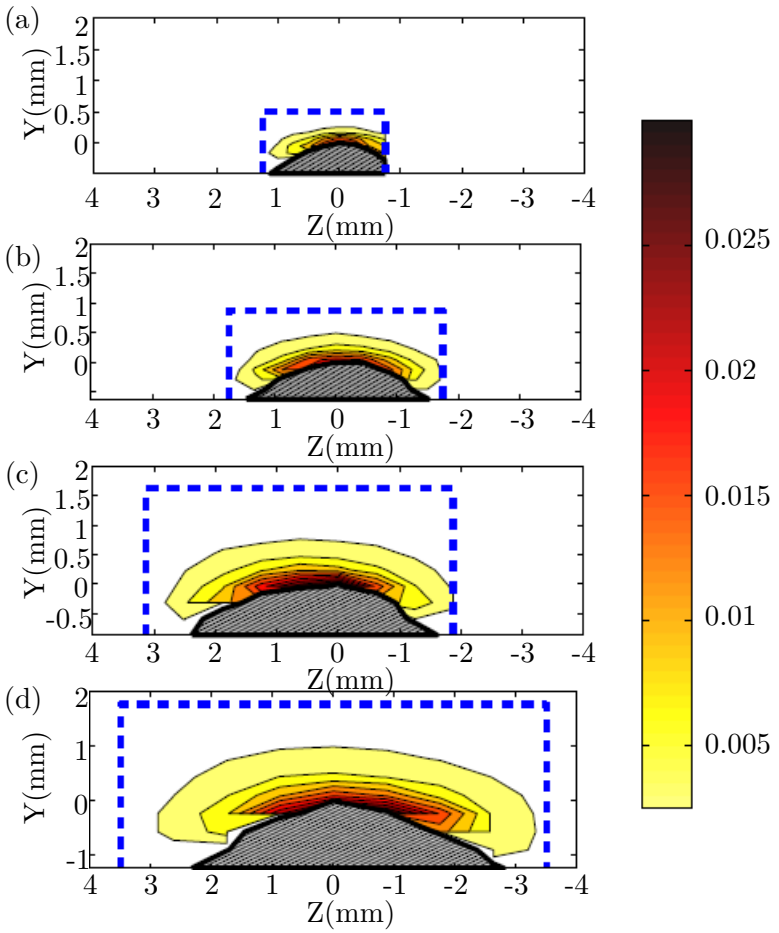

Figure 1.11 – Distribution of the crystallinity around a fatigue crack tip for four different values of tearing energy (deformed configuration): (a) T =4 620 J/m^2, (b) T =7 290 J/m^2, (c) T =10 390 J/m^2, (d) T =14 140 J/m^2 [92]

it leads to the following relation:

$$T = W_0 l_0 \tag{1.15}$$

with T the tearing energy, W_0 the strain energy density per unit undeformed volume and l_0 the height of the undeformed sample.

In addition of the tearing energy measurement, the crack growth rate is measured by measuring the crack size at different time. Results show that the more the material is crystallized, the more tearing energy is required to propagate the crack, which tends to prove that SIC slows down the crack growth rate.

1.3.4 Influence of biaxiality loadings on the SIC

In all the studies presented earlier, SIC has been investigated through uniaxial tensile loadings. One may wonder what happens when the crystallizing material undergone biaxial loadings.

1.3.4.1 Crystallites produced by biaxial loading

Recently, Beurrot et al [6] compared X-ray diffraction patterns for the same material under uniaxial state, equibiaxial state and intermediate biaxial state. These patterns are showed in Fig.1.12. In the following, the crystallinity index is not discussed, but the

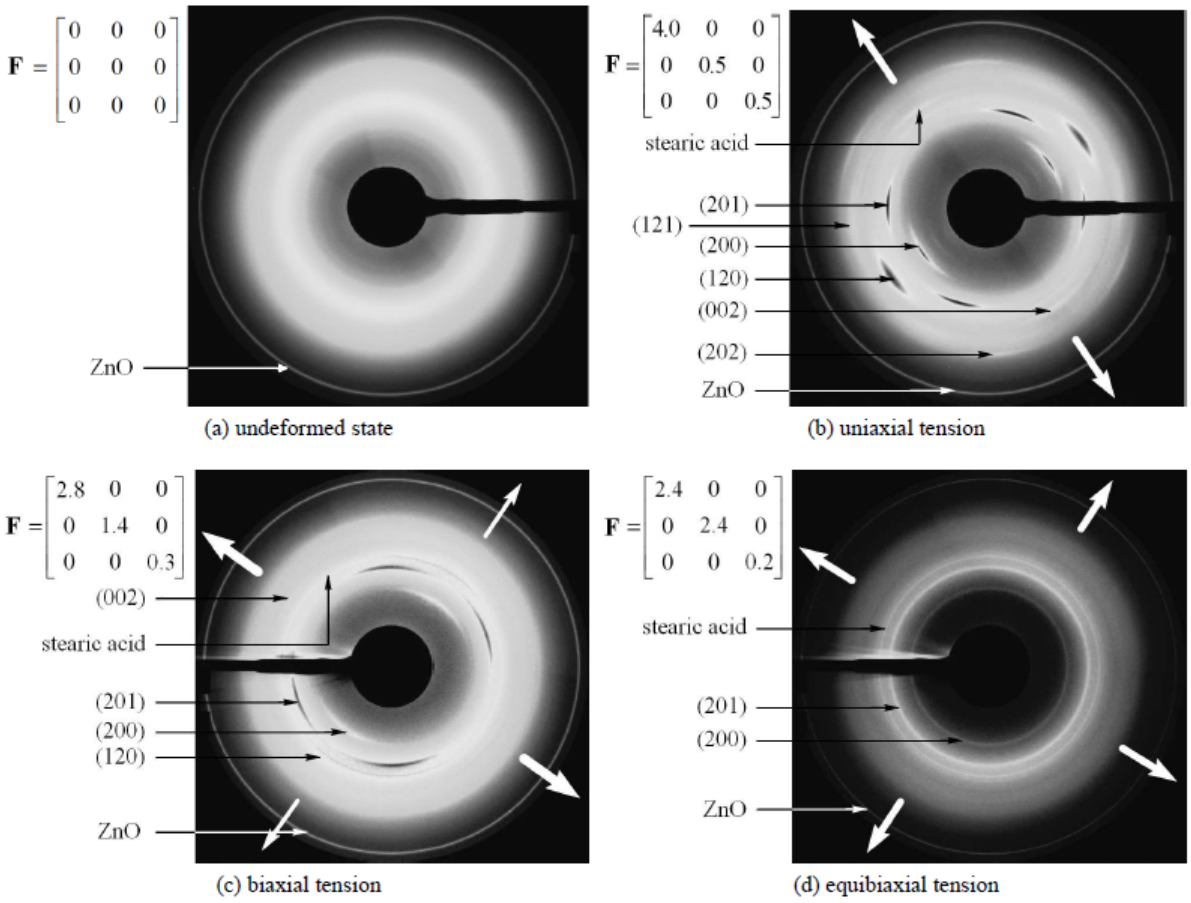

Figure 1.12 – X-ray pattern of NR in different deformation states (**F** is the deformation gradient tensor, white arrows show the tensile directions [6])

crystallites size and orientation are deduced from these diffraction patterns.

First, crystallite size and structure is deduced from the diffraction patterns. It appears

that, both the size and the structure of the crystallites is approximately identical for the three tests. Using the results seen previously that that shows the crystallites do not change significantly with the stretch, one can deduce that the crystallites do not depend on the strain state.

Then, crystallite orientation is deduced from diffraction patterns. The equibiaxial pattern presents rings, which shows that the crystallization is isotropic in the plane of tension, in opposition to the crystallization in the uniaxial pattern, in which the crystallites are oriented in the stretching direction. For the biaxial pattern, as it seems to make sense, the crystallites are oriented along the principal stretch direction, but the disorientation is higher than in the uniaxial state. To conclude, the higher the biaxiality, the higher the disorientation, until a total isotropic crystallization.

1.3.4.2 Frustration of SIC under biaxial loadings

The previous studies show that the crystallites formed are identical for biaxial loading and for uniaxial loading, and their disorientation increases with the biaxiality. However, the crystallinity level is not discussed, which leads to the question: does crystallization occur in equibiaxial state? In order to answer this question, another study [21] has been done, using uniaxial test and biaxial tests with several biaxiality coefficient, which represents the multiaxiality of the mechanical loading. They conclude that crystallinity is lower under biaxial strain states, and crystallization does not occur if the biaxiality is too important at room temperature. They suggest that during an uniaxial stretch, the different macromolecular chains can be aligned, which is necessary for the crystallization to occur, since biaxial loadings do not align enough the chains to allow crystallites to form. This is illustrated in Figure 1.13.

1.3.5 Conclusion

Since its discovery by Katz [51], the strain-induced crystallization phenomenon has been widely investigated, mainly using the X-ray diffraction technique. While this technique allows us to obtain many information about the crystallite size and orientations, this technique has some disadvantages. First, the technique required a relatively long acquisition time, which complicates measurement for higher strain rate. Moreover, the technique can only give the information at a single spot. Therefore, in case of crystallinity field heterogeneities, such as those at a crack tip, the spatial distribution of crystallinity

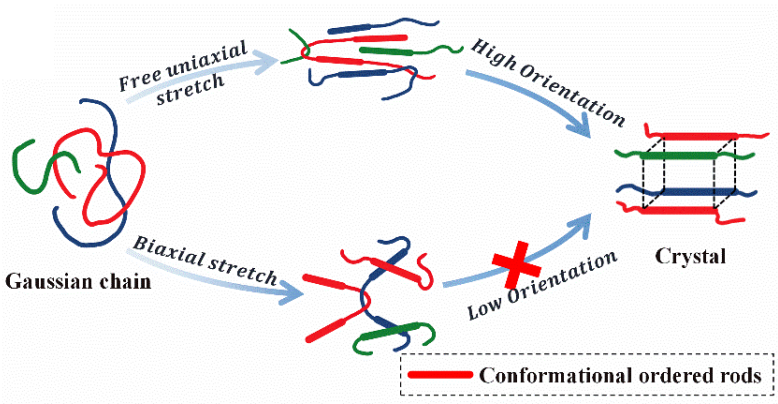

Figure 1.13 – Scheme of the formation of crystallites from oriented chains during uniaxial and biaxial stretch [21]

can only be obtained by sweeping the zone observed [92]. This could be a problem when the state of the material evolves with the time. More generally, a number of questions remains unanswered and alternative experimental techniques have to be used or developed to investigate the mechanisms involved in the deformation of rubbers, especially SIC.

However, the X-ray diffraction is not the only effect of SIC. Actually, SIC is a highly exothermal phenomenon [77]. It means that the crystallinity could be deduced from the temperature measurement of the specimen during the crystallization process. Such a method permits a simpler measurement of crystallinity map, since the advent of full-field temperature measurement technique. In this work, the calorimetric method will be used to measure the crystallinity and to bring new information for a better understanding of the phenomenon, such as a better measurement in case of large heterogeneities, or clues about the influence of the multiaxiality on the crystallinity.

1.4 Calorimetry

1.4.1 Generalities

Calorimetry is the science that measures heat transfer between bodies. Actually, the energy conservation law states that energy can neither be created nor destroyed, but that energy changes in form during energy transfer. Generally, these are made by heat absorption or production. In order to measure energy involved, it is necessary to use an isolated system, called calorimeter, which does not allow any matter or energy tranfert to take place with the environment.

Heat produced by a body can be determined from the temperature variation of this body as follows:

$$Q = mC\Delta T \tag{1.16}$$

with Q the quantity of heat transferred (in J), m the mass of the body (in kg), C the calorific capacity (in J/kg K) and ΔT the temperature variation of the body (in K). By convention, a positive heat quantity corresponds to heat absorbed by the body while a negative quantity indicates that the body gives heat to its surrounding environment.

To calculate the heat transferred between two systems, it is assumed that the heat given by a system is equal to the heat received by the second one.

Calorimetry is an effective analytical tool to characterize the thermophysical properties of a material. It allows the determination of the crystallization, melting and mesomorphic transition temperatures, as well as their corresponding enthalpy and entropy changes. Other parameters can be studied, such as the glass transition, as soon as the phenomenon impacts either the heat capacity or the latent heat. Calorimetry takes a special place among other methods, due to its simplicity of use and the clear physical meaning of every energetic characteristics, even though sometimes the interpretation can be difficult.

Several calorimetric methods have been developed, but the differential scanning calorimetry (DSC) appears as a very reliable technique in material science. The most common mode DSC is the linear scan. It consists in heating or cooling a sample at a constant rate. The primary outcome of such an experiment is a plot of the heat flow versus either the time ot the temperature. From the heat flow, the specific heat capacity can be deduced.

This method has been applied for instance to measure the solidification of autenitic stainless steel [101] at different cooling rate. Figure 1.14 represents the solidification for a same steel at three different cooling rates. As seen in the figure, the cooling rate has a high influence on the solidification mechanisms, especially the liquidus temperatures become lower with a higher cooling rate (1442.9 °C for a cooling rate of 25 K/ min versus 1454.7 °C for a cooling rate of 5 K/ min).

1.4.2 Calorimetry under stretch

Müller et al. [77] developed a stretching calorimeter, which allow to performed traction test on specimens while measuring at the same time the calorimetric response of the material. In his study, some classical cases has been investigated before handling with the case of rubber.

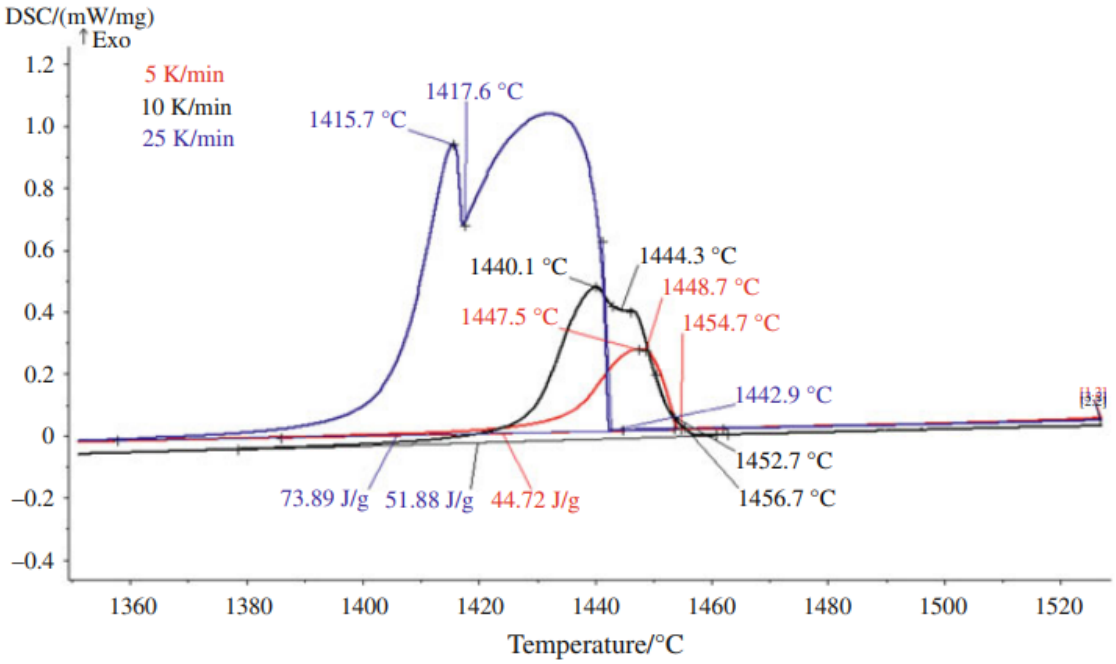

Figure 1.14 – DSC solidification curves for austenitic stainless steel at various cooling rate [101]

First, the case of pure elastic material has been investigated. Figure 1.15 represents both the heat flux (upper curve) and the force (lower curve) while performing mechanical cycle of a steel wire. This figure clearly shows the energetic elasticity behavior of the material, since the heat flux is negative (ie the specimen become cooler) when the material is stretched and the heat flux is positive (ie the specimen become hotter) when the material is compressed.

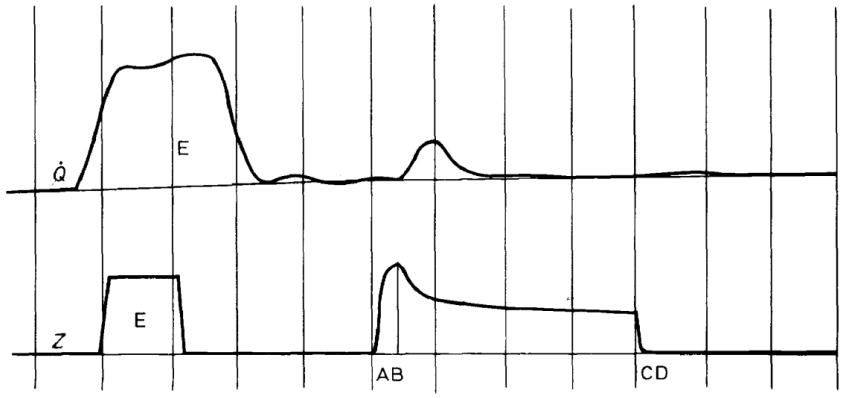

Figure 1.15 – Recording of the heat flux and the force of a steel-wire [77]

Second, the case of a pure plastic material has been investigated. Figure 1.16 represents both the heat flux (upper curve) and the force (lower curve) while performing mechanical cycle of a tin wire. At the end of the elongation, a relaxation of stress is observed.

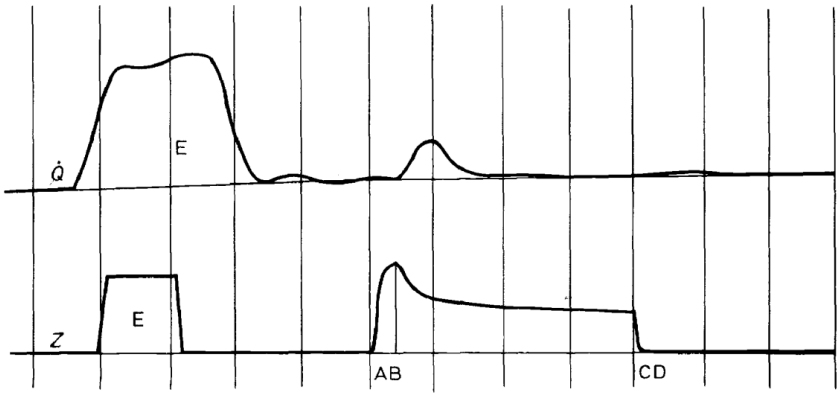

Figure 1.16 – Recording of the heat flux and the force of a tin-wire [77]

Then, the calorimetric response during the mechanical deformation of rubber, shown in Figure 1.17 is studied. Since a purely thermoelastic couplings would lead of a symmetrical heat flux curve in the loading and the unloading of the specimen, an asymmetry is observed. Moreover, heat production should stop as soon as the elongation process is finished, which does not corresponds to the observations made. The author explained this with the strain-induced crystallization phenomenon, which is an exothermal phenomenon. Moreover, the degree of crystallization can be calculated from the measured heat. Figure 1.18 represents the heat part due to crystallization process for different stretching level.

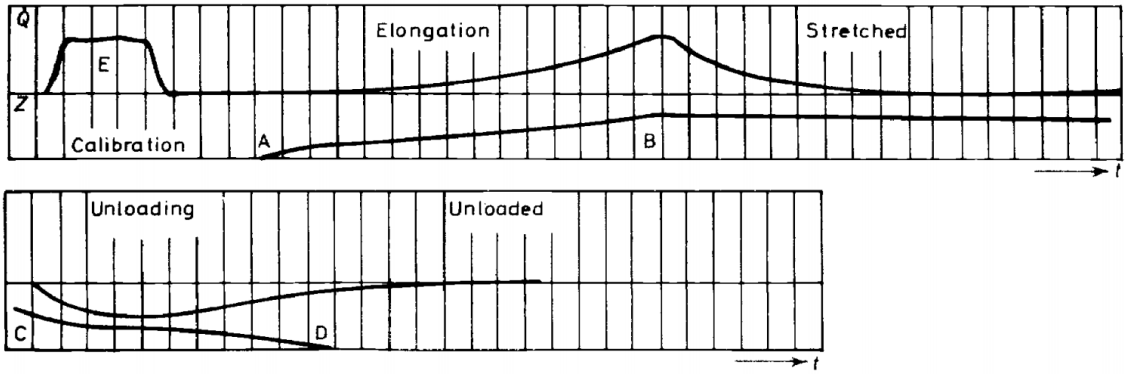

Figure 1.17 – Recording of the heat flux and the force of a rubber specimen [77]

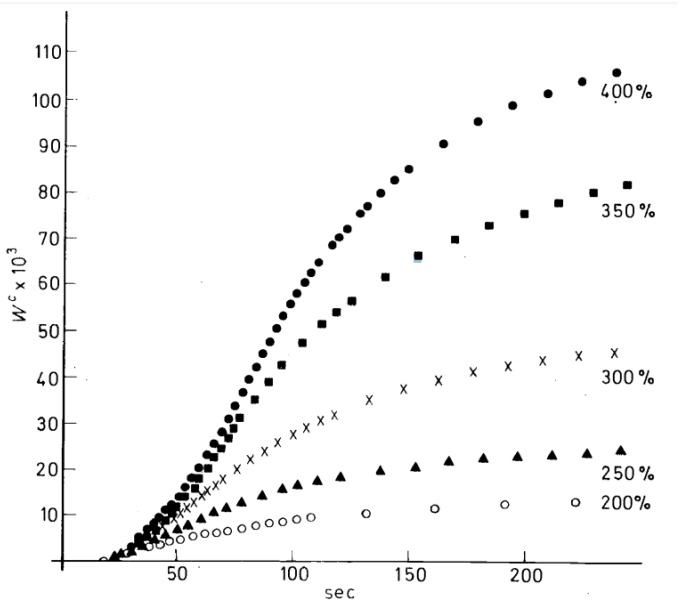

Figure 1.18 – Measured values of the crystalline part of heat for natural rubber as a function of the time [77]

However, the method presents a huge limitation; it can only measure a global, i.e. an averaged, heat flux. Therefore, it is impossible to detect any heterogeneities in the heat flux, typically induced by singularities like cracks, as shown in 1.19. This is the reason why surface calorimetry is an alternative measurement of interest, it is precisely described in the next paragraph.

Remark on the thermal stress analysis: calorimetry is widely used in material science in order to bring more information on the phenomena that occur during the mechanical deformation of a material. For instance, Boulanger et al. [12] use the calorimetry to study separately the thermoelastic couplings and dissipated energy induced by micro-structural defects on a dual phase steel. First, they consider the heat production due to thermoelastic couplings. Assuming that the thermoelastic behavior of the steel is linear, the heat power density can be approximated as [60]:

$$s_{the} = -\alpha T_0(\dot{\sigma} + \alpha E\dot{\theta}) \tag{1.17}$$

with s_{the} the heat source from thermoelastic couplings, σ the tensile stress, E the Young's modulus, T_0 the reference temperature and α the thermal expansion coefficient. Figure 1.20 represents the temperature variation uniaxially stretched with a loading amplitude of 360 MPa, a loading frequency of 50 Hz and a load ratio of 0. In this figure, the

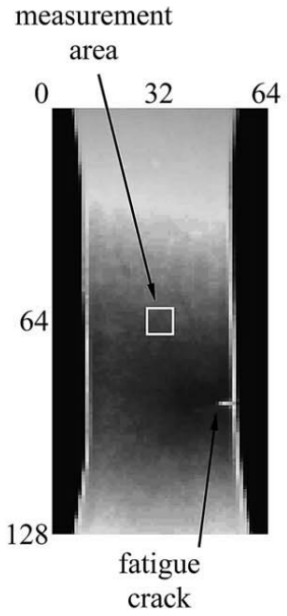

Figure 1.19 – Temperature field during crack propagation [12]

temperature variation θ_d due to the mechanical dissipation and thermoelastic effect are clearly visible.

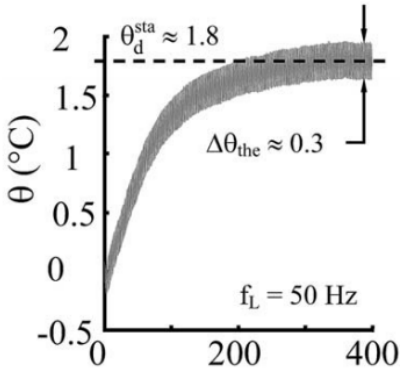

Figure 1.20 – Whole temperature evolution during a block at 50 Hz [12]

To study the thermoelastic behavior, tests were performed at a low loading frequency (1 Hz) to avoid dissipation. Figure 1.21 clearly shows a linear relation between the amplitude of temperature variation and the amplitude of the loading. Moreover, the slope of the curve is directly linked with the thermophysical parameters of the materials.

Then, the dissipation behavior is studied. Figure 1.22 represents the evolution of the mean dissipation $\bar{d_1}$ during blocks performed at increasing stress ranges, at the loading frequency of 50 Hz. Three stages can be observed:

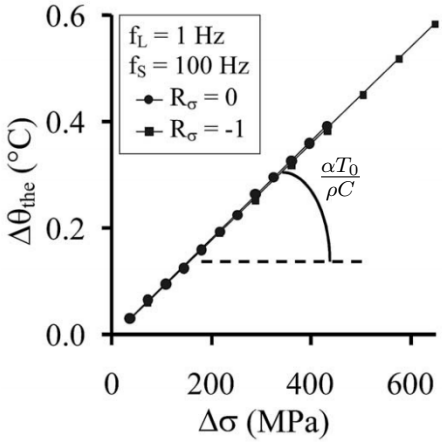

Figure 1.21 – Thermoelastic data checking [12]

— for low stress ranges, low $\bar{d_1}$ is observed, and increases linearly,
— for medium stress ranges, $\bar{d_1}$ remains approximatively constant during a block, however, the dissipation is not linear with the stress ranges,
— for high stress ranges, the dissipation decreases substantially until a stabilized value.

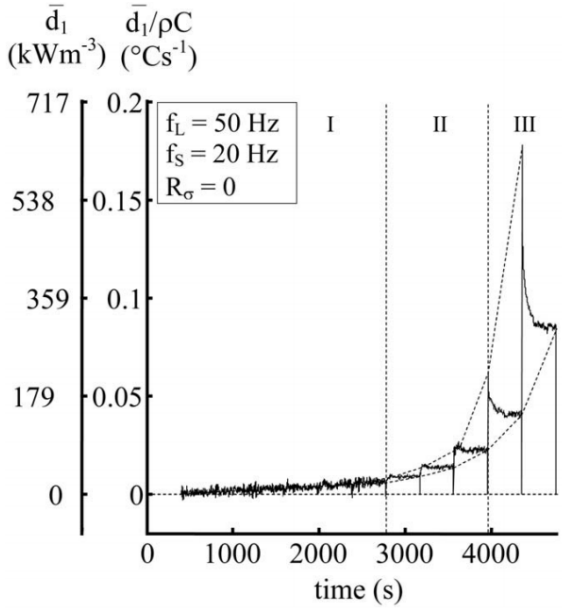

Figure 1.22 – Dissipation evolution during a block series [12]

1.4.3 Surface calorimetry using infrared thermography

In order to overcome the limitations of the calorimetric method, the use of infrared thermography, which can measure the full temperature field at a specimen surface, has been proposed to performe surface calorimetry. First of all, a brief recall on infrared thermography is given.

1.4.3.1 Infrared thermography

Infrared thermography (IRT) is based on the radiation emitted by a body. Actually, every body can lose some of their energy in the form of radiation, and can absorb the radiation of environment bodies. At the beginning of the 20^{th} century, Planck [83] determined the emittance of an ideal body, called black body, which corresponds to the radiation emitted per unit surface. This emitance, noted M_0, depends on the absolute temperature T:

$$M_0(T) = \sigma T^4 \tag{1.18}$$

with σ =5.67.10^{-8} W $\cdot$ m^{-2} $\cdot$ K^{-4} the Stephan-Boltzmann's constant.

Actually, most of measures are made in term of luminance, which is defined as the radiated power per unit solid angle. The integration of the luminance over a hemisphere is equal to the emittance, which is, in the case where the luminance does not depend on the direction, leads to:

$$L_0 = \frac{M_0}{\pi} \tag{1.19}$$

with L_0 the luminance of a black body.

Since a black body represents an ideal body, which emits the maximum power for a given temperature, real materials emit a fraction of this power. The emissivity ε of a material corresponds to the ratio between the luminance of a real body L and a black body L_0, and is within the range of 0 and 1:

$$\varepsilon = \frac{L}{L_0} \tag{1.20}$$

Various parameters affect the emissivity of a material, such as the temperature, the wavelength or the direction of the measurement.

1.4.3.2 Quantitative infrared thermography measurement

An IR camera is a device with a matrix of thermal sensors, which measure the radiation flux. Two main sensor types can be used:

— quantic sensors are detectors that are directly sensitive to photons received. They are the most sensitive types of sensor, but need to be cooled.

— bypolometric sensors are sensible to the heating due to the radiation. The main advantages is that they can be used without any cooling system. However, their thermal resolution is lower than quantic sensors one.

In material science, quantic sensors are increasingly used as they provide an accuracy of the order of 20 mK.

In fact, the sensors do not measure the whole radiation, but only those in a certain bandwidth, in order to be less sensible to the atmosphere. Two spectral bandwidths can be used: from 2 to 5 µm and from 7 to 14 µm. Since the sensors measure only a part of the radiation and by assuming that the emissivity is constant over the bandwidth used, the luminance can be expressed as:

$$L(T) = \frac{\varepsilon \int_{\lambda_1}^{\lambda_2} M_0(\lambda, T) d\lambda}{\pi} \tag{1.21}$$

$$L(T) = \frac{\varepsilon \sigma' T^4}{\pi} \tag{1.22}$$

with σ' a constant that depends on the bandwidth used.

IRT is based on the measurement of radiation emitted by a body. However, since every body emit radiations, the light flux received by a sensor does not only depend on the radiation emitted by the specimen itself, but also on its surrounding environment [19]. Figure 1.23 represents the main radiations received by an IR sensor. In addition to the flux coming from the body, three main interferences can be observed:

— first, the surrounding environment may be reflected on the body surface, which leads to an additional flux seen by the sensor,

— second, the atmosphere can interfere in two separate ways. On the first hand, some of the radiation emitted by the body can be absorbed by the atmosphere. On the other hand, the atmosphere itself emits some radiations, which will be capted by the sensors,

— third, the optics absorbed some of the flux emitted from all sources before reaching the sensors.

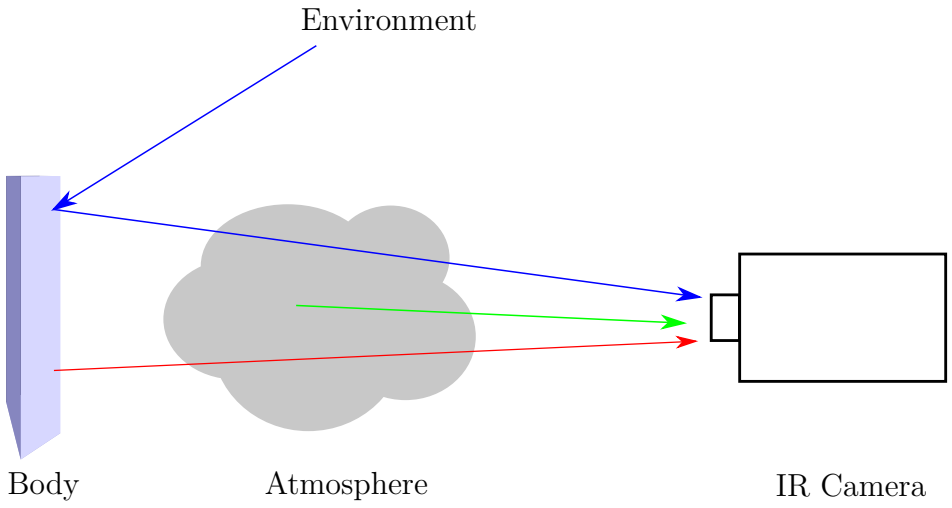

Figure 1.23 – Main contributions of total flux capted by IR sensors

As a first approximation, the luminance measured can be expressed as [74]:

$$L_{measure} = \tau_{opt} \left[\tau_{atm} \left(\varepsilon L_0(T) + (1-\varepsilon) L_0(T_{env}) \right) + (1-\tau_{atm}) L_0(T_{atm}) \right] \tag{1.23}$$

with τ_{opt} the transmission coefficient of the camera optics, τ_{atm} the transmission coefficient of the atmosphere, ε the emissivity of the body, $L_0(T)$ the luminance of a black body at the temperature T, T the temperature of the body, T_{env} the temperature of the environment and T_{atm} the temperature of the atmosphere.

By applying the expression of the luminance given by Equation 1.22 in the total luminance measured in Eq.1.23, the following formulation is obtained:

$$L_{measure} = \frac{\tau_{opt}\sigma'}{\pi} \left[\tau_{atm} \left(\varepsilon T^4 + (1-\varepsilon) T_{env}^4 \right) + (1-\tau_{atm}) T_{atm}^4 \right] \tag{1.24}$$

From this formulation, the temperature of the body can be deduced by:

$$T = \left(\frac{L_{measure}\pi}{\tau_{opt}\tau_{atm}\varepsilon\sigma'} - \frac{1-\varepsilon}{\varepsilon} T_{env}^4 - \frac{1-\tau_{atm}}{\tau_{atm}\varepsilon} T_{atm}^4 \right)^{1/4} \tag{1.25}$$

In order to determine the temperature of the body, the other parameters have to be known or measured. Depending on the distance between the camera and the body, and the hygrometry, the transmission coefficient of the atmosphere can be deduced using the

following formulation:

$$\tau_{atm} = e^{-\beta x} \tag{1.26}$$

with x the distance between the camera and the body and β the extinction coefficient, which depends on the hygrometry and the wavelength. Moreover, the ambient temperature T_{atm} has to be known. The environment temperature T_{env} can be obtained by using an wrinkled aluminum foil in place of the body, at the condition that the emissivity of the foil is low enough.

1.4.3.2.1 Emissivity measurement method As seen previously, the emissivity of a body must be known in order to determine its temperature from thermography measurement. Several measurement methods can be applied.

— a first method is based on an energy balance [42]. The method consists in heating the body to a known temperature, then measuring the heating power required in order to maintain this temperature constant. If their is no heat transfer by conduction nor convection with the environment, which is made by placing the body in a vacuum chamber, the power required to maintain the temperature constant is equal to:

$$P = \sigma(\varepsilon T^4 - \varepsilon_e T_e^4)S \tag{1.27}$$

with P the heating power required, ε the emissivity of the body, T the temperature maintain of the body, ε_e the emissivity of the chamber, T_e the temperature of the chamber and S the body surface.
Most of the time, the chamber is cooled, in order to have $\varepsilon T^4 \gg \varepsilon_e T_e^4$. In that case, the emissivity can be deduced by:

$$\varepsilon = \frac{P}{\sigma T^4 S} \tag{1.28}$$

This method is the only one that allows a direct measure of the hemispherical emissivity, which means that no reference point are needed. However, such a method requires a huge setup: (i) in order to vacuum the chamber, a pumping system is required. (ii) it involves a cooling system for the chamber, and heating system for the sample.(iii) samples have to be calibrated in size to obtaine a good estimation of their surface area.

— second method used is to compare the luminance of the body to the luminance of a black body. To do so, both the sample and the black body are heated to a given

temperature. Then, the luminance of both is measured by using an infrared sensor. The emissivity is then obtained by comparing the two luminances obtained [116]. Such a method enables the emissivity to be determined with less equipment than the first method described above. However, a reference point, represented by the black body, has to be used. Moreover, the emissivity is measured in a single direction, it is therefore necessary to measure it for multiple directions in order to obtain the hemispherical emissivity.

1.4.3.2.2 Narcissus effect One issue encountered when using an infrared camera is the Narcissus effect [40]. As seen before, the surrounding environment is reflected on the sample surface, and one of the surrounding object is the camera itself, which explains the name of this phenomena, and leads to an alteration of the image obtained. Many non-uniformity correction techniques have been developed in order to correct this phenomenon. The most used is the calibration-based method, which consists in recording a homogeneous radiance over the whole image, then in correcting each sensor separately. The homogeneous scene can easily be obtained by using a black body system.

Figure 1.24 shows a scene taken before and after a non-uniformity correction (NUC) of the sensor matrix.

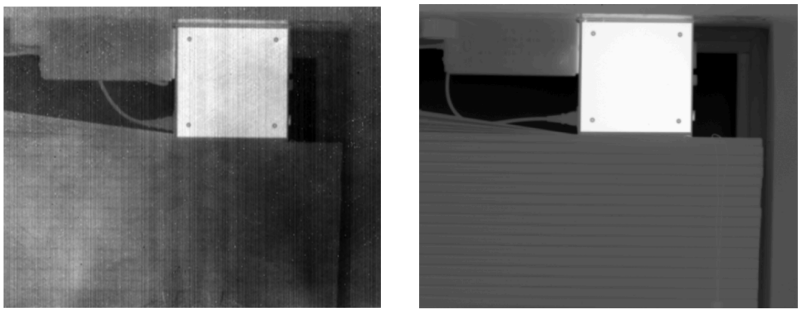

Non corrected scene Corrected scene

Figure 1.24 – IR image taken before and after the NUC [18]

1.4.3.3 Quantitative surface calorimetry

First, most of mechanical tests are performed under non-adabiatic conditions, which means that temperature variations are not only due to the material deformation, but also

to external parameters. Contrarily, the heat source produced or absorbed is intrinsic to the material deformation process. The following of this section will detail how the heat source can be obtained from temperature measurements, and the different phenomena that can be at the origin of heat source production/absorption. Since heat source can be obtained from the temperature, any temperature measurement system can be used.

In this section, the theoretical framework will be given for small strains, then it will be extended for large deformations. It is assumed that any thermomechanical system out of equilibrium can be considered as the sum of several homogeneous subsystem at equilibrium, describe using a set of n state variable : T the absolute temperature, ε the strain tensor and $n-2$ vector ξ which corresponds to internal variables. Let $\Psi = e - T\eta$ with Ψ the Helmholtz free-energy, e the specific heat energy and η the specific entropy. The local form of the two principles of the thermodynamics gives:

$$\rho\dot{e} = \sigma : \dot{\varepsilon} - \text{div } q + R \tag{1.29}$$

$$\rho T\dot{\eta} = d_1 - \text{div } Q + R \tag{1.30}$$

with ρ the mass density of the material, σ the Cauchy stress tensor, Q the heat flux vector, R the external heat flux, which can come from radiation for instance, and d_1 the intrinsic dissipation.

From the second principles, one can obtained the following formulation:

$$\rho T\dot{\eta} = \underbrace{-\rho T\frac{\partial^2\Psi}{\partial T^2}\dot{T}}_{\rho C\dot{T}} \underbrace{-\rho T\frac{\partial^2\Psi}{\partial T\partial\varepsilon} : \dot{\varepsilon}}_{S_{el}} \underbrace{-\rho T\frac{\partial^2\Psi}{\partial T\partial\xi}.\dot{\xi}}_{S_{otc}} \tag{1.31}$$

with C the specific heat capacity, S_{el} the heat source due to thermoelastic coupling and S_{otc} the heat source due to other thermomechanical couplings.

Assuming the Fourrier law $Q = -\kappa\text{grad } T$ with κ the conduction tensor, the heat diffusion equation can be written as:

$$\rho C\dot{T} - \text{div } (\kappa\text{grad } T) = S + R \tag{1.32}$$

with S the total heat produce by the material $S = d_1 + S_{el} + S_{otc}$.

If it is assumed that ρ and C are constant and κ is isotropic, i.e. $\kappa = kI$, with I the

identity matrix, the heat equation can be simplified as:

$$\rho C\dot{T} - k\Delta T = S + R \tag{1.33}$$

with Δ the Laplacian operator.

Since the IRT technique provides the temperature at the specimen surface, this formulation has to be simplified, using several assumptions. First, the temperature is assumed to be homogeneous in the thickness of the material, which gives the following formulation:

$$\rho C\dot{T} + \rho C\frac{T - T_{amb}}{\tau_{2D}} - k\Delta_{2D}T = S + R \tag{1.34}$$

with Δ_{2D} the in-plane Laplacian operator, T_{amb} the ambient temperature and τ_{2D} a time constant that characterizes the heat exchange in the out-of-plane direction by convection with the air.

Then, the external heat sources R are assumed to be constant over the time, and it comes:

$$\rho C\dot{\theta} + \rho C\frac{\theta}{\tau_{2D}} - k\Delta_{2D}\theta = S \tag{1.35}$$

with $\theta = T - T_{ref}$ the temperature variation.

In the case where the heat conduction can be neglected, such as in homogeneous temperature field, a "0D" formulation can be obtained:

$$\rho C\dot{\theta} + \rho C\frac{\theta}{\tau_{2D}} = S \tag{1.36}$$

However, this formulation only applies in case of small deformations, i.e. when the reference and deformed configurations can be superimposed. In case of large deformations, two formulations are obtained, depending of the configuration used.

In the Lagragian configuration, the heat equation is given by:

$$\rho_0 C\frac{d\theta}{dt} + \rho C\frac{\theta}{\tau} - k\,\mathrm{Div}(\mathbf{C}^{-1}\,\overrightarrow{\mathrm{Grad}}\,\theta) = S \tag{1.37}$$

with $\mathbf{C}$ the Cauchy-Green tensor. Here, the material is assumed to be incompressible.

In the Eulerian configuration, the heat equation is given by:

$$\rho C(\frac{\partial\theta}{\partial t} + V_x\frac{\partial\theta}{\partial x} + V_y\frac{\partial\theta}{\partial y}) + \rho C\frac{\theta}{\tau} - k\Delta_{2D}\theta = S \tag{1.38}$$

with V_x and V_y the velocity in the x-direction and y-direction respectively and (x, y) the position of the particle.

1.4.3.4 Some examples of surface calorimetry applied in material science in the case of small deformations

1.4.3.4.1 Thermoelastic stress analysis of chalcogenide glass Thermoelastic stress analysis (TSA) is a experimental technique that provides the surface stress field using IRT. This method is based on temperature changes that occur when a material deforms elastically. Many studies have applied this technique to measure the stress field at the surface of different materials. For instance, the TSA technique have been applied to chalcogenide glass [91].

In this study, several compression tests have been made on disc specimens with a circular hole at their center. Figure 1.25 shows the experimental setup used for this study.

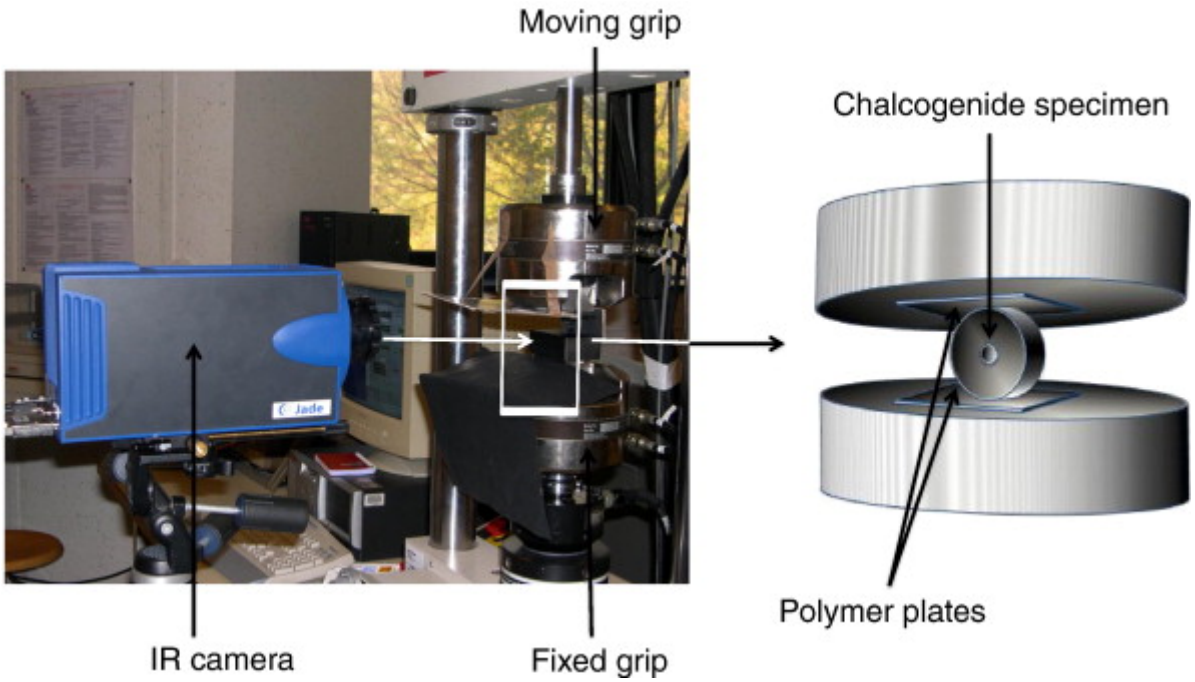

Figure 1.25 – Overview of the experimental setup [91]

Infrared thermography is used to measure the temperature in the specimen. Figure 1.25 represents the temperature variation field measured for two different tests.

The TSA approach enable to link the temperature variation with the stress. More

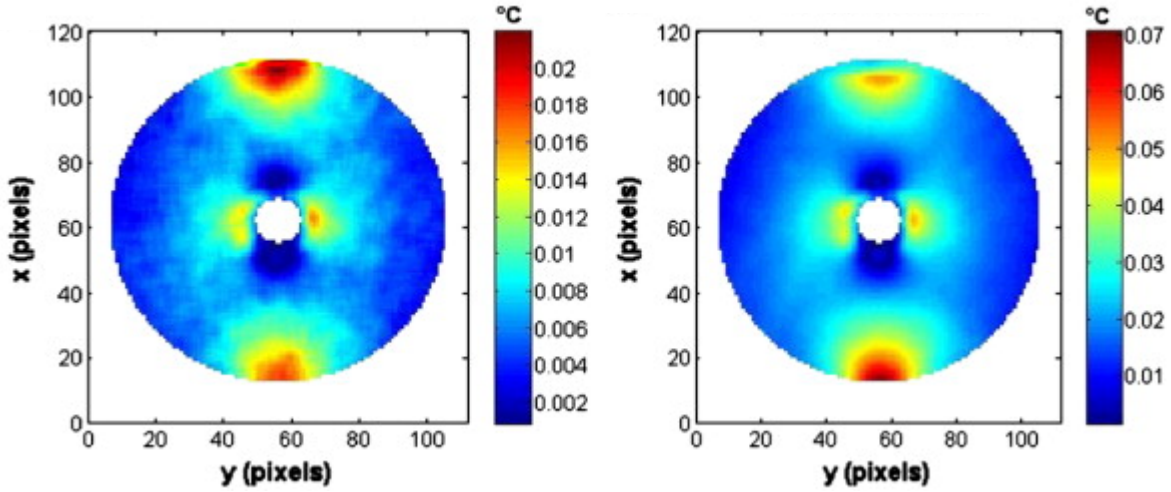

(a) $F = 44 \pm 36$N (b) $F = 132 \pm 108$N

Figure 1.26 – Map of temperature variation at the specimen surface for tests made at 3 Hz [91]

precisely, the trace of the Cauchy stress tensor, i.e. the sum of the principal stresses, can be obtained in the case of isotropic material. Figure 1.27 shows the map of absolute value of $\mathrm{tr}(\sigma)$. It permits to identify the zones of highest hydrostatic pressure, and to quantify the maximal hydrostastic pressure reached.

This study demonstrates that TSA is an interesting tool to investigate the thermoelasticity of chalcogenide glass, but the same technique could be applied for many other thermoelastic materials (see for instance Stanley and Chan [100]).

1.4.3.4.2 Thermomechanical analysis of the gum Metal Since thermomechanical couplings play an important role during the material deformation, several studies have been made using IRT, to better understand the behavior of new materials [24].

The study presented here has been performed on a titanium alloy, called Gum Metal, which presents specific mechanical properties, especially a low Young's modulus and a nonlinear superelastic-like large recoverable strain [82]. Uniaxial tests are performed on a flat specimen shown in Figure 1.28.

Figure 1.29 presents the stress and temperature variation curves versus the strain. On this curve, three different areas can be observed:

— at first, the stress is linear with the strain, and the temperature decreases. This is a typical thermoelastic response of a metal material,

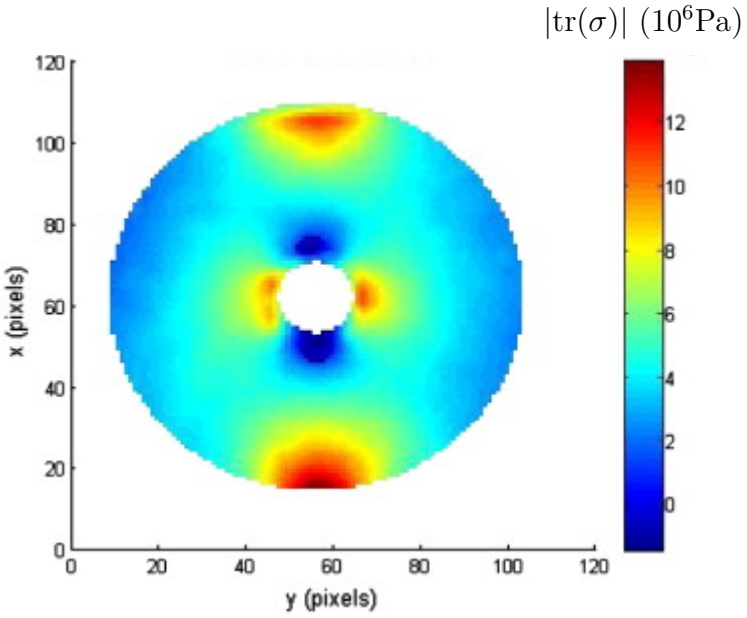

Figure 1.27 – Map of absolute value of $\mathrm{tr}(\sigma)$ for the test made at 3 Hz and $F = -132 \pm 108$N [91]

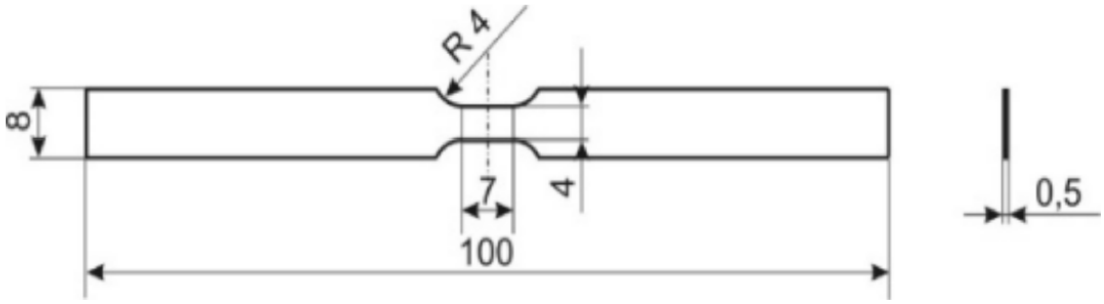

Figure 1.28 – Sample used in the study [82]

— then, while the yield stress is not reached yet, the temperature increases, as it will occur in a rubber material,
— finally, when the yield stress is reached, temperature increases, until the sample breaks.

Thanks to IRT, this study demonstrates the superelastic-like behavior of this type of material, which will not be possible without the information given by the temperature variation during the loading.

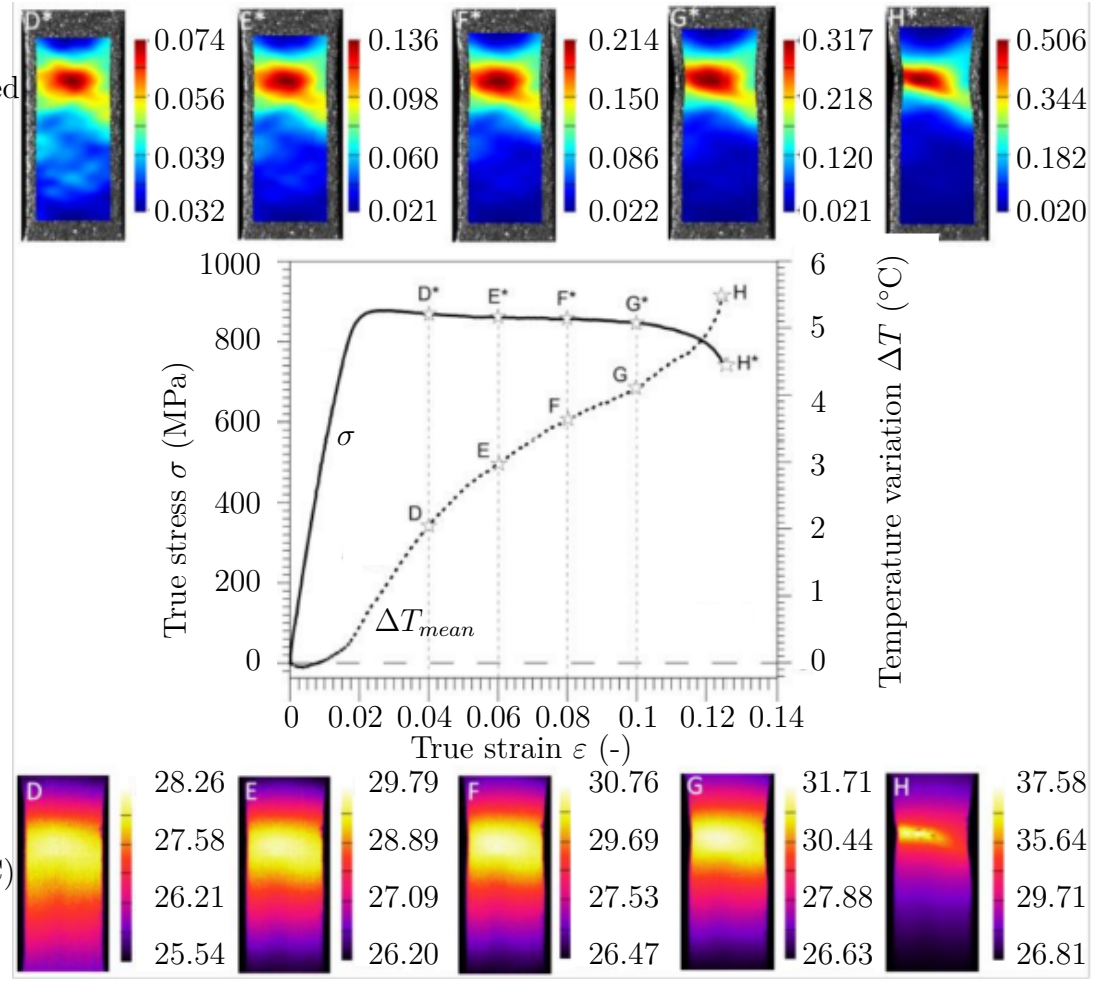

Figure 1.29 – Stress σ and temperature variation ΔT_{mean} versus strain ε [82]

1.4.3.4.3 Study of Lüders band propagation through surface based calorimetry Lüders bands are the result of the plastic strain localization under uniaxial strain deformation [65]. The formation of a Lüders band is preceded by a yield point and a drop of the flow stress, then the band appears between plastically deformed and undeformed material. Usually, the Lüders band starts at one of the specimen end and propagates toward the other end. During this propagation, the stress-strain curve is flat. Since the strain localization should be associated with localized heat production, Louche and Chrysochoos [62] proposed to study the Lüders propagation through surface based calorimetry. Figure 1.30 represents the map of heat produced by the material at different times.

On this figure, the Lüders band position is clearly visible. From these data, it is possible to demonstrate that Lüders band propagates at a constant velocity. Same experiment as been made for several cross-section speed, and Figure 1.31 represents the Lüders band

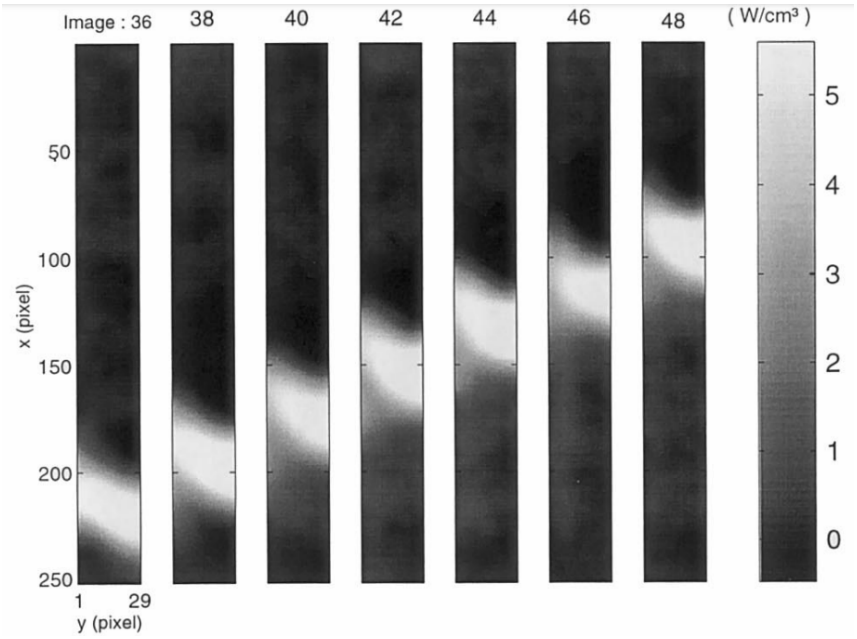

Figure 1.30 – Propagation along the specimen length of the Lüders band [62]

velocity against the cross-section velocity. A linear evolution is observed.

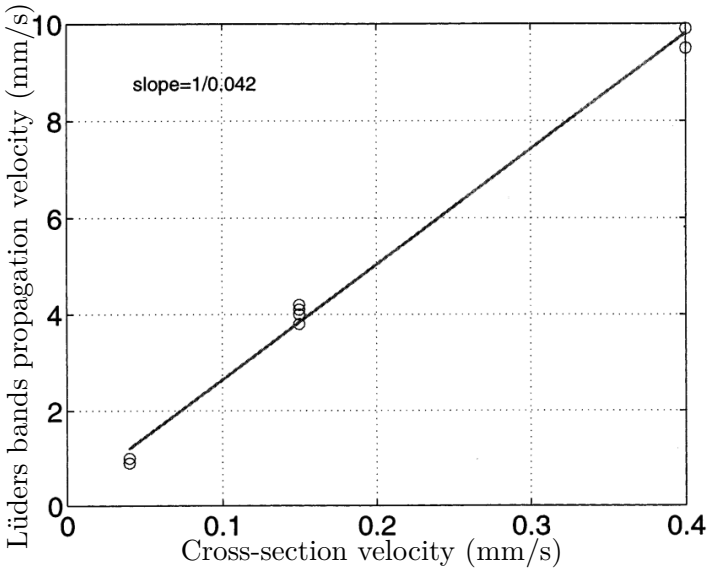

Figure 1.31 – Lüders band velocity versus cross-section velocity [62]

1.4.4 Some application of surface calorimetry in large deformations

1.4.4.1 Heat source field for heterogeneous mechanical loading

Since the mechanical behavior of rubber-like material depends on the loading case undergone by the specimen, they are often characterized through three homogeneous tests, one in uniaxial tension, one in pure shear and one in equibiaxial tension. It is commonly accepted that all loading cases can be deduced from these three ones. However, such a method presents several advantages. The main one is the long time to make the different specimens, the different tests and to analyze the different curves. Recently, Guélon et al. [39] proposed a new method, based on a single heterogeneous test that includes the three previously mentioned loading cases. Actually, these tests also contain all the intermediate loading cases.

Such a test has been performed in Toussaint et al. [108], using a three-branch specimen, shown in Figure 1.32. Using this test, uniaxial tension (UT) is obtained in the two vertical branches, equibiaxial tension (ET) is obtained at the specimen center and pure shear (PS) is obtained around the equibiaxial tension area, as seen in Figure 1.33.

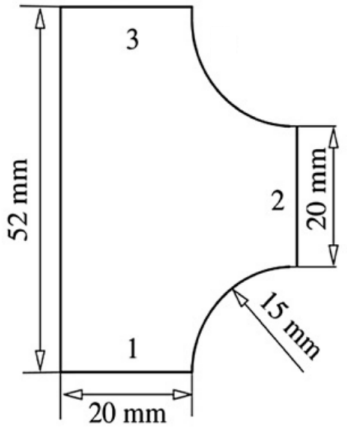

Figure 1.32 – Three-branch specimen used for the heterogeneous loading test [108]

Figure 1.34 presents the heat source map at the maximal displacement imposed, and compares with the loading condition presented in Figure 1.35. The maximal heat production seems to correspond to the uniaxial area with the highest stretch ratio reached. Authors claim that it is probably due to the combination of thermoelastic couplings and crystallization.

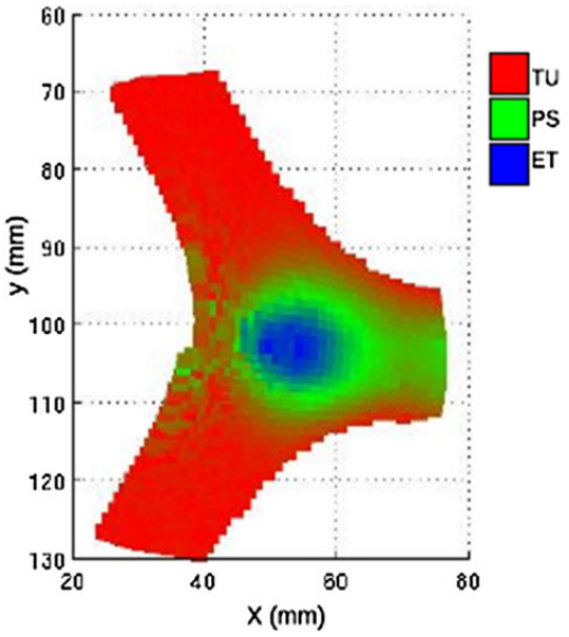

Figure 1.33 – Map of loading case using the three-branch specimen [108]

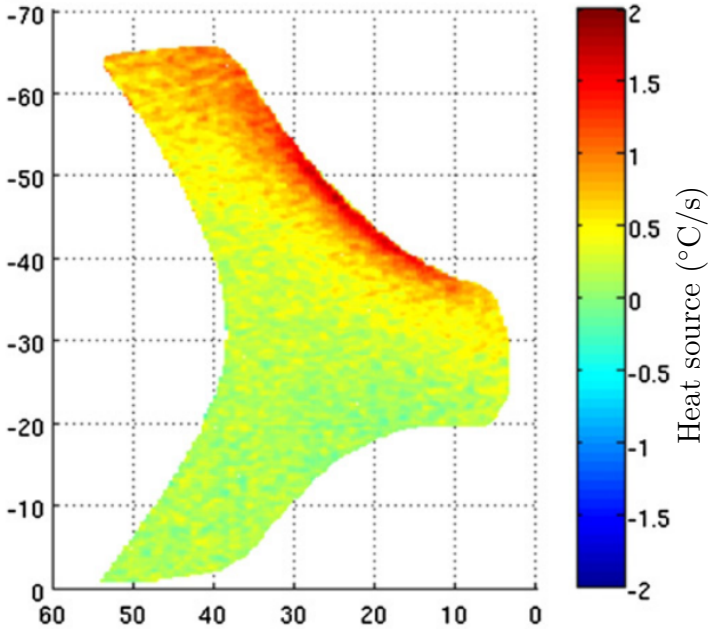

Figure 1.34 – Heat source map in the three-branch heterogeeous test [108]

1.4.4.2 Heat sources field around crack tip of rubber specimen

Studying the crack propagation in rubber-like material is a critical issue. Surface based calorimetry using infrared thermography is a relevant technique to investigate hetero-

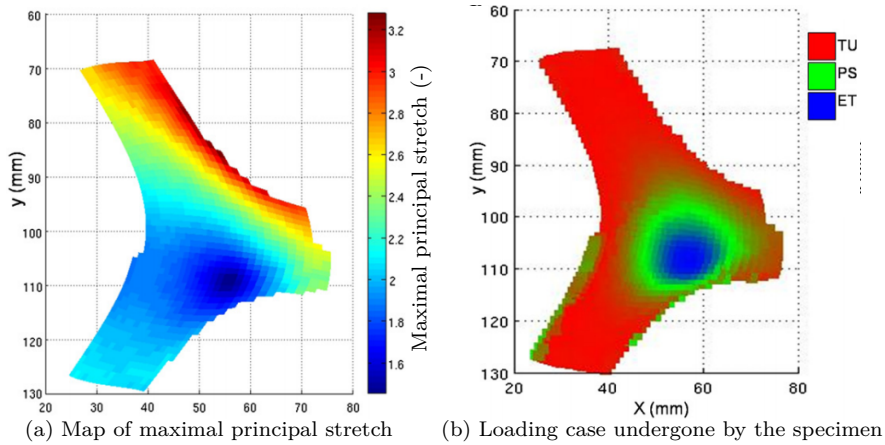

(a) Map of maximal principal stretch (b) Loading case undergone by the specimen

Figure 1.35 – Kinematic field in the three-branch heterogeeous test [108]

geneities in many materials, however in most of these studies, the strain level remains relatively small compared to strain level undergone by rubbers. Consequently, the tools developed to measure temperature fields provided by infrared thermography are no longer suitable for large deformations, especially when heterogeneous temperature fields are studied.

Pottier et al. [85] highlighted and addressed this issue, by measuring the temperature at a single spot during a rigid-body motion test of a rubber specimen. One side of the specimen is fixed in the moving grip, the second one is free. A frozen steel block is placed on the free side in order to generate a temperature gradient within the specimen. For such a test, it is assumed that the temperature should not change during the whole test. Figure 1.36 represents the temperature variation at a single spot for three configurations:

— curve *a* represents the temperature variation measured without any motion compensation technique. Since the material point moves but not the measurement zone, the measure is actually made for a set of material points with different temperature, which leads to the high temperature variation seen,

— curve *b* represents the temperature variation measured when applying a motion compensation technique. The aim of this motion compensation technique is to track material point in IR images during the whole test. To perform the motion compensation, the spot in the initial and final positions are manually localized in the infrared images and the position is interpolated for each intermediate position. Results shows a better result, however a small oscillation remains. This one is due to the non-uniformity of the IR detector matrix. Actually, when a thermally homogeneous scene is observed, the thermal field measured is not homogeneous

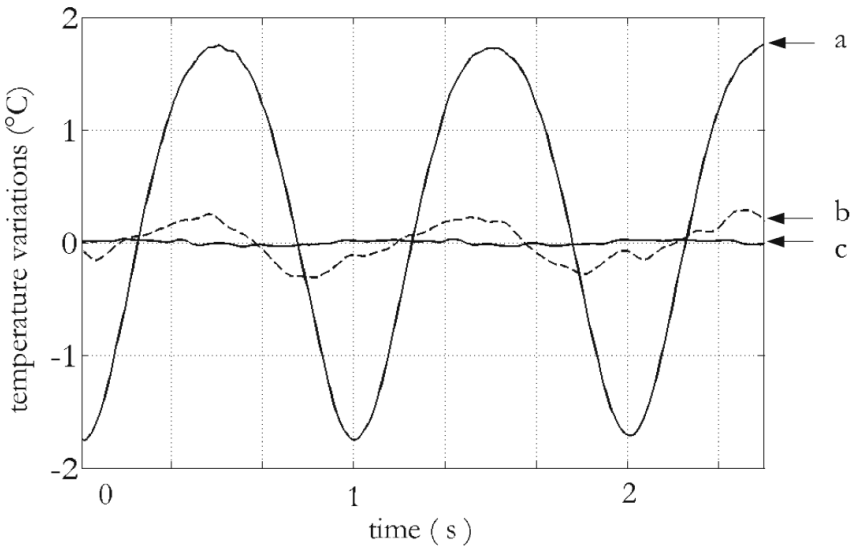

Figure 1.36 – Temperature variation measured during a rigid-body movement test [85]

due to this issue, as shown in Figure 1.37,

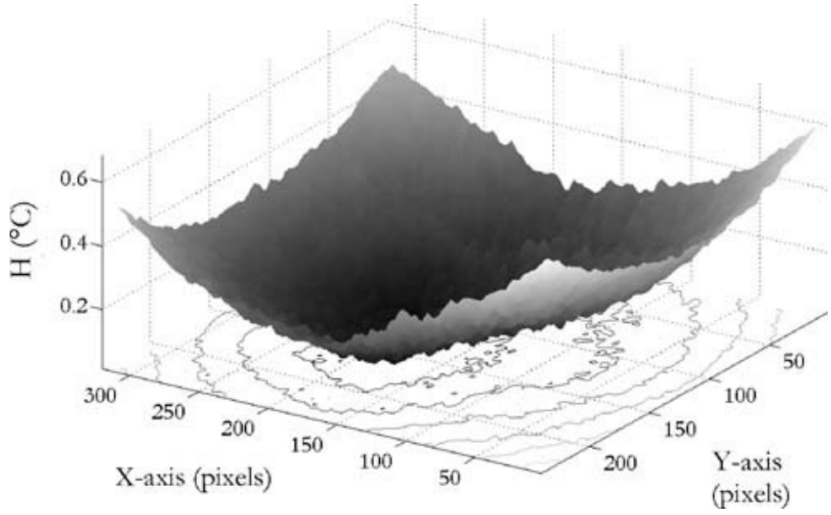

Figure 1.37 – Temperature distribution due to non-uniformity [85]

— curve *c* represents the temperature variation measured by both applying the motion compensation technique and taking into account the non-uniformity. It leads to a low temperature variation, which validates the processing.

Then, these corrections were used to measure the heat source absorbed by a carbon black filled natural rubber around a crack tip, represented in Figure 1.38. In this figure, it clearly appears that the maximum heat absorbed is obtained at the crack tip, and a

high heat absorption gradient is observed.

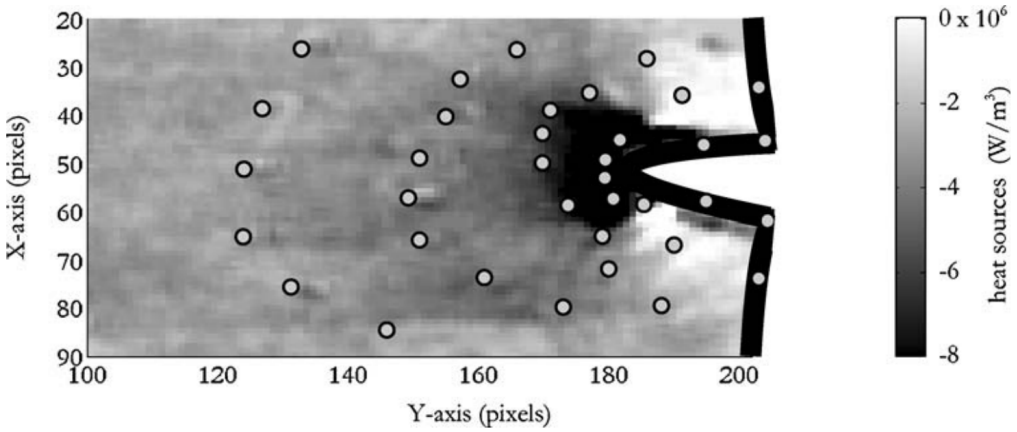

Figure 1.38 – Heat source map around the crack tip [85]

Later, Martinez et al. [71] also studied the heat source field around a crack tip in a carbon black filled Styrene-Butadiene Rubber (SBR). The temperature field is obtained by using a Non-Uniformity Correction (NUC) procedure and a motion compensation technique in order to avoid previously mentioned issues. However, the motion compensation technique used here is different. It uses Digital Image Correlation (DIC) technique on images obtained from a first optical camera, in order to follow the movement of materials point on an IR camera. Figure 1.39 represents the heat source field in the specimen for the maximum stretch ratio. It clearly show a high concentration of the heat source around the crack tip.

1.4.5 Conclusion on calorimetry under stretch

Even though the calorimetry under stretch appears to be an effective tool to provide additional information to purely mechanical analyses and is already widely used in material science, only few studies deals with calorimetry under large deformations, especially in presence of heterogeneities. It can be explained by the difficulty due to the large deformation formalism that complicates the IR images processing, and more specifically when a coupled measure with the full kinematic fields has to be performed. The few studies dealing with heterogeneous fields exhibits some lacks that have to be filled:

— firstly, in most of these studies, the metrological performances of the methodology proposed have not been evaluated. Actually, Pottier et al. [85] performed a metrological study on the temperature variation measured using the motion com-

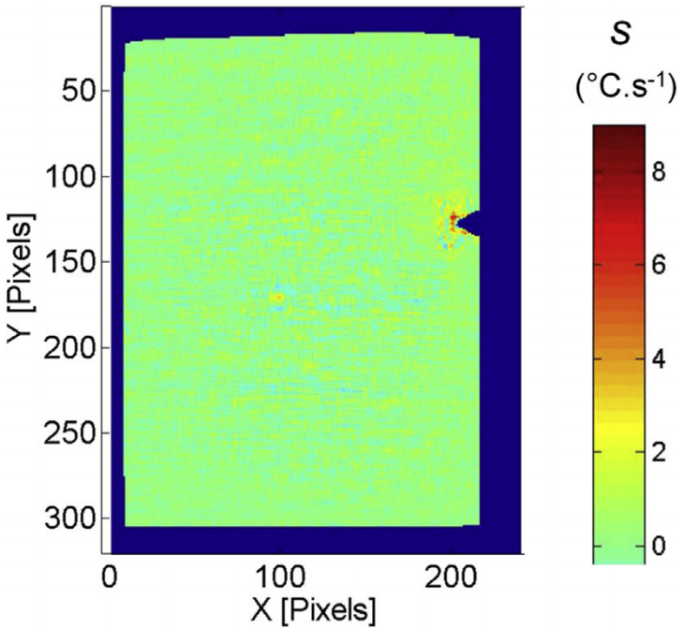

Figure 1.39 – Heat source map around the crack tip [71]

pensation technique, and concluded that the temperature variation obtained of approximatively 0.04 °C should be low enough to ensure a good accuracy, but no metrological study about the influence of this temperature variation on the heat source obtained was carried out,

— secondly, no link between the heat source produced by the specimen and the mechanisms that occur during the mechanical deformation of rubber-like materials has been made. While thermoelastic couplings and the strain-induced crystallization have been mentioned in Toussaint et al. [108], these phenomena have not being quantified,

— thirdly, no energy balance at any point of heterogeneous heat source fields has been made with rubber-like materials, even though an energy balance can provide fruitful information on the different phenomena that occur during the mechanical deformation of materials.

1.5 Conclusion

In the first part, the mechanical behavior of rubber-like materials has been recalled. A focus has been made on the strain-induced crystallization, since it is a phenomenon that

highly influences the mechanical behavior of the material. The crystallization is most of the time studied through the X-ray diffraction technique, which provides not only the crystallinity level, but also fruitful information about crystallite size and orientation. However, this method exhibits a huge limitation, which is that the crystallinity is obtained at a single spot. Since the crystallization is a highly exothermal phenomena, it could be possible to evaluate the crystallinity level from the heat produced by the material during its deformation. Such a method will bypass the limitation of the X-ray diffraction, since it is easier to measure full temperature field.

In the second part, calorimetry for large deformations has been described. While this method could provide useful information, only few studies use this method for large deformations, especially when heterogeneities appear, due to the complexity of implementing the method in large deformations.

This PhD thesis addresses two main issues:

— first, a calorimetric method to measure the crystallinity level will be developed. This method will be compared with the X-ray diffraction method in order to validate the measurement,

— second, a methodology to perform surface calorimetry under large deformations, even in presence of heterogeneities, will be developed. This methodology will be used for thermomechanical analysis of rubber-like materials and to provide and discuss information that it will provide.

Chapter 2

Surface calorimetry under large homogeneous deformations: application to strain-induced crystallization evaluation

Contents

2.1 Comparison of the strain-induced crystallinity measured in unfilled natural rubber from the X-ray diffraction and the infrared thermography methods

This study has been performed in collaboration with Dr P.-A. Albouy at Laboratory of Physics of Solids (Orsay), and a part has been published in *Review of Scientific Instruments* [57].

2.1.1 Introduction

Since the pioneering work by Katz [51] in 1925, the strain-induced crystallization (SIC) of rubber is classically investigated using the X-ray diffraction (XRD) method. Using this method, numerous studies were carried out dealing with different aspects, such as the crystalline structure [15, 48, 87, 102], chain orientation [105] and kinetics of crystallization [104, 111], non-exhaustively.

Concerning the crystallinity level measurement, Göritz and Müller [38] showed that since SIC is a exothermal phenomena, it can be quantified accurately using an alternative method based of calorimetry. However, the method were not used, possibly because that the crystallinity obtained is averaged upon the whole specimen, which prevents to study any heterogeneous crystallinity fields, typically at a crack tip.

Recently, Le Cam [56] proposed to couple the calorimetry method and IR thermography to study SIC in an unfilled natural rubber. Even though the crystallinity level found is in good agreement with the literature, no comparison between the two methods has been performed for the same materials. This is the aim of the present study.

2.1.2 Description of the calorimetric method

As explained before, the method is based on heat production during the crystallization of rubber. The method is composed of four steps, presented in Figure 2.1. Input data required are the temperature variation field θ, the time constant parameter of the heat equation τ, and the thermophysical parameters ρ, C, k and ΔH.

— The first step consists in calculating the total heat power density produced by the material, using the heat diffusion equation. For natural rubber, a strong increase

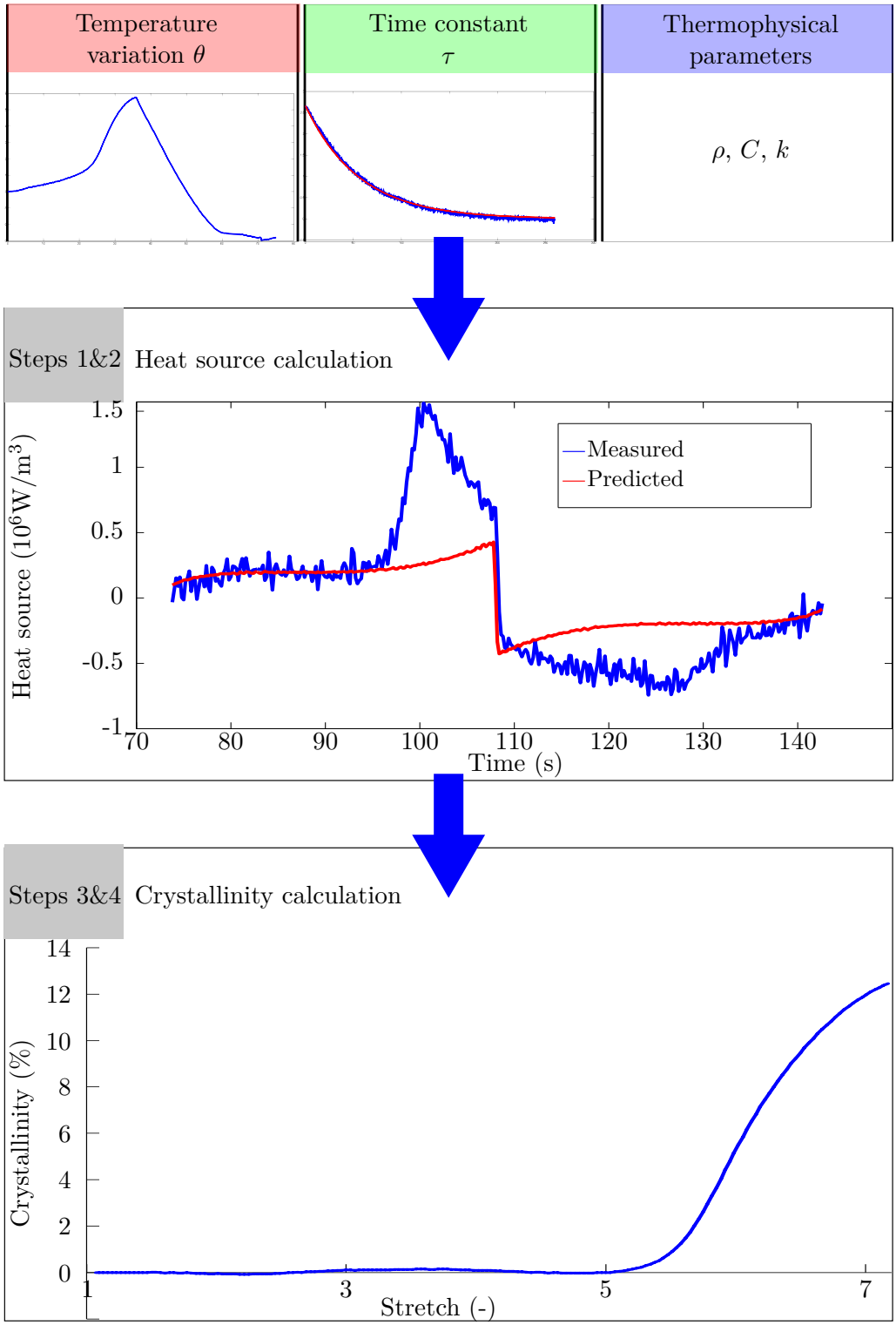

Figure 2.1 – Crystallinity measurement from IR thermography

of heat power density is seen as soon as the crystallization starts [38, 96].

— The second step deals with the prediction of heat source due to other phenomena than SIC. For rubber materials, is is mainly due to intrinsic dissipation and elastic couplings. The heat source from SIC is then deduced by subtracting the heat source from other phenomena from the total heat source produce by the material. Elastic couplings can be predicted by using a polynomial form, written as $S_{el} = \sum_{i=1}^{n} C_i (I_1 - 3)^i$.

— The equivalent temperature variation due to SIC, T_{cryst}, is then computed in Step 3. Actually, T_{cryst} is calculated by integrated the heat source over the time, as seen in Equation 2.1. The integration constant is determined by considering that T_{cryst} is equal to zero before the crystallization starts.

$$T_{cryst} = \int_{t_0}^{t_1} \frac{S_{cryst}(t)}{\rho C} \, \mathrm{d}t \tag{2.1}$$

— Step 4 consists in calculating the crystallinity from the equivalent temperature variation.

2.1.3 Comparison with the X-ray diffraction method

While evaluating the crystallinity from heat source seems to give equivalent results than those obtained from X-ray diffraction [56], a validation of the method should be performed by comparing results obtained from both method to the same material. X-ray diffraction measures has been made by Pr. Albouy at the LPS Orsay.

2.1.3.1 Experimental setup

The material considered here is an unfilled natural rubber vulcanized by sulfur with conventional activators and antioxidant agents. For the calculation, the density, specific heat and fusion enthalpy values are taken equal to 0.936 kg/dm^3, 1768 J/(kg · K) and 62 10^{3}J/dm^3. For unfilled natural rubber, ρ can be assumed to be constant since volume changes are small [23, 59] and C does not vary with the elongation, even when crystallization occurs [10, 73, 117]. The "Manufacture Française des pneumatiques Michelin" is acknowledged for providing the specimens.

Mechanical tests performed in this study is composed of two uniaxial tensile cycles at a stretch equal to 7,2. One test is performed at a loading rate of 100 mm/min and a

second one at a loading rate of 200 mm/min. The sample averaged dimension is equal to 19.3 mm in height, 7.2 mm in width and 1.4 mm in thickness.

Figure 2.2 shows the experimental setup used for the crystallinity measurement from calorimetric method. Tests are performed with the home-made biaxial testing machine presented in 3.2.2.2. For this study, the testing machine is used to stretch symmetrically the specimen in one direction. Temperature is measured using an FLIR IR camera at the specimen center, that does not move during the test, which means that no compensation technique is required in that case [108]. In order to reduce external radiation, grips are covered with a black body.

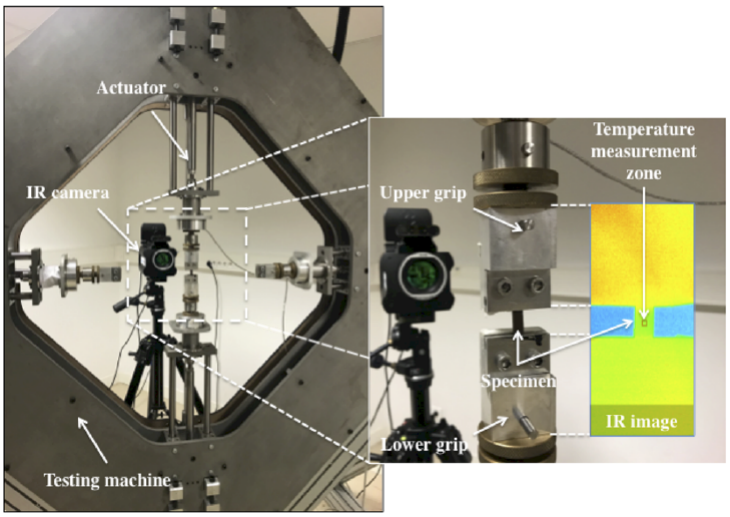

Figure 2.2 – Experimental setup for the temperature measurement

Figure 2.3 shows the experimental setup used for the crystallinity measurement from X-ray diffraction method.

2.1.3.2 Results

Figure 2.4 shows the temperature variation measured with the calorimetric method and the corresponding adiabatic one, which is deduced from the heat source. The fact that the adiabatic temperature does not evolve between the beginning and the end of the test validates the lack of any viscous effect during the tests, since the material produce as many heat during the loading than it absorbed during the unloading.

Figure 2.5 shows the heat source measured using Equation 1.35, and the prediction for heat source from elastic couplings only. During the loading, the heat source is positive

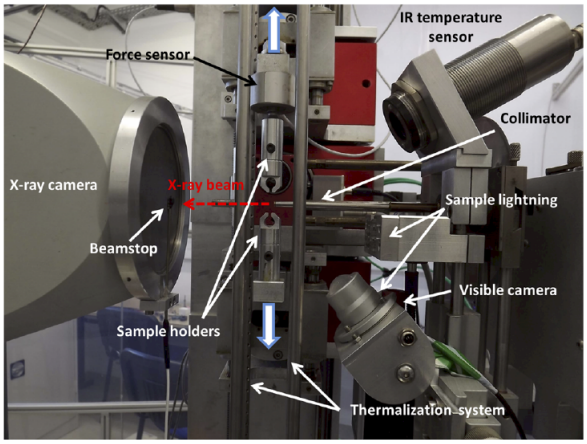

Figure 2.3 – Experimental setup for the crystallinity measurement from X-ray diffraction method

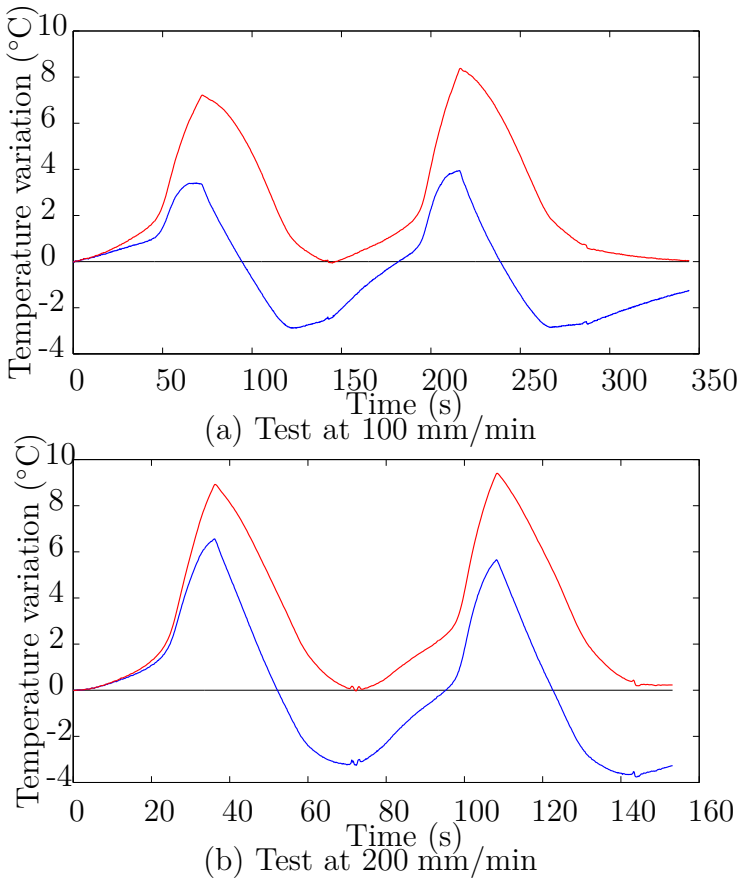

Figure 2.4 – Temperature variation evolution measured (in blue) and corresponding adiabatic temperature variation (in red) during the two mechanical tests

and increases with the stretch, with a strong increase when the crystallization starts. The heat source from elastic couplings prediction is made by using the following polynomial form.

$$S_{el} = C_1(I_1 - 3) + C_2(I_1 - 3)^2 + C_3(I_1 - 3)^3 \tag{2.2}$$

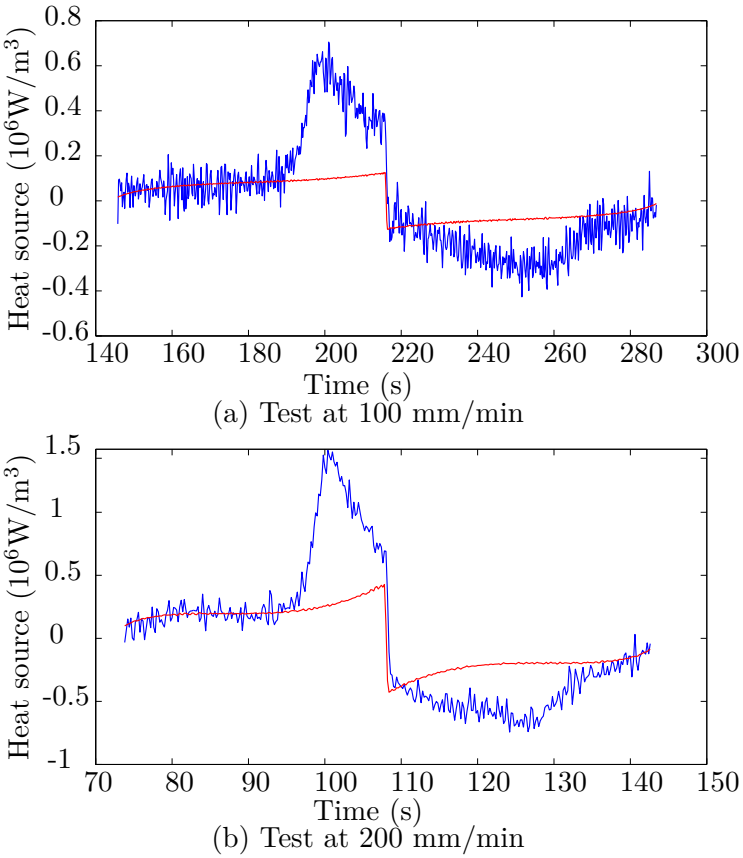

(a) Test at 100 mm/min

(b) Test at 200 mm/min

Figure 2.5 – Heat source evolution measured by infrared thermography (in blue) and heat source prediction for elastic couplings (in red) during the second cycle

The area between the two curves corresponds to the thermal energy due to SIC, and is used to obtained the temperature variation due to SIC T_{cryst}. It should be noted that before the crystallization starts, this temperature variation is equal to zero, since X-ray diffraction method shows that the crystallinity returns to zero at the end of each cycle. Crystallinity is finally obtained by using the fusion enthalpy:

$$\chi(t) = T_{cryst}(t)\frac{\rho C}{H} \tag{2.3}$$

Figure 2.6 shows the crystallinity measured from both the X-ray diffraction method

and the calorimetric method. Results obtained are in good agreement, which validates the calorimetric method for measuring the crystallinity level in elastomeric materials.

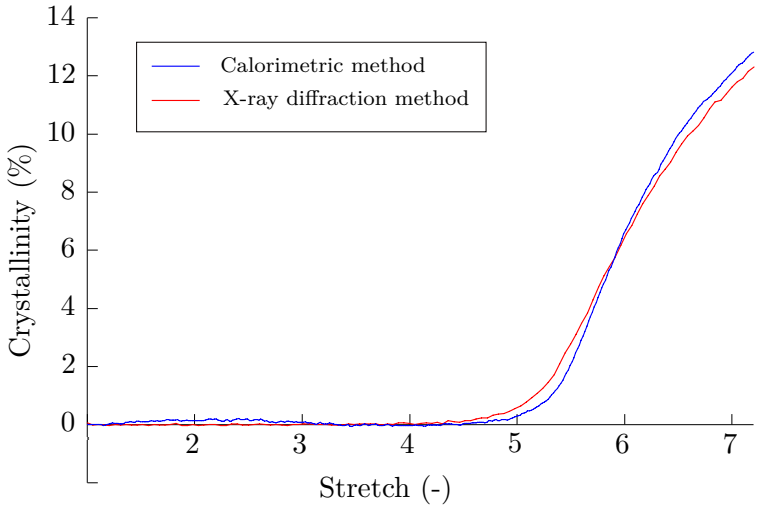

(a) Test performed at 100 mm/min

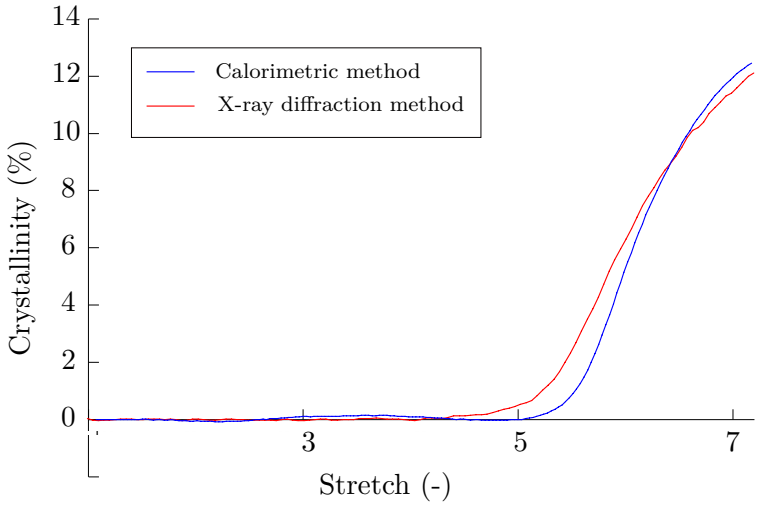

(b) Test performed at 200 mm/min

Figure 2.6 – Crystallinity measurement during the loading of the second cycle

2.1.4 Metrological study of the method

2.1.4.1 Creation of simulated data

In order to have a better comprehension of the performance of the method, a metrological study has been performed. For that purpose, simulated data have been created. The mechanical loading applied to the material, shown in Figure 2.7, correponds to a

single uniaxial loading at a rate equal to $\dot{\lambda} = 0.857$, which corresponds approximately to the test performed at 100 mm/min.

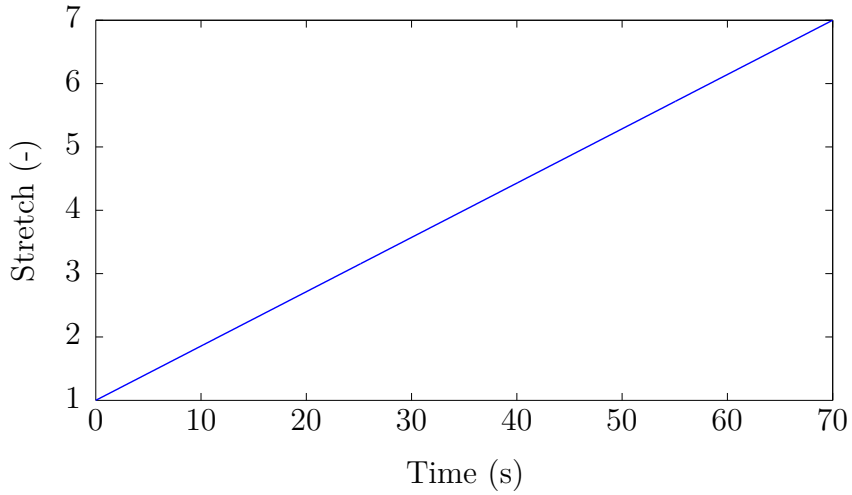

Figure 2.7 – Temporal evolution of the stretch for the simulated test

The crystallization of the numerical material starts at an elongation of 4.5, and grows in a quadratic way with the elongation. Figure 2.8 represents the crystallization versus stretch curve of the numerical material.

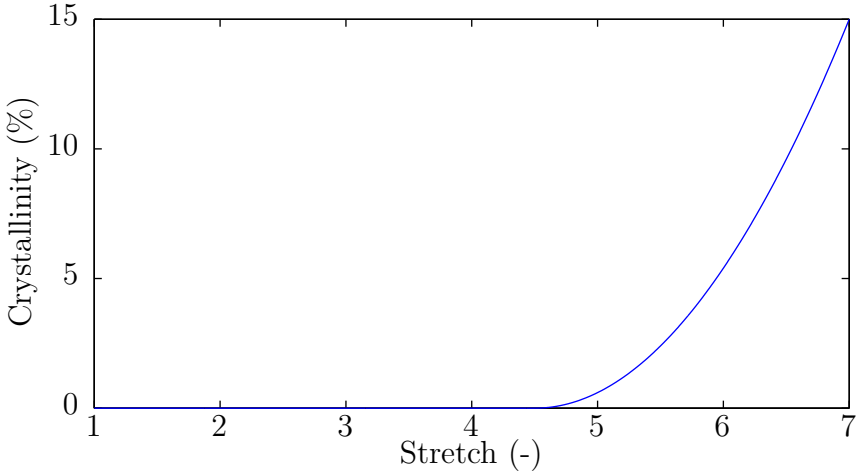

Figure 2.8 – Cristallization versus stretch for the simulated data

Then, the heat source is calculated. For the simulation, two phenomena produce heat. On one hand, thermoelastic couplings are simulated using the polynomial form $S_{el} = \left(\sum_{i=1}^{3} C_i (I_1 - 3)^i\right) \dot{\lambda}$ with $C_1 = 500\,000$, $C_2 = -100\,000$ and $C_3 = 20\,000$. On the second hand, the heat source from the strain-induced crystallization is written $S_{cryst} = H\dot{\chi}$ with

$H = 62\ 10^3 \mathrm{J/dm^3}$ the fusion enthalpy of the material. Figure 2.9 represents the two terms and the total heat source produced by the material.

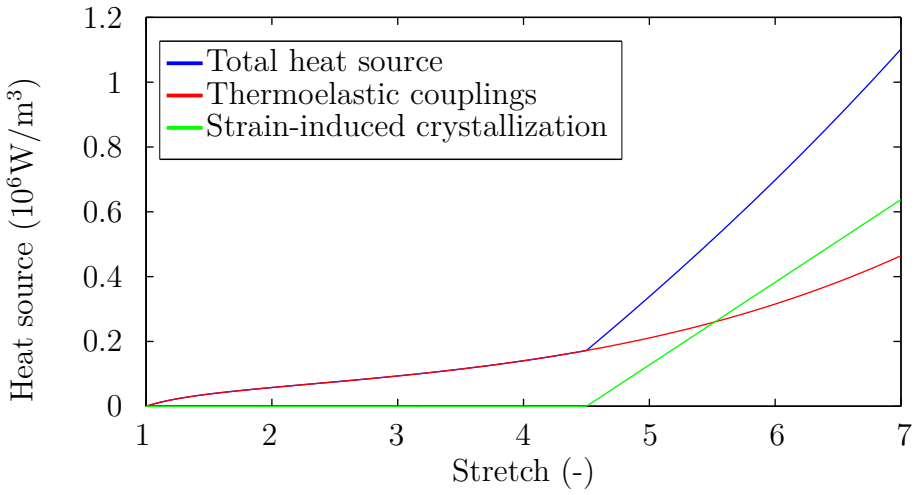

Figure 2.9 – Heat source versus stretch during the simulated test

From the heat source, the temperature variation can be deduced from the heat equation $S = \rho C_p \left(\dot{\theta} + \frac{\theta}{\tau}\right)$ with $\rho = 950$ kg/m^3 the mass density, $C_p = 1800$ J/(kg $\cdot$ K) the density specific heat and $\tau = \frac{200}{\sqrt{\lambda}}$ the time constant. To better simulate experimental data issued from an IR camera, a thermal noise is added to the temperature variation calculated, using a white noise with a standard deviation of 20 mK, which corresponds to the noise equivalent temperature deviation (NETD) of the IR camera used, which corresponds to the standard deviation of the temperature noise. Figure 2.10 represents the temperature variation obtained using this method.

2.1.5 Conclusion

In this section, two crystallinity measurement methods have been performed and compared for the same material: the infrared thermography based calorimetry and the X-ray diffraction techniques. Results obtained from both methods are in good agreement, which validates the calorimetry under stretch method to measure SIC. While the X-ray diffraction method provides more information, such as crystallites size and their orientations, the calorimetry method has the benefit to be easier to use.

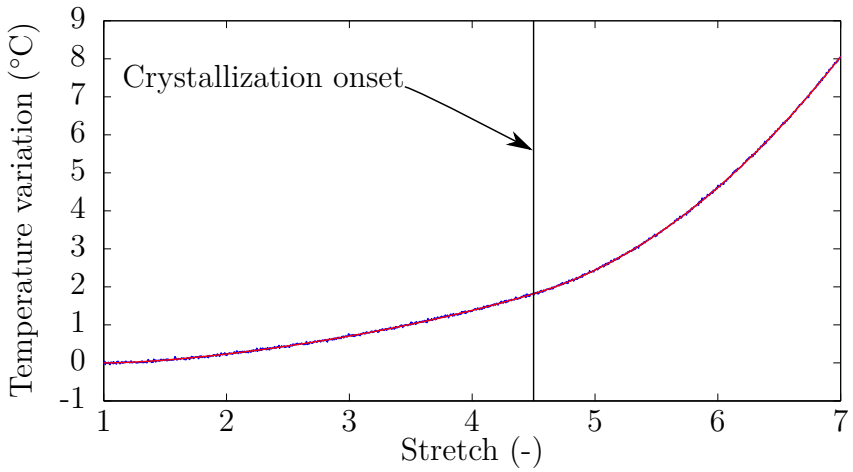

Figure 2.10 – Temporal evolution of the temperature variation for the simulated test

2.2 Influence of the multiaxiality on the crystallinity

2.2.1 Introduction

Physical phenomena involved in the mechanical behavior of NR are numerous and complex. The addition of fillers makes the deformation mechanisms even more complicated, as it induces viscosity, stress softening, increases cavitation and strongly affect the SIC phenomena. Several experimental techniques have been used to investigate these mechanisms as well as different mechanical tests such as stress relaxation and cyclic loadings. Nevertheless, each of these techniques provides only piecemeal information. In this context, several assumptions have been formulated, without being able to verified them. For example, the energy involved in the hysteresis loop is considered to be mainly due to intrinsic dissipation and would therefore be converted into heat.

Furthermore, SIC is generally investigated under uniaxial loadings and very few studies address the multiaxiality effect on SIC. Beurrot-Borgarino [7] and Brüning [14] reported X-ray diffraction measurement on unfilled NR under equibiaxial loading. The main problem encountered in their studies is to reach a sufficient stretch level for crystallization. Beurrot-Borgarino [7] solved this issue by adding carbon black fillers in order to decrease the crystallization onset. The material has been tested under uniaxial, biaxial and equibiaxial loadings, and found similar crystallites for each tests.

A recent study have investigated the effects of multiaxiality in the crystallization of an unfilled NR using X-ray diffraction [21]. The authors found that the biaxiality frustrates SIC, and no crystallization emerges up to a ratio between the maximum and minimum

principal stretches of 1.6. However, they were unable to reach either high stretches levels or high biaxiality level. The question of the effects of multiaxiality on SIC is therefore still open.

In the previous section, a new technique for measuring the strain-induced crystallinity has been validated. In the present section, the effect of a multiaxial loading is investigated for a lowly filled rubber. This study has been carried out in collaboration with Prof. M. Itskov's team at Aachen University. In this team, Dr. N. Vu Ngoc used the experimental results to propose a new model for SIC in rubber. This modeling approach is the second part of the paper, and does not appear in the present manuscript. The present study has been the subject of an article submitted in *Journal of the Mechanics of Physics of Solids* [52]

First, the basis of energy balance over a loading cycle will be presented. Then the experimental setup, the material and tests performed will be described. Finally the results obtained under uniaxial and biaxial loading will be presented and discussed.

2.2.2 Energy balance in elastomeric materials

Recently, several studies have shown that the energy involved in the hysteresis loop is not entirely converted into heat. A part of it can be used by the material to change its micro structure. For instance, Le Cam [55] has shown that in unfilled natural rubbers, the hysteresis is due to SIC, more specifically it is due to the difference in kinetics of crystallization and melting. Furthermore, the contribution of fillers added to elastomers to the hysteresis loop is not systematically the preponderant one, as energy can be stored in the deformed filler network, see for instance Loukil et al. [64] for carbon black filled nitrile rubber. Thus, determining the part of the mechanical energy stored in filled crystallizing natural rubbers due to SIC and the filler network is very important for constitutive modeling. In the following, continuum quantities required for such an energy balance are listed.

— The total strain energy density (per unit referential volume) W_{strain} is the energy supplied mechanically to the material during the loading and the unloading,

$$W_{strain}^{load} = \int_{loading} \pi \, d\lambda \text{ and } W_{strain}^{unload} = \int_{unloading} \pi \, d\lambda, \text{ respectively,} \tag{2.4}$$

where π denotes the first Piola-Kirchhoff stress in the loading direction and λ is

the corresponding stretch.

— The mechanical energy involved in the hysteresis loop W_{hyst}^{cycle} and the energy rate P_{hyst}^{cycle} are determined as follows:

$$W_{hyst}^{cycle} = W_{strain}^{load} - W_{strain}^{unload}, \; P_{hyst}^{cycle} = \frac{W_{hyst}^{cycle}}{t_{cycle}}, \tag{2.5}$$

where t_{cycle} denotes the duration of the cycle.

— Integrating the heat source over time of each cycle gives the mean intrinsic dissipation $\tilde{\mathcal{D}}_{int}$:

$$\tilde{\mathcal{D}}_{int} = \frac{1}{t_{cycle}} \int_{cycle} S \; dt. \tag{2.6}$$

— The difference between P_{hyst}^{cycle} and $\tilde{\mathcal{D}}_{int}$ represents the energy stored in each cycle as

$$P_{stored}^{cycle} = P_{hyst}^{cycle} - \tilde{\mathcal{D}}_{int}. \tag{2.7}$$

— The stored energy ratio γ_{se} is defined as

$$\gamma_{se} = \frac{W_{stored}^{cycle}}{W_{hyst}^{cycle}} \tag{2.8}$$

and further characterizes the ability of the material to store energy.

- If γ_{se} tends to 0, no energy is stored during the deformation. The whole hysteresis loop is due to the intrinsic dissipation.
- If γ_{se} tends to 1, the whole hysteresis loop is due to stored energy and no intrinsic dissipation is detected. This is typically the case in unfilled natural rubber [96].

It should be noted that this ratio can be influenced by both the strain range and the strain rate applied to the specimen [53].

2.2.3 Experimental setup

2.2.3.1 Material

The material considered in the present study is a natural rubber (*cis*-1,4 polyisoprene) vulcanized with 1.5 phr of sulfur and filled with carbon black aggregates, between 10 and 20 phr. Values of the density ρ, the heat capacity C and the thermal conduc-

tivity D are issued from the literature and are chosen equal respectively to 0.94 kg/dm^3, 1750 J/(kg · K) and 0.2 W/(m · K). The Cooper Standard is acknowledged for providing the specimens.

2.2.3.2 Loading conditions and specimen geometries

Two types of tests were carried out with different specimen geometries: uniaxial tension of a dumbbell-like specimen and biaxial tension of a cruciform specimen. The latter leads to heterogeneous strain/stress fields, which enabled us to investigate multiaxial effects on both the thermomechanical response and SIC.

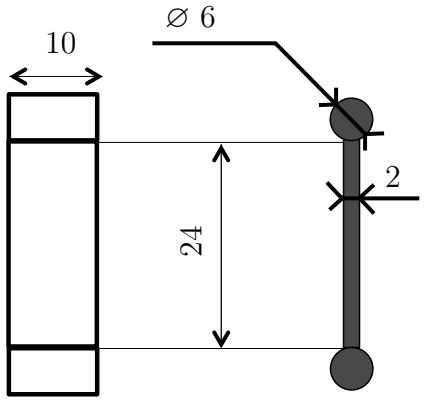

Figure 2.11 – Sample geometry used for uniaxial tests (dimensions in mm)

2.2.3.2.1 Uniaxial loading conditions Uniaxial tensile tests were performed with a 24 mm long, 10 mm wide and 2 mm thick specimen, with cylindrical branch ends to avoid any slippage in the machine grips, as depicted in Figure 2.11. This geometry leads to a homogeneous uniaxial strain/stress state in the entire specimen except in the zones close to the grips (see the specimen geometry).
Four types of uniaxial tensile tests (#1 to #3*b*) were carried out kinetically controlled at the velocity of 300 mm/min. Stretch profiles of the tests are shown in Figure 2.12. The loading was applied symmetrically by the two vertical actuators of the biaxial testing machine shown in Figure 2.13 and described in the next paragraph. In Test #1, 3 cycles at increasing maximum stretch levels; 2.5, 4 and 6 were applied. This test enables us to characterize the typical phenomena involved in the mechanical response as the hysteresis loop, the permanent set, the accommodation, also referred to as the Mullins effect in the literature [78], and the stress hardening at large strains.

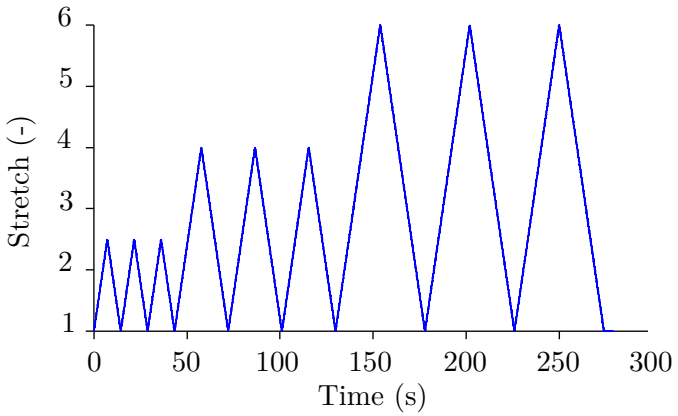

(a) Test # 1: without relaxation phases

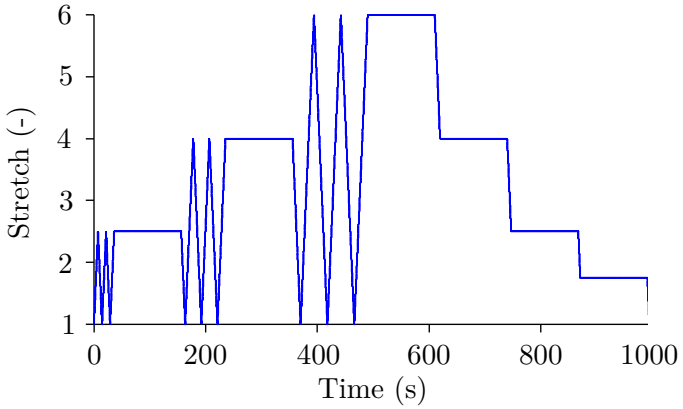

(b) Tests # 2 and # 3b: with relaxation phases

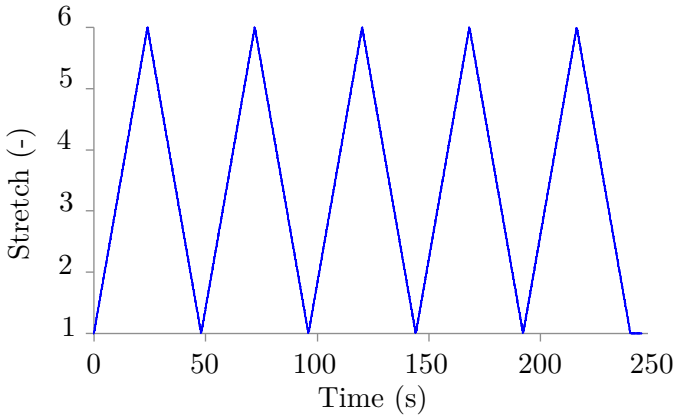

(c) Test# 3a: preconditionning phases

Figure 2.12 – Stretch versus time curves for the four uniaxial tensile tests performed at 300 mm/min

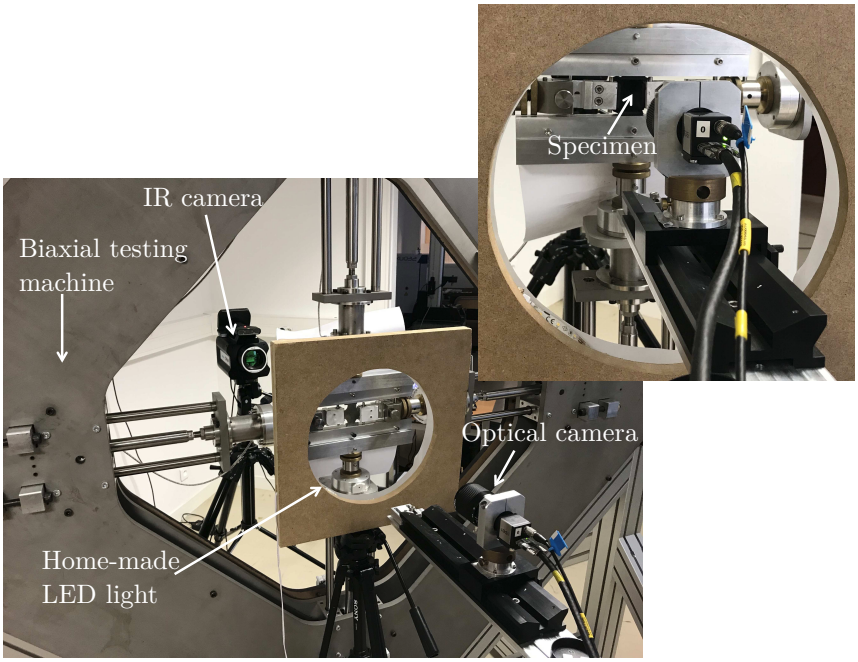

Figure 2.13 – Overview of the experimental setup

In order to better investigate the time dependency of the mechanical response due to both the viscosity induced by fillers and SIC, Test #2 included relaxation phases of 60 s in the stretch profile of Test #1:

- at the end of the last loading of each set,
- during the last final unloading at decreasing stretches equal to 6, 4 and 2.5.

Test #3*b* corresponded to Test #2 but the material was preconditioned during Test #3*a* in order to remove the Mullins effect, observed in the mechanical response of Test #2. Note that in contrast to the most of previous studies the permanent set observed after Test #3*a* was further taken into account. For Test #3*b*, the stretch imposed has been calculated by considering the same initial length as for Test #3*a*.

2.2.3.2.2 Biaxial loading conditions Multiaxial loading effects were investigated in a biaxial test with a cross-shaped specimen. The specimen extremities were wrapped around a metallic roll. The initial lengths in the horizontal and vertical directions are slightly different as 39.5 and 49.5 mm, respectively. The specimen geometry is shown in Figure 2.14.

Figure 2.13 presents an overview of the experimental setup. It is composed of a home-made biaxial testing machine with four independent electrical actuators controlled by an

in-house LabVIEW program. Two cameras (infrared (IR) and optical) are placed on both sides of the specimen. The four specimen branch ends were displaced up to 150 mm at a rate of 150 mm/min (see Figure 2.15).

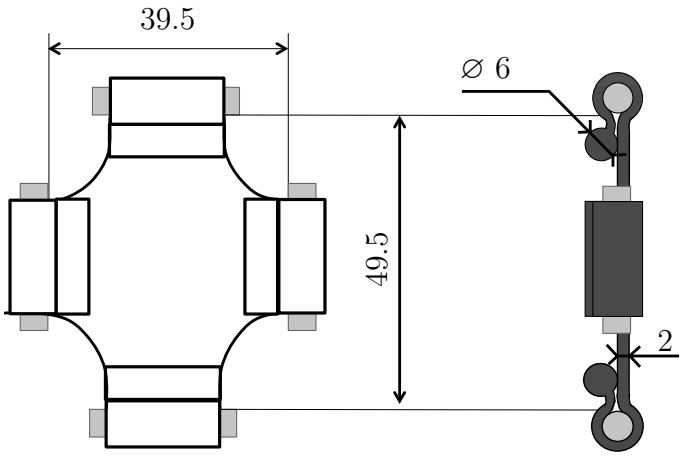

Figure 2.14 – Sample geometry used for the biaxial test (dimensions in mm)

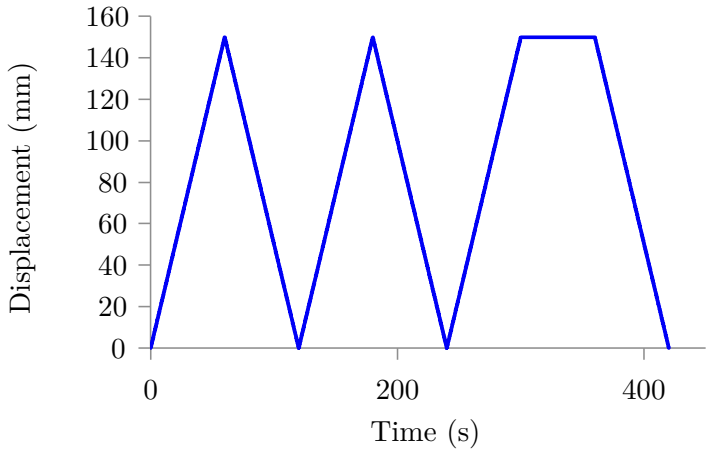

Figure 2.15 – Profile of the mechanical loading applied for the biaxial tensile test

2.2.3.3 Full kinematic field measurement

In order to characterize the strain state at the center of the cruciform specimen during the biaxial test, 5 images per second were stored by a IDS camera equipped with a 55 mm telecentric objective. The charge-coupled device (CCD) of the camera has 1,920 × 1,200

joined pixels. The displacement and strain fields were determined by the digital image correlation (DIC) technique. The software used for the correlation process was SeptD [115]. To this end, a white paint was sprayed on the surface of the specimen before testing. A suitable contrast in terms of gray level is ensured at the specimen surface with a home-made LED lamp (Figure 2.13), which provides a uniform cold lighting. In this configuration, a Region Of Interest (ROI) of 500 × 700 px is observed by the digital camera in the undeformed state. The spatial resolution was equal to 35.8 µm/px. Due to large displacement of the points during the test, the ROI was reduced to 320 × 340 px. The displacement was determined with a ZOI of 20 × 20 px and a grid step of 20 px. Therefore, the spatial resolution of the displacement field, defined as the smallest distance between two independent points was 20 px, i.e. 0.716 mm. This is sufficient considering that in the observed zone strain gradients are relatively small for such specimen geometry.

2.2.3.4 Full thermal field measurement

Temperature measurements were performed by using a cooled FLIR IR camera equipped with a focal plane array of 640 × 512 pixels and detectors operating in wavelengths between 1.5 and 5.1 µm. The thermal and kinematic measurements were synchronized at 5 images per second. The integration time was 2623 µm. The calibration of camera detectors was performed with a black body using a one-point Non-Uniformity Correction (NUC) procedure at this acquisition frequency. The thermal resolution or noise equivalent temperature difference (NETD) is 20 mK for a temperature range between 5 and 40 °C. The spatial resolution of the thermal field was 212 µm/px. The IR camera was switched on several hours before testing in order to stabilize its internal temperature. The surface emissivity of the material was evaluated by comparing the temperature of the specimen surface placed in an oven and heated to 50 °C with the one of a black body regulated at the same temperature. The emissivity of 0.94 was obtained. In uniaxial tests, the temperature is averaged in the central zone of the specimen with almost zero displacement. The size of the zone has no significant effect on the temperature measurement since the temperature variation to be quantified has the order of magnitude of several K while the thermal resolution is equal to 20 mK and the temperature field is homogeneous in this zone. In the biaxial test, the temperature is measured at the specimen center, where no displacement occurs during the test.

2.2.4 Results

2.2.4.1 Uniaxial tensile tests

In this section, the mechanical response measured in the four tests is first discussed. Then, the corresponding temperature variation and heat source are characterized. From the heat source, the intrinsic dissipation due to viscosity and stress softening as well as the relative part of the hysteresis loop corresponding to energy stored in the material are determined. The strain-induced crystallinity is finally evaluated by using the methodology described in Section 2.1.

2.2.4.1.1 Mechanical responses Results of Test #1 are shown in Fig. 2.16(a). The classical mechanical response of a filled rubber under cyclic loadings: non-linear elasticity, large strains undergone, hysteresis loop and the well-known accommodation first highlighted by [11] and deeply investigated by Mullins and co-workers from the 1940s [78] can be seen here. Note that the accommodation level is significant even though the amount of fillers is inferior to 20 phr. This was previously highlighted by [43]. Therefore, a low amount of fillers is sufficient to significantly activate the Mullins effect, but not the viscosity. The three other tests aim at characterizing both the accommodation and viscous effects. Fig. 2.16(b) shows the mechanical response during the specimen preconditioning (Test #3a). The material is loaded at a maximum stretch of 6 and the stabilized response is similar to that one obtained if cycles at lower maximum stretches are applied before (see Fig. 2.16(a), Test #1).

Including relaxation phases at the end of the last loads of each set of 3 cycles does not affect the stress-strain response of the following cycles (see Fig. 2.16(c)). The stress relaxation is mainly observed for the maximum stretch of 6. When the specimen is preconditioned (Test #3b, Fig. 2.12(d)), the Mullins effect no longer appears in the mechanical response. The hysteresis loop can only be due to viscosity and SIC. According to diagram in Fig. 2.16(d), hysteresis increases much stronger at $\lambda = 6$ in comparison to $\lambda = 4$ than at $\lambda = 4$ in comparison to $\lambda = 2$. Since SIC starts slightly before $\lambda = 4$, we can conclude that this increase is mostly due to SIC. Furthermore, during the last unloading where three pauses were applied, viscous effects are very small. Indeed, in contrast to crystallization, melting is assumed to occur instantaneously. Thus, the only stress recovery effect should have been due to viscosity. As the relaxation is very low at $\lambda = 4$ (stretch close to onset of SIC), the effect of viscosity on the relaxation should be low

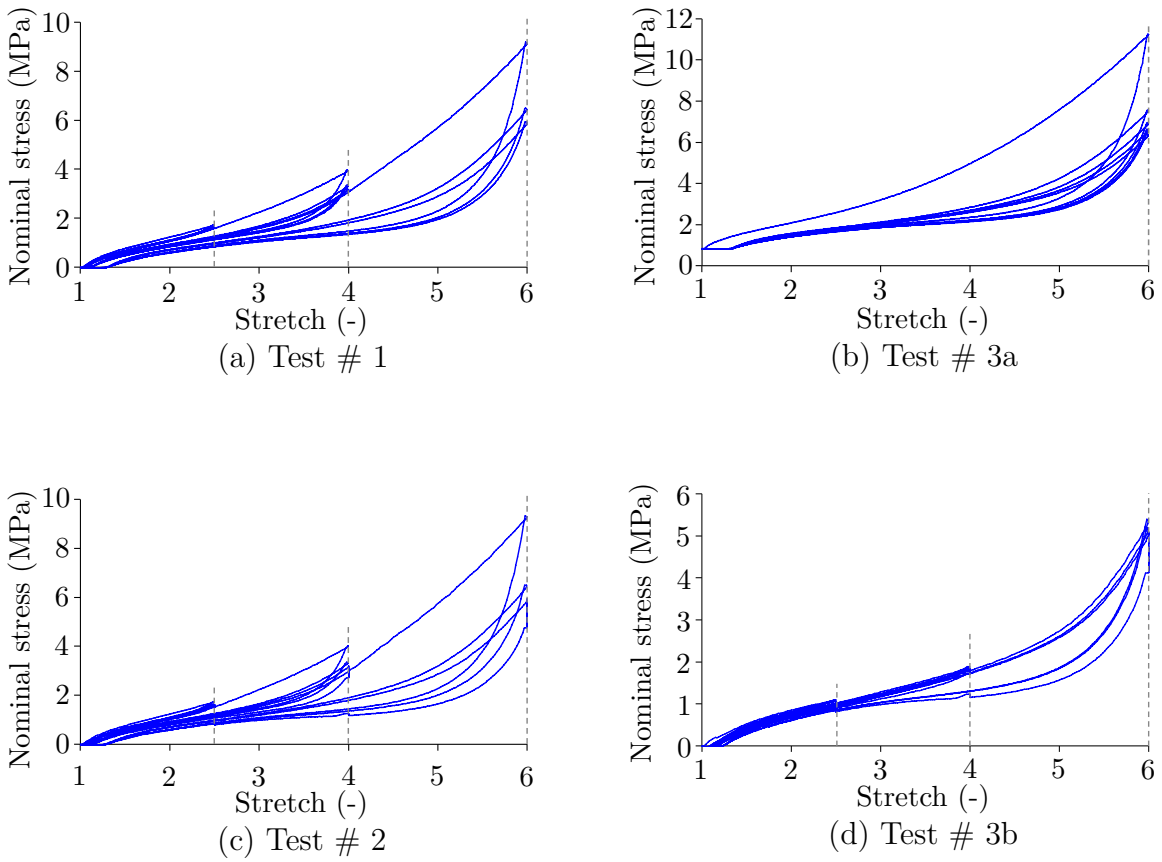

Figure 2.16 – Experimental stress-stretch curves

compared to that of SIC. These different conclusions cannot be definitely drawn solely on the basis of the mechanical response and further investigations are carried out with the calorimetric measurements.

2.2.4.1.2 Thermal responses The thermal response measured during the different tests is illustrated in Figure 2.17. We can observed here rather weak self-heating of the material, meaning that the intrinsic dissipation produced at each cycle and therefore the viscous effect is low. This is in good agreement with the previous analysis. Furthermore, in contrast to unfilled natural rubbers (see [3, 50, 95]), the thermoelastic inversion is not observed in the thermal response. This is explained by the fact that the heat produced by the intrinsic dissipation is superior to the heat absorbed by the material at the very low stretches. As the tests were conducted under non-adiabatic conditions, which is generally the case for quasi-static characterization test, the thermal response does enable us to

quantify neither the intrinsic dissipation nor the crystallinity. To this end, a calorimetric analysis is required.

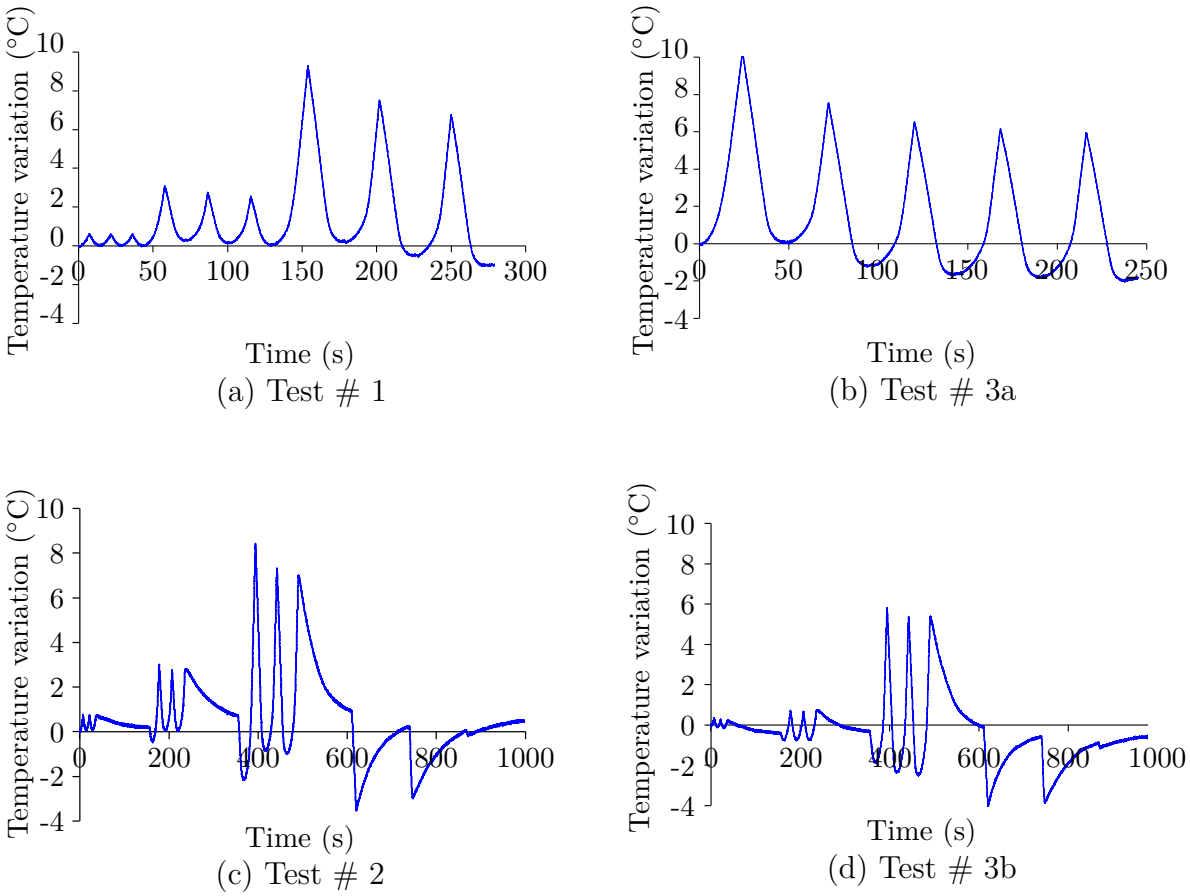

Figure 2.17 – Experimental temperature variation evolution curves

2.2.4.1.3 Calorimetric responses Figure 2.18 presents the calorimetric responses of Tests #1, #2, #3*a* and #3*b*, determined from the temperature measurements and the simplified heat diffusion equation (Equation 1.35). First of all, no significant difference was observed between the first three cycles at $\lambda = 2$ in non pre-conditioned materials. Moreover, the heat source is quite symmetrical between loading and unloading. A strong difference in the accommodation is obtained between the first loading and the following ones. The area between them, which appears in color in the diagrams, corresponds to the energy dissipated due to the Mullins effect.

Furthermore, the heat sources for cycles at the maximum stretches of 4 and 6 were symmetrical. The occurrence of a asymmetry when increasing the stretch is the typical

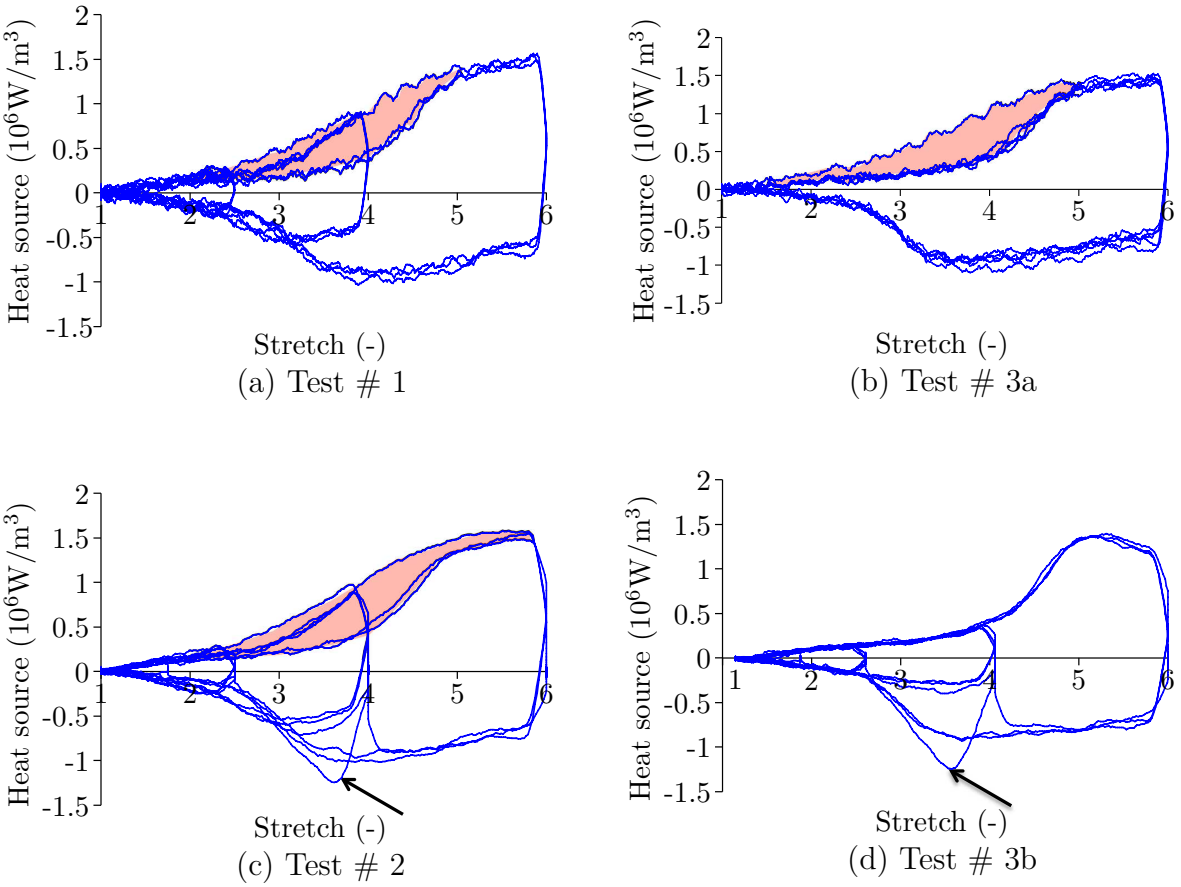

Figure 2.18 – Experimental heat source evolution curves

calorimetric signature of SIC (see for instance [96] or [53]). During the stabilized loading cycles in Test #1, a strong increase in the slope of the heat source curve is observed when SIC starts. This increase is observed at stretch of 2.7 and 3.1 approximately for the loading cycles with the maximal stretch amplitude of 4 and 6, respectively. Test #3*a* led to the same result. This is due to the permanent set effect that increases the initial length (14% and 30% for cycles at maximum stretches of 4 and 6, respectively). One can therefore account for this permanent set to recalculate the onset of SIC as if the specimen was previously accommodated and has higher initial length. In this case, the onset of SIC return to a same stretch value, i.e. 2.4. Thus, the influence of the permanent set, preconditioning and the maximal cyclic stretch on the onset of SIC is very complex and should further be studied. This is why, the exact conditions used to evaluate this onset have to be clearly explained, which is not the case in many studies.

For the tests with relaxation phases (Tests #2 and #3*b*), similar conclusions can be

drawn. Nevertheless, focusing on the unloads, a strong heat absorption is observed after the pause at $\lambda = 4$ ((see arrows in Figs. 2.18(c) and (d))). This level of heat absorption was not reached without this pause. The only explanation for this phenomenon is that the SIC is time dependent process and the pause allows the crystallinity degree to increase. Therefore, more energy is absorbed due to additional melting when the stretch decreases from 4. The fact that this effect was not observed at $\lambda = 6$ has to be further investigated with respect to the crystallite typology and the fact that the SIC kinetic rate increases when the maximum stretch applied increases [47]. This is an important experimental result for modeling SIC. It should finally be noted that after prestretch to $\lambda = 6$, the asymmetry in the cycles is less important at $\lambda = 4$.

The mean intrinsic dissipation $\tilde{\mathcal{D}}_{int}$ can be obtained as a time integral of the heat sources over the cycle time, normalized by the cycle duration (see Equation 2.6). Then, $\tilde{\mathcal{D}}_{int}$ was calculated for the third cycle of each stretch amplitude and is only due to viscosity. From Figure 2.19, we can observe that $\tilde{\mathcal{D}}_{int}$ evolves quasi-linearly with the stretch. This is an important information for modeling the viscosity in filled natural rubber.

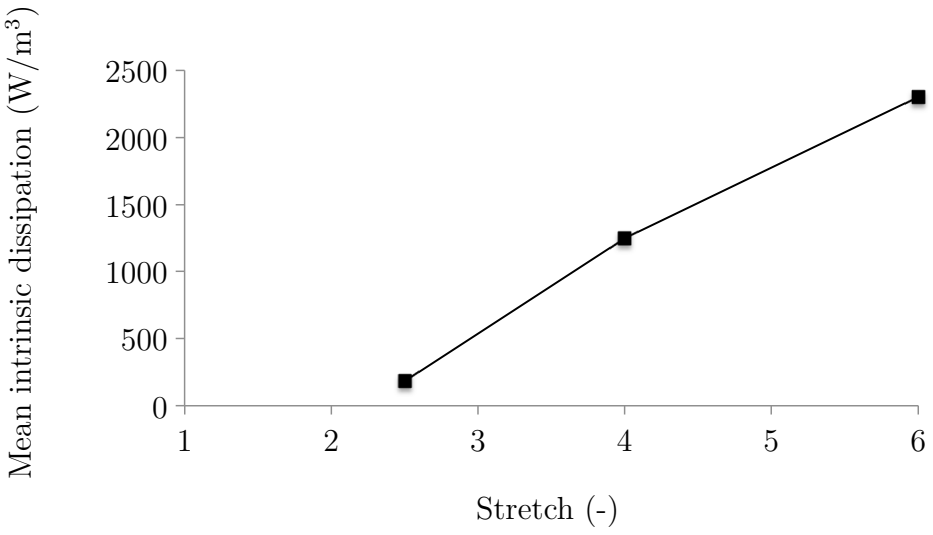

Figure 2.19 – Mean intrinsic dissipation due to viscosity only versus stretch evaluated from the thermodynamic (mechanically and thermally stabilized) cycles of Test #1

As the heat sources during the unloads were all superimposed for tests without relaxation phases, the energy involved in the accommodation (Tests #1, #2 and #3*a*) can be approximated as the areas in red color in Figures 2.18(a), (b) and (c). In practice, it consists in considering that the third cycles of each stretch amplitude is fully accommodated. The mean intrinsic dissipation due to the accommodation (the calorimetric signature of

the Mullins effect) is evaluated by subtracting the mean intrinsic dissipation obtained at the third from the first cycles [71]. Figure 2.20 illustrates the results obtained for Tests #1. From this figure, it becomes apparent that the mean intrinsic dissipation produced by the Mullins effect increases with the stretch, but the slope is lower than the one of the intrinsic dissipation due to viscosity only. Indeed, the Mullins effect contributes to 81%, 64% and 58% to the mean intrinsic dissipation involved during the first cycles at the maximal stretches of 2.5, 4 and 6, respectively. This is the same order of magnitude as [71] found for a 50 phr carbon black filled natural rubber.

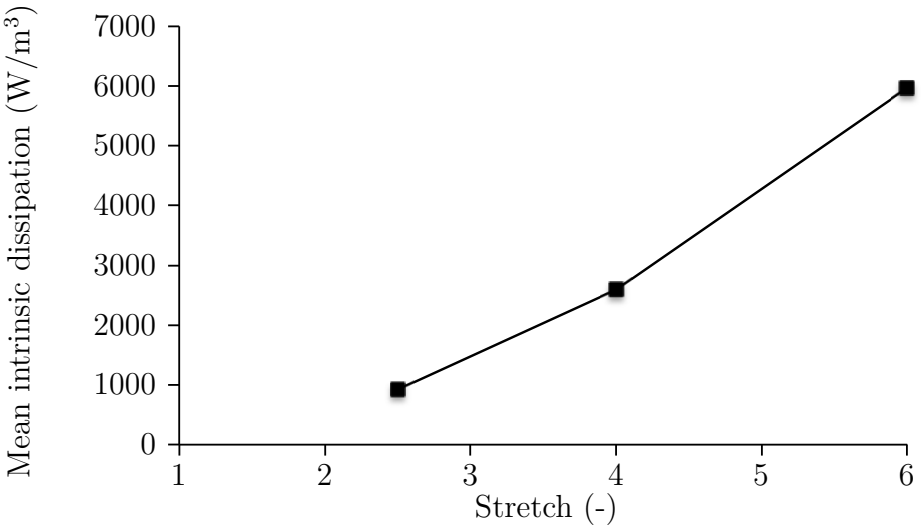

Figure 2.20 – Mean intrinsic dissipation due to Mullins effect versus stretch evaluated from Test #1

2.2.4.1.4 Energy balance Energy balance is investigated in order to evaluate relative contributions of the physical phenomena involved in the hysteresis loop. Recently, it was shown that the viscosity is not the only origin of the hysteresis loop. Indeed, energy stored and fully or partially released with a different rate also contributes to the hysteresis loop. This energy storage can be due not only to SIC [53, 55], but also to the filler network [64]. These studies clearly highlight that the hysteresis loop cannot be modeled by the contribution of the material viscosity only. To quantify the relative contribution of the energy storage in rubbers, the γ_{se} ratio has recently been introduced in [64] and is used in Fig. 2.21. Generally, γ_{se} varies between 0 (the hysteresis is only due to viscosity) and 1 (the hysteresis is only due to energy storage). For the latter case, the example of the unfilled NR is reported in the diagram. For Test #1, the viscosity is responsible for more

than 80% ($\gamma_{se} < 0.2$) of hysteresis at a maximal stretch of 2 and 4. Increasing the stretch, and as a result the crystallinity, reduces the viscosity and increases the energy storage up to about 50%. Obviously, such an effect is of an important benefit for limiting the self-heating and the energy available for damage, which explains the remarkable mechanical properties of filled natural rubbers.

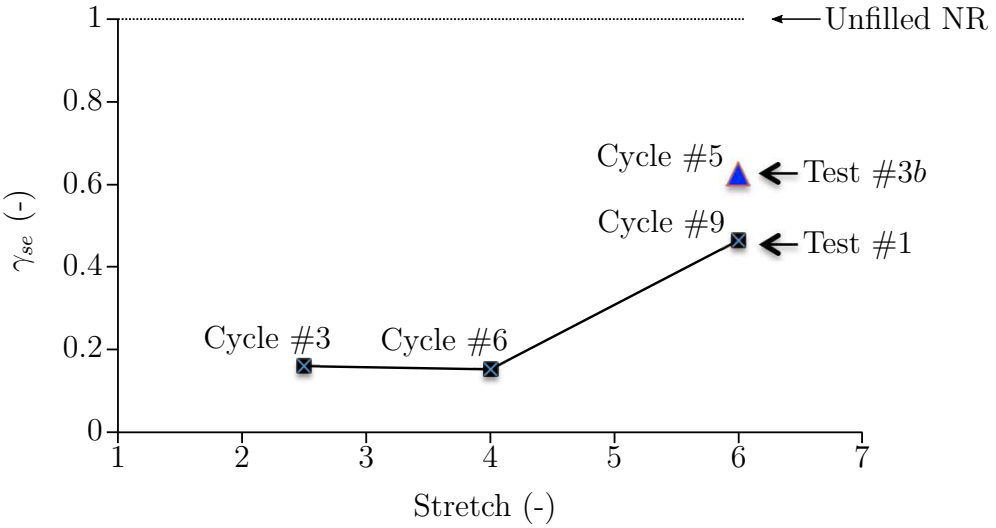

Figure 2.21 – γ_{se} evaluated from thermomechanic cycles: cycles #3, #6 and #9 for Test #1 and cycle #5 for Test #3*b*. As an indication, the vaue of γ_{se} is approximately 1 for unfilled natural rubber

2.2.4.1.5 Strain-induced crystallinity The strain-induced crystallinity has been evaluated with the methodology described in Section 2.1 from the last cycle of Test #3*a*. In Figure 2.22, the crystallinity versus stretch is plotted. The heat source without crystallization is predicted by the following polynomial:

$$s_{predicted} = C_1(\lambda - \lambda^{-2}) + C_2(\lambda - \lambda^{-2})^2 + C_3(\lambda - \lambda^{-2})^3 \tag{2.9}$$

The polynomial coefficients were identified by fitting the heat source curve before SIC starts, i.e. at a stretch equal to 3.2. The thermal energy due to SIC corresponds to the area between the two curves. The temperature variation due to SIC and the crystallinity is then calculated by using the methodology described in Section 2.1. Figure 2.23 gives the crystallinity versus stretch. The maximum value reaches 13.2% and is in a good agreement with the measurement performed by using X-ray diffraction in [66] in a natural rubber with a formulation (sulfur amount and filler amount) close to the present one.

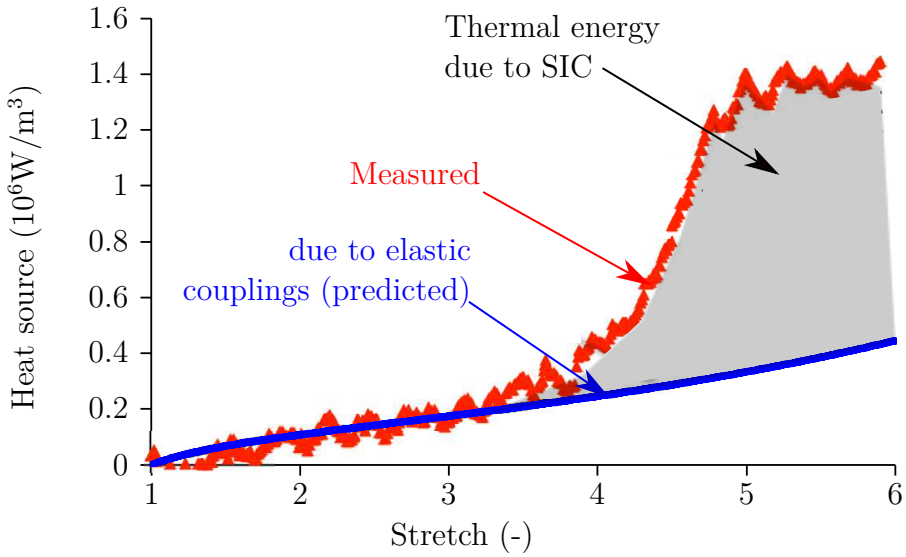

Figure 2.22 – Evaluation of the thermal energy due to SIC for the 5^{th}

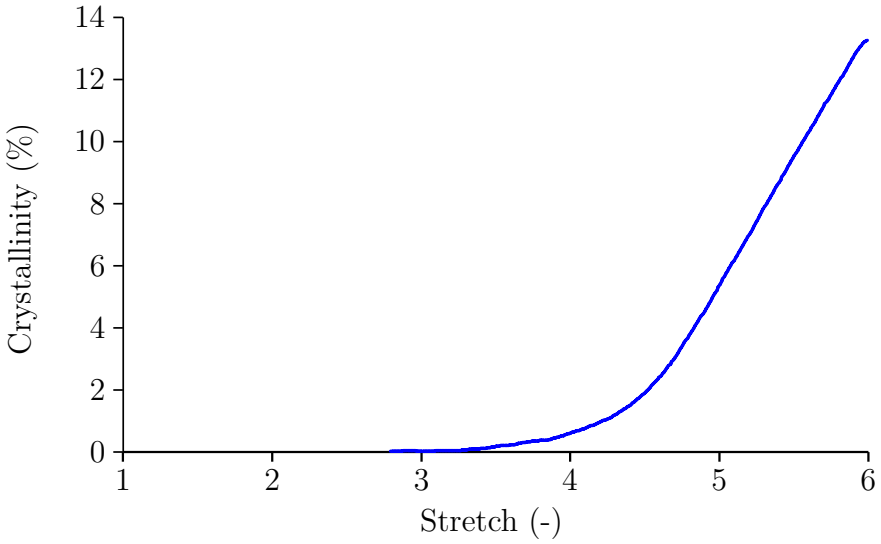

Figure 2.23 – Evaluation of the strain-induced crystallinity

2.2.4.2 Biaxial tensile test

Previously, SIC was studied all, but under uniaxial loadings. Rare studies investigate multiaxial effects on SIC, although the phenomenon appears to be strongly affected by the biaxiality of the strain state. In the case of unfilled natural rubber, an increase of the biaxiality coefficient from uniaxial tension was recently found to suppress or strongly reduce SIC in [22]. Specifically, the authors found that no crystallization emerges even

under large stretch levels up to specimen fracture. It should be noted that the maximum value of the biaxiality coefficient was equal to 0.6. In contrast, [7] tested a filled natural rubber under uniaxial, biaxial and equibiaxial loading conditions. They found similar crystallites under uniaxial and equibiaxial tension: their size was of the same order of magnitude and the lattice parameters were identical. Under equibiaxial tension, they found an index of crystallinity equal to 1.09 % at $\lambda = 4$. Furthermore, the orientation of the crystallites highly depended on the biaxiality level: the disorientation is constant and small between uniaxial and planar tension; the greater the biaxiality, the greater the disorientation under biaxial tension, the crystallites do not have a preferred direction under equibiaxial loading. Thus, the question of how the multiaxiality loading affects on SIC is under-explored and new characterization techniques could therefore be used to enrich the knowledge in this field.

This section aims to characterize the thermal and calorimetric responses of the filled natural rubber under a highly multiaxial strain state, i.e. under a high value of the biaxiality coefficient. The strain-induced crystallinity is also evaluated by the surface calorimetry technique presented in Section 2.1 and discussed according to [7] and [22].

2.2.4.2.1 Kinematics of the specimen's center The kinematics of the zone at the specimen center was investigated from the DIC measurements. Figure 2.24 provides the principal stretches and the biaxiality coefficient in the specimen plane with respect to time and the displacement imposed in each branch. The boxes in gray color stand for the parts of the test where buckling occurred. The maximal principal stretch exceeded 3 for the maximum displacement applied, which is very close to the stretch at which crystallization started under uniaxial tension. The biaxiality coefficient is plotted in this figure. Its value varies between 0 (shear) and 1 (equibiaxial tension) during the cycles. It is to note that its value is superior to 0.8, which is close to the equibiaxial loading condition, for maximum principal stretches superior to 2.

2.2.4.2.2 Thermal and calorimetric response of the specimen's center Figure 2.25 gives the temperature and the heat source versus time and displacement applied in each branch. The heat source has been calculated by accounting for the change in the biaxiality coefficient in the calculation of $\tau(\lambda, B) = \tau_0 \lambda^{-B-1}$. During the first loading, a strong heat production occurred due to the Mullins effect (Circles #1 and #2), so that it was not possible to distinguish the heat produced by the thermo-elastic couplings, the

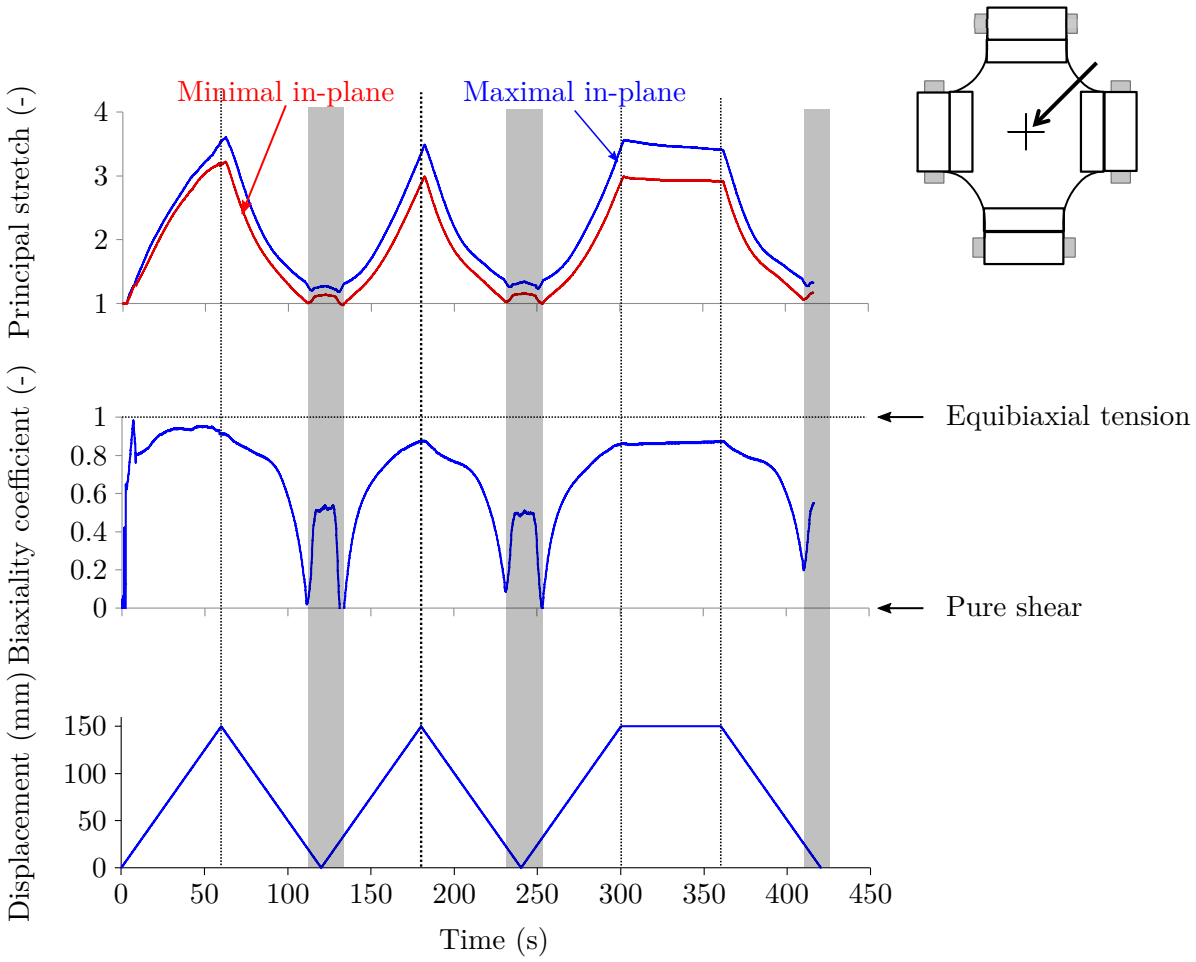

Figure 2.24 – Principal stretches, biaxiality coefficient and displacement at the specimen center versus time

viscosity and the crystallization if any from the heat produced by the Mullins effect. During the next cycle, a significant change in the curve slope was observed during the first loading, which is the typical signature of SIC (see Box #1). It should be noted that the heat absorbed during the unloading at Cycle #1 is superior to that absorbed at Cycle #2, due to the fact the material is stiffer at the end of the first cycle. The heat absorbed is therefore higher than for the following cycles.

The difference between Cycles #2 and #3 is the relaxation phase. When the displacement is kept constant in the branch, a strong heat production is still observed, while the thermo-elastic couplings do not produce heat anymore. This heat production can be due to intrinsic dissipation and/or to crystallization. To distinguish the two contributions, the heat absorbed during the unloading of Cycles #2 and #3 is examined. The fact that the

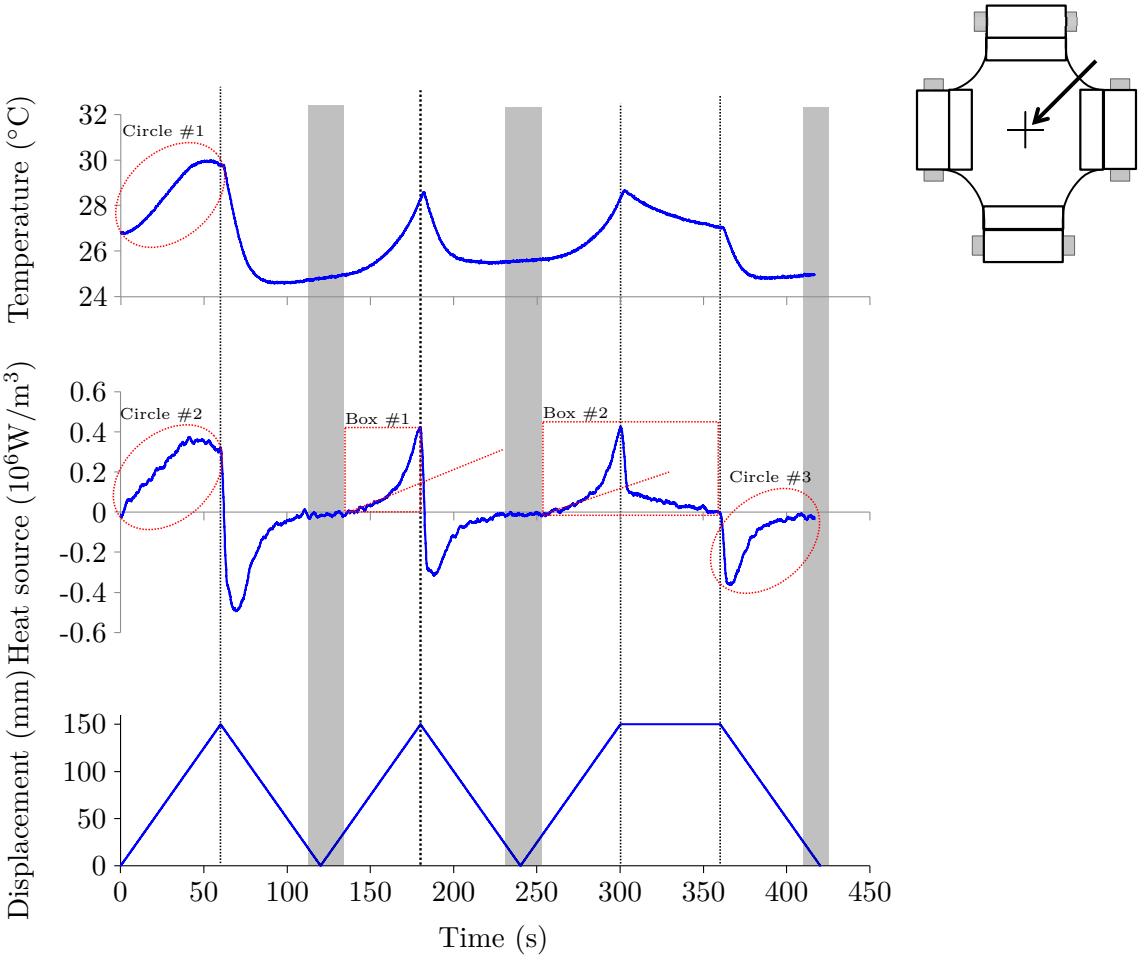

Figure 2.25 – Temperature, heat source and displacement at the specimen center versus time

heat absorbed during the unloading of Cycle #3 is is superior to that absorbed during the unloading of Cycle #2 highlights that the main contribution to the heat production due relaxation is SIC. Indeed, if viscosity was the preponderant effect, the heat absorbed during the unloading of Cycles #2 and #3 would had been the same.

2.2.4.2.3 Discussion The previous session has shown that the filled natural rubber considered crystallizes under biaxial tension. This result is in a good agreement with the one obtained in [7] for a natural rubber vulcanized with 1.2 phr of sulfur and filled with 50 phr of N330 carbon black. In their study, authors carried out XRD measurements in the case of three deformation states: uniaxial, biaxial and equibiaxial tension. They found that crystallites are similar in the three deformation states: the lattice parameters of the crystal

unit cell were identical and the size of the crystallites is of the same order of magnitude. Therefore, the present study confirms the first results obtained with XRD on the effect of multiaxiality on SIC infilled natural rubber. Nevertheless, this is in contradiction with results obtained in unfilled natural rubber by [22], who found that no crystallization occurs when increasing the biaxiality coefficient up to 0.6. In their study, the authors provided neither the precise specimen geometry they used, nor the boundary conditions they applied. It is therefore difficult to discuss on their results at the local scale. The question is therefore whether the presence of charges alone could explain this difference in results.

In her study, [7] also evaluated the index of crystallinity. Under equibiaxial tension at principal stretches equal to 2.4 in the plane of tension, the author found a crystallinity index equal to 1.09%. In our present study, an attempt was made to evaluate the crystallinity under biaxial loading. Under uniaxial tension, the crystallinity is evaluated by using Equation. 2.3. Under biaxial loading, an important question arises: does the multiaxiality of the strain field have an effect on the fusion enthalpy? As Beurrot found that the size the crystal unit cell and the size of the crystallites are of the same order of magnitude between uni and biaxial loadings, it is assumed here that crystallinity can still be determined from the temperature increases due to crystallization ΔT_{cryst} and the enthalpy of fusion.

Figure 2.26 gives the heat source obtained during the second loading (curve in red). The heat source due to elastic couplings only (curve in blue) is predicted by using the polynomial form described in Equation. 2.2: $C_1(\lambda - \lambda^{-2B-3}) + C_2(\lambda - \lambda^{-2B-3})^2 + C_3(\lambda - \lambda^{-2B-3})^3$ to account for the biaxial strain state. It is to note that the strong increase in the heat source is obtained at a principal maximum stretch for which the biaxiality coefficient is close or superior to 0.8, i.e. a value close to 1 (equibiaxial tension).

Figure 2.27 shows the crystallinity obtained. The crystallinity evaluated under uniaxial loading is reported in order to highlight the effect of the variation in the biaxiality coefficient. It clearly appears that increasing the biaxiality coefficient from -0.5 to 0.8 led to a decrease in the crystallization onset from 3.2 to 2.6. At a maximum principal stretch equal to 3.4, the crystallinity reached 1,74%. This seems to be in a good agreement with what found Beurrot, as the amount of carbon black fillers is lower in the present case.

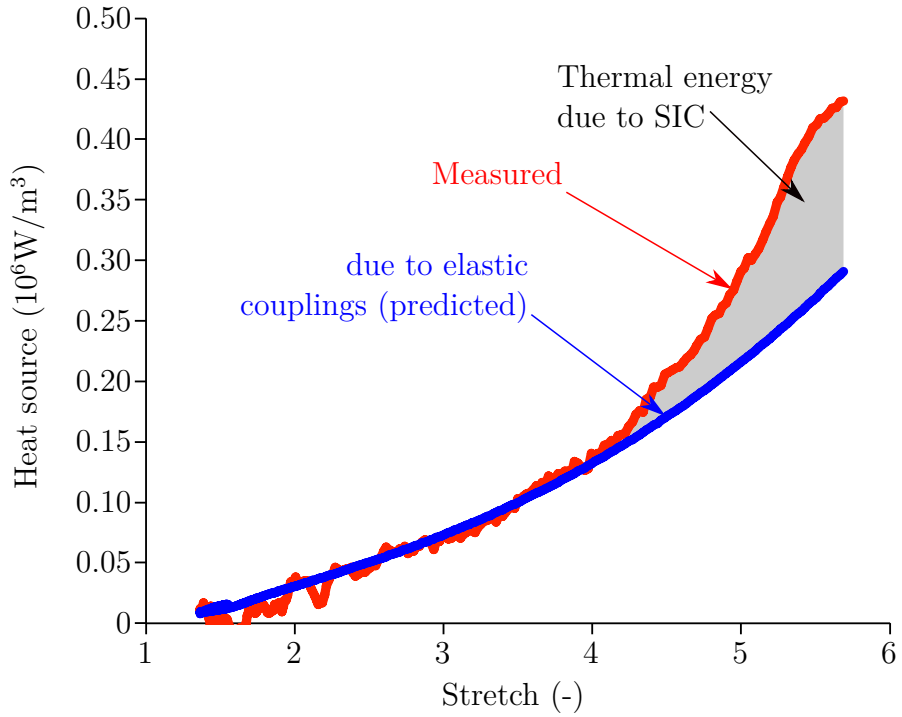

Figure 2.26 – Principal stretches, biaxiality coefficient and displacement at the specimen centre versus time

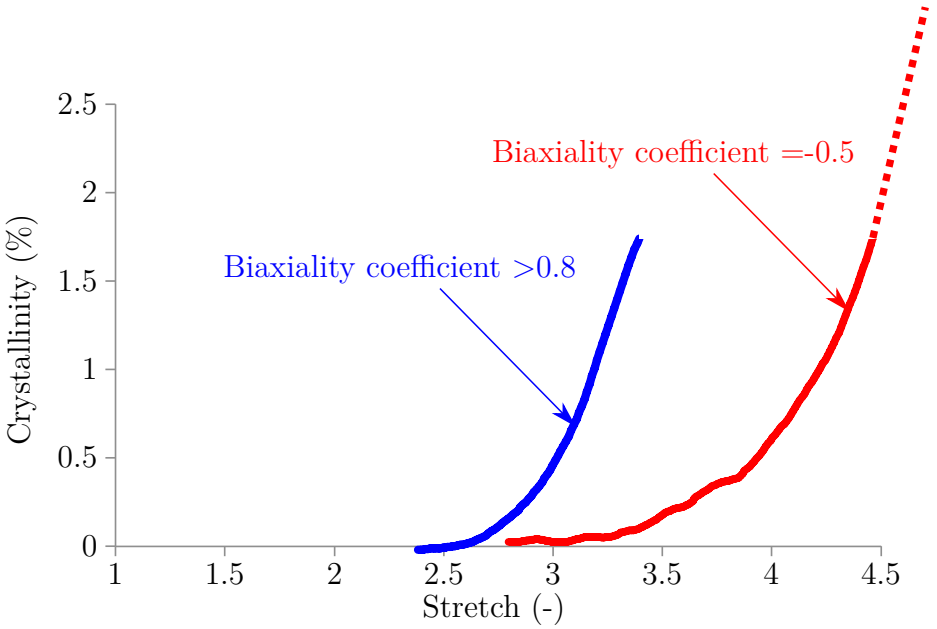

Figure 2.27 – Crystallinity versus stretch and biaxiality coefficient

2.2.5 Conclusion

In this second part of Chapter 2, the first full thermomechanical and calorimetric characterization of a filled crystallizing natural rubber under uniaxial and biaxial loadings has been presented. Under uniaxial loading, several conditions have been tests. It consisted in sets of several cycles at increasing maximum stretches, with and without accommodation, with and without pause. The corresponding calorimetric response has been determined from the thermal response and the simplified formulation of the heat diffusion equation. A complete energy balance was carried out for determining the intrinsic dissipation due to viscosity and stress softening. It was shown that the hysteresis loop in the strain-stress relationship mainly corresponded to energy stored in the material, i.e. the contribution of the viscosity is low. The pourcentage of energy stored has been quantified with respect to the maximum stretch applied. The strain-induced crystallinity and the crystallization onset were also evaluated from the heat power density response. Biaxial test was then carried out with a cruciform specimen. The signature of crystallization was detected in the calorimetric response. Kinematic measurements in the central zone of the specimen showed that the crystallization onset was obtained at a principal stretch equal to 2.6 with a biaxiality coefficient of 0.8. This indicates that:

1. filled natural rubber crystallizes under high biaxiality coefficient if the principal stretch level applied is high enough,

2. increasing the biaxiality coefficient decreases the crystallization onset (from 3.2 to 2.6 in the present case).

This confirms the results obtained by Beurrot-Borgarino [7] in a natural rubber filled with a larger amount of carbon black fillers. Crystallinity has been evaluated from the calorimetric response by applying the methodology proposed by Le Cam [56], which was validated with X-ray diffraction measurements in the case of uniaxial loadings. The crystallinity was found to reach 1.74% at a maximum principal stretch equal to 3.4. These experimental results provide quantitative information of paramount of importance for modeling the complex behavior of filled natural rubber.

2.3 Extension of the surface calorimetry technique to the 1D situation for investigating SIC heterogeneity under homogeneous macroscopic loading

2.3.1 Introduction

In Section 2.1, a method for evaluating the crystallinity from surface calorimetry has been presented and validated. It has been shown that the crystallinity values are in a very good agreement with those obtained with the XRD technique. While the XRD does not only give the crystallinity level but also information about crystallites size and orientation, the method can only give the information at a single X-ray spot. This limitation can induce issues of importance in case of crystallinity heterogeneity, such as at a crack tip [92]. Typically, in case of heterogeneous crystallinity fields, a scan has to be performed. This means that the crystallinity is not determined at the same time from one point to another in the field.

Surface calorimetry method overcomes this limitation, since the full-field of crystallinity comes from the processing of the temperature field, obtained with infrared thermography. In this section, the calorimetric method is used to measure the crystallinity field in a homogeneous uniaxial tensile test in order to investigate possible crystallinity heterogeneity. This study has been motivated by previous observations carried out in our research group, which are not reported here.

2.3.2 Experimental setup

2.3.2.1 Material and specimen geometry

In the present study, two unfilled natural rubbers with different sulfur amounts were considered, 1.2 phr and 1.6 phr, denoted 0NR1.2 and 0NR1.6 in the following. Since the strain-induced crystallization is strongly dependent on the vulcanization rate, these two materials will allow us to determining the influence of the vulcanization rate on the results. The specimen geometry is also taken into account, the different geometries are reported in Table 2.1.

For this study, the heat capacity C and the mass density ρ have been taken equal to 1858 $\mathrm{JK^{-1}m^{-3}}$ and 957.6 $\mathrm{kg/m^3}$. The "Manufacture Française des pneumatiques Michelin" is acknowledged for providing the specimens. Also Klara Loos, Michael Johlitz and

Material / Geometry	0NR1.2	0NR1.6
Thin specimen	L = 12 mm l = 9.64 mm e = 2 mm	L = 12 mm l = 8.36 mm e = 2 mm
Large specimen	L = 12 mm l = 18.8 mm e = 2 mm	L = 12 mm l = 16.1 mm e = 2 mm

Table 2.1 – Geometries of the different specimens used

Alexander Lion

2.3.2.2 Mechanical tests

The same experimental setup than the one used in Section 2.1 is used in this study (see Figure 2.2).

The specimens have been stretched symmetrically to ensure a motionless specimen center, i.e. the middle section contracts along the horizontal direction, but does not move in the vertical direction. The mechanical loading applied corresponded to 3 loading/unloading uniaxial tensile cycles. The maximal displacement of each actuator was set at 36 mm, which corresponded to an elongation of 7. The loading rate was equal to 150 mm/min for each grip, therefore300 mm for the stretching rate. Temperature measurements were performed by using a FLIR infrared camera equipped with a focal plane array of 640x512 pixels and detectors operating in wavelengths between 1.5 and 5.1 µm. The integration time was equal to 2700 µs. The acquisition frequency was equal to 50 Hz, and images were stored at the rate of 20 Hz. The calibration of camera detectors was performed with a black body using an one-point NUC procedure at this acquisition frequency. The thermal resolution, or noise equivalent temperature difference (NETD), was equal to 20 mK for a temperature range between 5 and 40 °C. The infrared camera is switched on several hours before the test in order to stabilize its internal temperature. The emissivity was set at 0.94 [1].

1. Emissivity of elastomer surfaces has been measured in [20]

2.3.2.3 Stretch measurement

Stretch level evolution is determined by measuring the displacement of each grip and the initial length of the specimen. We recall here that the specimens have cylindrical ends which avoid any slippage with the grips. A residual strain was observed during the first cycle. This residual strain have been taken into account to recalculate the stretch. For the reader information, Figure 2.28 represents the stretch level with and without correction by taking into account the residual strain.

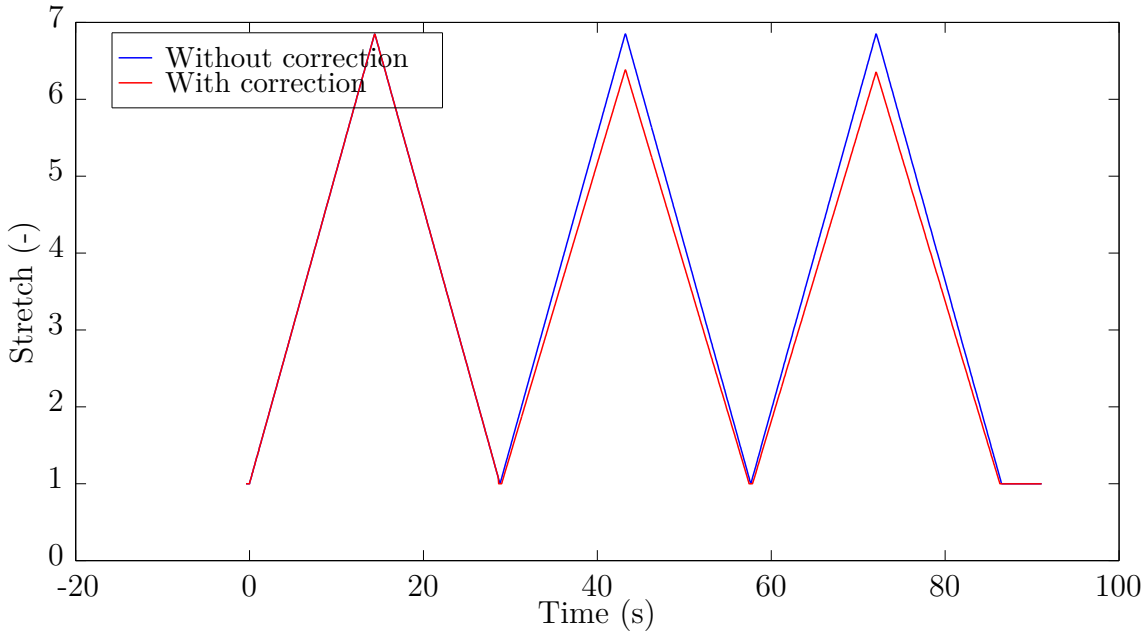

Figure 2.28 – Stretch level during a test

2.3.2.4 Motion compensation technique

Since specimens undergone large displacement during the test, material points move from pixel to pixel in the IR images. A motion compensation method has been developped to follow the material points along the width at the median section of the specimen, where no vertical displacement occurred. It means that the displacement of each point of the section can be obtained from the displacement of the two side bounds. Their position, and subsequently their displacement during the test, was obtained by using a edge detection algorithm. In the present study, the edge detection algorithm is obtained by applied a gradient operation along the horizontal direction, then the image obtained is segmented. Figure 2.29 illustrates the results of this motion compensation method.

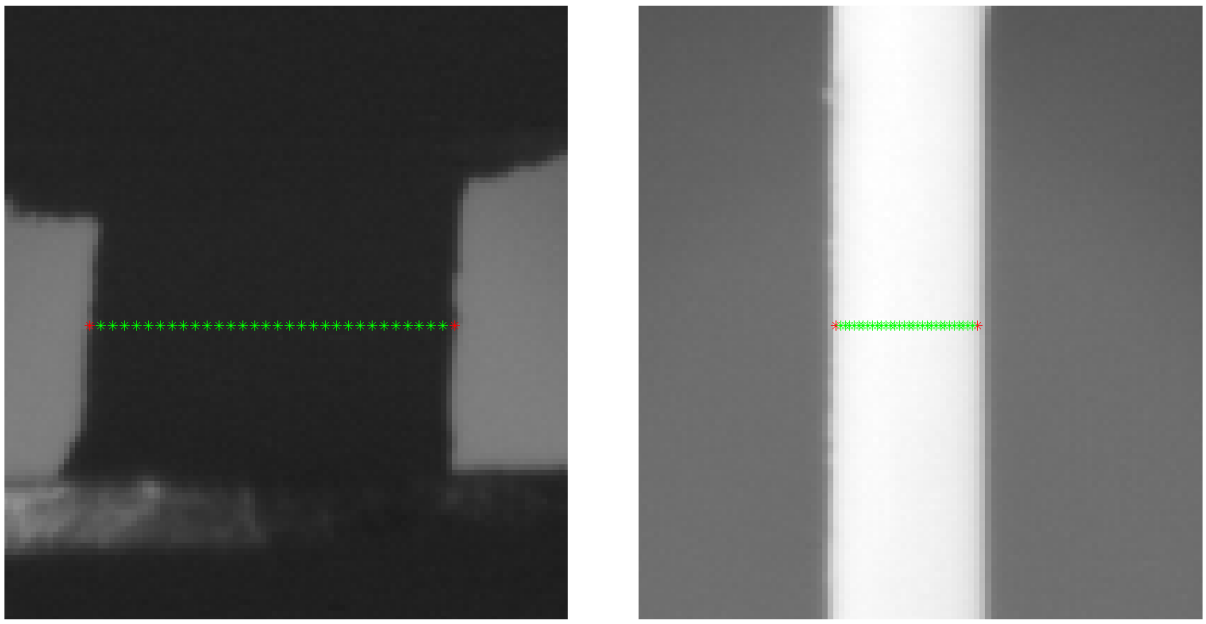

(a) Undeformed state (b) Deformed state

Figure 2.29 – Results of motion compensation method

Figure 2.30 compares the distance between two measurement points during the test with the spatial resolution of the camera. This figure clearly shows that the distance between two measurement point is higher than the spatial resolution, which mean that the temperature measurement of each material points is independent from the others.

2.3.2.5 Determining the 1D crystallinity field

Once the motion compensation method was applied, and the temperature evolution obtained, the calorimetric method described in Section 2.1 was used. The first step of the method aims at measuring the total heat source produced by the material, by using the heat equation. The second step of the method is to predict the heat source if no crystallization occurs. This is made by using the polynomial form presented in Section 2.1. Figure 2.31 represents both the heat source measured and the heat source predicted due to thermoelastic couplings only.

The heat source from SIC is then deduced by subtracting the total heat source with heat source predicted. The equivalent temperature variation T_{cryst} can then be determined from Equation 2.1. It can easily be obtained from the integration of the heat source over the time, and assuming that it is equal to 0 before the crystallization starts. Last, the crystallinity is deduced from T_{cryst} and the fusion enthalpy ΔH.

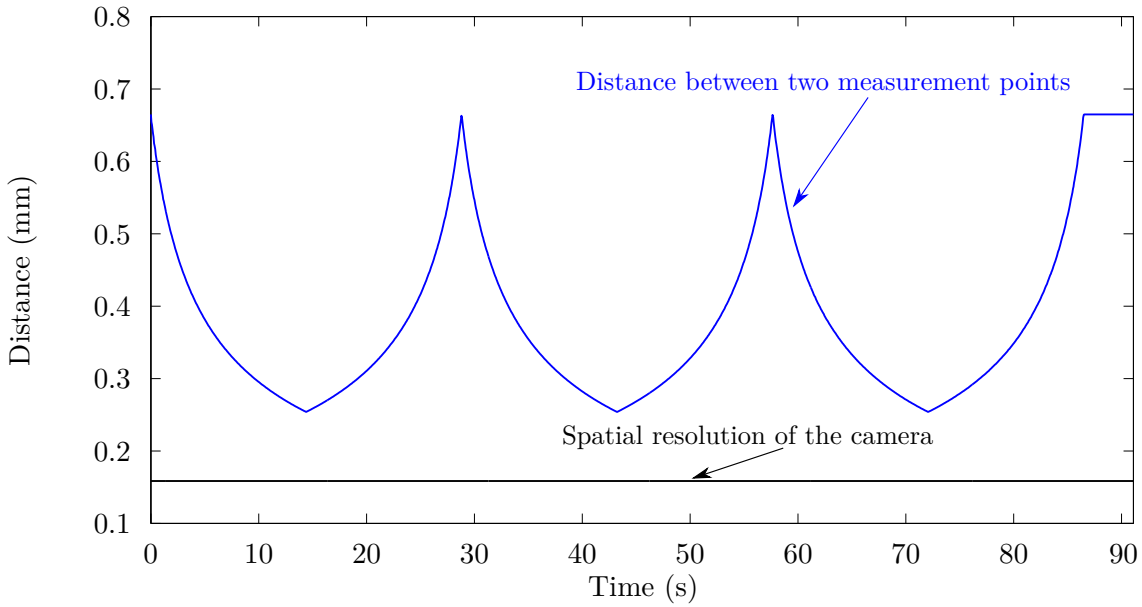

Figure 2.30 – Comparison of the distance between two measurement point with respect to the spatial resolution of the camera

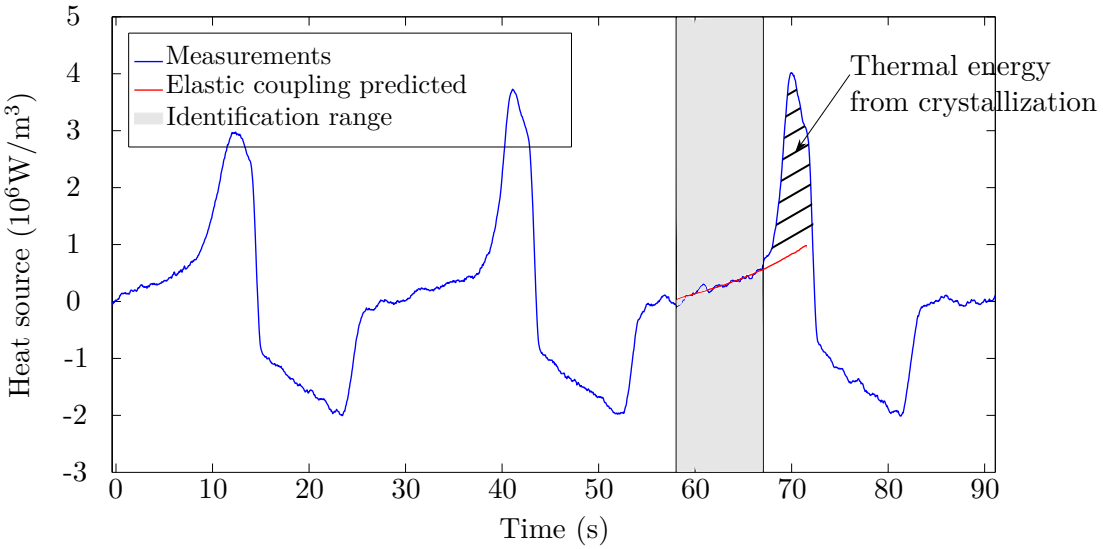

Figure 2.31 – Time evolution of heat source during the mechanical test of the thin 0NR1.2 specimen

2.3.3 Results

Figure 2.32 shows the crystallinity versus stretch curve during the third mechanical load for the different materials and geometries. The crystallinity shown is observed by the calorimetric method, using the mean temperature of the different point followed. A small

difference can be observed for the 0NR1.2 material, which can be due to the difference of geometry used for the sample, while the geometry does not seem to affect the crystallinity for the 0NR1.6 material.

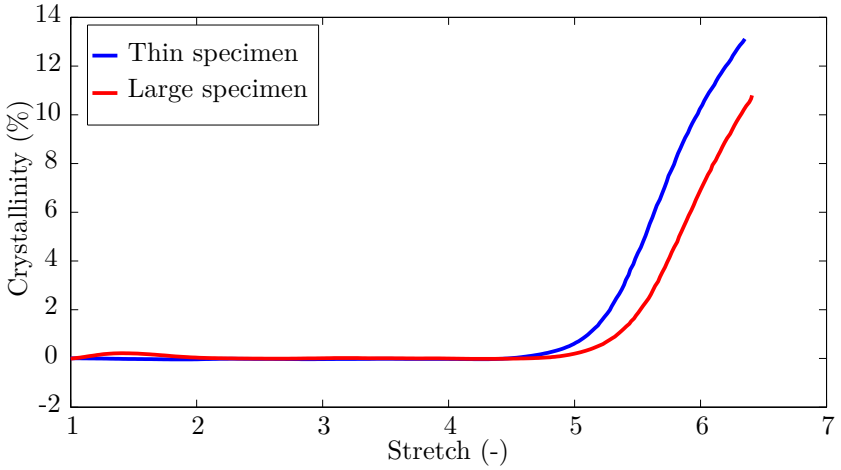

(a) 0NR1.2 material

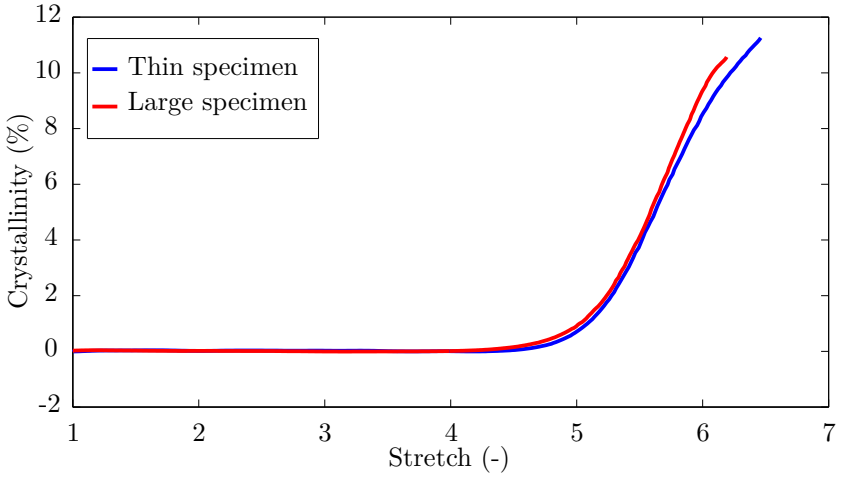

(b) 0NR1.6 material

Figure 2.32 – Mean crystallinity level versus stretch

2.3.3.1 Results obtained in the 0NR1.2 rubber

Figures 2.31 and 2.32 present the mean crystallinity results, that could be obtained using the X-ray diffraction method, but the main benefit of the calorimetric method is to measure the crystallinity at several points at the same time. Figure 2.33 represents the crystallinity obtained during the third stabilized mechanical load for the thin specimen of 0NR1.2 material. This figure highlights that the crystallinity is not homogeneous even

though the mechanical test is assumed to be homogeneous. Figure 2.34 presents the profile

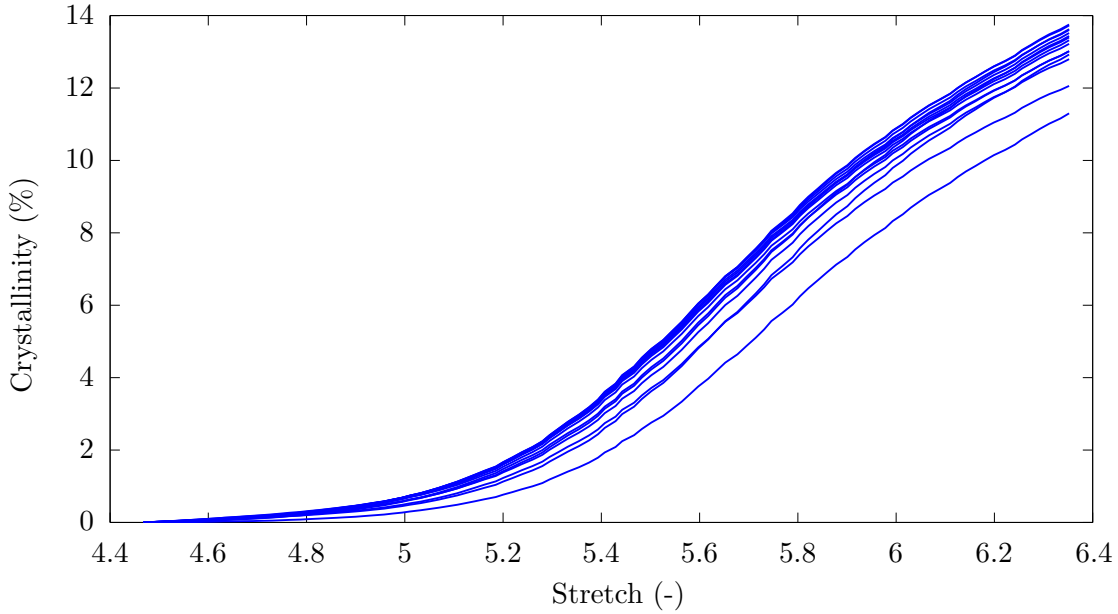

Figure 2.33 – Crystallinity measurement on the 0NR1.2 specimen

of crystallinity in the median section of the two specimens at the maximal displacement imposed.

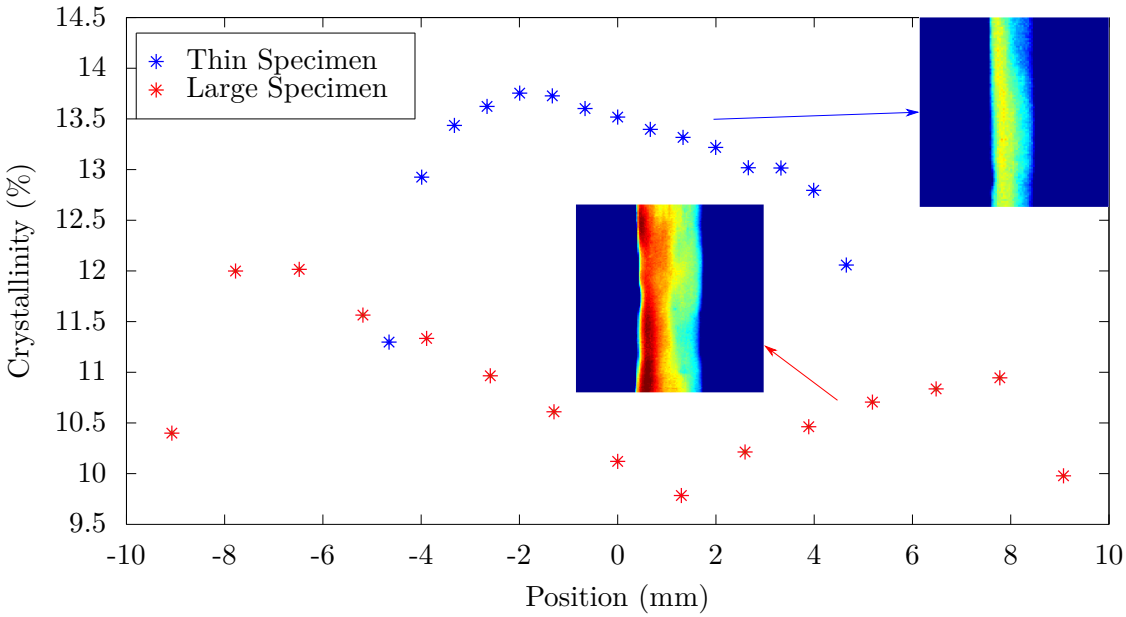

Figure 2.34 – Crystallinity profiles of 0NR1.2 specimens at the maximum stretch

From these experiments, some observations can be made:

— for a same global stretch, the crystallinity seems to be lower in a larger specimen. It could be explained by the fact that SIC is influence by the multiaxiality, as studied in Section 2.2,
— however, the crystallinity profile shows that, whatever the width of the specimen, crystallinity is lower at the edge than at the specimen center.

2.3.3.2 Results obtained in the 0NR1.6 rubber

The second material tested is the 0NR1.6. As for the 0NR1.2, the crystallinity is not homogeneous in the specimen while the mechanical loading is assumed to be homogeneous. Figure 2.35 represents crystallinity measured during the third mechanical loading.

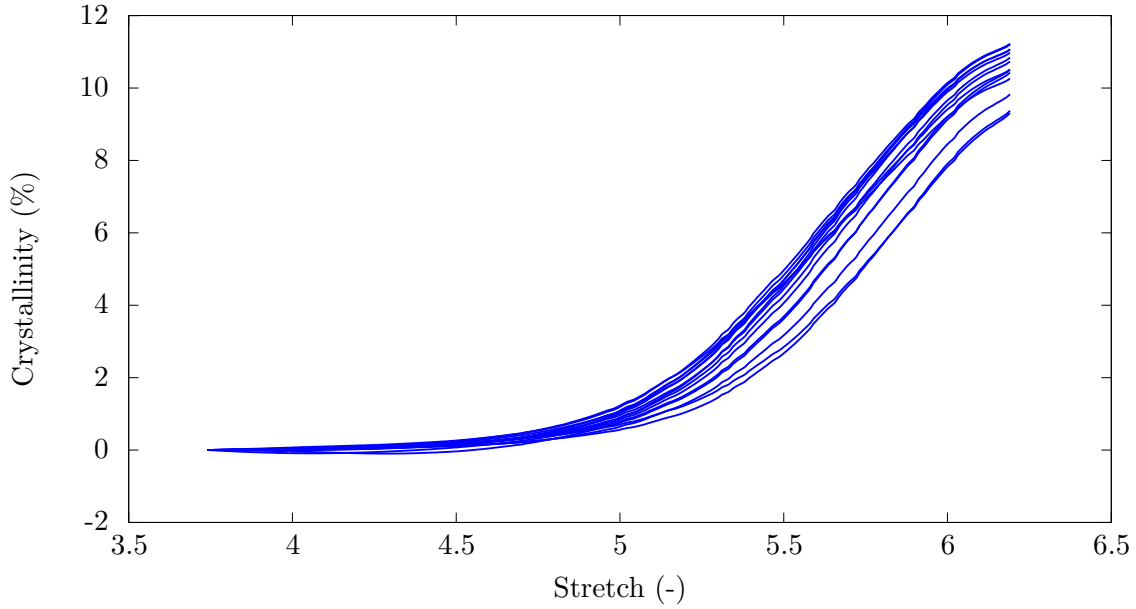

Figure 2.35 – Crystallinity measurement on the 0NR1.6 specimen

Figure 2.36 represents the crystallinity profile in each tests. As for the first material, the crystallinity seems to be lower at the specimen's edges. However, the crystallinity level does not seem to be significantly affected by the specimen's width.

2.4 Conclusion

In this chapter, a new method based on heat production during the crystallization process has been developed to study SIC. After describing the methodology, the results

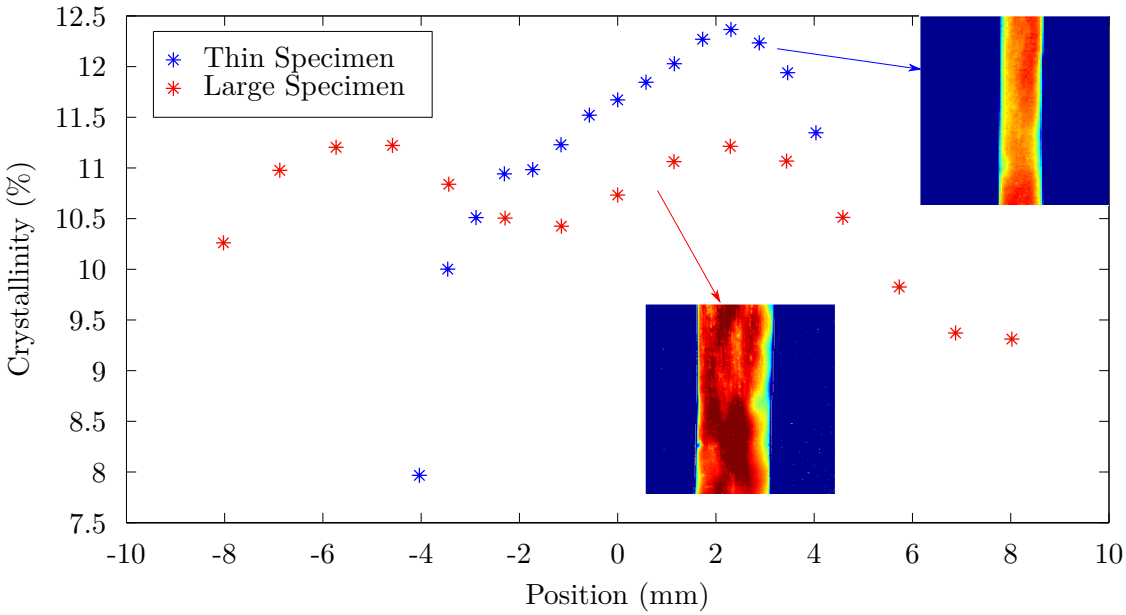

Figure 2.36 – Crystallinity profiles of 0NR1.6 specimens at the maximum stretchs

obtained with this method has been compared to those obtained with the X-ray diffraction technique. It has been shown that these two methods give equivalent results. Then, the multiaxiality influence has been studied in a filled natural rubber. This study gives two main results. Firstly, SIC occurs even with a high biaxiality ratio. Secondly, the stretch level for the crystallization onset decreases with the multiaxiality. Last, the main benefit of the calorimetric method compared to the X-ray diffraction technique is that information is provided at several points at the same time. Results show that SIC takes place heterogeneously, even in macroscopic homogeneous strain states. This results highlights the interest of performing full-field measurement for a better comprehension of the crystallization of rubber. This heterogeneity could be due to microscopic heterogeneities, such as the presence of impurities or a non-homogeneous distribution of chain length, but no microscopic analysis investigation have been performed.

Chapter 3

Extension to the 2-Dimensionnal studies

Contents

3.1 Methodology for coupling full kinematic field and infrared thermography

Due to the large deformation undergone by rubber specimen, material points observed by both the CCD and the IR cameras move from pixel to pixel, as seen in Figure 3.1.

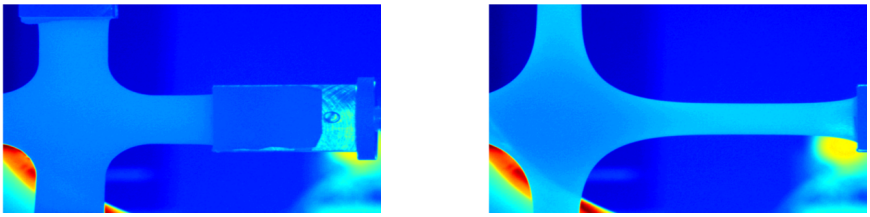

(a) IR Image before deformation (b) IR Image after deformation

Figure 3.1 – IR images during the mechanical test

While the DIC technique can be used to measure displacement field from optical images, the displacement has to be also evaluated on IR images in order to obtain the temperature evolution of the material points during the test. Several movement compensation techniques have been proposed in the case of elastomers, using only IR images such as in Pottier et al. [85], or by coupling full infrared and displacement field as in Samaca Martinez et al. [71, 72]. Such technique has also been developed for other materials, for instance in Chrysochoos et al. [25] and Bodelot et al. [9] for steel, or Louche et al. [63] for shape memory alloys. In this chapter, a new method to couple DIC and IRT is first described, then the method will be validated by testing it during a rigid-body movement, and a metrological study of the method is performed.

3.1.1 Description of the method

3.1.1.1 Digital image correlation

3.1.1.1.1 The digital image, starting point of DIC DIC is based on the comparison of a reference image and a deformed one. To use DIC method, we have to define what is precisely a digital image.

A digital image is a representation of a real image, represented as a set of small areas called pixels. Each pixel is related to a number, which represents the brightness or the color of this area. One should note that the color is homogeneous in a given pixel.

Digital images have some characteristics. The first one is the color depth of the image. It represents the number of bits used to describe the color of one pixel. For example, Figure 3.2 represents the different gray level a pixel can have, depending on the number of bits used to code it.

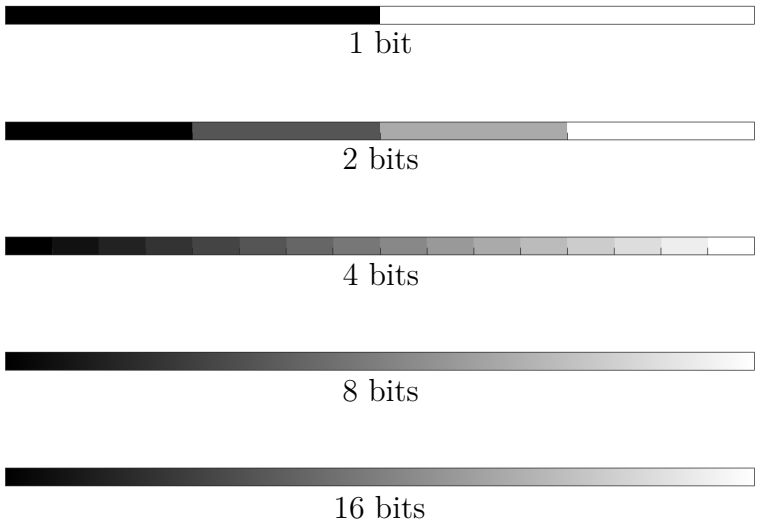

Figure 3.2 – Graycolorbar depending on the number of bits used

The type of the image can also change. For instance, colored images are often described using the RGB (for red, green, blue) type. In that case, the color of one pixel is represented by 3 numbers, one for the red value, one for the green and one for the blue. Using 8 bits per pixel per color, each RGB pixels are coded on 24 bits, which represents a total of 16 777 216 different colors. Digital images tend to produce big files, but they can be compressed. A common way is to record them by groups instead of recording each pixel seperately. However, this leads to image alteration.

3.1.1.1.2 The principles of DIC DIC is a method that evaluates the displacement field of a sample [46], by comparing an image at the surface or in a sample at a deformed state with a reference image of the sample at the undeformed state, for instance. This technique is based on the optical flow and assumes that any changes in the image is due to the displacement.

The reference image gray level is represented by a discrete function $f(x, y)$, which

becomes on the deformed images $f^*(x^*, y^*)$:

$$f^*(x^*, y^*) = f^*(x + u(x, y), y + v(x, y)) \tag{3.1}$$

with $u(x, y)$ and $v(x, y)$ the displacement function over the two different directions. The objective is to find these functions.

For that purpose, a correlation coefficient [115] is used:

$$Cor = 1 - \frac{\int_{\Delta S} f(x, y) f^*(x^*, y^*) dxdy}{\sqrt{\int_{\Delta S} f(x, y)^2 dxdy \int_{\Delta S} f^*(x^*, y^*)^2 dxdy}} \tag{3.2}$$

with ΔS the surface of the studied images. In case of perfect correlation, i.e. $f(x, y) = f^*(x^*, y^*)$, this correlation coefficient is equal to 0, else it is in the range of 0 and 1. In fact, the DIC is an optimization process of the two displacement functions.

Even if the gray level of the deformed image f^* is a discrete function, the accuracy of DIC is lower than the pixel. In fact, if there is no noise in the signal, the lowest displacement measurable is equal to 2^{-n} pixel, with n the number of bits used to code the gray level. In fact, since experimental images are not perfect, the accuracy is lower, but can achieve a precision around $1/100^{\text{th}}$ pixel.

To perform the optimization, a function form has to be chosen. Actually, two different approaches exist to perform DIC:

— the first approach is the subset-based local DIC. It consists in dividing the whole image into several subimages, called zone of interest (ZOI). Then, each ZOI is processed independently from each others. In that case, the displacement function is often interpolated into bilinear or bicubic function. Figure 3.3 represents the local DIC principles,

— the second approach is the global DIC. It considers the whole image and uses mechanical assumption, such as a continuous displacement field, to perform the DIC. The form function can be found using finite-element method for instance, but more complex models exist that can take into account other phenomena such as crack growth. Figure 3.4 represents the global DIC principles.

Recently, Wang and Pan [118] compared these two approaches, and the main conclusion is that local DIC outperforms global DIC, as soon as that the subset size is high enough. However, global DIC has the benefit to allow a direct connection between experimental data and numerical simulations, if the same finite-element basis is used.

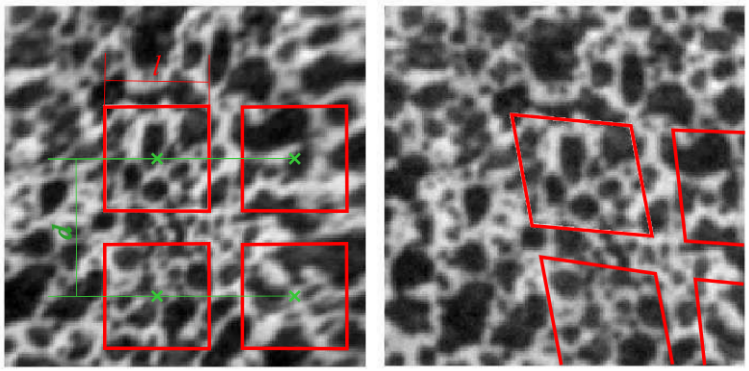

Reference image Deformed image

Figure 3.3 – Local DIC principles

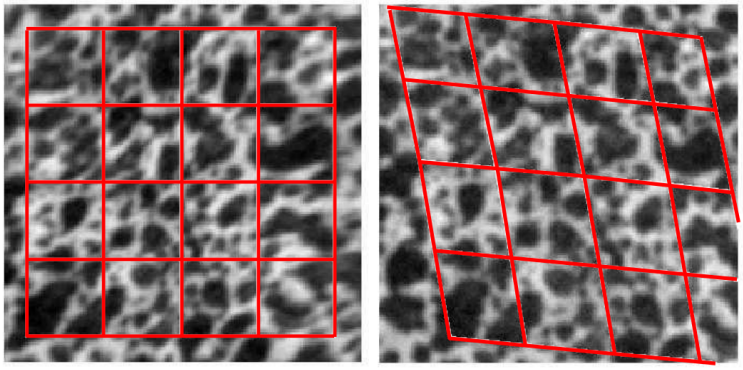

Reference image Deformed image

Figure 3.4 – Global DIC principles

DIC requires a random pattern (a speckle) at the specimen surface. This speckle can be natural, for instance with the roughness of the material, or artificial, for instance by spraying paint at the specimen surface. Matt painting must be used, to avoid any reflection. Some empirical rules have been defined [115]:

— the average spot size must be lower than 20 pixels. Indeed, if the spot size is higher than the subset size, no displacement can be measured,

— the gray level must vary between 0 and 255 excluded, in the case where the image is coded using 8 bits per pixel. It means that no saturation must be observed on

images,

— gray level has to evolve steadily between two neighboring pixels.

3.1.1.2 Compensating the displacement of material points in IR images

The aim of the method is to be able to transfer information from one camera to the other one by using a common basis, as seen in Figure 3.5.

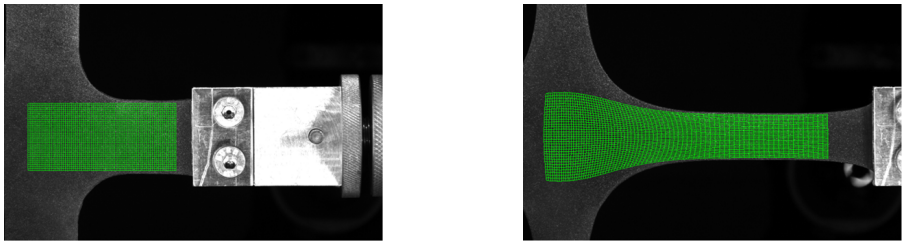

(a) DIC grid results

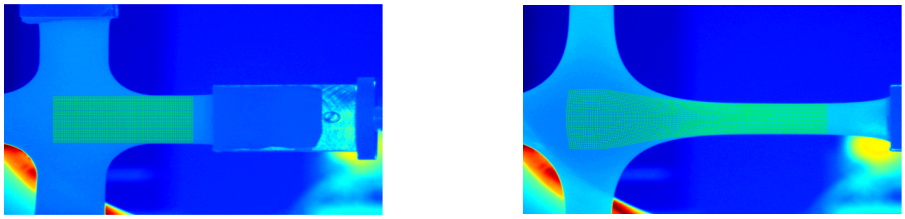

(b) Transposition of DIC grid on IR images

Figure 3.5 – Transposition of DIC grid from CCD images to IR images

It requires to calibrate spatially both cameras before performing the test. The calibration is performed by using a calibration pattern, which is composed of two sets of four holes that form a large (ABCD) and small (abcd) rectangle, as shown in Figure 3.6. The size of the rectangle chosen depends on the relative resolution of the fields considered. It has to be placed at the same location as the specimen would be during the test.

Holes are used as common markers for both IR and CCD images. Their position are determined using a mark tracking algorithm. First, the area which contains each marker is selected by hand, as shown in Figure 3.7 Then, for each area, a threshold is defined, i.e. each pixel value is compared with a reference one. Each pixel under this reference value is set to 0 (full black pixel) and each pixel over this reference value is set to 255 (full white pixel). Figure 3.8 represents the resulting thresholding for a single marker area. Finally, the barycenter of either black or white pixels (chosen by the user) is calculated. Figure 3.9

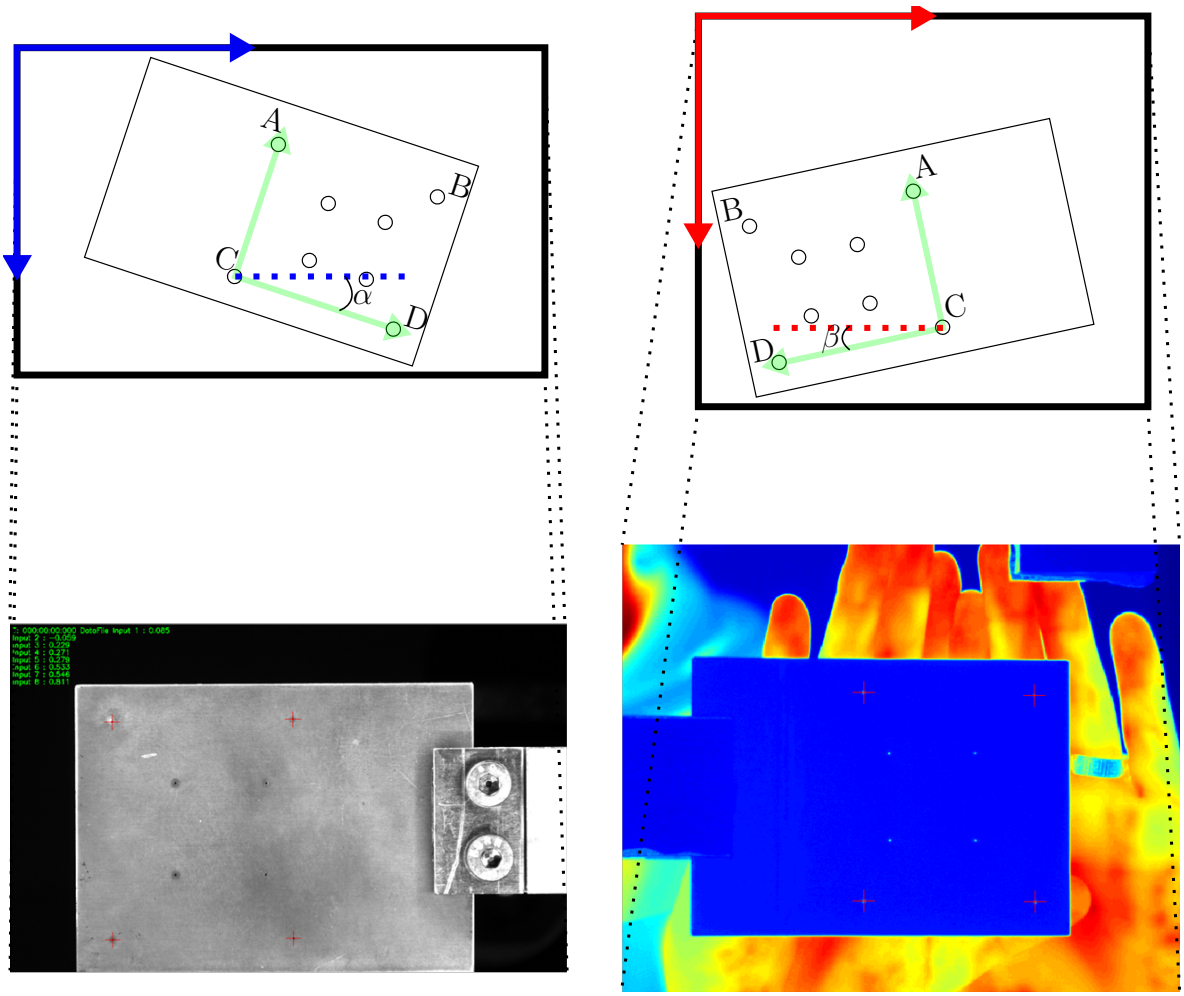

Figure 3.6 – Calibration pattern used to perform the spatial calibration of the two cameras

represents the results of this operation for a single marker. This operation is made for the four markers and the 2 cameras. At the end of the mark track algorithm, the position of the four markers in both CCD and IR images is known. For both cameras, two operations are performed. The first one is a translation and a scaling operation, which defines the point C as the origin of the common coordinate system, and converts the distance from pixel to millimeter. For the CCD camera, this operation is performed using the following formulation:

$$x_{translation} = (X_{camera} - X_{C_{camera}}) \frac{L_X}{I_{opt}}; I_{opt} = cos(\alpha) * (\Delta X) - sin(\alpha) * (\Delta Y) \quad (3.3)$$

$$y_{translation} = (Y_{camera} - Y_{C_{camera}}) \frac{L_Y}{J_{opt}}; J_{opt} = sin(\alpha) * (\Delta X) + cos(\alpha) * (\Delta Y) \quad (3.4)$$

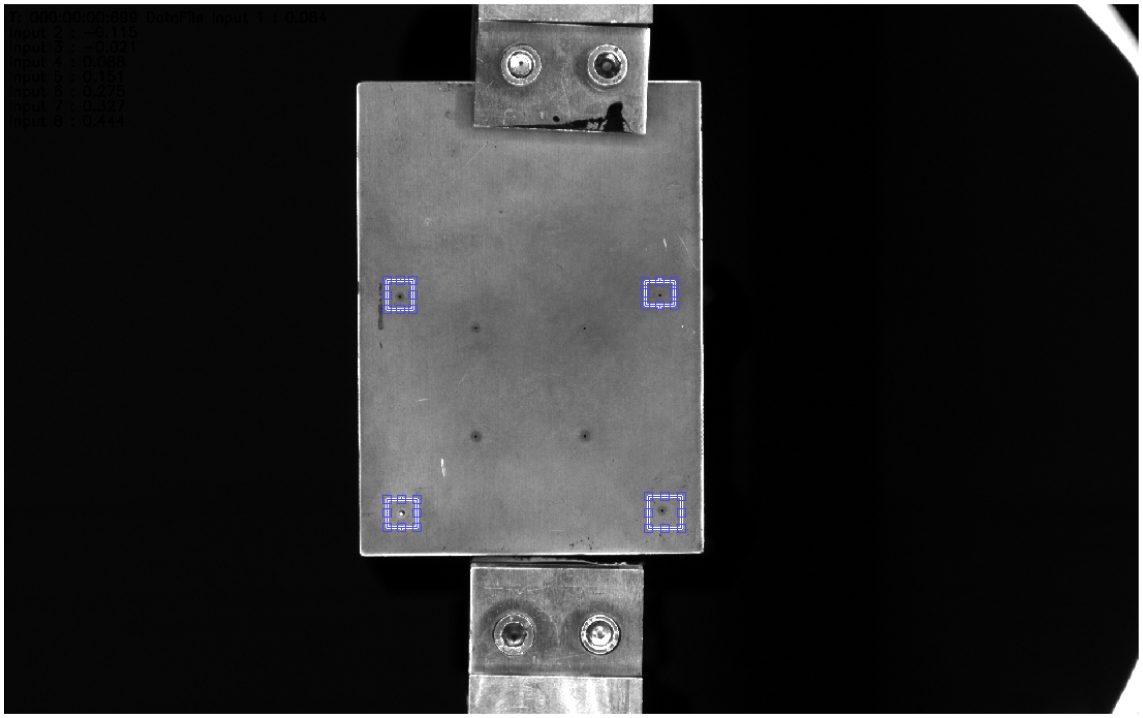

Figure 3.7 – Selection of the four areas

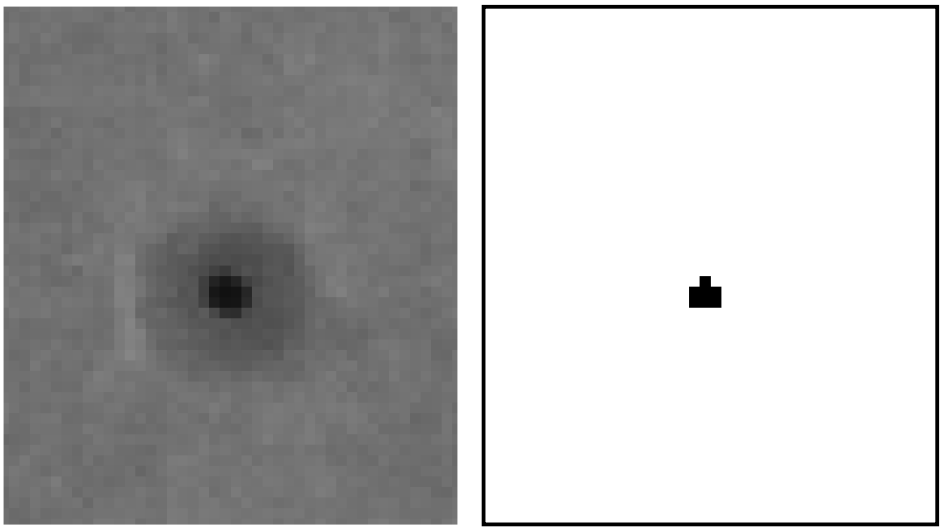

(a) Area around one marker (b) Thresholding of the area

Figure 3.8 – Thresholding operation

with x and y the position in the translated coordinate system (in mm), X_{camera} and Y_{camera} the position of the pixel in the camera coordinate system (in pixels), $X_{C_{camera}}$ and $Y_{C_{camera}}$ the position of the point C in the camera coordinate system (in pixel), α the angular

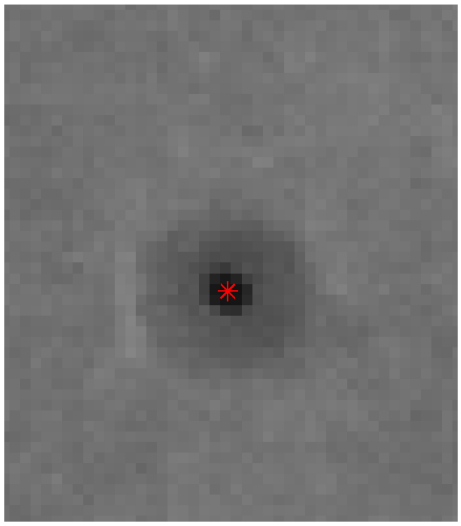

Figure 3.9 – Marker center determination

deviation between the two coordinate systems), ΔX and ΔY are the horizontal/vertical distance between two measured markers in the image (in pixel) and L_X and L_Y are the horizontal/vertical distance between two markers on the calibration pattern (in mm). The second operation to be performed is a rotation of the coordinate system, in order to take into account the angular variation of the two cameras.

3.1.1.3 From the displacement field to deformation field

Actually, DIC gives the displacement at each nodes of a grid. From these displacements, the principal stretches are determined. For that purpose, square elements are created, each corner of a square element corresponding to a grid nodes where the displacement has been measured. Within a square element i, the horizontal and vertical displacements, ${}^iU$ and ${}^iV$ respectively, are assumed to be bilinear of the position:

$$\begin{cases} {}^iU(X,Y) = a + bX + cY + dXY \\ {}^iV(X,Y) = e + fX + gY + hXY \end{cases} \tag{3.5}$$

with a, b, c, d, e, f, g and h eight parameters that can be identified from displacement measurement of the four corner of the square element. The calculation is carried out by considering the square element center to be the origin of the coordinate system. Finally, the deformation gradient tensor $\mathbf{F}$ at the square element center is obtained by using

Equation 3.6:

$$\mathbf{F} = \begin{pmatrix} \frac{\partial x}{\partial X} & \frac{\partial x}{\partial Y} \\ \frac{\partial y}{\partial X} & \frac{\partial y}{\partial Y} \end{pmatrix} = \begin{pmatrix} \frac{\partial X+^i U}{\partial X} & \frac{\partial X+^i U}{\partial Y} \\ \frac{\partial Y+^i V}{\partial X} & \frac{\partial Y+^i V}{\partial Y} \end{pmatrix} = \begin{pmatrix} 1+b & c \\ f & 1+g \end{pmatrix} \tag{3.6}$$

From the gradient deformation tensor obtained, the principal stretches are easily deduced. First, the left Cauchy-Green tensor $\mathbf{B} = \mathbf{F}\mathbf{F}^T$ is calculated and diagonalized, which gives:

$$\mathbf{B} = \begin{pmatrix} \lambda_1^2 & 0 \\ 0 & \lambda_2^2 \end{pmatrix} \tag{3.7}$$

with $\lambda_1 \geq \lambda_2$, where λ_1 and λ_2 are the maximal and minimal in-plane principal stretches, respectively.

The biaxiality coefficient, which characterizes the loading case locally undergone by the material, can be obtained from the two in-plane principal stretches as follows:

$$B = \frac{\ln \lambda_2}{\ln \lambda_1} \tag{3.8}$$

3.1.1.4 Temperature monitoring

Once the two cameras are "spatially calibrated" and the digital image correlation performed, the temperature monitoring of each material point studied can be obtained. For each of these points, the position is known in the IR images. Since the spatial resolution of the two cameras is different and that the DIC does not provide an integer number of pixels for the displacement, most points followed will not be in a exact spot of an IR pixel, but between several ones. This explains why the temperature is deduced by a bilinear interpolation of the temperature, using the neighboring IR pixels, as illustrated in Figure 3.10. The temperature at the followed point is equal to:

$$T(x, y) = ax + by + cxy + d \tag{3.9}$$

with T the temperature of the followed material point, which has a position (x, y) and a, b, c and d four parameters that can be found using the four neighboring IR pixels temperature temperature value T_1, T_2, T_3 and T_4 which have the position (x_1, y_1), (x_2, y_2), (x_3, y_3) and (x_4, y_4), respectively.

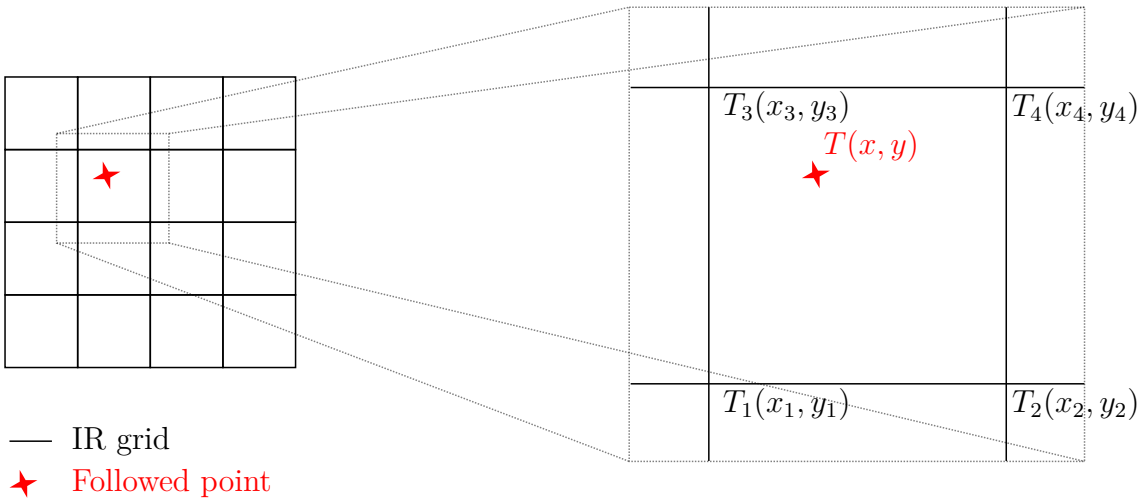

Figure 3.10 – Principles of the bilinear interpolation

3.1.2 Metrological consideration

In this section, the precision obtained using such a method, as well as the different parameters that are involved.

3.1.2.1 Validation of the coupling method

In order to validate the method, a first metrological study is performed, using a rigid-body movement. In that case, the temperature of points should not change during the whole displacement. The specimen used for this metrological study is a cooper plate. This plate has been painted in black color in order to reduce reflections effects. In order to be able to evaluate the performance of the method, the temperature field seen by the IR camera of the specimen should not be homogeneous. For that purpose, a temperature pattern is added by attaching a piece of cardboard with reliefs, as shown in Figure 3.11.

Since no temperature variation should occur during the translation, the performance of the method will be evaluated by measuring the standard deviation of the temperature of each material point, and will be compared with the Noise Equivalent Temperature Deviation (NETD) of the IR camera.

For this metrological study, the influence of different experimental parameters on the performance of the method is studied:

— the first parameter to be studied is the image acquisition frequency. Figure 3.12 shows the cartography of the standard deviation of the temperature variation. As seen on these maps, a pattern which corresponds to the pattern of the cardboard

(a) Specimen used

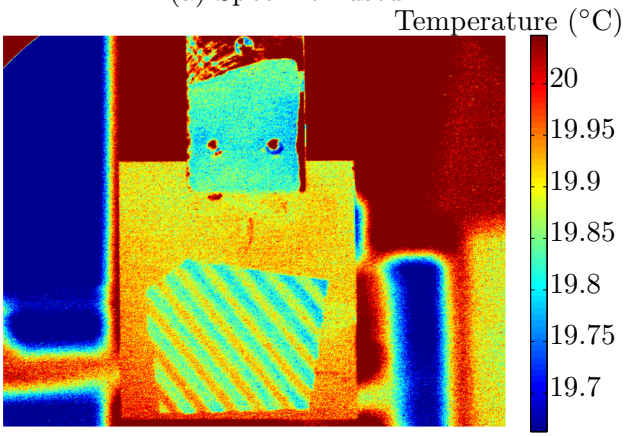

(b) Temperature field seen by the IR camera

Figure 3.11 – Specimen used to perform the validation of the motion compensation technique

is observed. Figure 3.13 represents the mean standard deviation for each test. It demonstrates the good performance of the method, since the deviation obtained is close to the NETD of the IR camera. Moreover, the acquisition frequency seems to have only a small influence on the performance,

— the second parameter to be studied is the loading rate applied to the specimen. Figure 3.14 shows the cartography of the standard deviation of the temperature variation. As for the previous results obtained, the temperature pattern is visible. Figure 3.15 represents the mean standard deviation for each test. In the loading rate range studied, the performance of the motion compensation technique does not evolve significantly. However, it should be noted that with a higher loading rate, the motion blur phenomenon can appears, which impacts the accuracy of the DIC technique, and by extension of the motion compensation method,

— the third parameter to be studied is the distance between the specimen and the

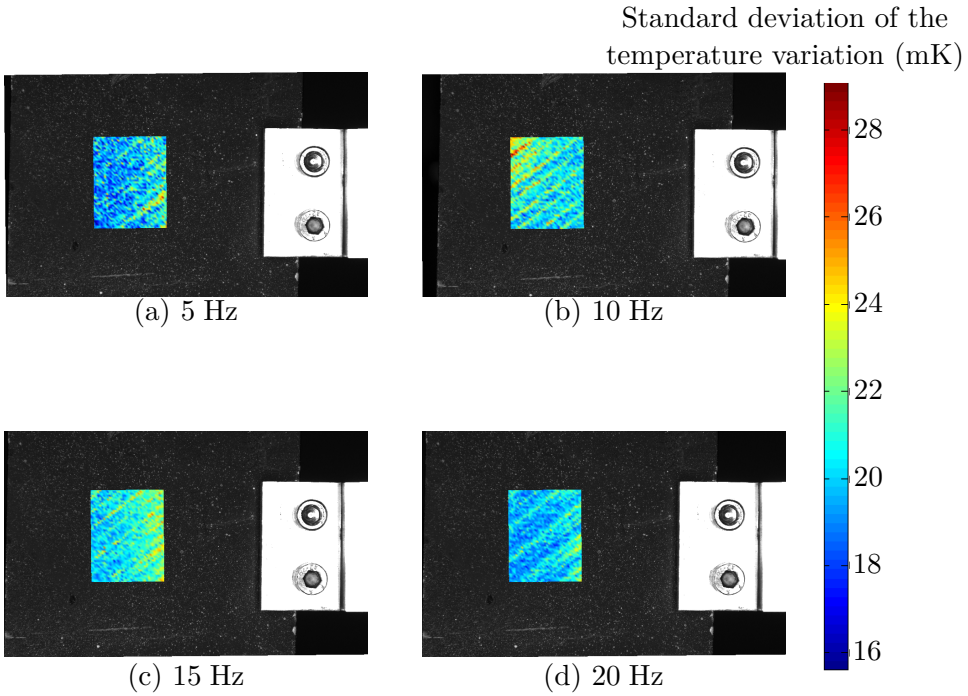

Figure 3.12 – Cartography of the standard deviation of the temperature variation obtained for several acquisition frequency

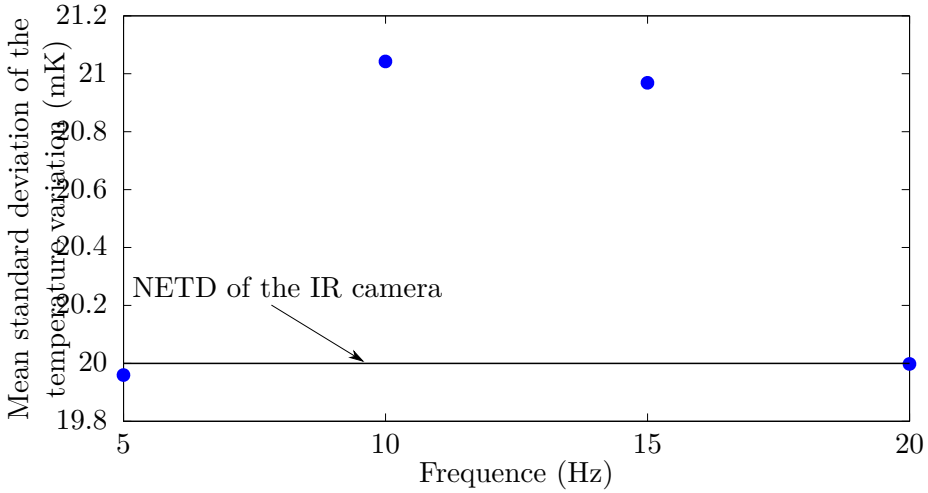

Figure 3.13 – Performance of the motion compensation technique versus the acquisition frequency

CCD camera. Figure 3.16 shows the cartography of the standard deviation of the temperature variation. As for the previous results obtained, the temperature pattern is visible except for the test with the camera close to the specimen. Figure 3.17 gives the mean standard deviation for each tests. The performance of the method

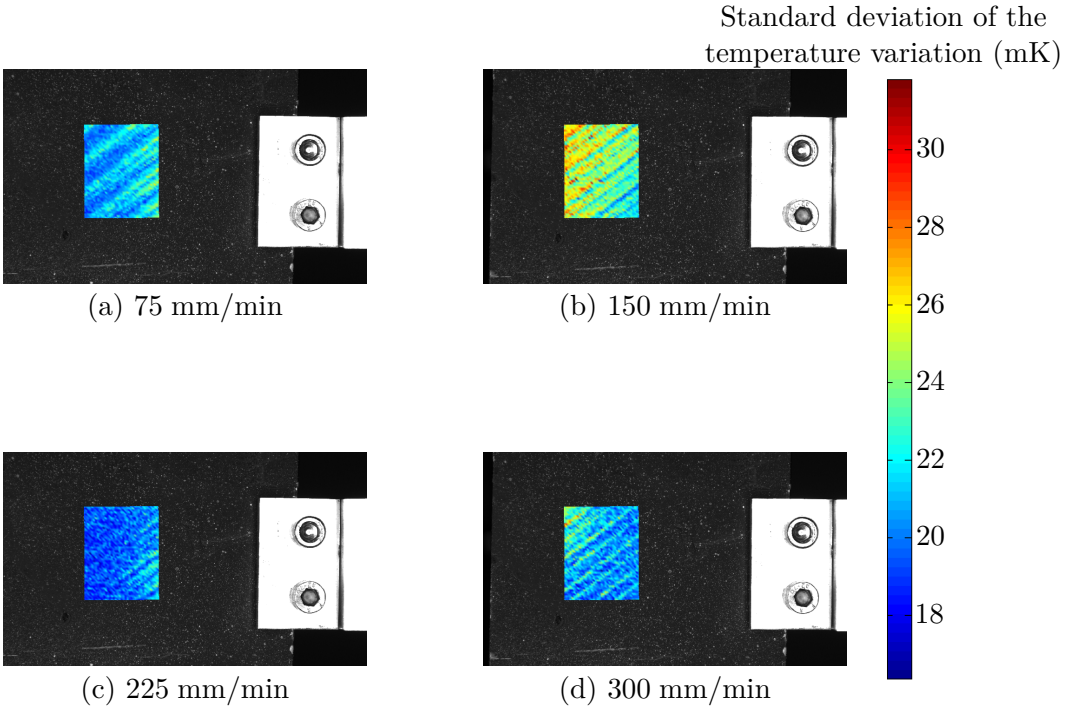

Figure 3.14 – Cartography of the standard deviation of the temperature variation obtained for several loading rate

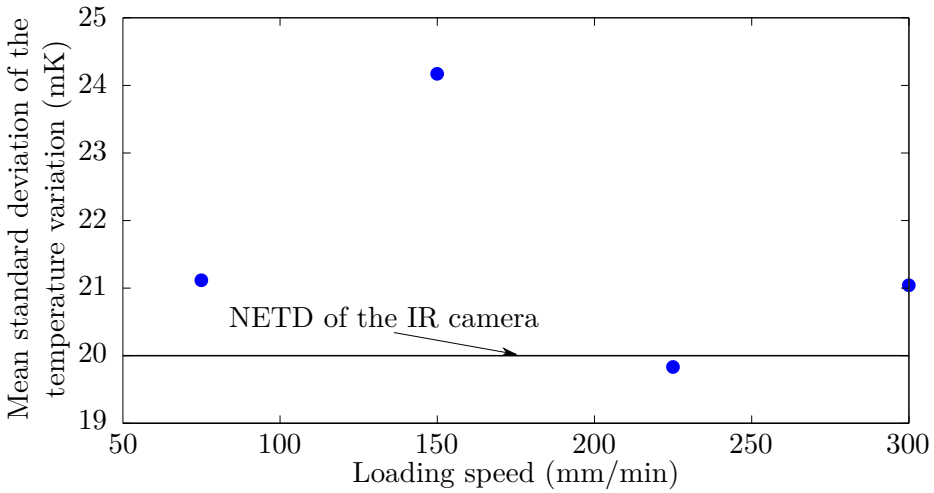

Figure 3.15 – Performance of the motion compensation technique versus the loading rate

decreases with the distance. This could be easily explained by the fact that with a higher distance, the spatial resolution of the camera increases, i.e. each pixel corresponds to a larger area of the specimen. In that case, a same error in the DIC technique in term of pixel leads to a higher error of the displacement on the specimen, and in the case of heterogeneous temperature field, an higher error of

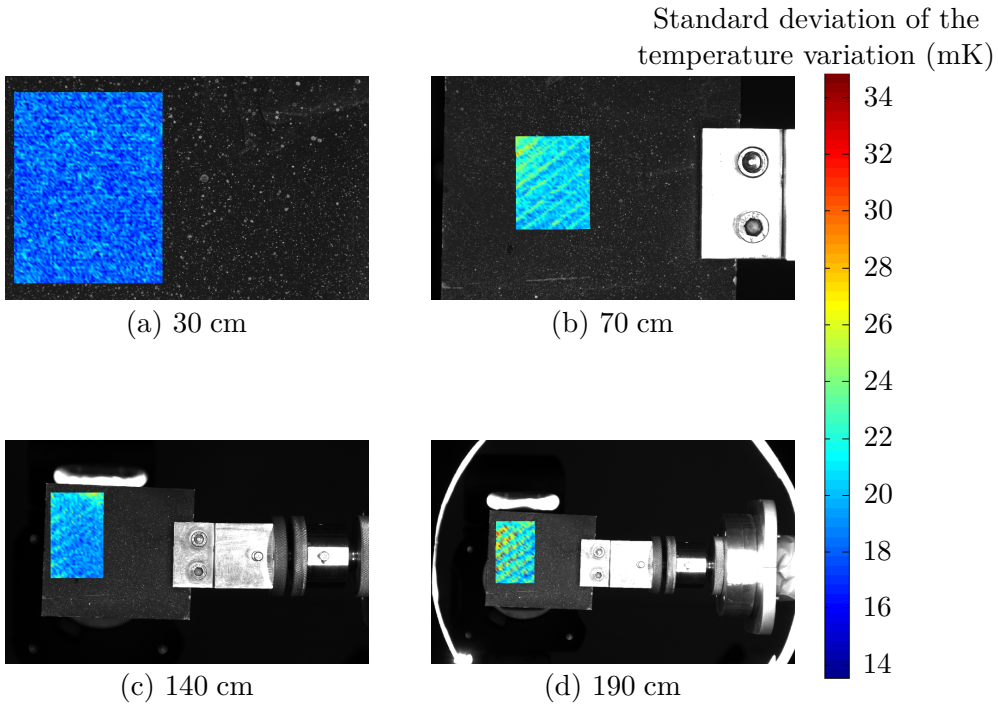

Figure 3.16 – Cartography of the standard deviation of the temperature variation obtained for several distance between the CCD camera and the specimen

the temperature. It should be noted that, for a constant loading rate, the motion blur phenomenon appears if the distance is too close, as shown in Figure 3.18,

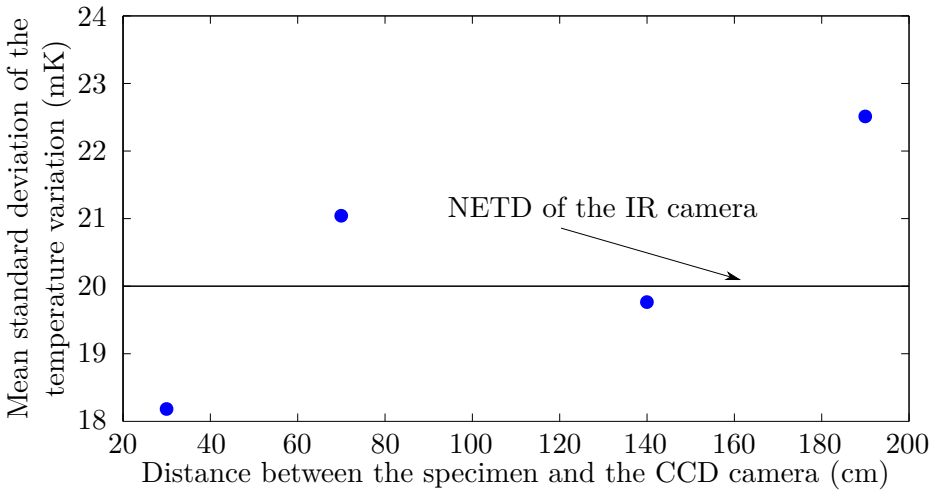

Figure 3.17 – Performance of the motion compensation technique versus the distance between the CCD camera and the specimen

— the last parameter to be studied is the distance between the specimen and the

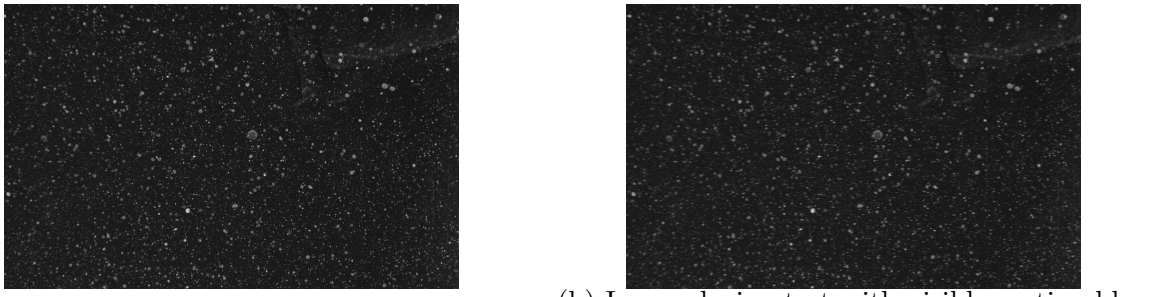

(a) Reference image

(b) Image during test with visible motion blur

Figure 3.18 – Motion blur seen for higher loading rate

IR camera. Figure 3.19 shows the cartography of the standard deviation of the temperature variation. As for the previous results obtained, the pattern is visible. Figure 3.20 represents the mean standard deviation for each test. In the distance

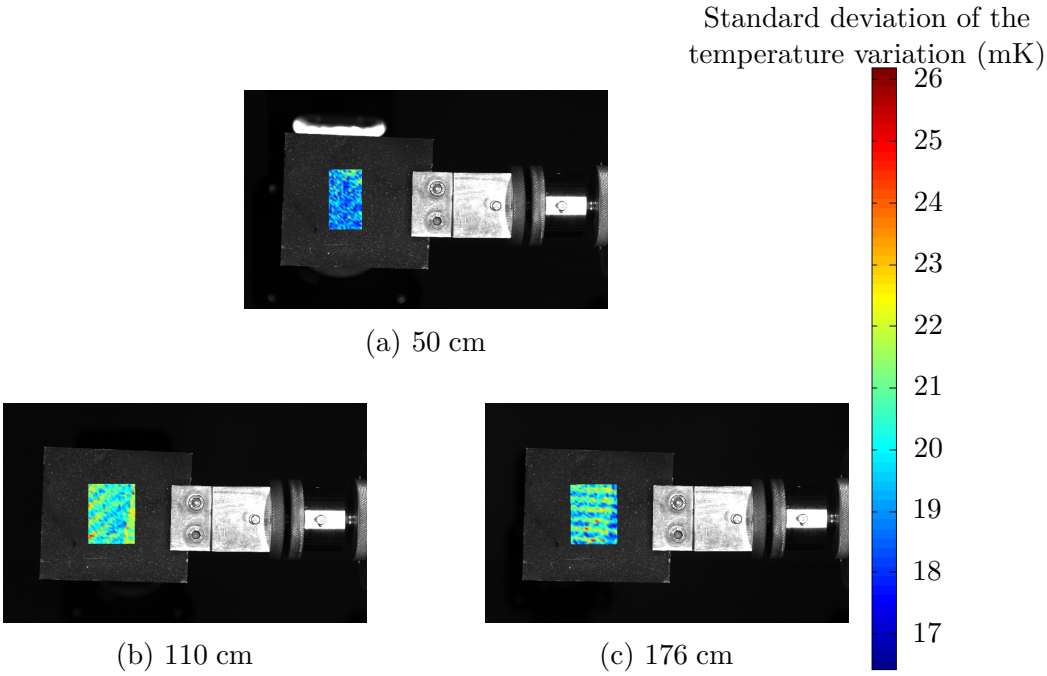

(a) 50 cm

(b) 110 cm

(c) 176 cm

Figure 3.19 – Cartography of the standard deviation of the temperature variation obtained for several distance between the IR camera and the specimen

range studied, the performance of the motion compensation technique does not evolve strongly. However, with a higher distance, the spatial resolution of the IR images increases, which decreases the precision, especially for high temperature gradient.

To conclude, this metrological study shows the performance of the method. The influ-

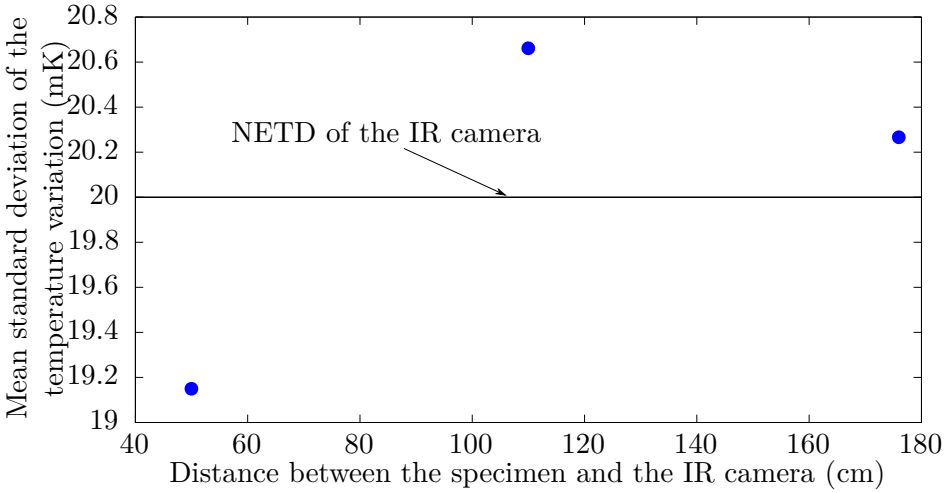

Figure 3.20 – Performance of the motion compensation technique versus the distance between the IR camera and the specimen

ence of different experimental parameters has been investigated. The most influential is the distance between the CCD camera and the specimen, since for a same displacement error in the DIC technique in term of pixel leads to a higher error of the displacement on the specimen, and in the case of heterogeneous temperature field, an higher error of the temperature. However, for all tests, the temperature deviation found is close to the NETD of the IR camera, which validates the motion compensation technique.

3.1.2.2 Influence of halo effect

While the motion compensation technique have been characterized, a second phenomena have been highlighted in Pottier et al. [85], which is the halo effect. They concluded that this effect can be limited by using a non-uniformity correction. They also verified that this phenomena is stabilized approximatively one hour after the IR camera was switched on.

For that purpose, the IR camera is switched on an hour before performing the test. Then, a non-uniformity correction is performed using a black body. IR images of this black body are stored at different times. Figure 3.21 presents images obtained at four different times. It clearly shows that in spite of the non-uniformity correction, the halo pattern reappears with the time.

Figure 3.22 shows the time evolution of the amplitude of this halo pattern. As observed on this figure, the halo pattern intensifies strongly the first hours, but still evolves after.

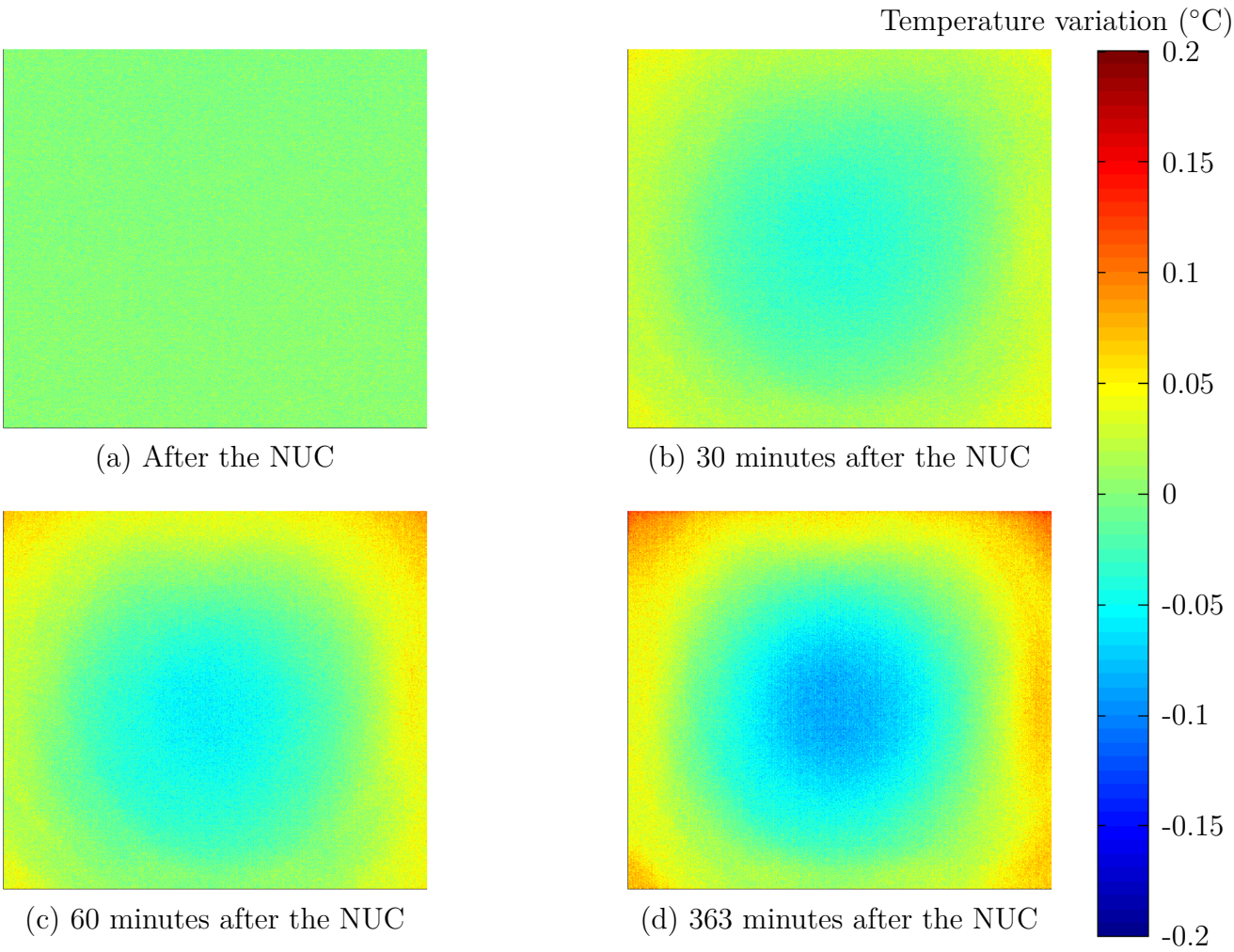

(a) After the NUC

(b) 30 minutes after the NUC

(c) 60 minutes after the NUC

(d) 363 minutes after the NUC

Figure 3.21 – Specimen used to perform the validation of the motion compensation technique

To conclude, the halo is a second source of errors. In order to reduce the influence of the halo on temperature measurement, two solutions can be performed:

— first, the test can be made quickly after the non-uniformity correction. This will limit the formation of the halo pattern, and thus limit the temperature variation due to the halo pattern.
— second, if the test can not be performed rapidly after the NUC, for instance if the test required takes a long time, the halo pattern have to be characterized, and taken into account before measuring the temperature variation.

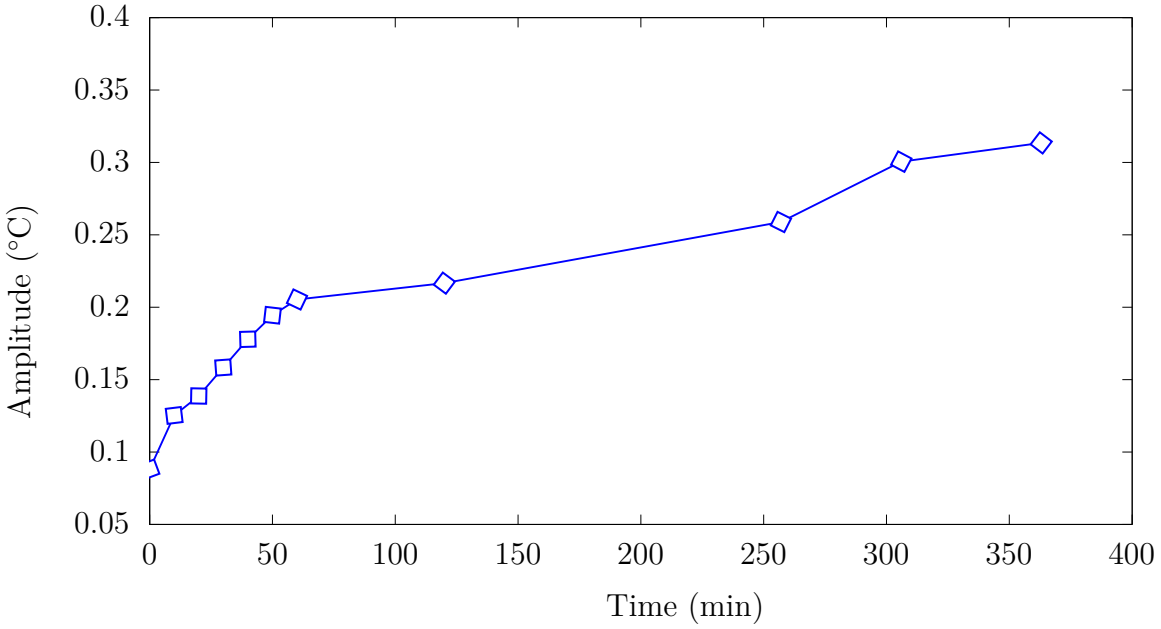

Figure 3.22 – Evolution over time of the halo pattern amplitude

3.1.2.3 Metrological study on simulated data

The test performed on the rigid-body movement allows us to validate the motion compensation technique using the spatial calibration of the two cameras. It also shows that the temperature noise obtained after the motion compensation technique is mostly due to the thermal sensitivity of the IR camera as long as there is no high thermal gradient, with respect to the spatial resolution of the camera.

To estimate errors on both deformation and heat emitted fields, a procedure has to be defined. It consists in an uniaxial tensile test, which is simulated. The coupling method is applied to the set of images obtained from the numerical simulation. It is precisely described in the following.

3.1.2.3.1 Generation of simulated data The first step here is to simulate a mechanical test by the finite element method. The test simulated is a uniaxial tensile test with a rectangular sample. Its length is equal to 123.54 mm, its width to 29.82 mm and its thickness to 2 mm. The numerical simulation is performed using ABAQUS. A vertical displacement on both the upper and lower bound equal to 70 mm is applied at a speed of 150 mm/min. The mechanical behavior of the sample is modeled by a Neo-Hookean model, with a parameter C_{nh} equal to 0.24 MPa.

Then, the set of images has to be created from the simulation. First, CCD images

are created, by deforming a speckle image using the displacement field obtained from the finite element method, a spatial resolution, chosen here equal to 0.15 mm/px, and an acquisition frequency, here equal to 5 Hz. Figure 3.23 gives images obtained using this method.

(a) Undeformed speckle image (b) Deformed speckle image

Figure 3.23 – Images created by the deformation of a speckle image

After that, IR images are built. The first step here is to obtained the temperature, by applying the heat equation to the material. The initial temperature is supposed to be homogeneous, and equal to 20 °C. Thermal diffusion within the material is neglected in this study, the heat equation is simplify to its "0D" formulation:

$$S = \rho C \left(\dot{\theta} + \frac{\theta}{\tau} \right) \tag{3.10}$$

ρ and C are supposed to be constant during the whole test, however the time constant τ depends on the strain state. For an uniaxial tensile test, assuming that the material is incompressible, it can be obtained using the following formulation:

$$\tau = \frac{\tau_0}{\sqrt{\lambda}} \tag{3.11}$$

Neo-Hookean model is used to determine heat source produce by the material (more details are provided in Section 3.2.2), and is expressed as followed for uniaxial tension:

$$S = 2C_{nh} \left(\lambda - \lambda^{-2} \right) \frac{d\lambda}{dt} \tag{3.12}$$

After determining the time evolution of the specimen's temperature during the simulated test, IR images are created, by applying a constant temperature equal to 18 °C to each pixel outside the simulated specimen, and the calculated temperature to each pixel inside the specimen. Images are computed at the same times as for CCD images, at a acquisition frequency of 5 Hz, for a spatial resolution of 0.5 mm/px. In order to better simulate IR images obtained from an infrared camera, an thermal noise is added to the images. For this purpose, the thermal noise is characterized for the IR camera. Figure 3.24 represents the power density and probability density of the measured thermal noise, and shows that the noise can be modelized using a white noise with a standard deviation of 20 mK.

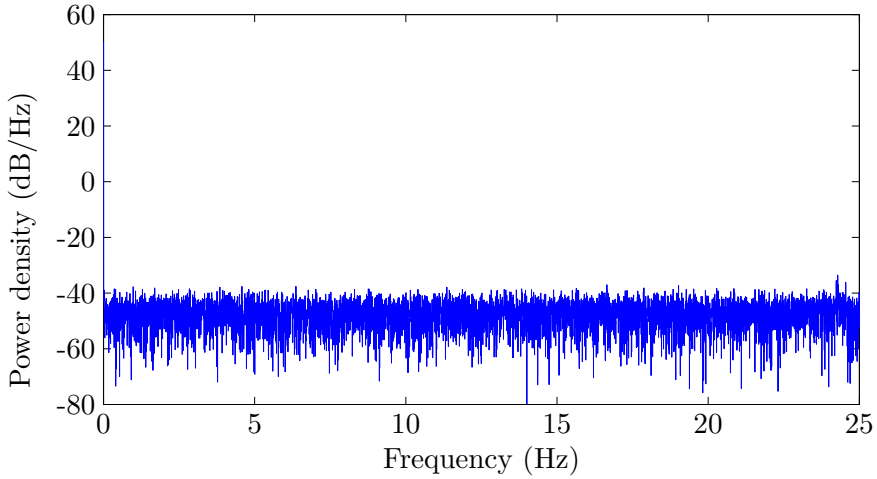

(a) Thermal noise power density

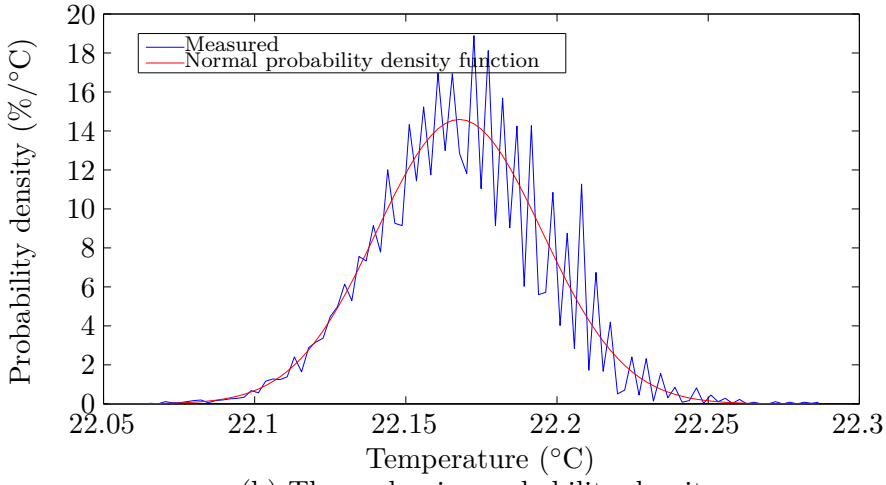

(b) Thermal noise probability density

Figure 3.24 – Power density of thermal noise measured

A thermal noise is then added to simulate thermal noise on images obtained from an infrared camera. The noise added has a mean value equal to 0 K and a standard deviation equal to 20 mK. Figure 3.25 represented images obtained using this method.

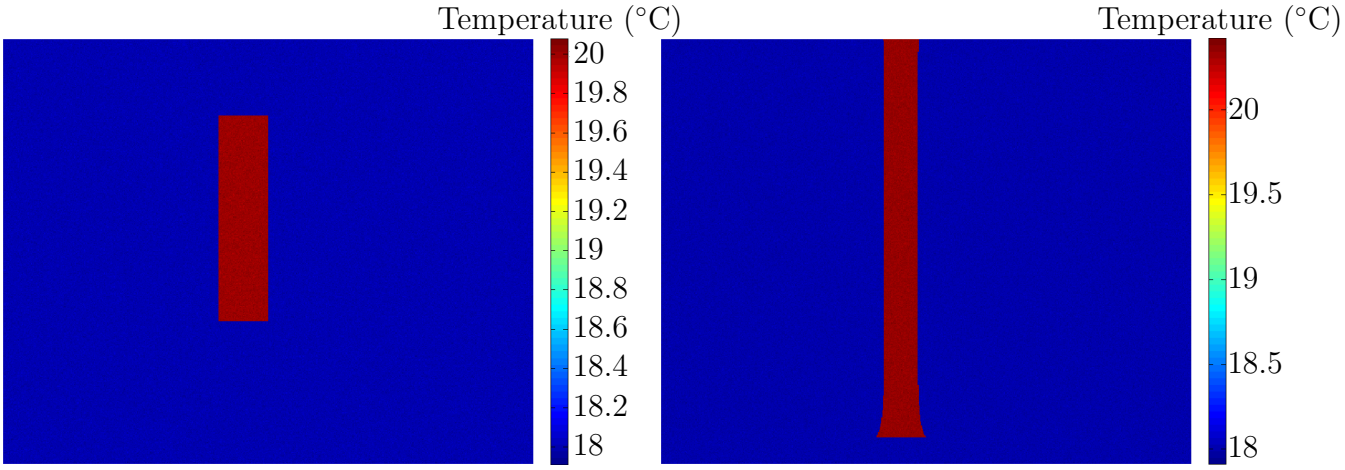

(a) IR image at the undeformed state (b) IR image at a deformed state

Figure 3.25 – IR images created

3.1.2.3.2 Kinematic field metrological study First, a metrological study on the kinematic field is performed. For that purpose, DIC is performed, using the software 7D, on CCD images created. For this study, the grid step is set to 10 pixels, which means that the displacement will be measured every 10 pixels, and the ZOI size will change between 4 and 20 pixels.

Figure 3.26 presents the maximal principal stretch at a single point measured using this method for several ZOI size. The figure clearly shows that a ZOI size too small can lead to an error on the measured stretch, but increasing the size more than 10 pixels improves only slightly the precision on the stretch level.

The biaxiality coefficient is also considered in this study. In the case of an uniaxial tensile test, it must be equal to -0.5 at every time. The biaxiality coefficient can be determined from the two principal stretches: $B = \frac{\ln(\lambda_2)}{\ln(\lambda_1)}$. Figure 3.27 represents the biaxiality coefficient at a single point measured for several ZOI size. The figure shows that the more the material is stretched, the less the error. However, ZOI size does not seem to influence the precision on the biaxiality coefficient. At time 0, when the material is at its undeformed state, biaxiality coefficient can not be measured, which explained the high error at the beginning of the curve.

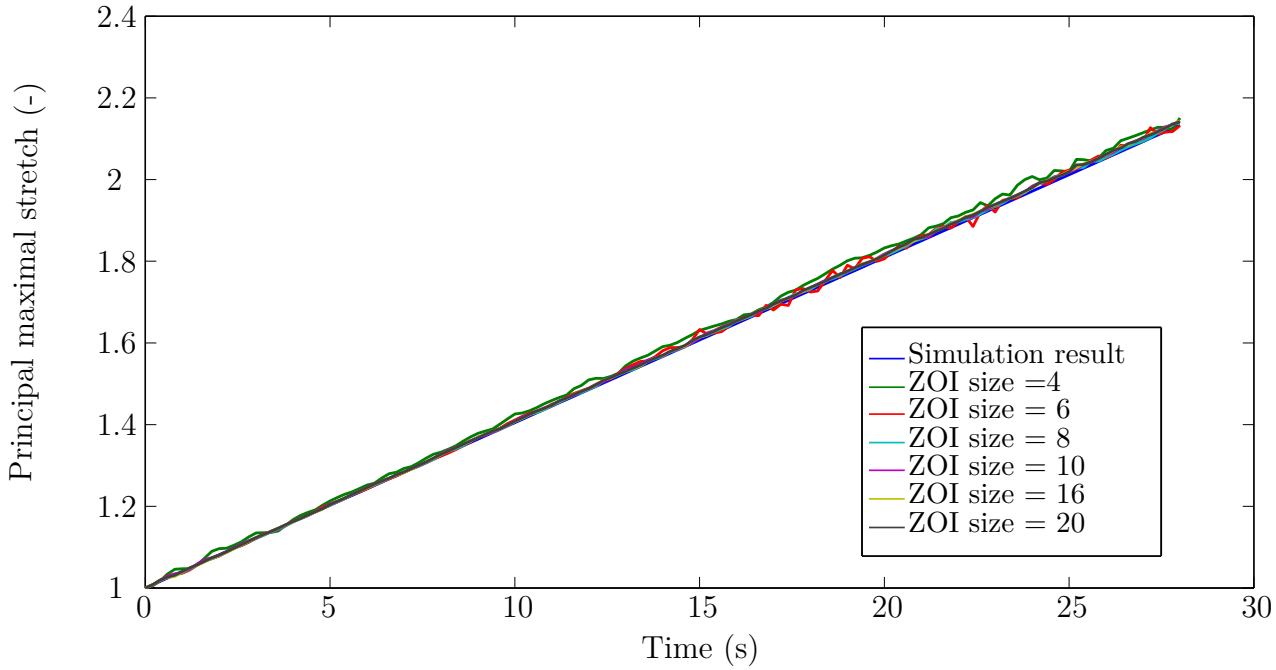

(a) Principal maximal stretch measured using different ZOI size

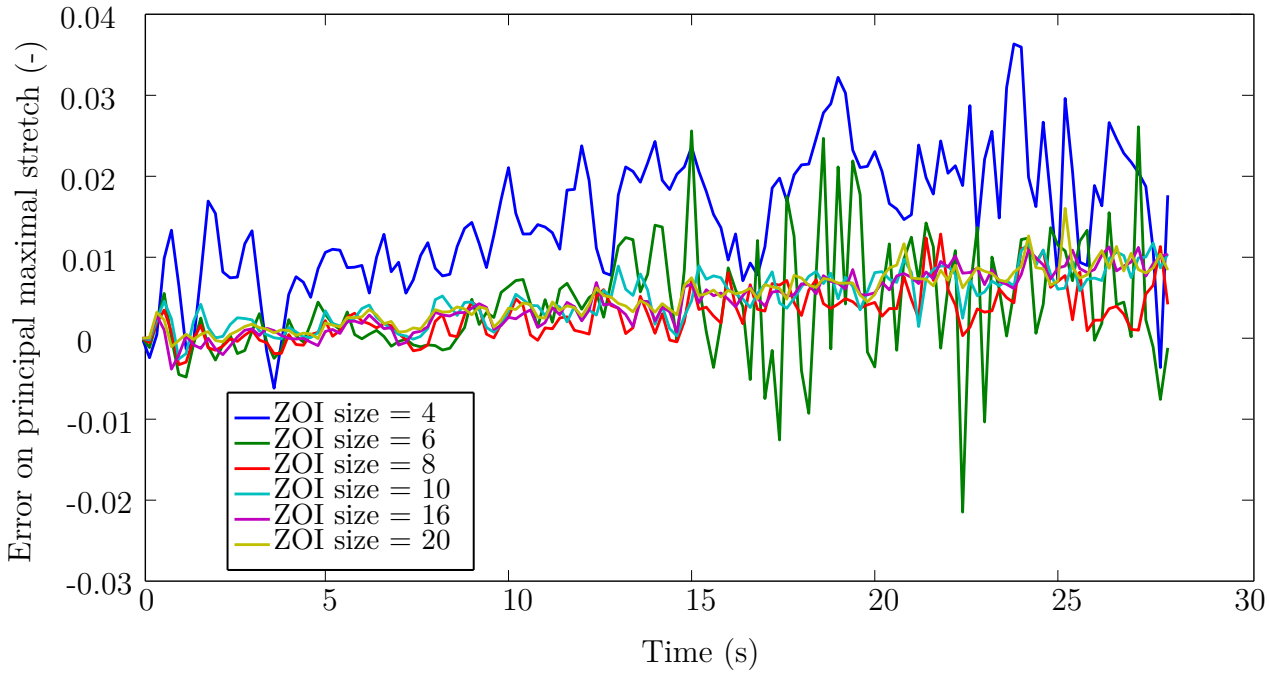

(b) Error on principal maximal stretch measured using different ZOI size

Figure 3.26 – Temporal evolution of the elongation measured for different ZOI size

3.1.2.3.3 Calorific field metrological study Then, a metrological study is performed on the thermal field. First, using the spatial calibration of the two cameras, the

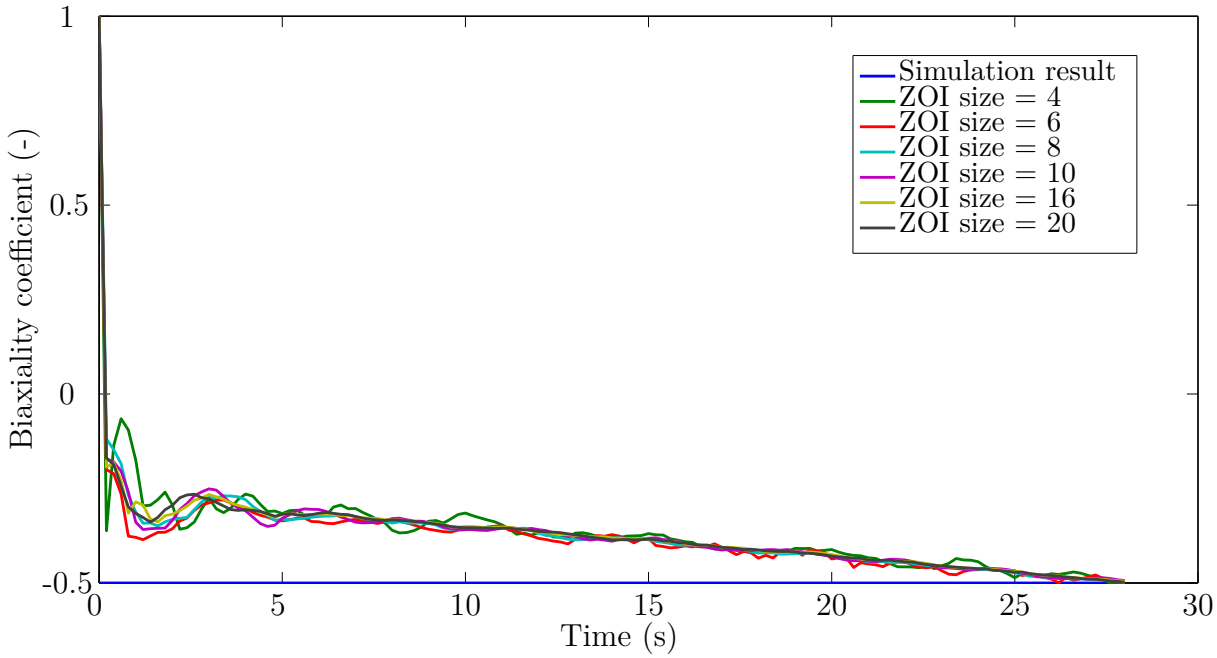

Figure 3.27 – Temporal evolution of the biaxiality coefficient measured for different ZOI size

motion compensation technique is performed to measured the temperature at the different point where the kinematic field have been measured. For this study, the ZOI size is fixed to 10 pixels. Then, the heat equation is used to obtain the heat produced by the material during the test. The heat source is measured for raw temperature and temperature filtered with different filters. In this study, a mean filter is used, and different sizes of filter have been made to observe the influence of the filter on the heat source measured. Figure 3.28 represents the heat source measured at a single point for several size filter.

The figure clearly shows that a temporal filter has to be used in order to reduce the thermal noise from IR images. A size of 10 seems to be well suited in this case.

3.1.2.4 Metrological study of the heat diffusion term

The previous metrological study has investigated the performance of the motion compensation method on several values, such as the stretch and the heat source. However, in this study, the conduction term of the heat source , which is equal to $-k\,\mathrm{Div}\,\mathbf{C}\,\overrightarrow{\mathrm{Grad}}\,\theta$ in the Lagrangian configuration and $-k\Delta_{2D}\theta$ in the Eulerian configuration, has been neglected, since the temperature variation should be homogeneous in the specimen. A metrological study is then necessary.

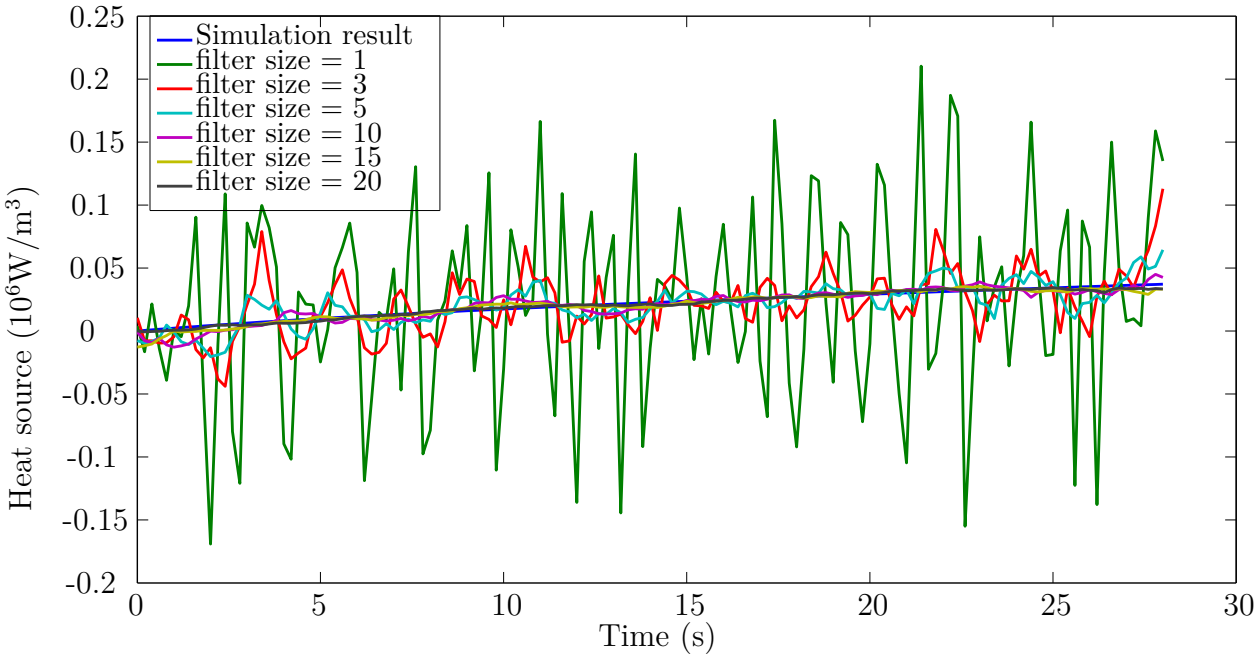

Figure 3.28 – Temporal evolution of the heat source produced by the specimen measured for different temporal filter size

3.1.2.4.1 Calculation of the heat conduction term using the Lagrangian configuration The first step of the method is an oversampling operation. Actually, during the mechanical deformation of a material, the different material points followed by the DIC technique will move away from each other. While this does not affect the two others terms in the heat equation, it highly affects the resolution, and by extension the accuracy, on the heat conduction term. The oversampling point positions are obtained by using a bilinear interpolation, as shown in Figure 3.29. The second step is the determination of

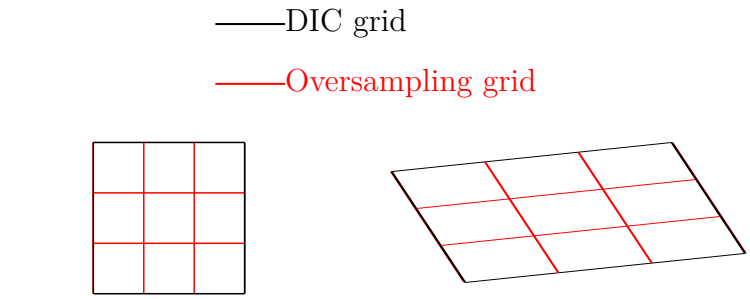

(a) at undeformed state (b) at deformed state

Figure 3.29 – Oversampling principle

the temperature of the different points obtained with the oversampling process. This is

made using the exact same method than the method used for monitoring the temperature variation for the points obtained by the DIC technique. Due to the thermal noise on IR images, a spatial filter can be used before doing this operation. When the temperature of the oversampling points is obtained, the temperature gradient is calculated using the finite difference method.The third step of the method is to determine the Cauchy-Green tensor $\mathbf{C} = \mathbf{F}^T\mathbf{F}$. The different terms of the deformation gradient tensor $\mathbf{F}$ are already known at the material points followed by the DIC technique, they are first determined for each oversampling points by bilinear interpolation. Then, the Cauchy-Green tensor $\mathbf{C}$ is then computed and inverted. The tensor is definitely invertible since it is defined symmetric. After that, the term $\mathbf{C}^{-1}\overrightarrow{\text{Grad}}\,T$ is calculated for each oversampling points. The last step is to calculate the divergence of the term previously obtained. This operation is obtained by using the finite difference method.

3.1.2.4.2 Calculation of the heat diffusion term using the Eulerian configuration The heat conduction term is also evaluated using the Eulerian configuration. The first step is to applied a discrete Laplacian filter on IR images. Then, the conduction term is evaluated at the different material points by using a bilinear interpolation of the Laplacian, in the same way the temperature has been monitored previously. Due to the thermal noise, an averaging filter is applied before performed the discrete Laplacian operation.

3.1.2.4.3 Data used The CCD images are obtained by numerically deforming a speckle image. The numerical deformation imposed is a homogeneous vertical stretch, which leads to a deformation gradient tensor equal to $\mathbf{F} = \begin{pmatrix} 1 & 0 \\ 0 & \lambda \end{pmatrix}$. The spatial resolution of the image is equal to 0.026 mm/px. Figure 3.30 shows the images obtained at both the undeformed and deformed state. It could corresponds to out-of-plan pure shear in the case of an incompressible rubber-like material. This formulation is for the validation of the conduction term in the heat diffusio equation in a case as simple as possible.

The IR images are also obtained by numerically deforming in the same way that CCD images. The spatial resolution of the image is equal to 0.15 mm/px. The initial temperature field for the study is a Gaussian surface, expressed as followed:

$$T(x, y) = A \exp^{\frac{(x-x_0)^2+(y-y_0)^2}{\sigma}} \tag{3.13}$$

with $A = 5$ represents the maximal temperature, which is obtained at the position (x_0, y_0),

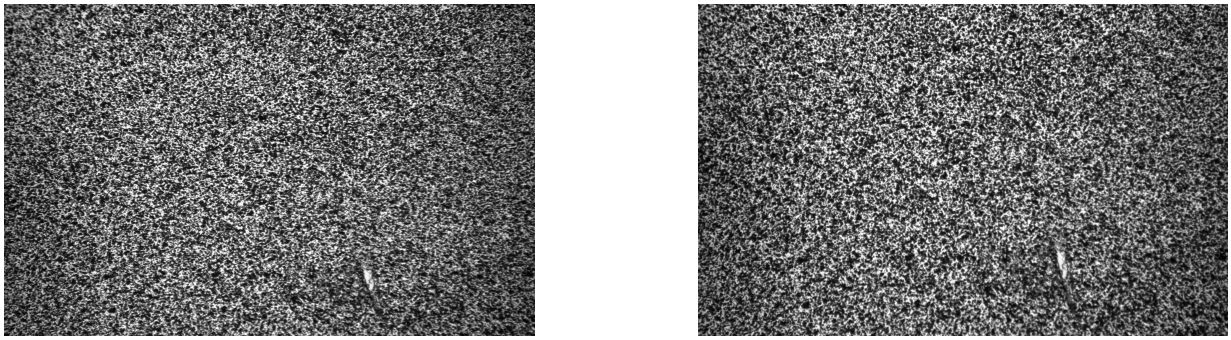

(a) Undeformed speckle image (b) Deformed speckle image

Figure 3.30 – CCD images obtained by the numerical deformation of a speckle

and $\sigma = 10$ represents the spreading of the Gaussian surface (in mm). Knowing both the temperature and deformation field, the analytical solution can be calculated, and will be used to deduce the performance of the method. A numerical noise is added on the IR images obtained to better simulate data that can be obtained with an IR camera. Figure 3.31 shows the images obtained at both the undeformed and deformed states.

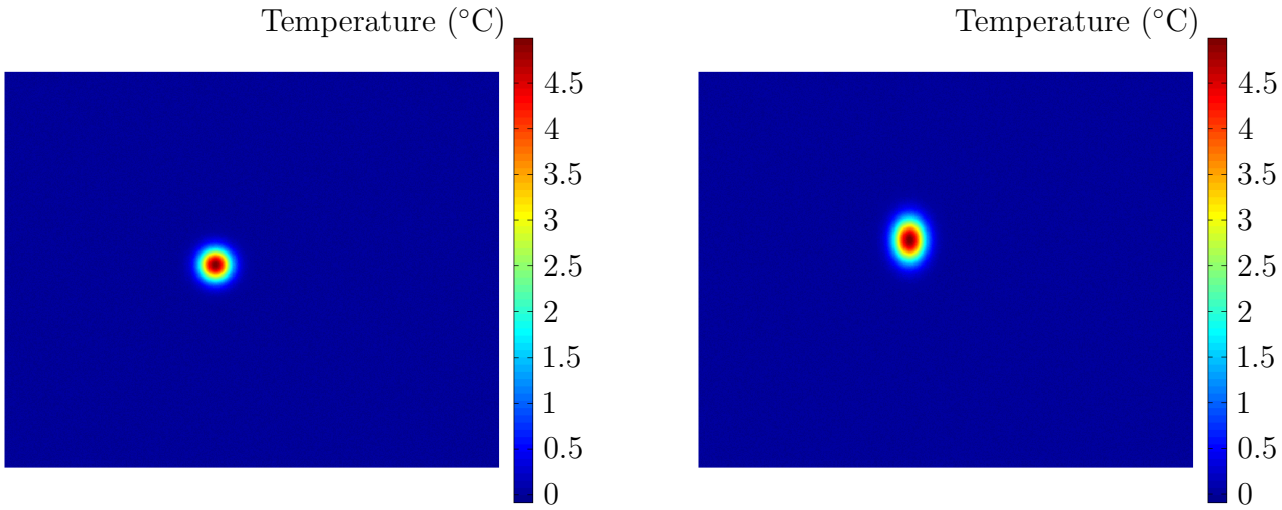

(a) Undeformed temperature field (b) Deformed temperature field

Figure 3.31 – IR images obtained by the numerical deformation of a gaussian temperature field

3.1.2.4.4 Performance of the method The coupling method has been used to measure the temperature and kinematic fields at the same positions. Then, the two methodologies described previously are used to obtain the heat source due to the conduction

within to the material.

Figure 3.32 presents the results obtained, for the undeformed state at the left hand side and at the deformed state at the right hand side. For these figure, neither spatial filter nor oversampling have been used.

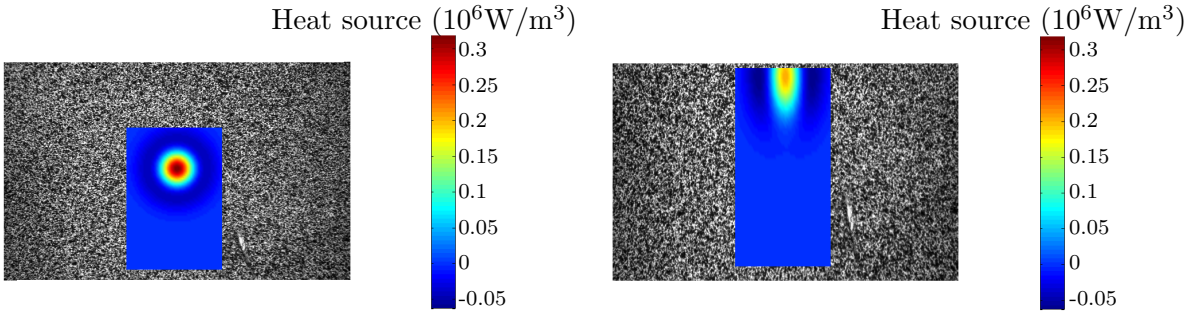

(a) Analytical solution

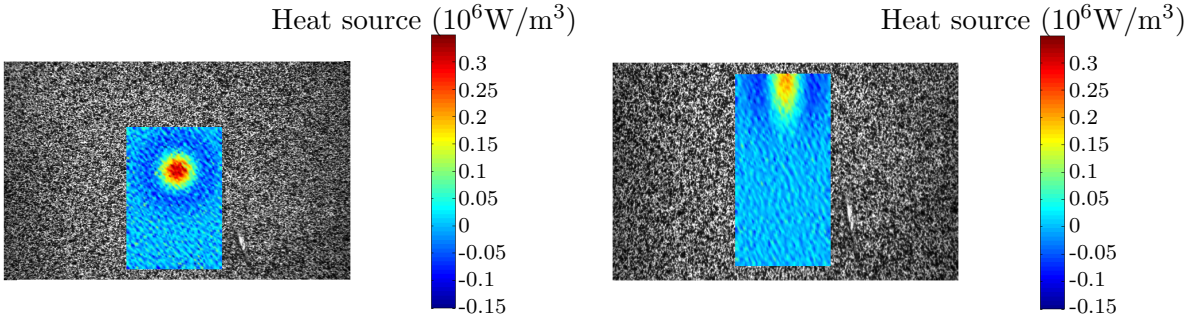

(b) Calculated using the Lagrangian configuration

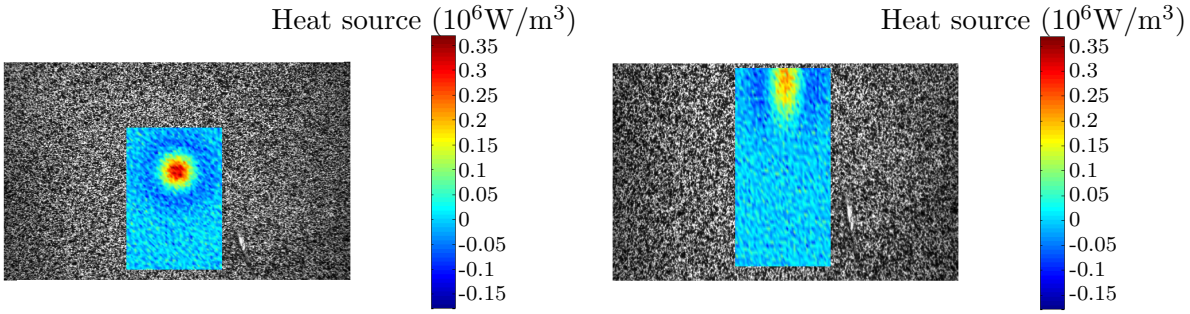

(c) Calculated using the Eulerian configuration

Figure 3.32 – Conduction term of heat source calculated using the two methodology described previously

The figure shows that the methodology is able to measure correctly the conduction term of the heat diffusion equation, whether it is using the Lagrangian or the Eulerian description. However, in this study, the thermal gradient is relatively large in regard to

the spatial resolution of the two cameras. A second study has been performed using a smaller Gaussian form for the temperature, shown in Figure 3.33

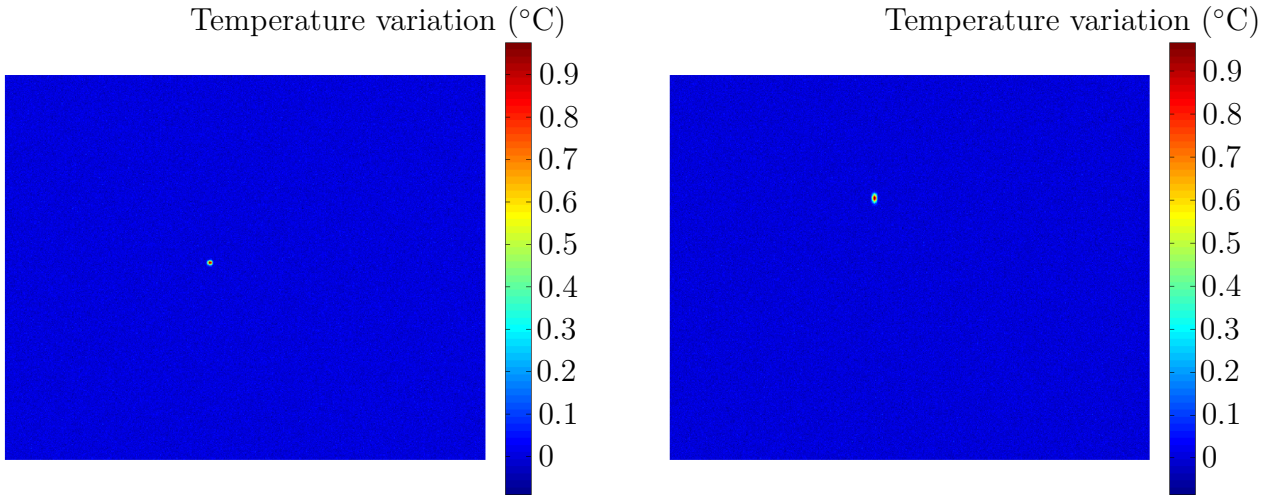

(a) Undeformed temperature variation field (b) Deformed temperature variation field

Figure 3.33 – IR images obtained by the numerical deformation of a smaller gaussian temperature field

Figure 3.32 presents the results obtained, for the undeformed state at the left hand side and at the deformed state at the right hand side. For these figures, neither spatial filter nor oversampling have been used. The figure shows that the Gaussian pattern is observed, however a relatively large error is observed, especially at the Gaussian's center (approximately 30% for the Lagrangian description and 50% for the Eulerian description). In order to reduce this error, strategies including oversampling and filtering operation have been tested, however these solutions exhibit some flaws: the oversampling operation makes the final result obtained more influenced by the thermal noise, since the distance between two points is lower, while an average filter reduces the signal amplitude, which also reduces the heat source due to conduction.

3.2 Application to the local scale inverse identification of hyperelastic consitutive parameter

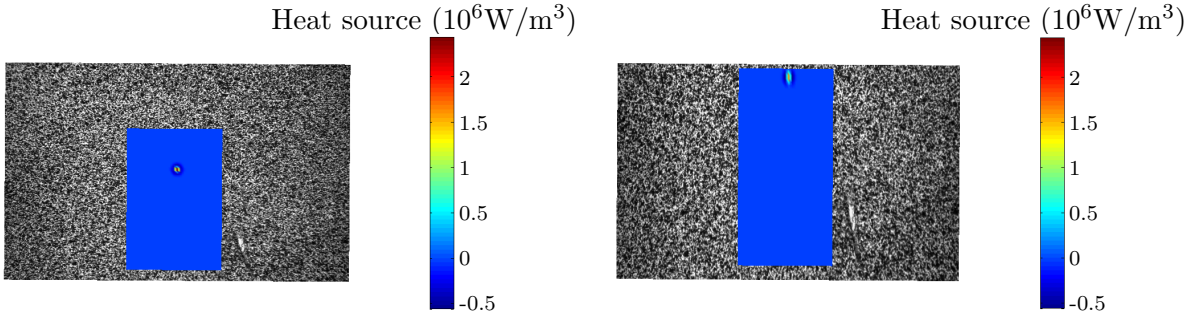

(a) Analytical solution

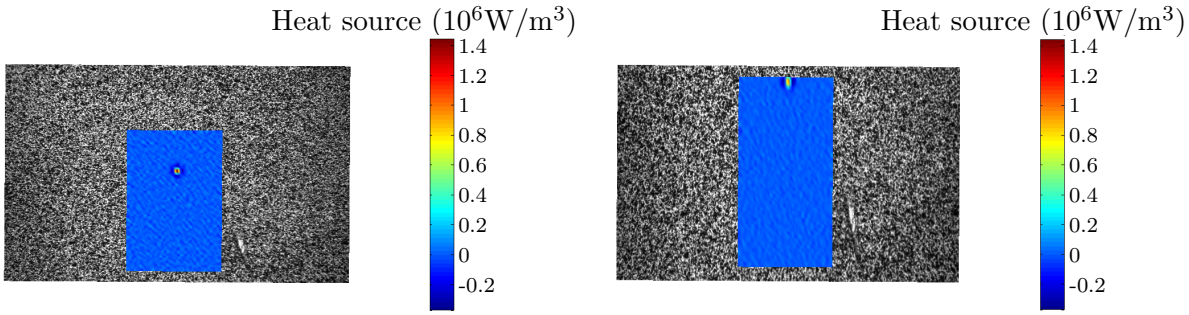

(b) Calculated using the Lagrangian configuration

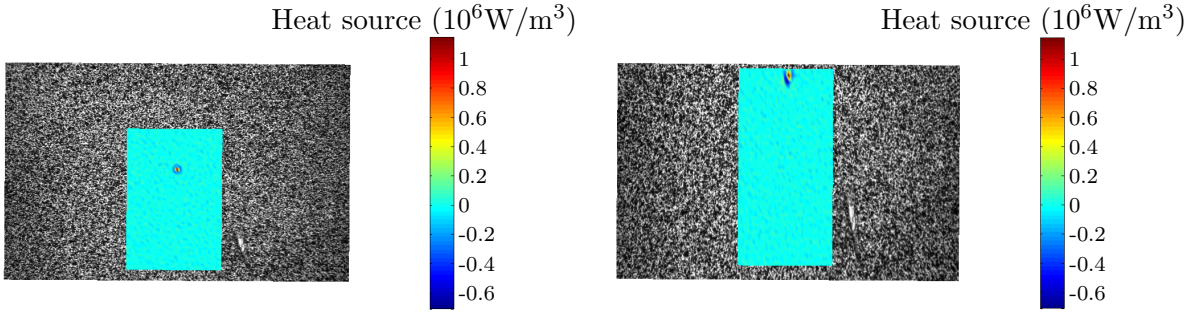

(c) Calculated using the Eulerian configuration

Figure 3.34 – Conduction term of heat source calculated using the two methodology described previously

3.2.1 Introduction

Even though the mechanical response of rubber-like material is governed by several complex physical phenomena, hyperelasticity is often used as a first approximation (see for instance the review by Marckmann and Verron [68]). Since hyperelastic models do not take into account all of these phenomena, their constitutive parameters generally depend on the loading case undergone by the material. This is the reason why constitutive param-

eters are classically identified using three homogeneous tests, namely the uniaxial tensile test (UT), the pure shear test (PS) and the equibiaxial tensile test (EQT). These tests are represented in Figure 3.35. It is commonly admitted that these three tests provide

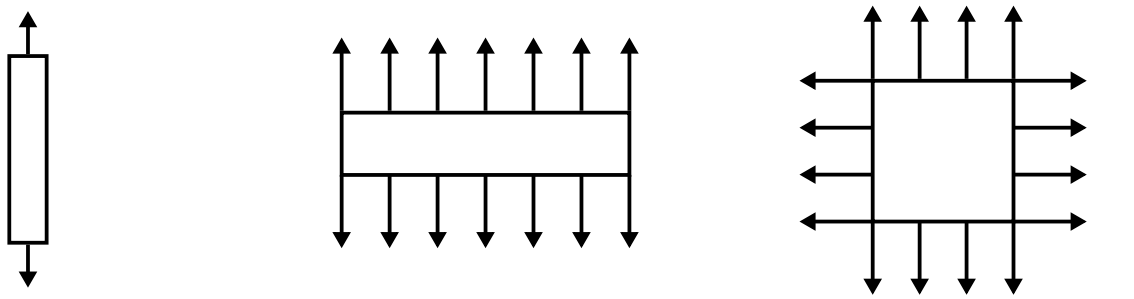

(a) Uniaxial tensile test (b) Pure shear test (c) Equibiaxial tensile test

Figure 3.35 – Samples geometries used for the three homogeneous tests for the characterization of rubber

a good representation of the possible strain states. A trade-off between results from the three tests is then made to obtain a set of parameters that can be assumed to be intrinsic to the mechanical behavior of the material. Such identification way exhibits several disadvantages. First, for each test, the strain state is assumed to be homogeneous upon the whole specimen, which is a strong assumption, especially for the PS test and the EQT test. Then, each test required a specific specimen geometry, which requires different molds and testing machines. Last, the obtention of the intrinsic parameters set is a matter of debate. For instance, should the identification be made for a same maximal stretch, or a same deformation energy, or other quantities?

Recently, an alternative approach has been proposed, based on a single heterogeneous test that induces the three strain states above mentioned, and a wide range of intermediate states. This approach is detailed in Promma et al. [86] and Guélon et al. [39]. In these studies, a three-branch or a four-branch specimen is used, where UT appears in the branches, EQT at the specimen center and PS in a ring-shaped area between UT and EQT. This kind of approach became possible thanks to the advent of full-field measurement techniques, such as digital image correlation (DIC) or the grid method (GM). From this approach, several strategies have been used to perform the inverse identification of constitutive parameters, mainly the finite element model updating (FEMU) [36] and the virtual field method (VFM) [86]. However, both strategies required to know boundary conditions, which can be challenging to measure experimentally.

The proposed method has been the subject of an article published in *Strain* [20]. The

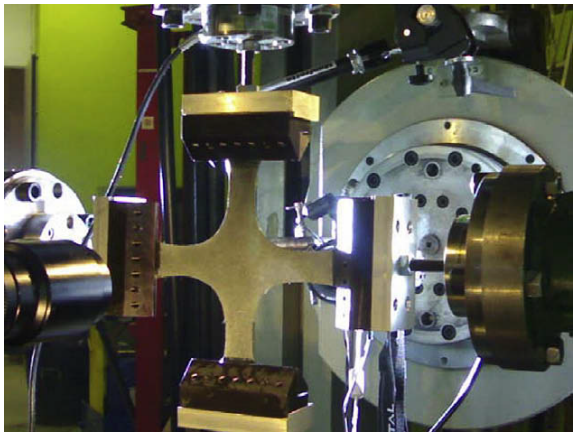

(a) Bidirectionnal tensile test on a cross-shaped specimen [86]

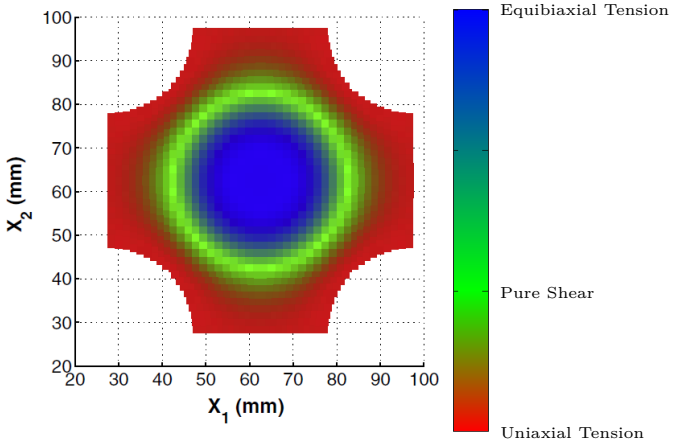

(b) Loading case undergone by the specimen from FEM simulation [86]

Figure 3.36 – Illustrations of a heterogeneous test with a four-branch specimen [86]

method proposed enable us to identify the constitutive parameters at the local scale by reconstructing the heat source field from two different approaches: one from the kinematic field and a given thermomechanical model that contains the parameters to identified, and one from the heat equation and the temperature field measurement. Then, the constitutive parameters are identified by minimizing the difference between the heat source measured and the one predicted from the kinematic measurement. Therefore, the method is obviously more suitable for materials with a strong thermoelastic couplings and a low thermal conductivity, which is the case for elastomers.

The heat source produced by the material can be deduced from the temperature measurement and the heat equation, described in Equation 1.35. The heat source from thermoelastic couplings is given by:

$$T\frac{\partial \mathbf{P}}{\partial T} : \dot{\mathbf{F}} \tag{3.14}$$

3.2.2 Application to the Neo-Hookean model

In the current study, the method is applied to the identification of the Neo-Hookean parameter.

3.2.2.1 Heat source prediction from the Neo-Hookean model

As explained earlier, the prediction of the heat sources evolution during the deformation process requires the choice of thermomechanical model. In this section, the Neo-Hookean model is chosen, and can be written as:

$$W = \mathbf{P} : \mathbf{F} = \frac{1}{2} NkT(I_1 - 3) \tag{3.15}$$

with W the strain energy, N the the number of network chains per unit volume, k the Boltzmann's constant and I_1 the first invariant of the left Cauchy-Green deformation tensor $\mathbf{F}\mathbf{F}^T$.

If the material is mechanically incompressible, which is the case for elastomers, I_1 is written as:

$$I_1 = \lambda^2 + \lambda^{2B} + \lambda^{-2(B+1)} \tag{3.16}$$

with λ the principal maximal stretch and B the biaxiality coefficient.

By implementing the Neo-Hookean model for the strain energy of the material, the heat source produced by the material during its mechanical deformation is written:

$$S = NkT \left[\left(\lambda + B\lambda^{2B-1} - (B+1)\lambda^{-2B-3} \right) \frac{d\lambda}{dt} + \dot{B} \ln(\lambda)(\lambda^{2B} - \lambda^{-2(B+1)}) \right] \tag{3.17}$$

For temperature variations that do not exceed few degrees, the value of NkT remains nearly equal to NkT^{ref}, with T^{ref} the initial temperature, and does no affect the heat source significantly. For instance, at 293 K, which corresponds to 20 °C, an increase of 1 K change the value of NkT by approximately 0.34%. This is the reason why NkT^{ref} is considered here instead of NkT. For sake of simplicity, the Neo-Hookean parameter to be identified is denoted C_{nh} and is equal to: $C_{nh} = \frac{1}{2} NkT^{ref}$.

In the case that the biaxiality coefficient remains constant during the test, i.e. $\dot{B} = 0$, Equation 3.17 can be simplified to:

$$S = 2C_{nh} \left(\lambda + B\lambda^{2B-1} - (B+1)\lambda^{-2B-3} \right) \frac{d\lambda}{dt} \tag{3.18}$$

3.2.2.2 Experimental setup

3.2.2.2.1 Material and specimen geometry In the present study, an unfilled nitrile rubber is considered. This material does not produce detectable intrinsic dissipation and does not crystallize under tension [64]. Therefore, the heat source is only due to thermoelastic couplings, and Equation 3.18 applies. The PCM Technologies S.A.S company is acknowledged for providing the specimens.

The geometry used is shown in Figure 3.37. Its total length is 125 mm and its thickness is 2 mm.

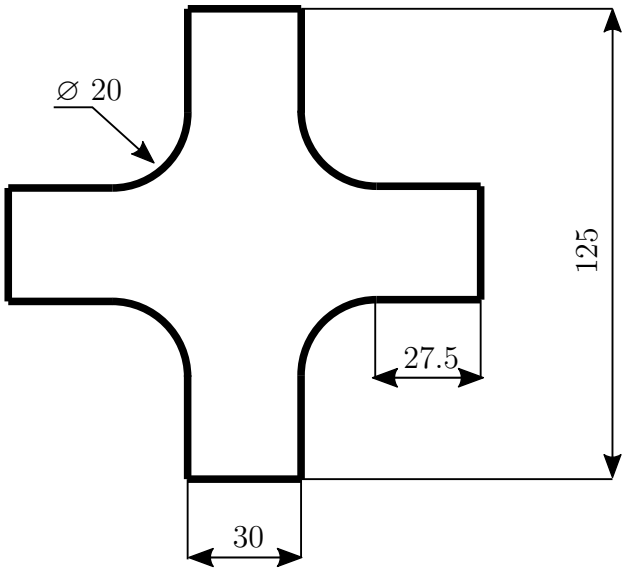

Figure 3.37 – Specimen Geometry

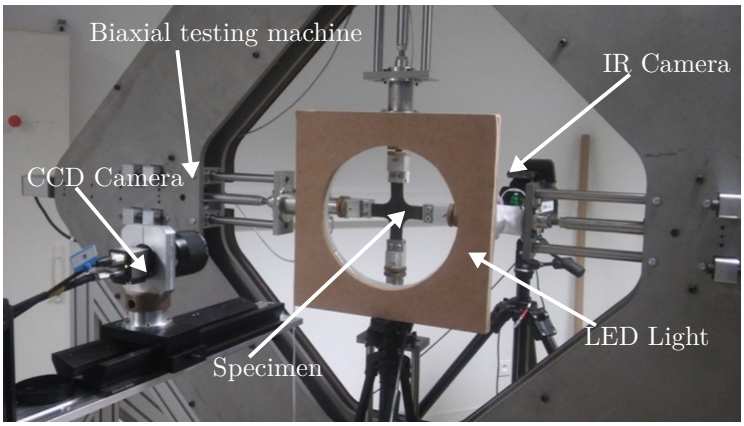

Figure 3.38 – Experimental Setup

3.2.2.2.2 Loading conditions Figure 3.38 presents an overview of the experimental setup used for this study. It is composed of a CCD camera to measure the kinematic field at the specimen surface and an infrared camera to measure the thermal field at the specimen surface, on both sides of a home-made biaxial testing machine. This machine is composed of four independent RCP4-RA6C-I-56P-4-300-P3-M (IAI) electrical actuators. They are driven by a CON-CA-56P-I-PLP-2-0 controller and four PCON-CA (IAI) position controllers. An in-house LabVIEW program piloted these actuators.

In the present study, a single equibiaxial loading is carried out. Each independent actuator is controlled in the same way. In this case, the specimen center is motionless. The displacement and loading rate are set at 70 mm and 150 mm/min respectively for each actuator.

Temperature measurements are performed by using a FLIR infrared camera equipped with a focal plane array of 640x512 pixels and detectors operating in wavelengths between 1.5 and 5.1 µm. The integration time is equal to 2700 µs, and the acquisition frequency is equal to 25 Hz. The calibration of camera detectors is performed with a black body using an one-point NUC procedure at this acquisition frequency. The thermal resolution, or noise equivalent temperature difference (NETD), is equal to 20 mK for a temperature range between 5 and 40 °C. The spatial resolution of the thermal field is equal to 300 µm/px. The infrared camera is switch on several hours before the test in order to stabilize its internal temperature. Both cameras are trigged at the same frequency of 5 Hz, to measure kinematic and thermal fields at the same time.

To obtained the temperature field, the emissivity of the material must be evaluated. In the present case, the specimen have been placed in an oven and heated at 50 °C. The emissivity is then obtained by comparing the temperature of the specimen with the temperature of a black body regulated at the same temperature. The experimental setup is shown in Figure 3.39. The emissivity obtained is equal to 0.94, which is in good agreement with the emissivity of rubber in the literature.

3.2.2.3 Kinematic field measurement

Images are stored with an IDS camera equipped with a 55-mm telecentric objective. The resolution of the camera is 1920x1200 pixels, with a spatial resolution of approximately 100 µm/px.

For this study, DIC is performed using the 7D software developed by P. Vacher. The grid step, i.e. the distance between two independent ZOI is defined to 10 pixels and the

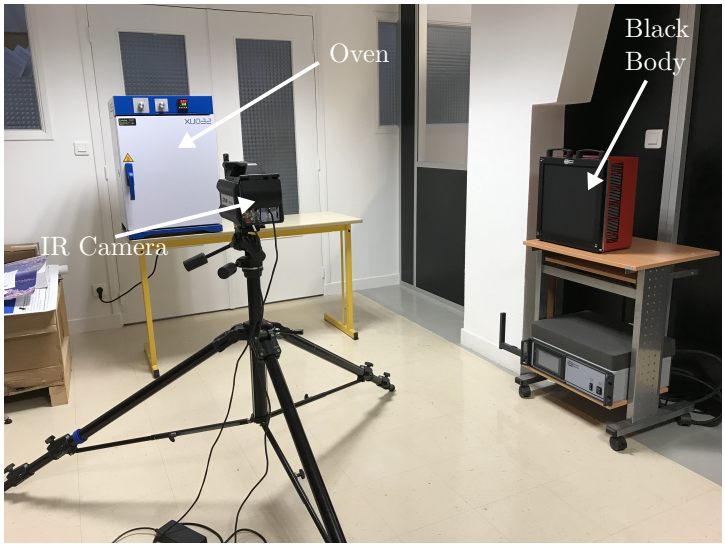

Figure 3.39 – Experimental setup used for the determination of the material emissivity

subset size is defined to 10 pixels.

3.2.2.4 Results

In this section, the full kinematic and thermal fields are first presented. Then, the heat source field reconstruction is explained. Finally, different identification strategies are detailed.

3.2.2.4.1 Heterogeneity induced by the mechanical test Figure 3.40 illustrates the displacement field obtained at the maximum loading applied by the DIC technique.

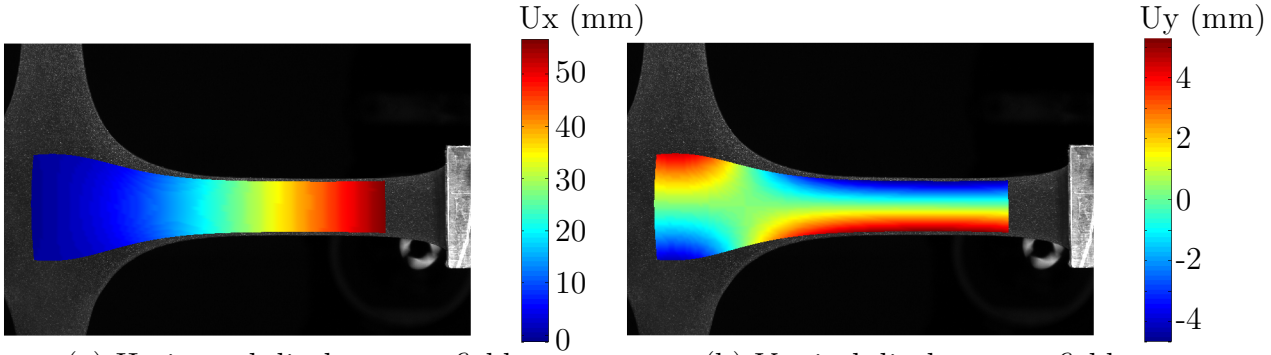

(a) Horizontal displacement field (b) Vertical displacement field

Figure 3.40 – Displacement fields measured at the maximal global displacement

Both the principal stretch and the biaxiality coefficient are determined by using the

methodology described in Section 3.2.2.3. It enables us to investigate the heterogeneity induced by the mechanical test. For that purpose, different representations are used, as explained in Promma et al. [86]:

— Each material point can be plotted as a point in the (I_1, I_2) plane (see Fig. 3.41a). I_1 and I_2 are calculated by assuming that the material is incompressible, and are expressed as:

$$\begin{cases} I_1 = \lambda^2 + \lambda^{2B} + \lambda^{-2(B+1)} \\ I_2 = \lambda^{2(1+B)} + \lambda^{-2} + \lambda^{-2B} \end{cases} \tag{3.19}$$

Note that in this representation, three curve are also plotted, corresponding to the EQT, PS and UT states, and all these three curves are meeting at the point (3,3), which corresponds to the undeformed state. The diagram here has been established for the maximum global displacement applied. The diagram highlights that all loading cases, from EQT to UT by PS, are well represented with this mechanical test, as all intermediate loading cases. However, the strain range for UT state is larger than for EQT state. It should be noted that specimens with shorter branches reduce this strain range difference.

— Fig. 3.41b represents the map of strain state at the maximal global stretch, which can be deduced from the biaxiality coefficient. It highlights the spatial distribution of the strain states on the specimen: UT are applied in the branches, EQT at the specimen center and PS in a ring-shaped area between the two previous ones.

— Fig. 3.41c represents the map of maximal principal stretch at the maximal global displacement. It shows that the branches, where UT is applied, the specimen is more stretched than at the specimen center, where EQT is applied. This is in agreement with the higher strain range for UT seen in Figure 3.41a.

In Equation 3.18, the heat produced by the material from thermoelastic coupling using the Neo-Hookean model is given assuming that the biaxiality coefficient remains constant over the time. Figure 3.42 gives the time evolution of the biaxiality coefficient of five different point. It shows that the biaxiality coefficient remains approximatively constant, as long as the global displacement is high enough to avoid a bad signal to noise ratio (at the beginning of the test) or buckling (at the end of the test).

3.2.2.4.2 Application of the motion compensation technique The motion compensation technique described in Section 3.1 is then applied to track the temperature

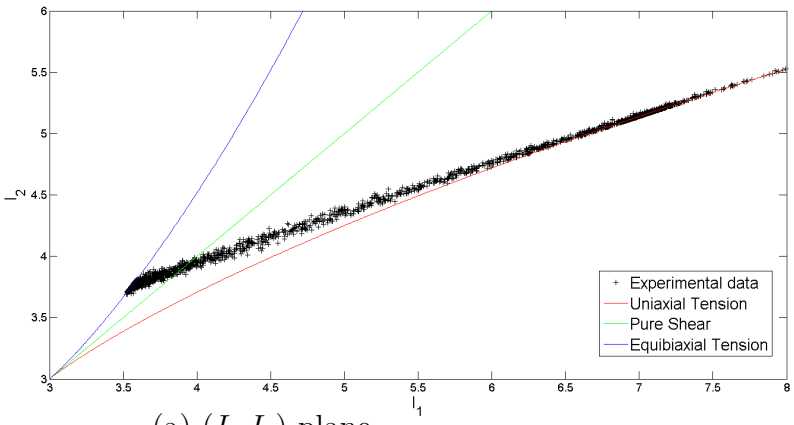

(a) (I_1,I_2) plane

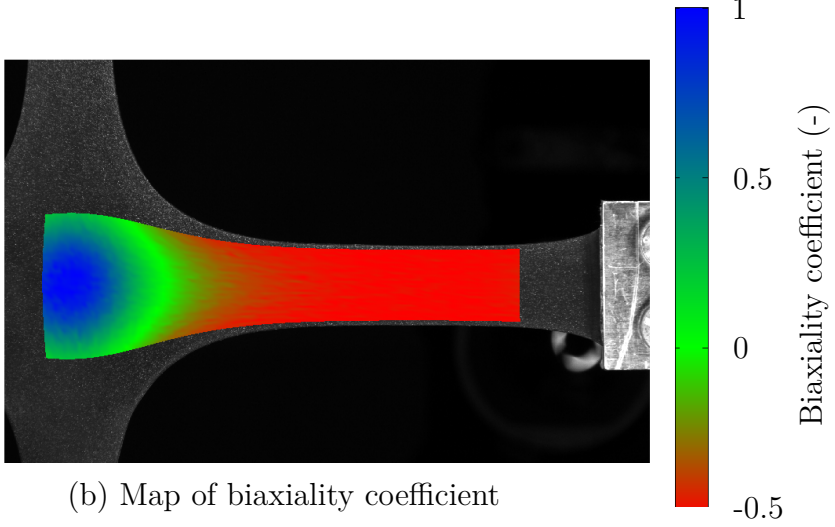

(b) Map of biaxiality coefficient

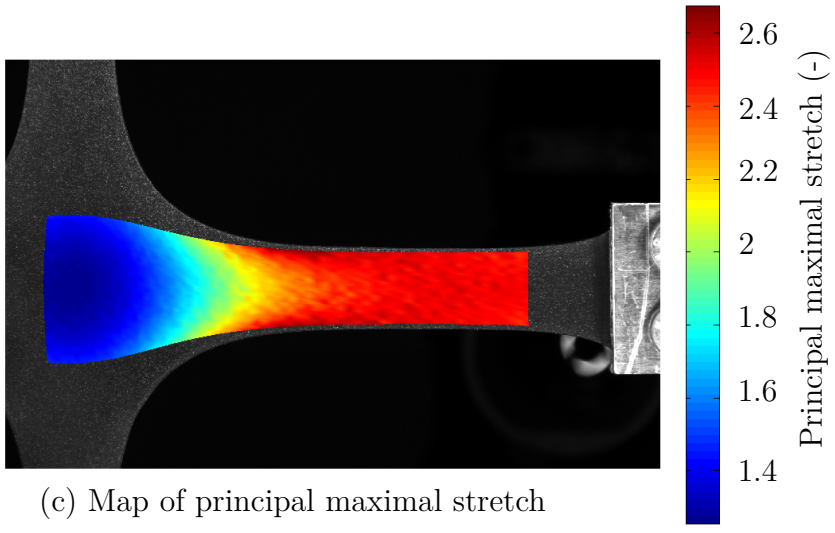

(c) Map of principal maximal stretch

Figure 3.41 – Heterogeneities induced by the mechanical test

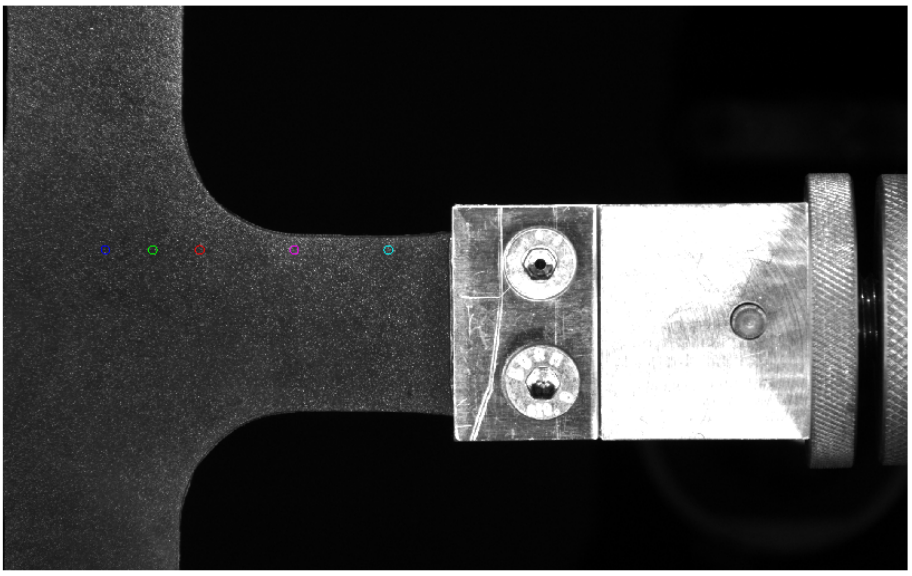

(a) Points followed to characterize the time evolution of biaxiality coefficient

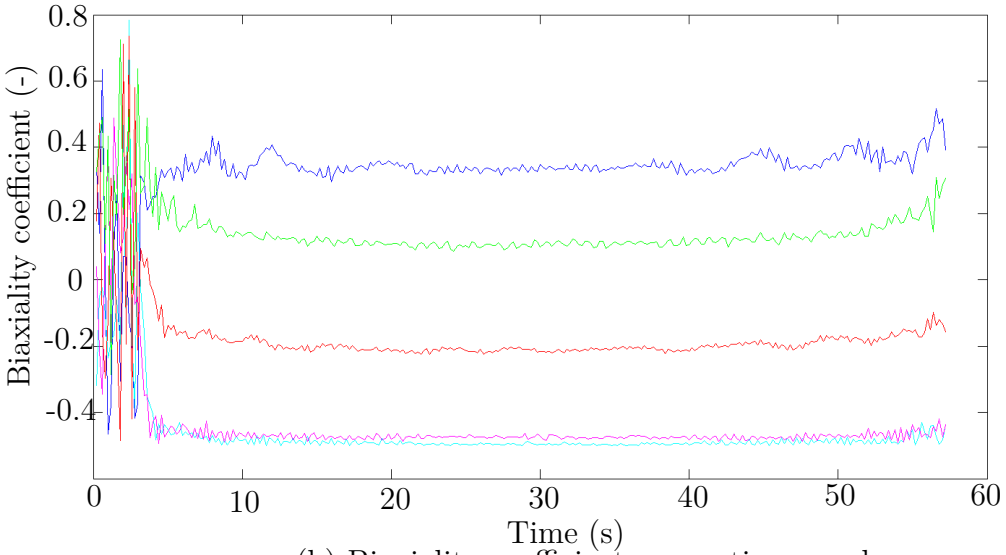

(b) Biaxiality coefficient versus time graph

Figure 3.42 – Characterization of the time evolution of the biaxility coefficient during the mechanical test

variation of each square element center. The first step is to transpose the DIC grid on IR images. Then the temperature of the different point are deduced, as shown in Figure 3.43.

3.2.2.4.3 Heat source reconstruction The heat source can be reconstructed from the temperature variations measured using Equation 1.35. In this equation, some param-

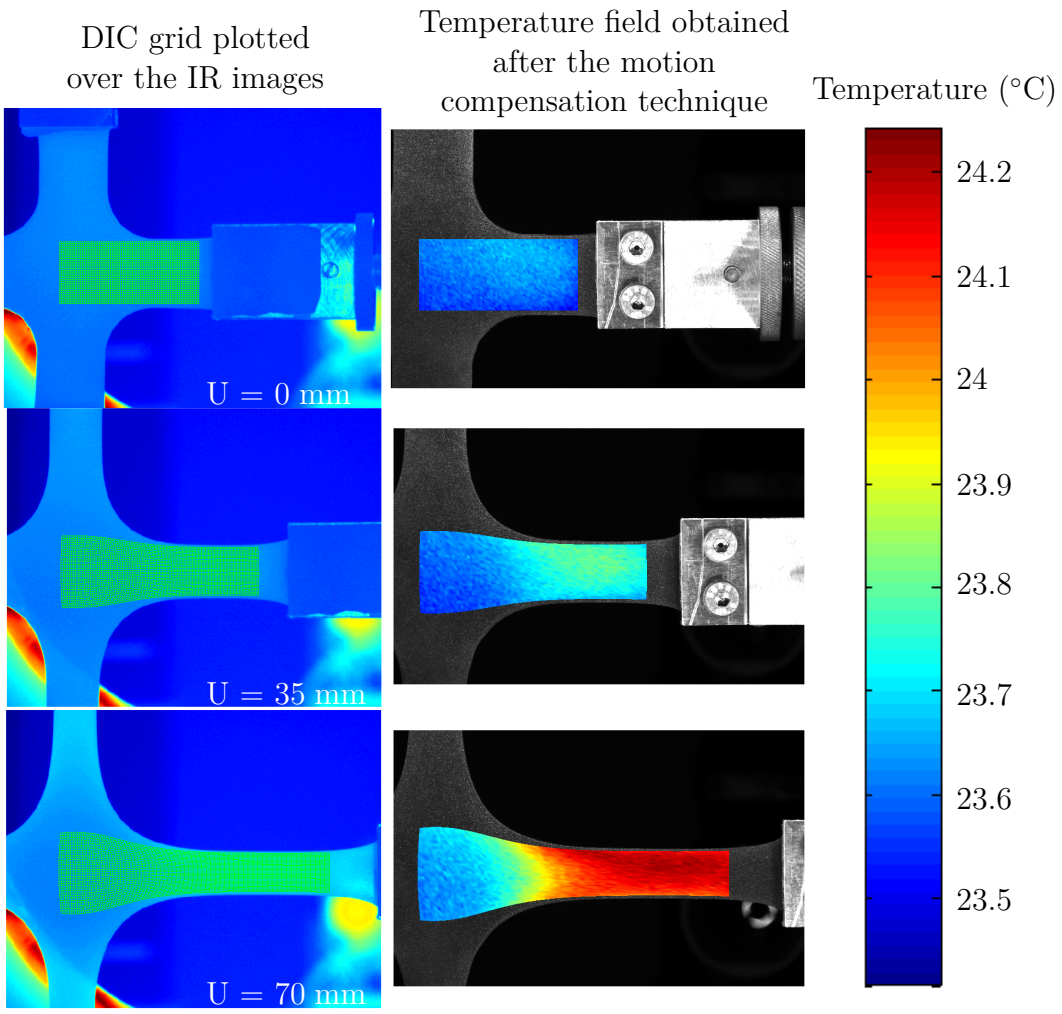

Figure 3.43 – Results of the motion compensation technique developped

eters are intrinsic to the material, and are supposed to be known, but the time constant τ does not only depend of the material, but also on experimental conditions, so it has to be characterized. Its evaluation is all the more important that the test is performed at a low loading rate, which leads to a significant heat diffusion by convection with the ambient environment

The evaluation of τ is first performed at the undeformed state. It is made by heating the material and measuring the temperature during the return to the thermal equilibrium state. Then, the measured temperature curve is fitted by an exponential curve, as shown in Figure 3.44. In this study, the average value of τ at the undeformed state, denoted τ_0, is equal to 198 s.

Then, the evolution of τ with the strain state is characterized, as shown in Figure 3.45.

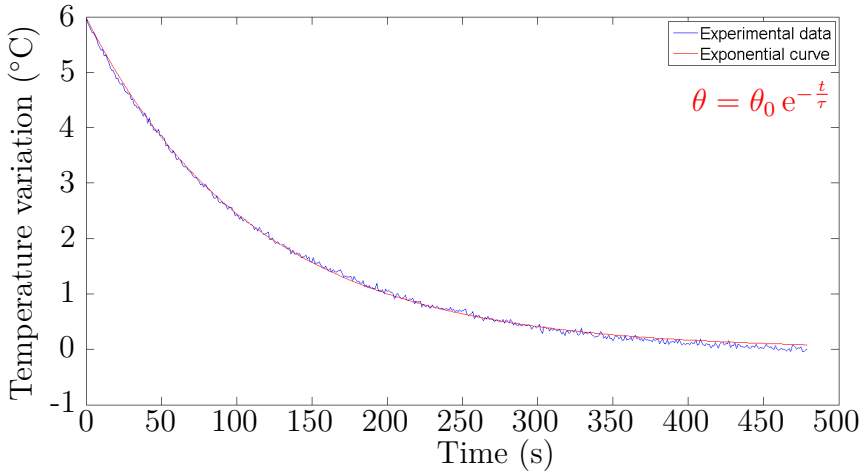

Figure 3.44 – Fitting of the experimental temperature by an exponential curve

The time constant is measured for different stretch and biaxiality coefficient, then results obtained are compared with a formula that takes into account the thickness variation, represented in the figure by the surface. This figure highlights the good evaluation of the time constant with Equation 3.20.

$$\tau(\lambda, B) = \tau_0 \lambda^{-B-1} \tag{3.20}$$

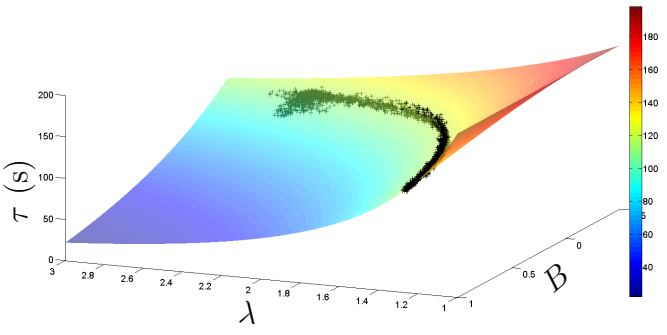

Figure 3.45 – τ versus the stretch λ and the biaxiality coefficient B

Once the time constant is characterized, the heat source field can be reconstructed by applying Equation 1.35. As an illustration, Figure 3.46 provides the heat source field at the maximal global displacement.

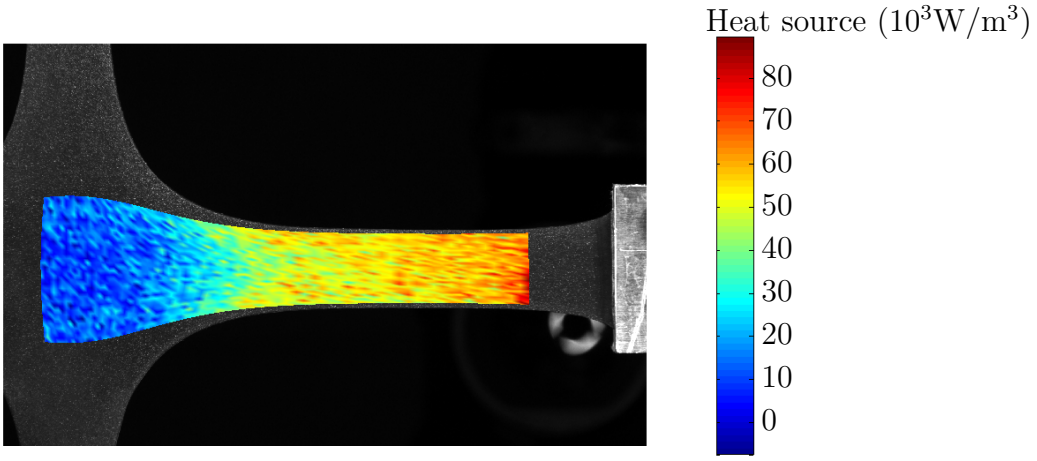

Figure 3.46 – Map of heat source measured by IR thermography at the maximal global displacement

3.2.2.4.4 Identification of the Neo-Hookean parameter The constitutive parameter can be determined by the least square method. Two different approaches have been considered.

The first approach is to perform the identification at a global scale. In that case, the objective function to be minimized is defined by $\Phi(C_{nh}) = \sum_i \sum_t (S(i,t) - S_{nh}(i,t,C_{nh}))^2$, where i is the number of the square element, t is the time, S_{nh} the heat source calculated from the Neo-Hookean model and S the heat source measured with IR thermography. Using this approach, a value of approximately 0.2 MPa have been found.The advantage of the method is that the identification can be made at a local scale, which means here that each square element can be processed separately, in order to find a field of constitutive parameter. In that case, the objective function to be minimized is defined by $\Phi(C_{nh}, i) = \sum_t (S(i,t) - S_{nh}(i,t,C_{nh}))^2$. Figure 3.47 shows results obtained using this approach. This figure highlights how the loading case can influenced the value of constitutive parameters, which is a well-known result since the pioneering work carried out by Treloar [112].

3.2.3 Metrological study of the method

While the previous study demonstrates that the method allow the identification of a Neo-Hookean parameter of a rubber material, it does not allows to estimate the precision of the method. For that purpose, a metrological study on this method is performed.

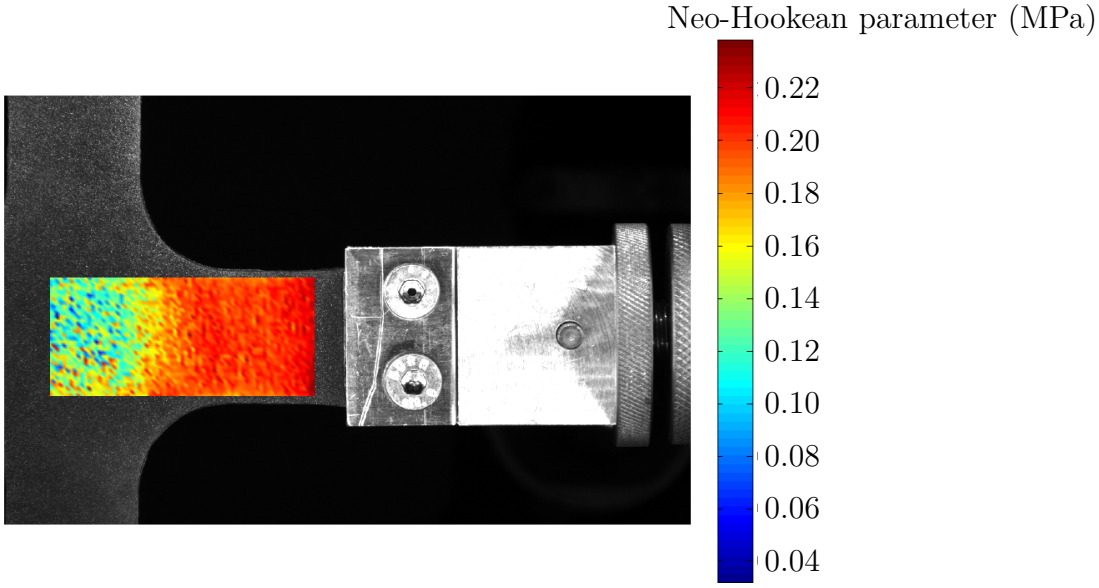

Figure 3.47 – Map of Neo-Hookean parameter found using a local scale approach of the method

3.2.3.1 Metrological study on simulated data

First, the identification method is applied to simulated data from Section 3.1.2.3. For this study, several ZOI size and temporal filter have been tested, and for each set of parameters, the Neo-Hookean parameter has been identified, using both the global and local scale method. Metrology on heat produced and kinematic field have already been presented in Section 3.1.2.3, this metrological study will be focused on the precision of the Neo-Hookean parameter.

3.2.3.1.1 Results obtained with global scale method First, the global scale method is used to determined the Neo-Hookean parameter of the material. Figure 3.48 represents results obtained using this method for several temporal filter and ZOI size.

This figure shows that, except in the case where the ZOI size for the DIC is too small and a temporal filter is used for the temperature, really good results are obtained.

3.2.3.1.2 Results obtained with local scale method Then, the local scale method is used to determined the Neo-Hookean parameter of the material. Since this method does not give a single value, but a whole field of Neo-Hookean parameter, and the fact that the Neo-Hookean parameter should be constant over the specimen, mean value and standard deviation of parameters identified will be studied in the following. Figure 3.49 represents

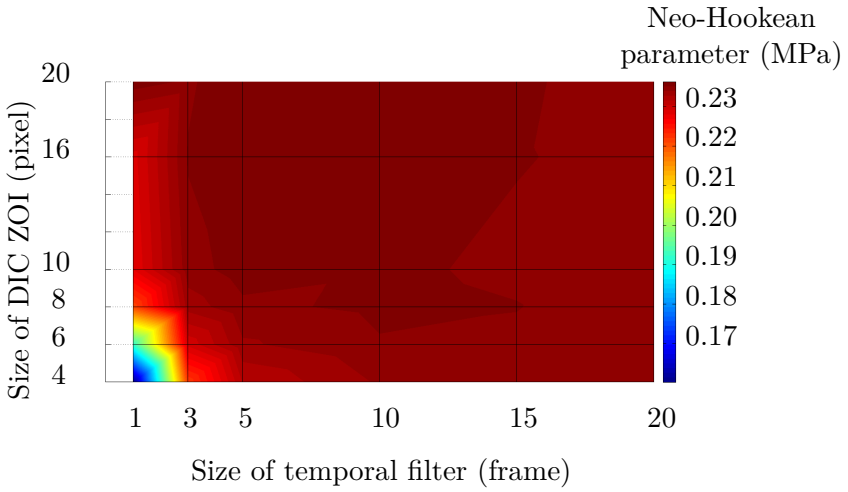

(a) Neo-Hookean parameter identified using the global scale method for several temporal filter and ZOI size

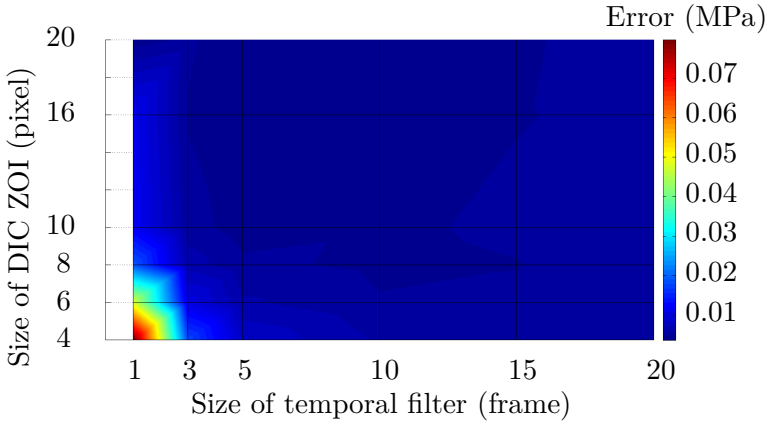

(b) Error made on the Neo-Hookean parameter identified using the global scale method for several temporal filter and ZOI size

Figure 3.48 – Identification results obtained using the global scale method

mean value obtained using this method for several temporal filter and ZOI size.

This figure shows that, except in the case where the ZOI size for the DIC is too small and a temporal filter is used for the temperature, really good results are obtained. Moreover, results obtained are close from those obtained with the global method.

Figure 3.50 represents the standard deviation obtained using this method for several temporal filter and ZOI size.

This figure highlights the fact that the temporal filter size are the main parameter that influence the deviation obtained in the Neo-Hookean parameter field.

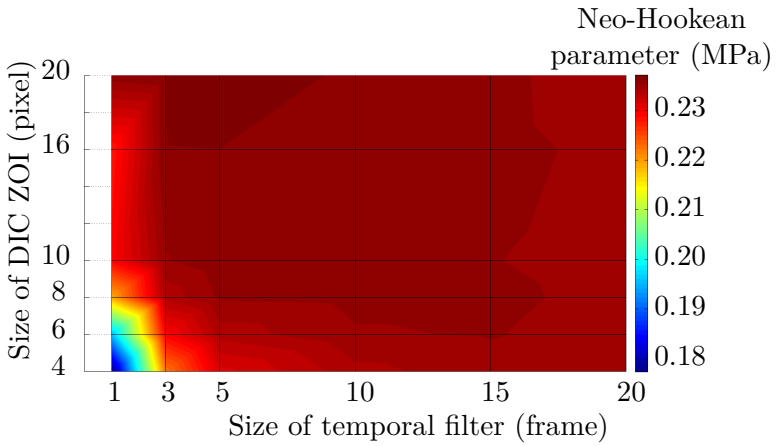

(a) Neo-Hookean parameter identified using the local scale method for several temporal filter and ZOI size

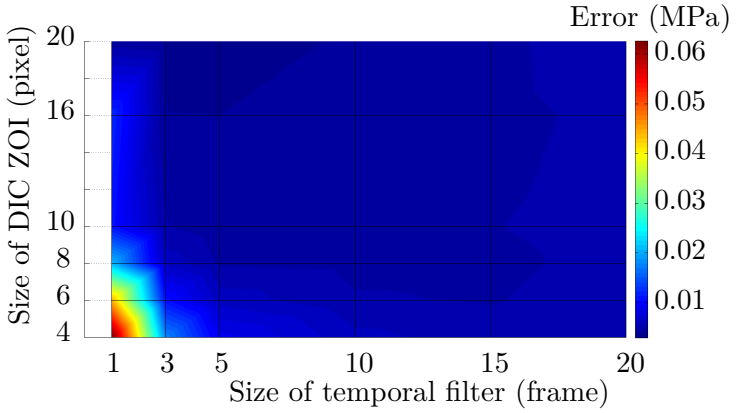

(b) Error made on the Neo-Hookean parameter identified using the local scale method for several temporal filter and ZOI size

Figure 3.49 – Identification results obtained using the local scale method

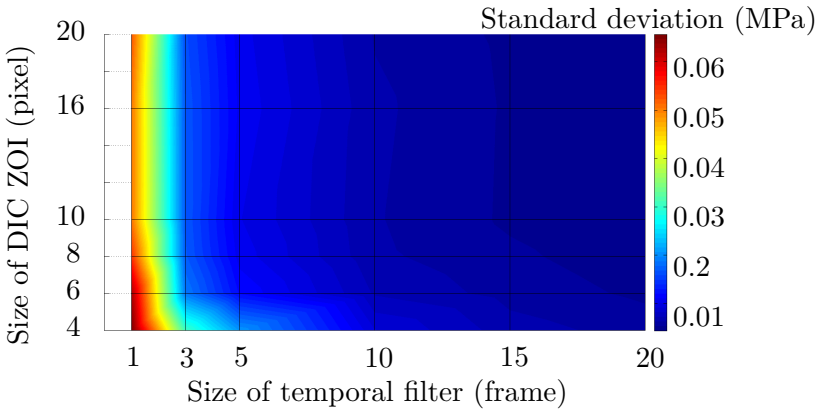

Figure 3.50 – Standard deviation obtained on identification results using the local scale method

To conclude, the metrological study performed here shows that this method can give good results, to lower temperature noise for the heat reconstruction, which can be made by applying a mean filter. However, this study has been performed on a simulated specimen that can be perfectly thermomechanically described using a Neo-Hookean model.

3.2.3.2 Metrological study on nitrile rubber specimen

To better see performance of the identification method, it has also been performed on a real uniaxial tensile test on a unfilled nitrile rubber sample. The specimen's length is equal to 123.54 mm, its width to 29.82 mm and its thickness to 2 mm. The mechanical loading applied is composed of three uniaxial cycles of loading/unloading, and each cycle will be processed separately. The displacement and loading rate are set at 70 mm and 150 mm/min respectively for each actuator.

3.2.3.2.1 Kinematic field measured The strain state (UT) is assumed to be homogeneous upon the whole specimen. Figure 3.51 shows the maximal stretch and the biaxiality coefficient field measured during the mechanical loading. The figure clearly confirms that the specimen undergo uniaxial tension at every point, but also that the stretch level is not totally homogeneous during the test, especially in the specimen's end.

3.2.3.2.2 Thermal field measured Since the test is not mechanically homogeneous, heat source produced by the material during its deformation must be heterogeneous too. Figure 3.52 shows the heat source field measured during the mechanical loading. The figure shows that the heat source field is not homogeneous on the specimen, although no link between kinematic fields and heat source field can be made.

3.2.3.2.3 Results of the identification The identification is then performed for different temporal filter and ZOI size, first at the global scale, i.e. a single Neo-Hookean parameter for the whole specimen. Figure 3.53 represents results obtained from the global identification for each cycle.

On this figure, several features can be seen:

— First, for each mechanical cycle, a lower Neo-Hookean parameter is found when using a small ZOI size and temporal filter

— Second, for each mechanical cycle, using a high temporal filter size lower the influence of the ZOI size.

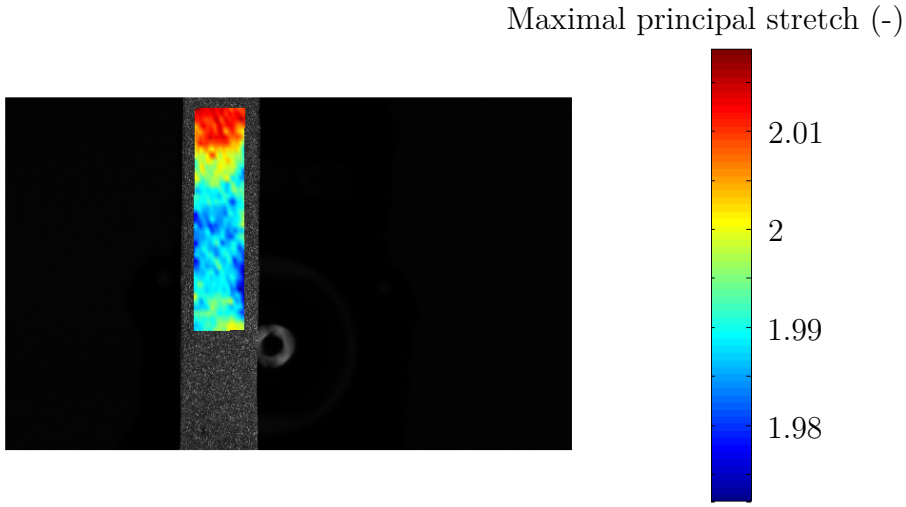

(a) Maximal principal stretch field

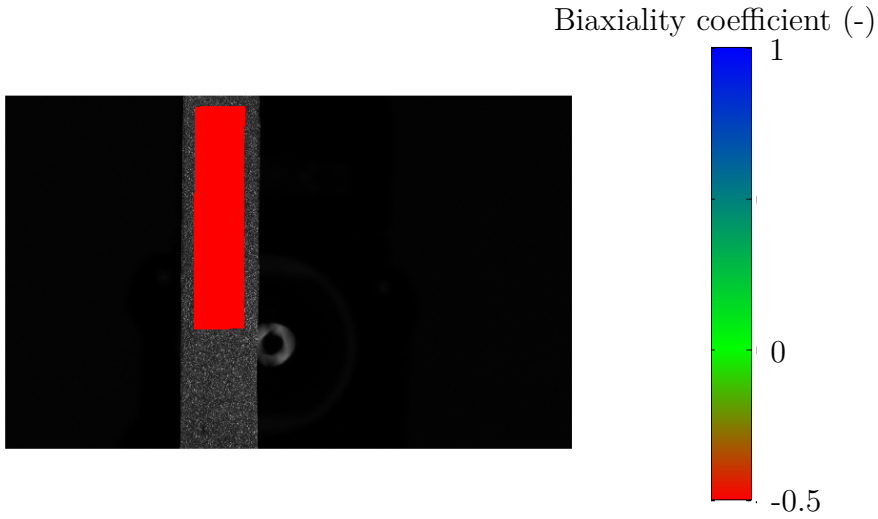

(b) Biaxiality coefficient field

Figure 3.51 – Strain fields measured during the uniaxial test

Then, the identification is performed at the local scale, i.e. each square element is processed separately, which is presented in Figure 3.54, both in terms of mean and standard deviation values. On this figure, same features can be seen on mean values, represented at the left hand side. In addition to this, standard deviation results clearly show that the filter size have a higher influence in the deviation than the ZOI size. One exception can be spotted for the first mechanical cycle, in which a ZOI size of 6 pixels leads to a high standard deviation of Neo-Hookean parameter, regardless of the filter size.

While these results gives information on the influence of these parameters on the

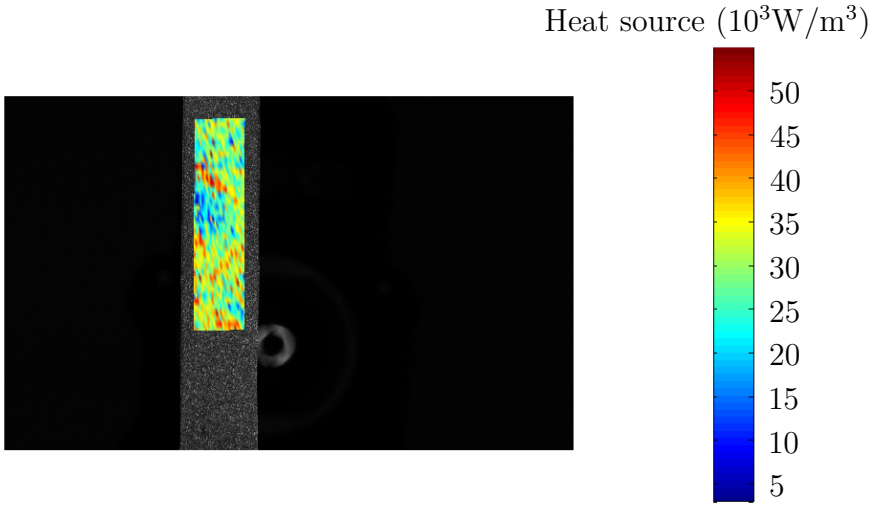

Figure 3.52 – Heat source field measured during the uniaxial test

results, the quality of the identification can not be deduced.

3.2.4 Conclusion

In this section, a new inverse identification method is proposed, which is based on the reconstruction of heat source field from two different approaches: a first one from the heat equation, and requires to measure the temperature field, and a second one based on a thermo-mechanical model, and requires to measure the kinematic field. Since this method is only based on local values, such as temperature and strain, boundary condition are no required to perform the identification. The method is used for identifying the Neo-Hookean parameter of an unfilled nitrile rubber, both at a global and local scales.

Due to the large displacement undergone by the specimen, the couplings methodology described in Section 3.1 has to be used.

In this study, the method is used to measured the Neo-Hookean parameter of a nitrile specimen, but could potentially be used for other models, as long as a link between the modelization and the heat source production can be explicited.

3.3 Application to the characterization of bimaterials samples

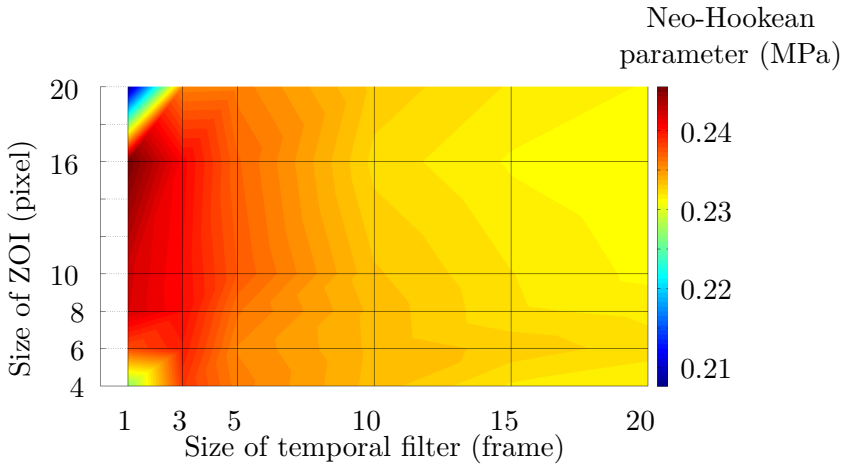

(a) Cycle 1

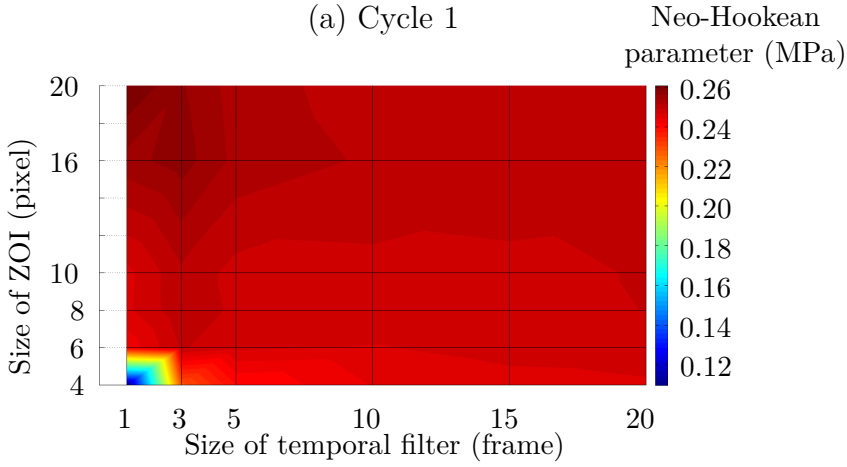

(b) Cycle 2

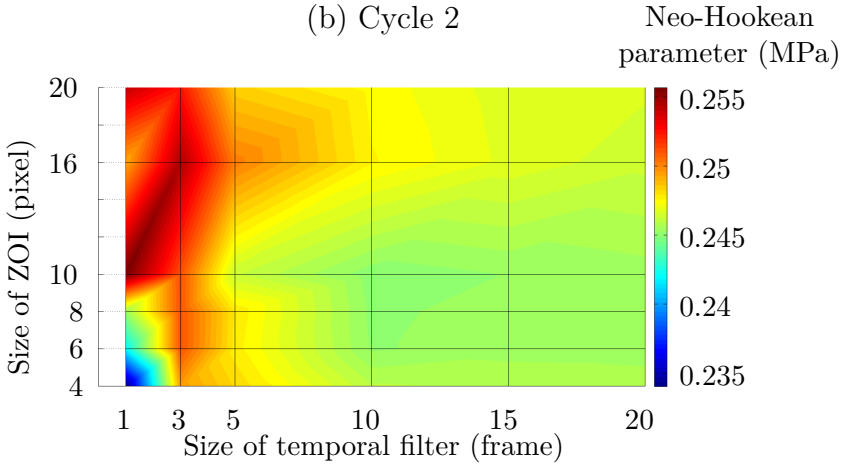

(c) Cycle 3

Figure 3.53 – Identification results obtained using the global scale method

3.3.1 Introduction

While the injection process has been used for years to produce complex geometry parts in short times, a variation of this method is beginning to emerge in the recent years to

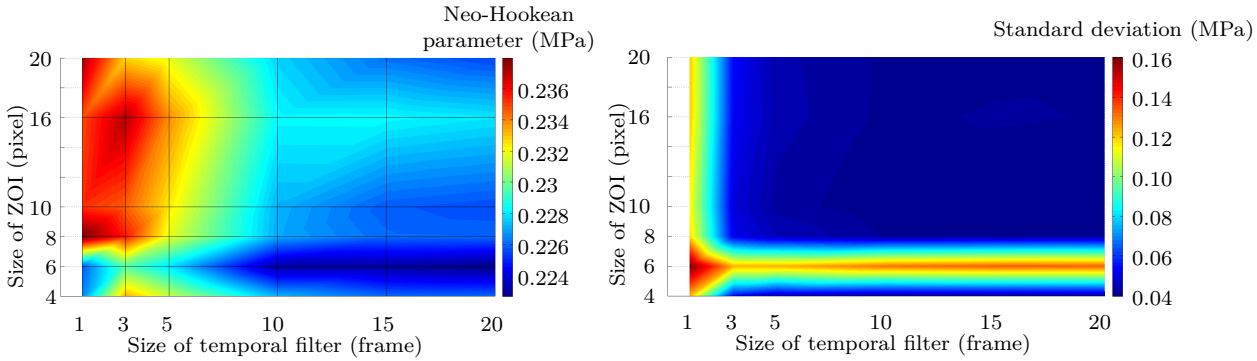

(a) Cycle 1

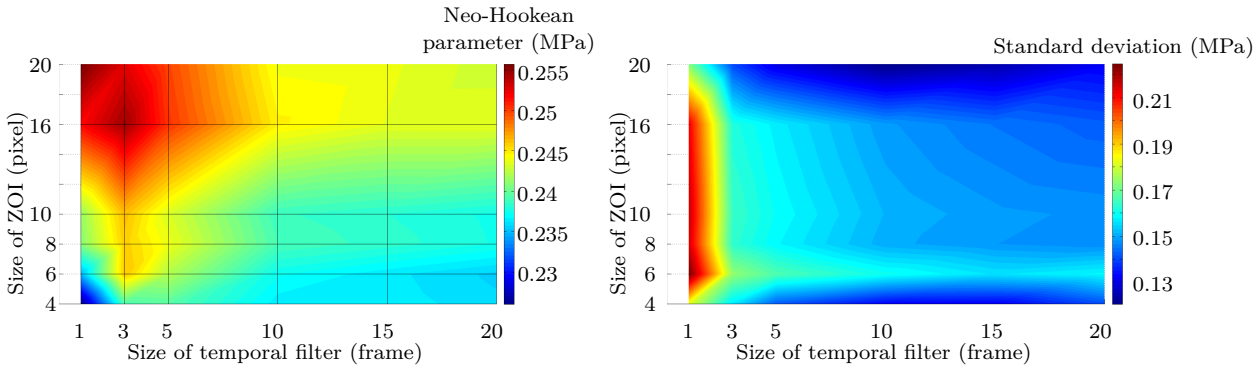

(b) Cycle 2

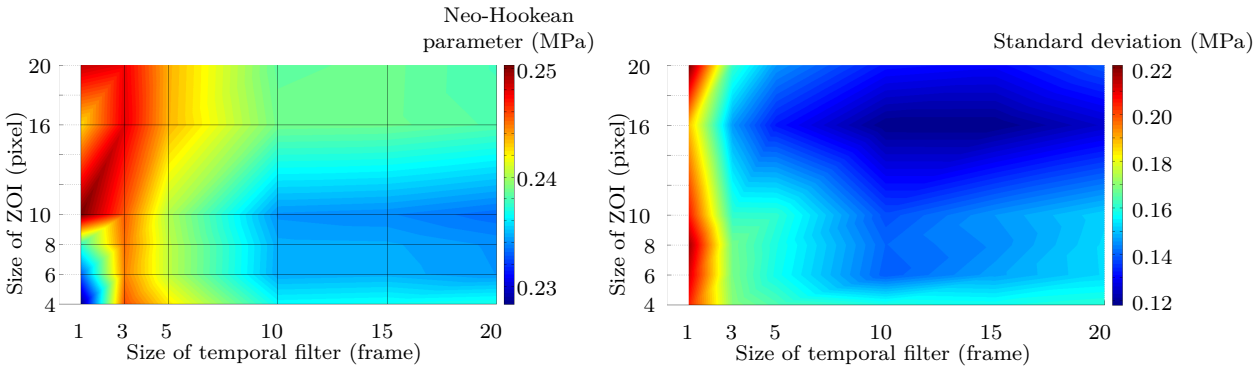

(c) Cycle 3

Figure 3.54 – Identification results obtained using the local scale method

answer to the new needs of the industry. The overmoulding method consists in joining two polymeric parts without using any adhesives. This injection technique is used in several sectors such as automotive, where weather seals are obtained by joining extrude profiles by overmoulding. In order to isolate from noise, water and dust, soft-soft combination are mostly used. The classical soft-soft combination is made of ethylene-propylene-diene-monomer rubber, but thermoplastic elastomer vulcanized (TPV) are more and more used. These materials have a great interest since they exhibit elastomeric properties with the

processability of thermoplastics.

Overmoulding fusion bonding has been the subject of numerous studies (see for instance Candal et al. [16]). Nevertheless, most studies deals with hard-soft combination, and soft-soft combination seems not be very explored. Even though mechanical models and experimental tests are reported in the literature, they reach their limits in the case of soft-soft combination, and new experimental studies are required to enhance the knowledge of deformation processes in the vicinity of the interface.

In the present section, the coupling method described in Section 3.1 is used to study the thermomechanical behavior of soft-soft combinations of overmoulded TPV. This study has been made in collaboration with Cooper Standard, who provided the specimens, in the framework of the PhD thesis of Pierre Le Mouellic, who made the specimens and mainly contributed to the analysis dealig with the physical mechanisms involved in the behavior of the specimens.

3.3.2 Experimental setup

3.3.2.1 Materials

The materials considered here are two thermoplastic elastomers called TPV1 and TPV2. TPV1 is an injection molding grade while TPV2 is an extrusion grade. These profiles were inserted in a specific mold, which is presented in Figure 3.55, and were overmolded. Two melt temperatures are tested for TPV1, 190 °C and 260 °C.

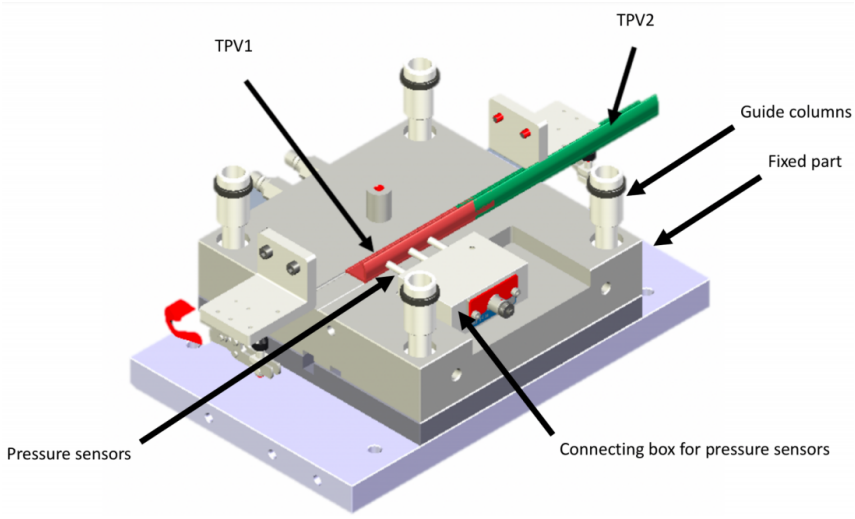

Figure 3.55 – Overmolding mold (Provided by Pierre Le Mouellic)

Once the overmolding was performed, rectangular bi-materials specimens were cut out from the overmolded parts. As shown in Figure 3.56, their dimensions were 75 mm long, 15 mm wide and 2 mm thick. Fused deposition modeling printed rolls of 6 mm were glued to the ends of the specimens in order to prevent any slipping between the specimens and the jaws, which shape has been designed accordingly.

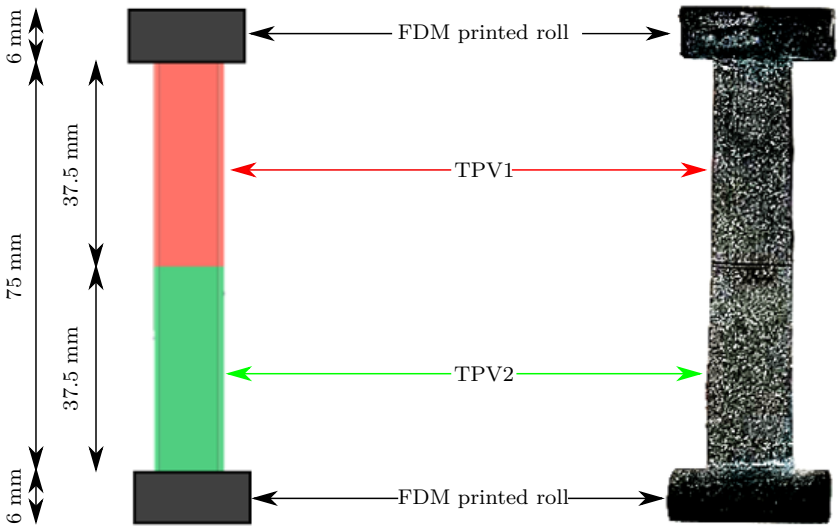

Figure 3.56 – Specimen used

3.3.2.2 Mechanical test

Figure 3.57 gives an overview of the experimental setup. It is composed of an optical and an infrared cameras on both sides of a home-made biaxial testing machine. The tensile machine used is composed of four independent actuators driven by an in-house LabVIEW program. This machine enables us to stretch symmetrically the specimens. In the present case, the specimens are mounted in the vertical direction.

Two types of loading were applied. The first one corresponds to a monotonous tensile test until specimen failure at a loading rate of 36 mm/min per actuator. The second one corresponds to a cycle loading at the same loading rate. Since the displacement at failure strongly differs from the two different overmolding temperatures, 4.3 mm per actuator for the specimen overmolded at 190 °C and 22 mm per actuator for the specimen overmolded

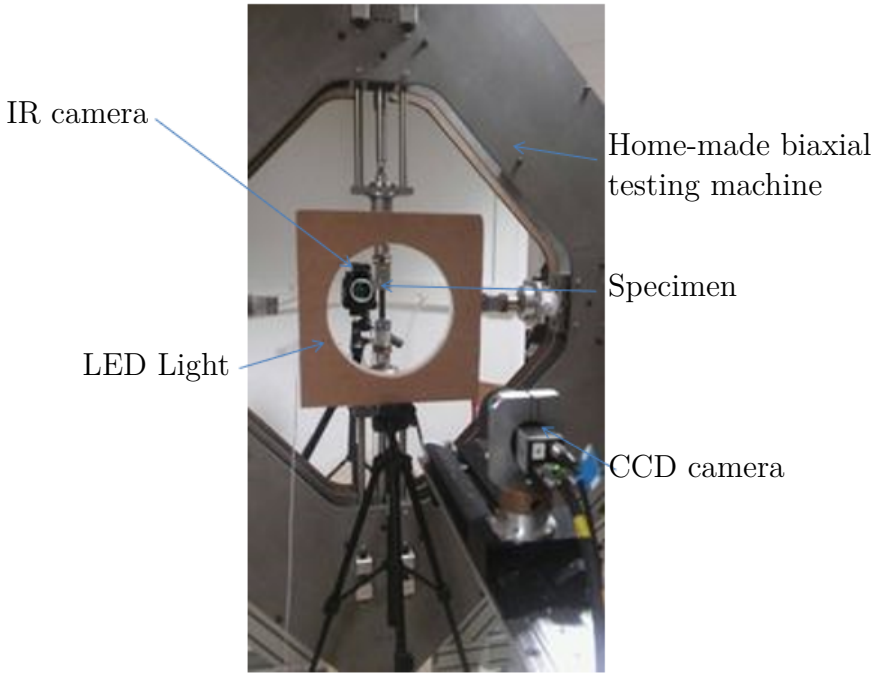

Figure 3.57 – Overview of the experimental setup

at 260 °C, the maximal displacement imposed for the mechanical cycle will differ with the specimen.

Images of the specimen surface were stored at a frame rate equal to 10 Hz with a IDS camera equipped with a 55 mm telecentric objective. The charge-coupled device (CCD) of the camera has 1920×1200 joined pixels. The displacement field at the specimen surface was determined by using the DIC technique, using the 7D software. Data for the image acquisition and the DIC analysis are summarized in Table 3.1 and Table 3.2.

Full temperature measurements were performed by using a FLIR IR camera, which detectors operating in wavelengths between 1.5 and 5.1 µm, equipped with a focal plane array of 640×512 pixels. The integration time was equal to 2700 µs and the acquisition frequency was equal to 50 Hz. The calibration of camera detectors was performed with a black body using a one-point Non-Uniformity Correction (NUC) procedure at this acquisition frequency. The thermal resolution or noise equivalent temperature difference (NETD) is equal to 20 mK for a temperature range between 5 and 40 °C. The spatial resolution of the thermal field was equal to 300 µm/px. The IR camera is switched on several hours before testing in order to ensure its internal temperature to be stabilized.

DIC Hardware parameters	**Detail**
Camera	IDS UI-3160CP Rev. 2
Image Resolution	1920 x 1200 pixels^2
Lens	55 mm C-mount partially telecentric. Constant magnification over a range of working distances ±12.5 mm of object movement before 1% error image scale occurs
Field-of-View	186.8×116.8 mm^2
Image Scale	10 pixels/mm
Stand-off Distance	1500 mm
Image Acquisition Rate	10 Hz
Patterning Technique	White spray on black specimen
Pattern Feature Size (approximation)	6 pixels

Table 3.1 – DIC Hardware parameters.

DIC Analysis parameters	**Detail**
DIC Software	7D©
Image Filtering	None
Subset Size	8 pixels/ 0.78 mm
Step Size	4 pixels/0.39 mm
Subset Shape Function	Affine
Matching Criterion	Zero-Mean Normalized Cross Correlation
Interpolant	Bi-cubic
Strain Window	5 data points
Virtual Strain Gauge Size	24 pixels/ 2.34 mm
Strain Formulation	Principal Maximal
Post-Filtering of Strains	None
Displacement Noise-Floor	0.011 pixels/ 10.7 µm
Strain Noise-Floor	0.0023

Table 3.2 – DIC Software parameters.

The infrared camera was triggered at the same frequency as the optical camera, i.e. 10 Hz. The emissivity of the material was set at 0.94. Due to large deformation undergone by the material, the material points observed by the IR camera move from pixel to pixel. The temperature variation at a given material point is obtained by using the methodology described in Section 3.1.

3.3.3 Results

3.3.3.1 Global mechanical behavior

Figure 3.58 presents the mechanical behavior during a monotonic tensile test until rupture of the specimens overmoulded at 190 °C and 260 °C. Figures 3.59 and 3.60 present the images of the specimens overmoulded at 190 °C and 260 °C at different times of the test, respectively. These times correspond to letters a to h and a to j for 190 °C and 260 °C, respectively. At the beginning of the test, the shape of the curves is close. The force-displacement relationship is almost linear. For higher displacement levels, the specimens overmoulded at 260 °C exhibits a higher stiffness. Moreover, the displacement at break is much lower for the specimens overmoulded at 190 °C (8 mm against 45 mm for the specimens overmoulded at 260 °C). For both overmoulding temperatures, specimen failure occurred at the interface. The failure was also adhesive, located at the interface, but occurs at a lower force in the case of samples overmoulded at 190 °C than for specimens overmoulded at 260 °C. For samples overmoulded at 260 °C, a striction at the interface during the test is noticeable (Figure 3.60, (h)). This phenomenon is not observed for those overmoulded at 190 °C. High relative deformations are reached for TPV2, while TPV1 shows low deformations. These remarks will be discussed in more details in the section dealing with the deformation field.

Figures 3.61 and 3.62 show the mechanical response in terms of force versus displacement during the mechanical cycle at a total displacement of 8 mm for the 190 °C overmoulded specimen and 25 mm for the 260 °C overmoulded specimen. For specimens overmoulded at 260 °C, a striction can be seen for TPV1 (Figure 3.60 (e)), but not on TPV2. This striction cannot be seen for specimens overmoulded at 190 °C. This has already been observed in the case of monotonous displacement test until failure (Figure 3.60, (h)). This aspect will be more precisely detailled. The load levels obtained for mechanical cycle are similar to the one obtained previously (Figure 3.58). The mechanical response exhibits a hysteresis for both specimens. This hysteresis loop can be associated with viscosity and/or damage. In the case of 190 °C overmolded specimens, the residal strain is 1.67 % against 5 % for the 260 °C.

The low residual strain obtained after relatively high strains applied shows that this is in good agreement with what can be found in Babu [4], who used the TPV deformation model developed by Soliman, Van Dijk, and Van Es [98] to explain the behavior of thermoplastic elastomers vulcanized. This model explains that the deformation behavior of

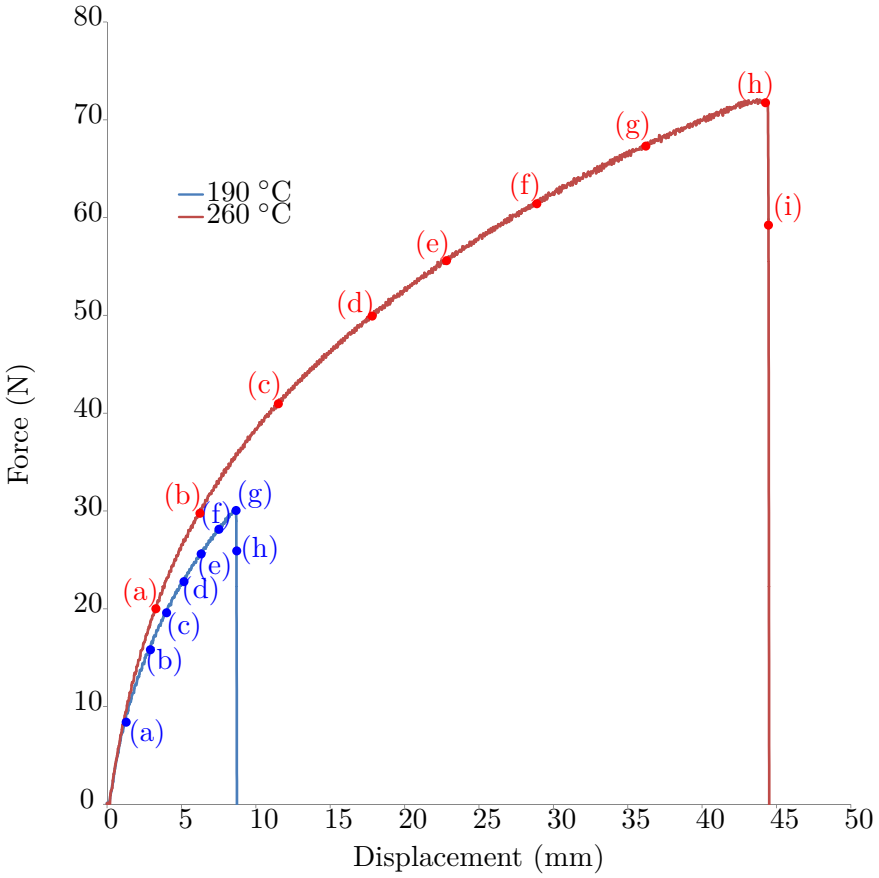

Figure 3.58 – Force-displacement evolution for each TPV, monotonic tensile test until rupture, overmoulded at 190 °C and 260 °C

TPV is the combination of matrix yielding and buckling of PP because of the recovering tendency of the cross linked EPDM particles (Figure 3.63). When stretching, the TPV matrix is acting as a glue between the EPDM particles, and the PP part in the perpendicular direction of loading yields. Then, during the recovery, the yielded PP is pushed back because of the recovery nature of EPDM. The mechanical response obtained was that of specimen made of two different TPV. It could be useful to be able to distinguish their response during the test. This is the reason why the following focus on the response of each TPV, using quantitative image techniques.

3.3.3.2 Full kinematic field measurements

The DIC technique enabled us to determine the kinematic field in each TPV. Figure 3.64 presents the stretch versus time for both injection temperatures and for monotonic tensile test until rupture. Figure 3.65 presents the stretch versus time for both injection

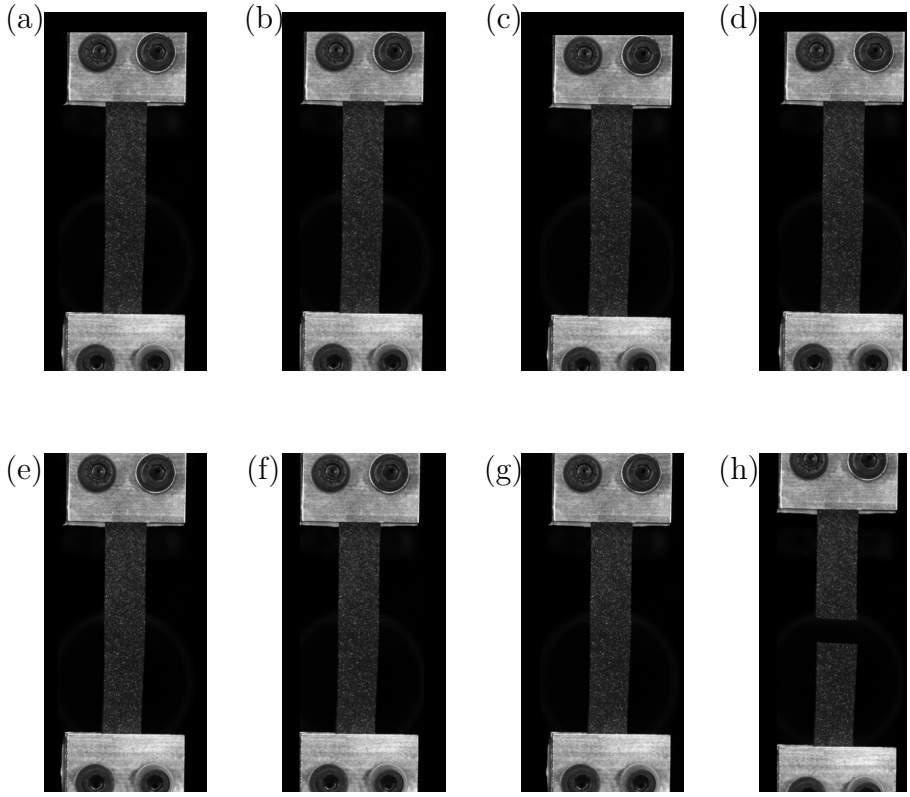

Figure 3.59 – Pictures related to Figure 3.58, specimens overmoulded at 190 °C

temperatures and for mechanical cycle test. From these two figures, it should be noted that TPV2 is much softer than TPV1. Therefore, the whole specimen is not submitted to a homogeneous loading and consequently, the interface cannot be considered as a crack in a homogeneous medium, meaning that it is complicated to apply the existing models of fracture mechanics of interfaces [13, 27, 28] in this case.

3.3.3.3 Full temperature field measurement

Measuring the thermal response associated with the mechanical response of materials provides very complementary information on the origin of elasticity (i.e. couplings between temperature and deformation), as well as on dissipative effects. Furthermore, the measurements can be processed using the heat diffusion equation in order to determine the heat source fields, which is equivalent to a surface calorimetry approach. Figure 3.66 shows the thermal response measured at the surface of the two TPV in specimen 190 °C for the tensile test at failure. It is observed that the temperature variation first decreases in the two materials. As the laboratory temperature is stabilized, the only explanation

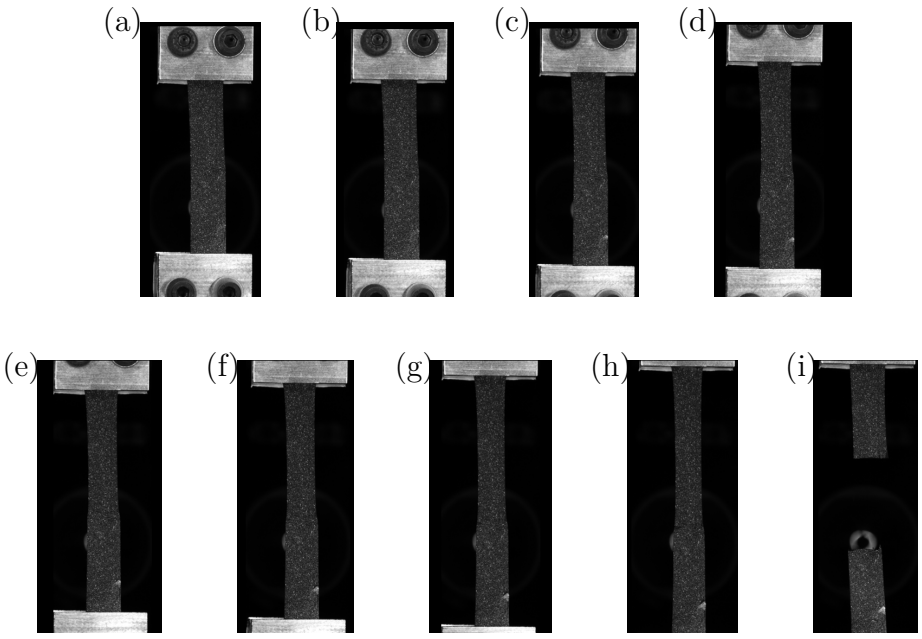

Figure 3.60 – Pictures related to Figure 3.58, specimens overmoulded at 260 °C

is that the isentropic coupling dominates the thermal response. Furthermore, in view of the very small temperature variations measured, the intrinsic dissipation caused by the viscosity is very low, even negligible. From a certain strain level, the curve slopes decrease and is inverted in the case of TPV2 for stretch equal to 1.05. Such a temperature evolution is in a strong analogy with what is observed in elastomers and is generally interpreted as a thermoelastic inversion [50]. In addition, it is possible that the level of intrinsic dissipation due to viscosity also increases. Figure 3.68 shows the response obtained with the 260 °C sample. Overall, we find the same trends as for the specimen 190 °C. Indeed, when zooming in on the first part of the curves, i.e. at the lowest strains, the orders of magnitude of temperature variation are the same. It should be noted that this increase in temperature can also be induced by a greater viscosity of the materials and therefore a greater intrinsic dissipation. As the interface is more resistant at 260 °C, the level of deformation reached in both materials is greater. This leads to one order of magnitude greater temperature variation in TPV1 between the 190 °C and 260 °C specimen. This issue will be addressed in more details during the analysis of the cyclic tests and the associated calorimetric response.

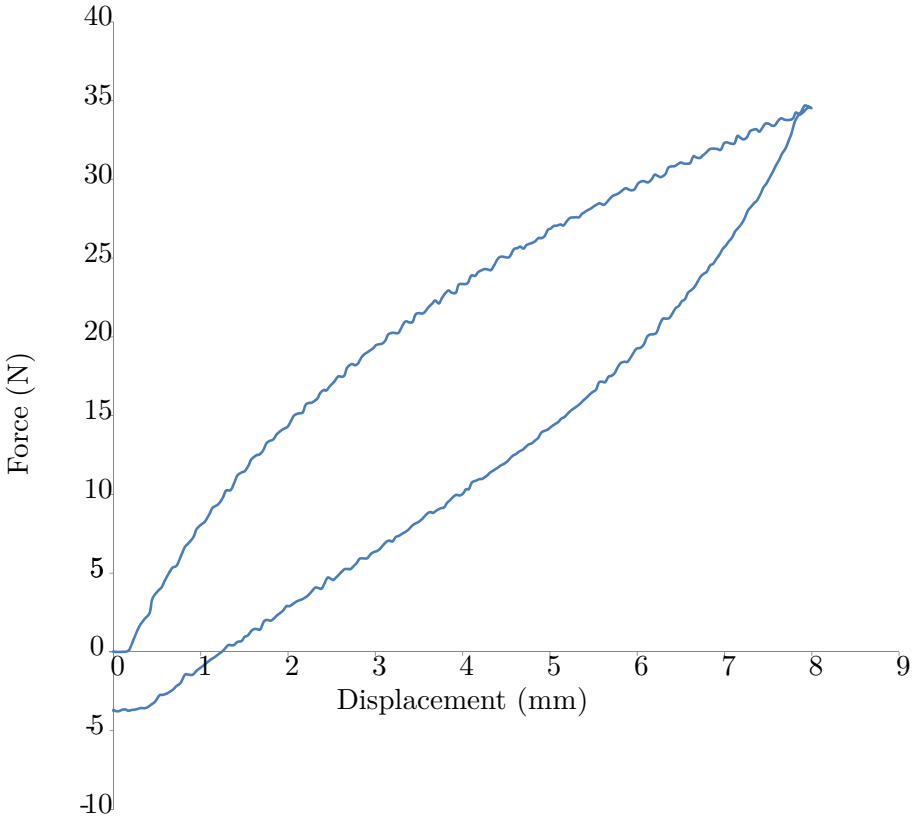

Figure 3.61 – Cyclic loading of 8 mm for specimen overmoulded at 190 °C

The analysis of the average temperature variation during the test in each of the two materials far from the interface, i.e. without thermal gradients induced by the stress and strain concentrations of the interface, enabled us showing that the elasticity of the TPVs constituting the specimen is both entropic and isentropic. A competition between the two type of elastic couplings occurs at the low strains. The isentropic coupling is first preponderant, then the entropic coupling takes over. Nevertheless, this analysis does not allow the study of the mechanical behavior and the effects of the interface in the different materials to be further investigated. This is the reason why Figure 3.67 and 3.69 show the temperature variation fields and the temperature variation profiles along the specimens at 190 °C and 260 °C, respectively. Note that these profiles were determined by averaging the temperature variations across the width. The temperature profiles along the specimen's length show a different thermal response for the two TPV as detailed previously, for the smallest and moderate strains (t = 2, 4 and 6s for specimen at 190 °C, and t=2.5, 15 and 30s for specimen at 260 °C), the thermal response is different from one TPV to another, but it is homogeneous in each TPV. The interface does not have a specific thermal

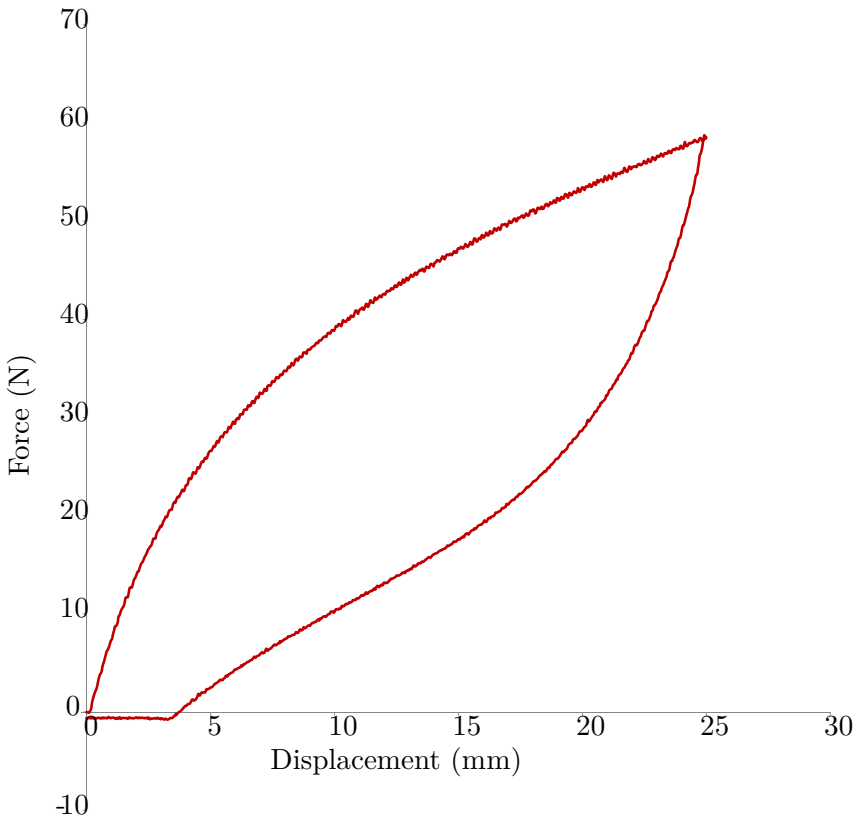

Figure 3.62 – Cyclic loading of 25 mm for specimen overmoulded at 260 °C

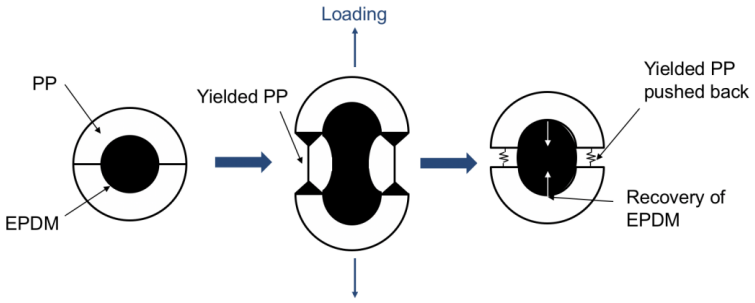

Figure 3.63 – Deformation mechanism of TPV [28]

signature. Nevertheless, for the highest strains, i.e. close to those at failure, the interface zone exhibits a strong singularity corresponding to a high heat production. Therefore, the strong increase in temperature can be seen as occurence of damage and a precursor of the interface failure. It should be noted that the influence zone of the interface is larger in TPV2 in specimen at 190 °C, approximatively 15 mm, while it is small in the case of specimen at 26 °C.

Figures 3.70 and 3.71 show the thermal response of the overmoulded specimens at

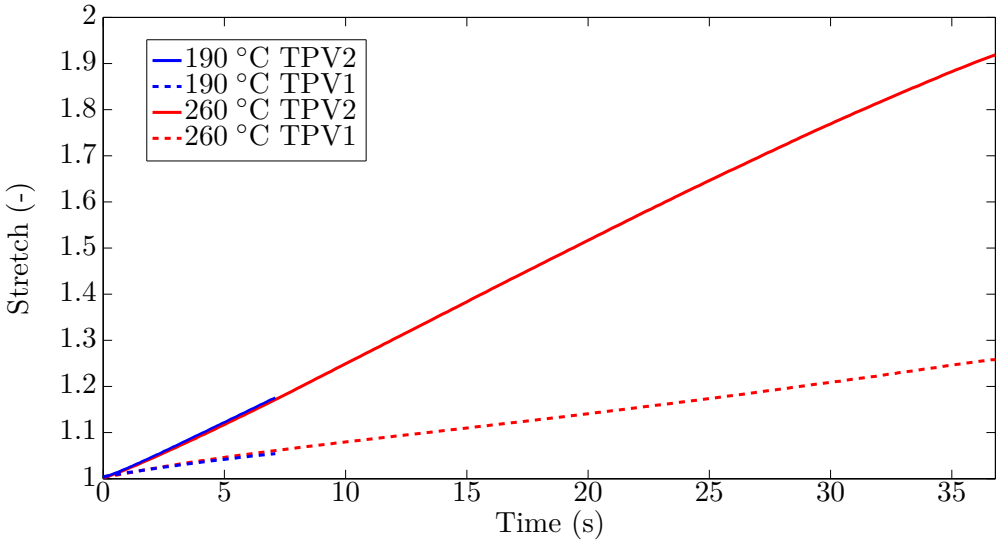

Figure 3.64 – Stretch-time evolution for each TPV, monotonic tensile test until rupture, overmoulded at 190 °C and 260 °C

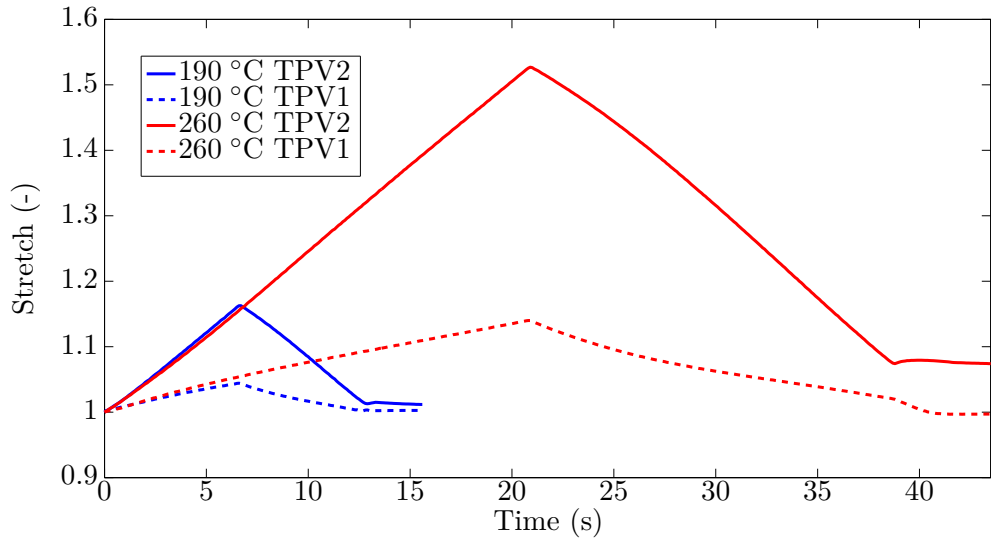

Figure 3.65 – Stretch-time evolution for each TPV, mechanical cycle, overmoulded at 190 °C and 260 °C

190 °C and 260 °C respectively for the mechanical cycle. The thermoelastic inversion for TPV2 is observed for both overmoulding temperatures during the loading phase. For the 190 °C overmoulded specimens, the TPVs temperature is increasing during the unloading phase reflecting intrinsic dissipations. For the 260 °C overmoulded specimens the temperature of TPV1 is increasing. Temperature is decreasing for TPV2, meaning that the calorific effect of viscosity decreases.

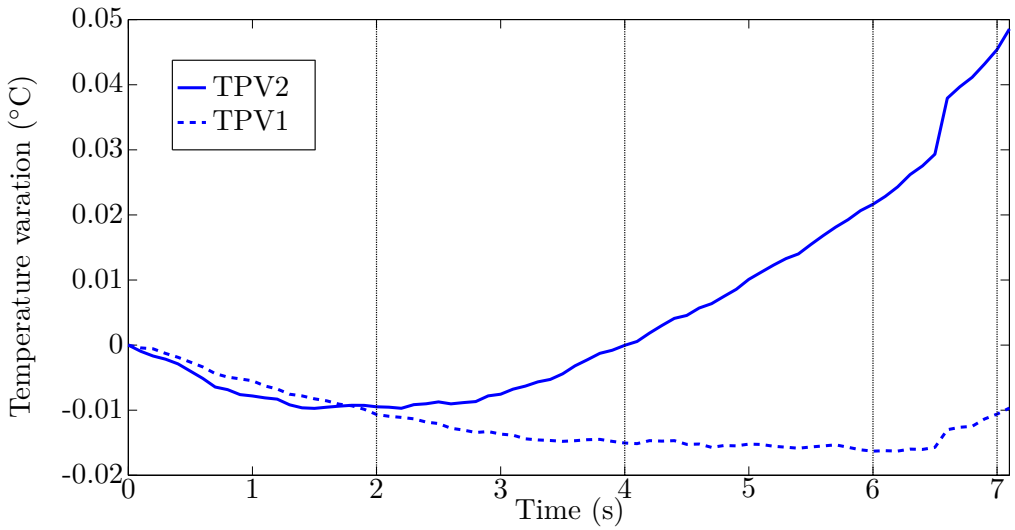

Figure 3.66 – Temperature change with stretch for specimen overmoulded at 190 °C, monotonic tensile test until rupture

3.3.4 Conclusion

This work presents the first thermomechanical study of an assembly of two thermoplastic elastomers by overmolding. A singular interface behavior can be observed due to the large difference of the two materials mechanical properties. This study highlights the difficulty to applied model of fracture in this type of parts, since they often deals with either a crack propagating in an homogeneous loading or fracture at a soft-hard interface. In addition, the influence of the overmoulding temperature have been studied. It was shown that the increase of the overmoulding temperature leads to a more resistant junction of the two elastomers. These information could be used in future work to implement models of the thermomechanical behavior of soft-soft overmolded junctions.

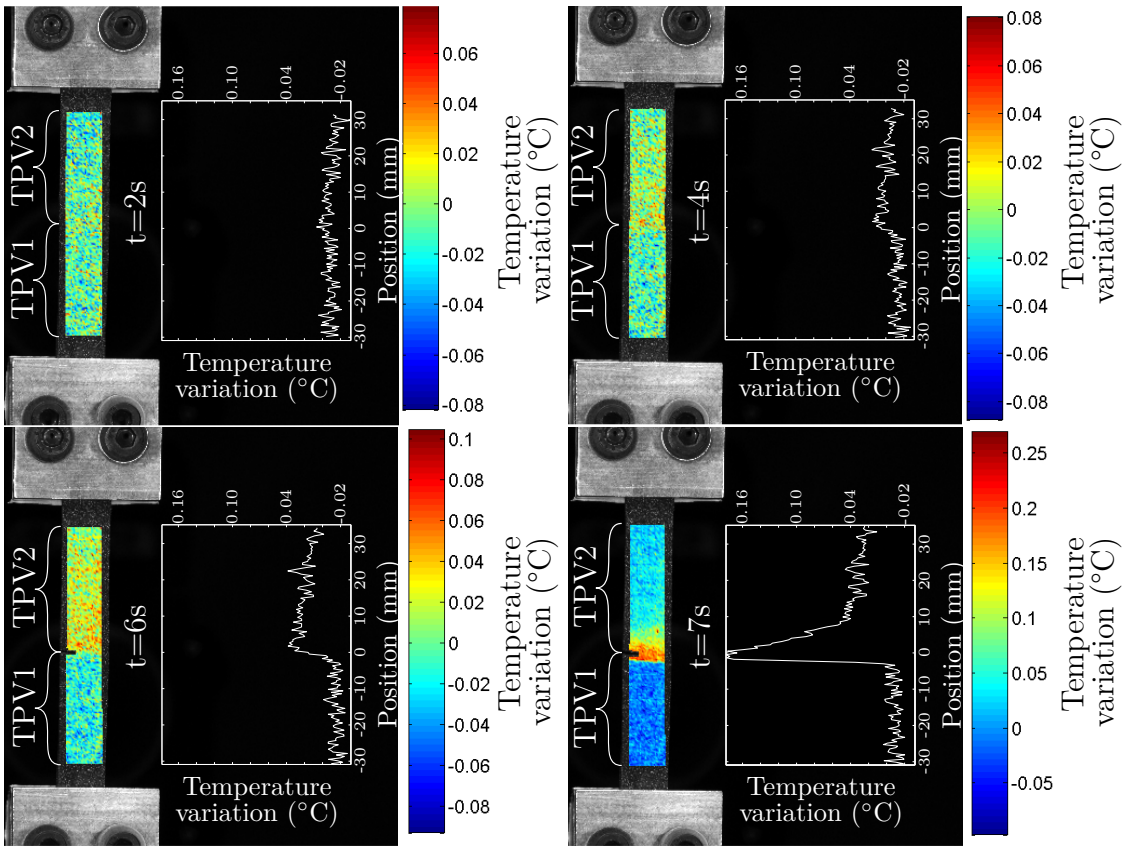

Figure 3.67 – Temperature variation fields and the temperature variation profiles along the specimen overmoulded at 190 °C

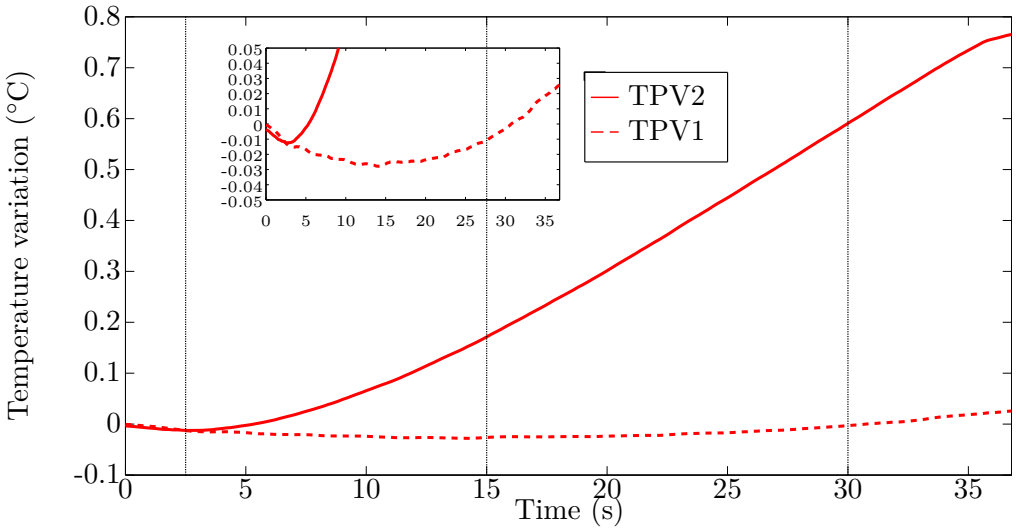

Figure 3.68 – Temperature change with stretch for specimen overmoulded at 260 °C, monotonic tensile test until rupture

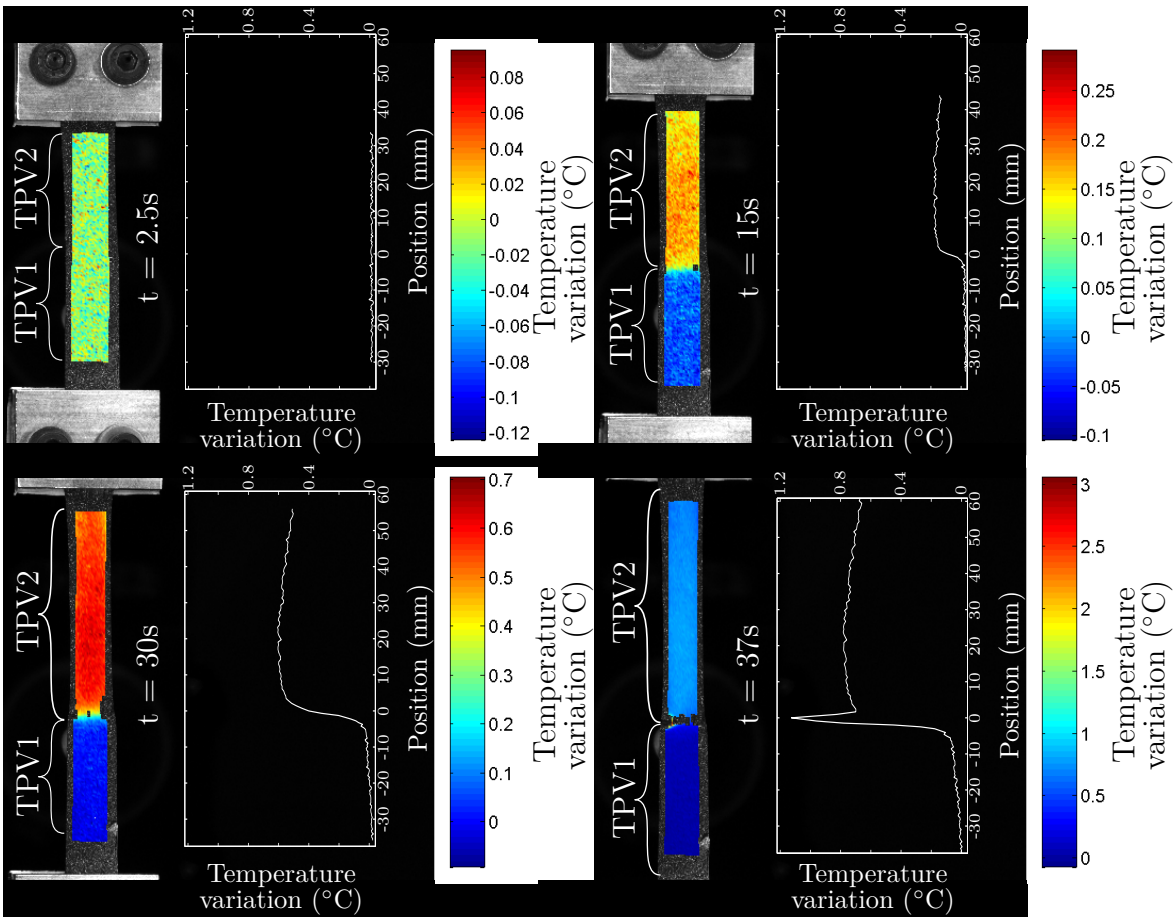

Figure 3.69 – Temperature variation fields and the temperature variation profiles along the specimen overmoulded at 260 °C

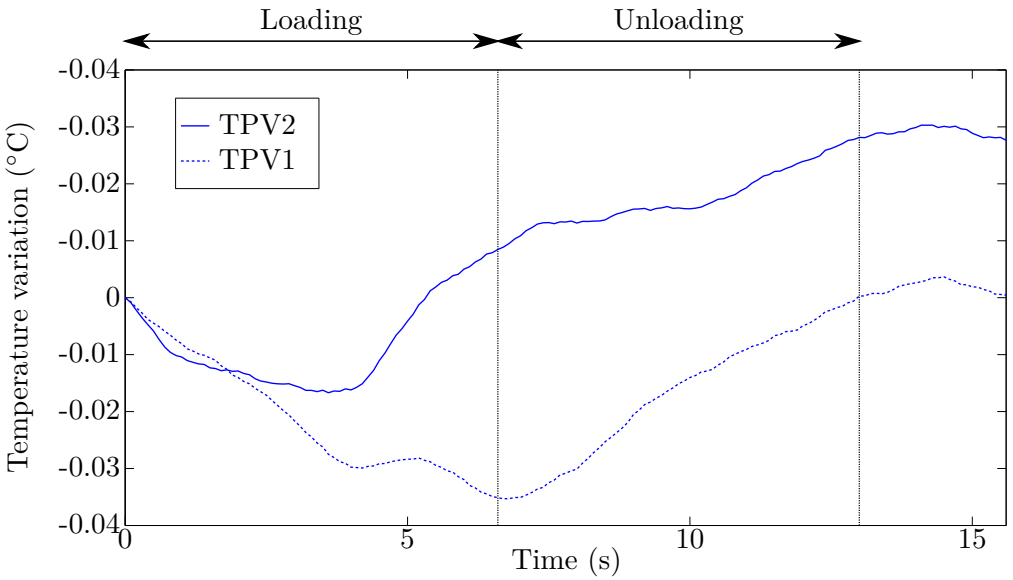

Figure 3.70 – Temperature change with time for specimen overmoulded at 190 °C, monotonic tensile test until rupture

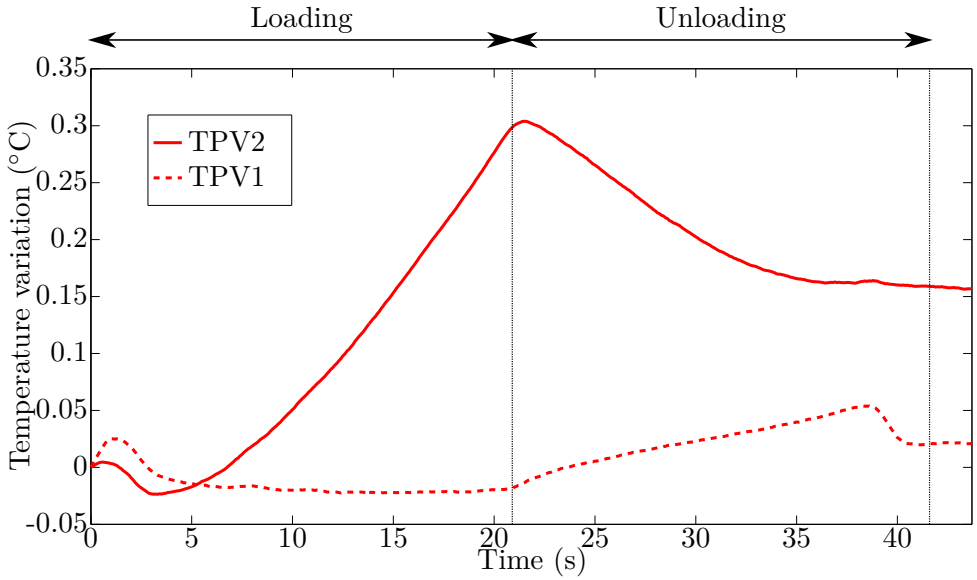

Figure 3.71 – Temperature change with time for specimen overmoulded at 260 °C, monotonic tensile test until rupture

Chapter 4

Evaluation of strain-induced crystallization field under large heterogeneous deformation states

Contents

4.1 Introduction

In Chapter 2, a method for evaluating the crystallinity from surface calorimetry has been presented and validated. It has been shown that the crystallinity values are in a very good agreement with those obtained with the XRD technique. While the XRD does not only give the crystallinity level but also information about crystallites size and orientation, the method can only give the information at a single X-ray spot. This limitation can induce issues of importance in case of crystallinity heterogeneity, such as at a crack tip [92]. Typically, in case of heterogeneous crystallinity fields, a scan has to be performed. This means that the crystallinity is not determined at the same time from one point to another in the field.

In Chapter 3, a methodology to performed coupled calorimetric and kinematic field measurement have been presented, based on infrared thermography and the digital image correlation. This method has been applied to large heterogeneous deformations.

In the present chapter, the calorimetric method to measure the crystallinity will be used with the coupling methodology, in order to measure full crystallinity field in a case presenting high heterogeneous deformation state, which is induced at a crack tip. This study is all the more relevant since the SIC phenomenon is often evoked to explain the high crack growth resistance of NR.

4.2 Experimental setup

4.2.1 Material and specimen geometry

In the present study, an unfilled natural rubber is used. This material is the 0NR1.2, provided by the Michelin company, which has been used in Section 2.3. The specimen geometry is shown in Figure 4.1. It is a pure shear specimen, on which a crack has been made using a razor blade.

4.2.2 Loading condition

Figure 3.38 presents an overview of the experimental setup used for this study. It is composed of a CCD camera to measure the kinematic field at the specimen surface and an infrared camera to measure the thermal field at the specimen surface, on both sides of a home-made biaxial testing machine. This machine is composed of four independent

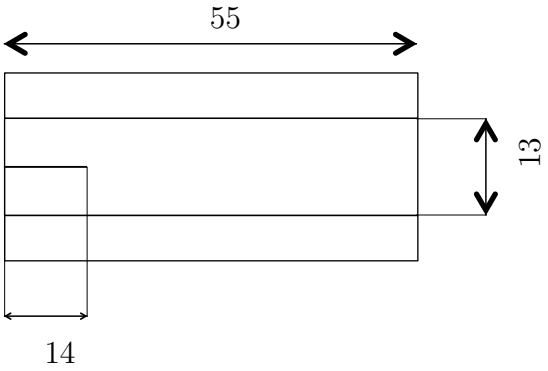

Figure 4.1 – Specimen geometry used

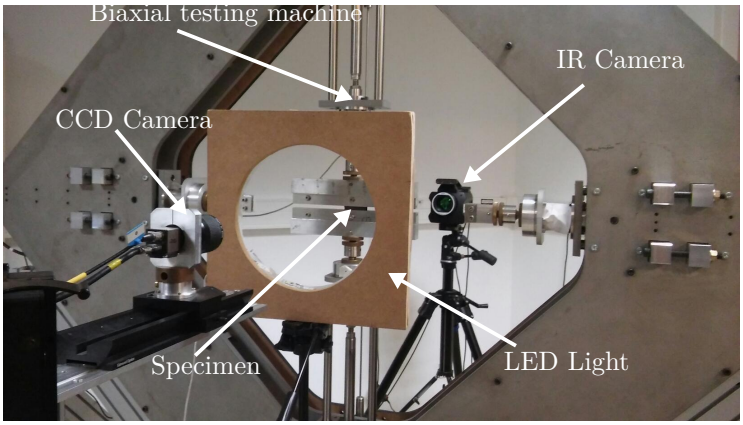

Figure 4.2 – Experimental Setup

RCP4-RA6C-I-56P-4-300-P3-M (IAI) electrical actuators. They are driven by a CON-CA-56P-I-PLP-2-0 controller and four PCON-CA (IAI) position controllers. An in-house LabVIEW program piloted these actuators.

In the present study, a single equibiaxial loading is carried out. Each independent actuator is controlled in the same way. In this case, the specimen center is motionless. The displacement and loading rate are set at 10 mm and 100 mm/min respectively for each actuator.

Temperature measurements are performed by using a FLIR infrared camera equipped with a focal plane array of 640x512 pixels and detectors operating in wavelengths between 1.5 and 5.1 µm. The integration time is equal to 2700 µs and the acquisition frequency is equal to 25 Hz. The calibration of camera detectors is performed with a black body using an one-point NUC procedure at this acquisition frequency. The thermal resolution, or noise equivalent temperature difference (NETD), is equal to 20 mK for a temperature range

between 5 and 40 °C. The spatial resolution of the thermal field is equal to 50 µm/px. The infrared camera is switched on several hours before the test in order to stabilize its internal temperature. Both cameras are trigged at the same frequency of 20 Hz, to measure kinematic and thermal fields at the same time. The emissivity of the material is set to 0.94 in the present study.

Images are stored with an IDS camera equipped with a 55-mm telecentric objective. The resolution of the camera is 1920x1200 pixels, with a spatial resolution of approximately 13 µm/px. For this study, DIC is performed using the 7D software developed by P. Vacher [115]. The grid step, i.e. the distance between two independent ZOI, is set to 4 pixels and the subset size to 10 pixels.

4.3 Results

4.3.1 Application of the coupling methodology

First, the coupling methodology has been applied, in order to measure the calorimetric and kinematic fields at the same point. Figure 4.3 represents the kinematic field. As expected, the stretch is highly heterogeneous, with a strong concentration near the crack tip. The strain state is in good agreement with measurements made in other studies (see for instance Martinez et al. [72]).

The heat source field, presented in Figure 4.4, is also evaluated. A heat source concentration is observed near the crack tip. It is in accordance with other studies presenting heat source field around a crack tip in rubber-like material [71, 85]. It can be explained by the fact that it is the most stretched area, thermoelastic coupling is higher than in other areas. Moreover, since the material is more stretched, this area should be more crystallized, as presented by Rublon et al. [92].

4.3.2 Application of the calorimetric method

Once the heat source field is obtained during the test, the calorimetric method to measure the crystallinity field can be performed. The first step is to identify the heat source before the crystallization starts. For confidential reasons, the results are not presented here.

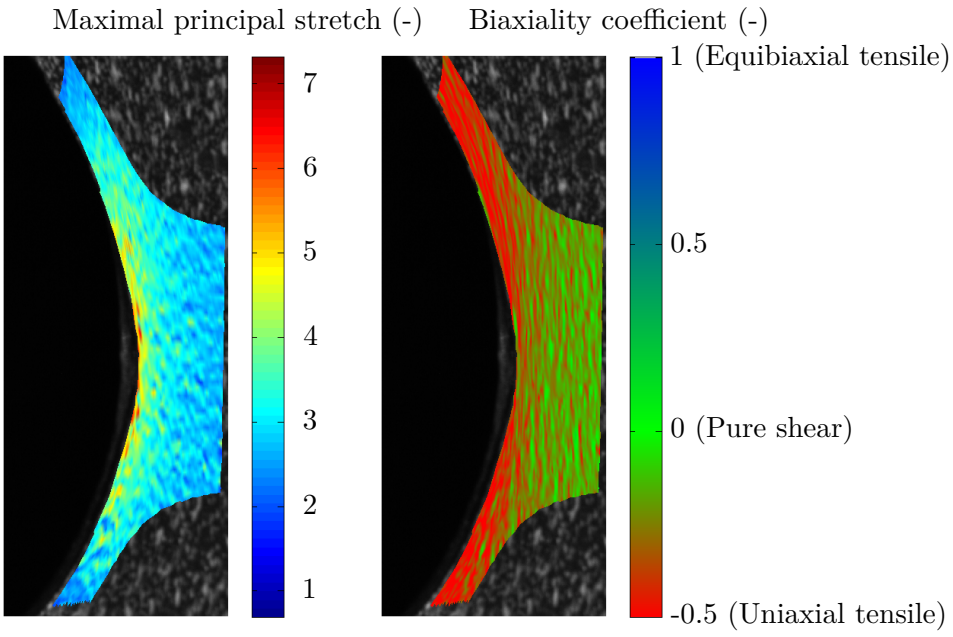

(a) Maximal principal stretch field (b) Strain state from the biaxiality cefficient field

Figure 4.3 – Kinematic fields measured near a crack tip at the maximal displacement imposed

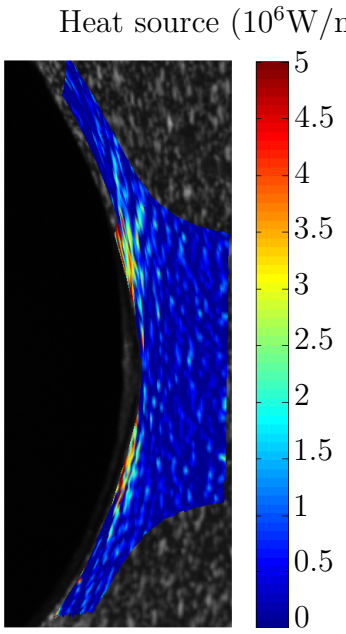

Figure 4.4 – Calorific field measured near a crack tip at the maximal displacement imposed

Conclusion and perspectives

The present work is in the general framework of the thermomechanical and calorimetric characterization of materials under large deformations. This topic has been the subject of various studies in recent years, since purely mechanical analyses have reached their limits. The advent of quantitative imaging techniques, both in the visible and in the infrared domain, gives access to both kinematics and thermal fields at a specimen surface. The aim of this work is to provide tools for coupling kinematic and thermal field measurement techniques in the case of large deformations. The aim is to apply such a technique to provide new information on the deformation precesses in rubbery materials, especially the SIC.

Chapter 1 gives the state of art on rubber-like materials and on calorimetric studies of materials behavior. In this chapter, it s shown that very few studies on surface calorimetry applied to large deformations has been reported in the literature. Moreover, in the only three studies found, the metrological performances of the methods used have not been characterized. Pottier et al. [85] detailed the necessity to both use a motion compensation technique and take into account the non-uniformity on IR images, but accuracy of the heat source field obtained has not been discussed. Links between the heat production and the different mechanisms that occur during the mechanical deformation of the material have been evoked by Toussaint et al. [108], but they have not being quantified or further discussed. Also, no energy balance has been performed. This state of the art clearly highlights that calorimetry under large deformations is underexplored for characterizing deformation mechanisms of rubbery material while it can provide information of paramount importance on the thermomechanical behavior of the material and subsequently on their modeling and that metrological aspects have to be further investigated. These two issues have motivated the present PhD thesis.

Chapter 2 illustrates the calorimetry under large deformation technique in 0D, assuming a homogeneous heat source field. Section 2.1 presents the first comparative study between the X-ray diffraction and the calorimetric method to measure the strain-induced crystallization of a unfilled natural rubber in uniaxial tensile. Results demonstrate that both methods give equivalent results, which confirms that the crystallinity can be accu-

rately quantified using the calorimetric method. In Section 2.2 the technique is applied to a filled natural rubber, both in uniaxial and biaxial tensile. Several results have been highlighted in this study. First, even under a high biaxiality coefficient, the crystallization still occurs, which confirms the results obtained by Beurrot, Huneau, and Verron [6]. Moreover, the multiaxiality seems to affect the crystallization, by reducing the stretch of the crystallization onset. Last, it was shown with energy balances performed that the hysteresis loop in the stress-strain relationship is mainly due to energy stored elastically within the material. These information of importance have provided information of importance that enables our academic partner at University of Aachen to propose a new SIC model for NR [52]. In Section 2.3, the 0D technique is extended to 1D to investigate heterogeneities of SIC taking place under a homogeneous loading, here the uniaxial tension. The motion compensation of the points tracked in the IR images are directly performed in the IR images, along a profile. The DIC technique is not used at this stage. The results obtained clearly highlight heterogeneities, whose causes require further investigations. This is the first observation of this effect, as it can not be evidenced by the X-ray diffraction technique while it is only applied at on point in the case of homogeneous loadings.

Chapter 3 extends the methodology to obtain a 2D heat source field, by coupling the DIC technique and the IR thermography. Section 3.1 described the coupling methodology. A metrological study has been carried out, in order to evaluate the performance and limitations of the method. In Section 3.2, the coupling methodology is used to identify the constitutive parameter of the Neo-Hookean model at the local scale. Section 3.3 presents the thermomechanical study of an assembly of two thermoplastics elastomers obtained by overmolding. This work shows the singular mechanical behavior close to the interface, and highlights the difficulty in modeling the fracture mechanics of soft-soft interface, as well as the interest in studying the thermomechanical behavior at a local scale.

Chapter 4 combined the 2D calorimetric technique with the methodology for the determination of the crystallinity developped in Chapter 2. Even though the results presented are exploratory ones, they clearly show that th technique enables use to characterize the calorimetric response of the zone in the crack tip vicinity and to evaluate the crystallinity field. Further, it enables us to perform energy balances in order to evaluate the intrinsic dissipation field. Finally, this works constitutes a basis for developing an Eulerian characterization of the heat source field.

This work opens a wide range of perspectives, since many mechanisms not well un-

derstood involved in highly deformable materials such as rubber, are either exothermal or endothermal. The complete thermomechanical analysis of these materials should bring fruitful information for a better comprehension of these phenomena. For instance, the viscosity and Mullins effect could be studied in the case of heterogeneous strain states, since both of them have a calorimetric signature.

Some improvement could be made on the coupling methodology. In the current state, the coupling method is performed using 2D DIC, which does not allow an access to the out-of-plane displacement. This lack of information requires to make an assumption on the out-of-plane stretch, typically the incompressibility of the material for rubber-like material. This issue could be bypassed using 2 or more CCD cameras and 3D DIC, which allows the measurement of the 3D displacement of the specimen surface. In the same way, an additional work should be done on the sensitivity of the temperature measurement to the surface inclination.

Last, the heat source due to conduction term is still very noise-sensitive, and neither the oversampling nor averaging operation gives satisfying outcomes, especially when the thermal pattern is relatively small in regards with the spatial resolution of the two cameras. Studies to find better strategies that make the operation less noise-sensitive, without reducing the signal could help having a better accuracy in the thermal conduction measurement, and by extension in the heat source produced by the specimen.

Reference

[1] P.-A. Albouy, J. Marchal, and J. Rault, « Chain orientation in natural rubber, Part I: The inverse yielding effect », *in*: *The European Physical Journal E* 17.*3* (2005), pp. 247–259.

[2] L. E. Alexander, S. Ohlberg, and G. R. Taylor, « X-Ray Diffraction Studies of Crystallization in Elastomers », *in*: *Journal of Applied Physics* 26.*9* (1955), pp. 1068–1074.

[3] R. L. Anthony, R. H. Caston, and E. Guth, « Equations of state for naturals and synthetic rubber like materials: unaccelerated natural soft rubber », *in*: *Journal of Physical Chemistry* 46 (1942), p. 826.

[4] K. Babu R. R.and Naskar, « Recent developments on thermoplastic elastomers by dynamic vulcanization », *in*: *Advanced Rubber Composites* (2010), pp. 219–247.

[5] N. Bekkedahl and L. A. Wood, « Crystallization of vulcanized rubber », *in*: *Industrial & Engineering Chemistry* 33.*3* (1941), pp. 381–384.

[6] S. Beurrot, B. Huneau, and E. Verron, « Strain-induced crystallization of natural rubber subjected to biaxial loading conditions as revealed by X-ray diffraction », *in*: *Jerrams, S. et Murphy, N., éditeurs: Constitutive Models for Rubber* 7 (2011), pp. 23–28.

[7] S. Beurrot-Borgarino, « Cristallisation sous contrainte du caoutchouc naturel en fatigue et sous sollicitation multiaxiale », PhD thesis, Ecole Centrale de Nantes (ECN), 2012.

[8] V.L. Biderman, « Calculation of rubber parts », *in*: *Rascheti na prochnost* 40 (1958).

[9] L. Bodelot et al., « Experimental setup for fully coupled kinematic and thermal measurements at the microstructure scale of an AISI 316L steel », *in*: *Materials Science and Engineering A-Structural Materials properties microstructure and Processing* 501 (2009), pp. 52–60.

[10] C.-G. Boissonnas, « Specific Heat of Strained Rubber », *in*: *Industrial & Engineering Chemistry* 31.*6* (1939), pp. 761–762.

[11] H. Bouasse and Z. Carrière, « Sur les courbes de traction du caoutchouc vulcanisé », *in*: *Annales de la Faculté des sciences de Toulouse: Mathématiques*, vol. 5, 1903, pp. 257–283.

[12] T. Boulanger et al., « Calorimetric analysis of dissipative and thermoelastic effects associated with the fatigue behavior of steels », *in*: *International journal of fatigue* 26.*3* (2004), pp. 221–229.

[13] H.R. Brown, « A molecular interpretation of the toughness of glassy polymers », *in*: *Macromolecules* 24.*10* (1991), pp. 2752–2756.

[14] K. Brüning, « In-situ Structure characterization of elastomers during deformation and fracture », PhD thesis, Technische Universität Dresden, Germany, 2014.

[15] C. W. Bunn, « Molecular structure and rubber-like elasticity I. The crystal structures of β gutta-percha, rubber and polychloroprene », *in*: *Proceedings of the Royal Society of London. Series A. Mathematical and Physical Sciences* 180.*980* (1942), pp. 40–66.

[16] M. V. Candal et al., « Study of the adhesion strength on overmoulded plastic materials using the essential work of interfacial fracture (EWIF) concept », *in*: *Journal of materials science* 43.*15* (2008), pp. 5052–5060.

[17] G. Chanclou, « Rupture de chaines polymères par oxydation controlée: application au recyclage des déchets élastomères », PhD thesis, Le Mans, 2000.

[18] S. Chang and Z. Li, « Single-reference-based solutions for two-point nonuniformity correction of infrared focal plane arrays », *in*: *Infrared Physics & Technology* (2019).

[19] Y.M. Chang, « An investigation into the factors affeting infrared temperature measurements for building applications », *in*: *Thermosense IX: Thermal Infrared Sensing for Diagnostics and Control* 780 (1987), pp. 11–18.

[20] S. Charlès and J.-B. Le Cam, « Inverse identification of constitutive parameters from heat source fields: A local approach applied to hyperelasticity », *in*: *Strain* 56.*2* (2020), e12334.

[21] X. Chen et al., « Frustrating Strain-Induced Crystallization of Natural Rubber with Biaxial Stretch », *in*: *ACS applied materials & interfaces* (2019).

[22] X. Chen et al., « Frustrating Strain-Induced Crystallization of Natural Rubber with Biaxial Stretch », *in*: *ACS Applied Materials & Interfaces* 11.*50* (2019), pp. 47535–47544.

[23] J.-M. Chenal et al., « Parameters governing strain induced crystallization in filled natural rubber », *in*: *Polymer* 48.*23* (2007), pp. 6893–6901.

[24] A. Chrysochoos, « Infrared thermography applied to the analysis of material behavior: a brief overview », *in*: *Quantitative InfraRed Thermography Journal* 9.*2* (2012), pp. 193–208.

[25] A. Chrysochoos et al., « Fields of stored energy associated with localized necking of steel », *in*: *J. of Mech. of Mater. and Struct.* 4 (2009), pp. 245–262.

[26] G. L. Clark et al., « Hysteresis in Crystallization of Stretched Vulcanized Rubber from X-Ray Data Correlation with Stress-Strain Behavior and Resilience », *in*: *Industrial & Engineering Chemistry* 32.*11* (1940), pp. 1474–1477.

[27] P.G. De Gennes, « Toughness of glassy polymers: a tentative scheme », *in*: *EPL (Europhysics Letters)* 15.*2* (1991), p. 191.

[28] D. S. Dugdale, « Yielding of steel sheets containing slits », *in*: *Journal of the Mechanics and Physics of Solids* 8.*2* (1960), pp. 100–104.

[29] D.J. Dunning and P.J. Pennells, « Effect of strain on rate of crystallization of natural rubber », *in*: *Rubber Chemistry and Technology* 40.*5* (1967), pp. 1381–1393.

[30] S.D. Gehman, « The Contribution of X-ray Research to the Knowledge of Rubber. », *in*: *Chemical Reviews* 26.*2* (1940), pp. 203–226.

[31] S.D. Gehman and J.E. Field, « An X-Ray Investigation of Crystallinity in Rubber », *in*: *Journal of Applied Physics* 10.*8* (1939), pp. 564–572.

[32] S.D. Gehman and J.E. Field, « X-ray structure of rubber-carbon black mixtures », *in*: *Industrial & Engineering Chemistry* 32.*10* (1940), pp. 1401–1407.

[33] A. N. Gent and A.G. Thomas, « Forms for the stored (strain) energy function for vulcanized rubber », *in*: *Journal of Polymer Science* 28.*118* (1958), pp. 625–628.

[34] A.N. Gent, « Crystallization and the relaxation of stress in stretched natural rubber vulcanizates », *in*: *Transactions of the Faraday Society* 50 (1954), pp. 521–533.

[35] A.N. Gent, « A new constitutive relation for rubber », *in*: *Rubber chemistry and technology* 69.*1* (1996), pp. 59–61.

[36] M. Giton, « Hyperelastic behaviour identification by forward problem resolution: Application to a tear test of a silicone-rubber », *in*: *Strain* 42.*4* (2006), pp. 291–298.

[37] J.M. Goppel and J.J. Arlman, « On the degree of crystallinity in natural rubber. 4. The degree of crystallization in frozen raw rubber and stretched vulcanized rubber », *in*: *Applied Scientific Research Section A-Mechanics Heat Chemical Engineering Mathematical Methods* 1.*5-6* (1949), pp. 462–474.

[38] D. Göritz and F.H. Müller, « Die kalorimetrische erfassung der dehnungskristallisation polymerer », *in*: *Kolloid-Zeitschrift und Zeitschrift für Polymere* 241.*1-2* (1970), pp. 1075–1079.

[39] T. Guélon et al., « A new characterization method for rubbers », *in*: *Polymer Testing* 28 (2009), pp. 715–723.

[40] B. Gutschwager and J. Hollandt, « Nonuniformity correction of imaging systems with a spatially nonhomogeneous radiation source », *in*: *Applied optics* 54.*36* (2015), pp. 10599–10605.

[41] G.R. Hamed, H.J. Kim, and A.N. Gent, « Cut growth in vulcanizates of natural rubber, cis-polybutadiene, and a 50/50 blend during single and repeated extension », *in*: *Rubber chemistry and technology* 69.*5* (1996), pp. 807–818.

[42] J. Hameury, B. Hay, and J.R. Filtz, « Measurement of total hemispherical emissivity using a calorimetric technique », *in*: *International journal of thermophysics* 28.*5* (2007), pp. 1607–1620.

[43] J. A. C. Harwood, L. Mullins, and A. R. Payne, « Stress softening in natural rubber vulcanizates. Part 2. Stress softening effects in pure gum and filler loaded rubbers », *in*: *Journal of Applied Polymer Science* 9 (1965), pp. 3011–3021.

[44] E.A. Hauser and H. Mark, « Zur Kenntnis der Struktur gedehnter Kautschukproben », *in*: *Kolloidchemische Beihefte* 22.*3-5* (1926), pp. 63–94.

[45] A. M. Healey, P. J. Hendra, and Y. D. West, « A Fourier-transform Raman study of the strain-induced crystallization and cold crystallization of natural rubber », *in*: *Polymer* 37.*18* (1996), pp. 4009–4024.

[46] F. Hild and S. Roux, « Digital image correlation: from displacement measurement to identification of elastic properties–a review », *in*: *Strain* 42.*2* (2006), pp. 69–80.

[47] B. Huneau, « Strain-induced crystallization of natural rubber: a review of X-ray diffraction investigations », *in*: *Rubber Chemistry And Technology* 84.*3* (2011), pp. 425–452.

[48] A. Immirzi et al., « Crystal structure and melting entropy of natural rubber », *in*: *Macromolecules* 38.*4* (2005), pp. 1223–1231.

[49] A.G. James, A. Green, and G.M. Simpson, « Strain energy functions of rubber. I. Characterization of gum vulcanizates », *in*: *Journal of Applied Polymer Science* 19.*7* (1975), pp. 2033–2058.

[50] J. P. Joule, « On some thermodynamic properties of solids », *in*: *Phil Mag 4th* 14 (1857), p. 227.

[51] J.R. Katz, « Röntgenspektrographische Untersuchungen am gedehnten Kautschuk und ihre mögliche Bedeutung für das Problem der Dehnungseigenschaften dieser Substanz », *in*: *Naturwissenschaften* 13.*19* (1925), pp. 410–416.

[52] V. N. V.N. Khiêm et al., « Thermodynamics of strain-induced crystallization in filled natural rubber under uni- and biaxial loadings. Part I: complete energetic characterization and crystallinity evaluation. », *in*: *Submitted to Journal of the Mechanics of Physics of Solids* (2021).

[53] A. Lachhab et al., « Energy stored during deformation of crystallizing TPU foams », *in*: *Strain* 54.*4* (2018), e12271.

[54] G.J. Lake, « Fatigue and fracture of elastomers », *in*: *Rubber Chemistry and Technology* 68.*3* (1995), pp. 435–460.

[55] J.-B. Le Cam, « Energy storage due to strain-induced crystallization in natural rubber: the physical origin of the mechanical hysteresis », *in*: *Polymer* 127 (2017), pp. 166–173.

[56] J.-B. Le Cam, « Strain induced crystallization in rubber: A new measurement technique », *in*: *Strain* 54 (2018).

[57] J.-B. Le Cam, P.-A. Albouy, and S. Charlès, « Comparison between x-ray diffraction and quantitative surface calorimetry based on infrared thermography to evaluate strain-induced crystallinity in natural rubber », *in*: *Review of Scientific Instruments* 91.*4* (2020), p. 044902.

[58] J.-B. Le Cam, B. Huneau, and E. Verron, « Failure analysis of carbon black filled styrene butadiene rubber under fatigue loading conditions », *in*: *Plastics, Rubber and Composites* 43.*6* (2014), pp. 187–191.

[59] J.-B. Le Cam and E. Toussaint, « Volume variation in stretched natural rubber: competition between cavitation and stress-induced crystallization », *in*: *Macromolecules* 41.*20* (2008), pp. 7579–7583.

[60] J. Lemaitre and J.L. Chaboche, « Mécanique des Matériaux Solides (Dunod, Paris, 1985) », *in*: *Mechanics of Solid Materials (Cambridge University Press, 1990)* (1990).

[61] A. Lion, « On the large deformation behaviour of reinforced rubber at different temperatures », *in*: *Journal of the Mechanics and Physics of Solids* 45.*11-12* (1997), pp. 1805–1834.

[62] H. Louche and A. Chrysochoos, « Thermal and dissipative effects accompanying Lüders band propagation », *in*: *Materials Science and Engineering: A* 307.*1-2* (2001), pp. 15–22.

[63] H. Louche et al., « Heat Source Processing for Localized Deformation with Non-Constant Thermal Conductivity. Application to Superelastic Tensile Tests of NiTi Shape Memory Alloys Experimental Mechanics », *in*: *Experimental Mechanics* 52 (2012), pp. 1313–1328.

[64] M.T. Loukil et al., « Stored energy accompagnying cyclic deformation of filled rubber », *in*: *European Polymer Journal* 98 (2018), pp. 448–455.

[65] W. Lüders, « Über die äusserung der elasticität an stahlartigen eisenstäben und stahlstäben, und über eine beim biegen solcher stäbe beobachtete molecularbewegung », *in*: *Dingler's Polytechnic Journal* 155 (1860), pp. 18–22.

[66] J. Marchal, « Cristallisation des caoutchoucs chargés et non chargés sous contrainte : Effet sur les chaînes amorphes », PhD thesis, PhD Thesis, Université Paris XI Orsay, France, 2006.

[67] G. Marckmann and E. Verron, « Comparison of hyperelastic models for rubber-like materials », *in*: *Rubber chemistry and technology* 79.*5* (2006), pp. 835–858.

[68] G. Marckmann and E. Verron, « Comparison of hyperelastic models for rubber-like materials », *in*: *Rubber Chemistry and Technology* 79 (2007), pp. 835–858.

[69] H. Mark and G. von Susick, « Über geregelte Mizellstrukturen von Kautschuk », *in*: *Kolloid-Zeitschr.* 46 (1928), pp. 11–21.

[70] J. E. Mark, B. Erman, and M. Roland, *The science and technology of rubber*, Academic press, 2013.

[71] J.R. Samaca Martinez et al., « Thermomechanical analysis of the crack tip zone in stretched crystallizable natural rubber by using infrared thermography and digital image correlation », *in*: *Polymer* 55.*24* (2014), pp. 6345–6353.

[72] J.R. Samaca Martinez et al., « Heat and strain measurements at the crack tip of filled rubber under cyclic loadings using full-field techniques », *in*: *Mechanics of Materials* 81 (2015), pp. 62–71.

[73] A.R. Mayor and C.-G. Boissonnas, « Variation de la chaleur spécifique du caoutchouc en fonction de l'allongement », *in*: *Helvetica Chimica Acta* 31.*6* (1948), pp. 1514–1532.

[74] W. Minkina and S. Dudzik, « Simulation analysis of uncertainty of infrared camera measurement and processing path », *in*: *Measurement* 39.*8* (2006), pp. 758–763.

[75] Y. Miyamoto, H. Yamao, and K. Sekimoto, « Crystallization and melting of polyisoprene rubber under uniaxial deformation », *in*: *Macromolecules* 36.*17* (2003), pp. 6462–6471.

[76] M. Mooney, « A theory of large elastic deformation », *in*: *Journal of applied physics* 11.*9* (1940), pp. 582–592.

[77] F.H. Müller et al., « Calorimetric investigations of deformation processes », *in*: *Pure Appl Chem* 23.*2, 3* (1970), pp. 201–217.

[78] L. Mullins, « Effect of stretching on the properties of rubber », *in*: *Rubber Chemistry and Technology* 21.*2* (1948), pp. 281–300.

[79] L. Mullins, « Softening of rubber by deformation », *in*: *Rubber chemistry and technology* 42.*1* (1969), pp. 339–362.

[80] S.C. Nyburg, « X-ray determination of crystallinity in deformed natural rubber », *in*: *British Journal of Applied Physics* 5.*9* (1954), p. 321.

[81] R. W. Ogden, « Large deformation isotropic elasticity–on the correlation of theory and experiment for incompressible rubberlike solids », *in*: *Proceedings of the Royal Society of London. A. Mathematical and Physical Sciences* 326.*1567* (1972), pp. 565–584.

[82] E. A. Pieczyska et al., « Thermomechanical studies of yielding and strain localization phenomena of gum metal under tension », *in*: *Materials* 11.*4* (2018), p. 567.

[83] M. Planck, « The theory of heat radiation », *in*: *Entropy* 144 (1900).

[84] S. Poompradub et al., « Mechanism of strain-induced crystallization in filled and unfilled natural rubber vulcanizates », *in*: *Journal of applied physics* 97.*10* (2005), p. 103529.

[85] T. Pottier et al., « Study on the use of motion compensation technique to determine heat sources. Application to large deformations on cracked rubber specimens », *in*: *Experimental Mechanics* 49 (2009), pp. 561–574.

[86] N. Promma et al., « Application of the virtual fields method to mechanical characterization of elastomeric materials », *in*: *International Journal of Solids and Structures* 46 (2009), pp. 698–715.

[87] G. Rajkumar, J. M. Squire, and S. Arnott, « A new structure for crystalline natural rubber », *in*: *Macromolecules* 39.*20* (2006), pp. 7004–7014.

[88] J. Rault et al., « Chain orientation in natural rubber, Part II: 2 H-NMR study », *in*: *The European Physical Journal E* 21.*3* (2006), pp. 243–261.

[89] R.S. Rivlin, « Large elastic deformations of isotropic materials IV. Further developments of the general theory », *in*: *Philosophical Transactions of the Royal Society of London. Series A, Mathematical and Physical Sciences* 241.*835* (1948), pp. 379–397.

[90] R.S. Rivlin and D.W. Saunders, « Large elastic deformations of isotropic materials VII. Experiments on the deformation of rubber », *in*: *Philosophical Transactions of the Royal Society of London. Series A, Mathematical and Physical Sciences* 243.*865* (1951), pp. 251–288.

[91] E. Robin et al., « First steps towards the thermomechanical characterization of chalcogenide glass using quantitative infrared thermography », *in*: *Journal of non-crystalline solids* 391 (2014), pp. 101–105.

[92] P. Rublon et al., « Multiaxial deformation and strain-induced crystallization around a fatigue crack in natural rubber », *in*: *Engineering Fracture Mechanics* 123 (2014), pp. 59–69.

[93] B. Ruellan et al., « Fatigue crack growth in natural rubber: The role of SIC investigated through post-mortem analysis of fatigue striations », *in*: *Engineering Fracture Mechanics* 201 (2018), pp. 353–365.

[94] B. Ruellan et al., « Fatigue of natural rubber under different temperatures », *in*: *International Journal of Fatigue* 124 (2019), pp. 544–557.

[95] J. R. Samaca Martinez et al., « Mechanisms of deformation in crystallizable natural rubber. Part 1: Thermal characterization », *in*: *Polymer* 54 (2013), pp. 2717–2726.

[96] J.R. Samaca Martinez et al., « Mechanisms of deformation in crystallizable natural rubber. Part 2: quantitative calorimetric analysis », *in*: *Polymer* 54.*11* (2013), pp. 2727–2736.

[97] S. Seghar, « Devulcanisation des caouchoucs par micro-onde: influance des liquides ioniques », PhD thesis, Université Mouloud Mammeri, 2015.

[98] M. Soliman, M. Van Dijk, and M. Van Es, « Deformation mechanism of thermoplastic vulcanizates investigated by combined FTIR- and stress-strain measurements », *in*: *Polymeric Materials Science and Engineering(USA)* 79 (1998), p. 108.

[99] D. P. Sprott, *Devulcanization of rubber crumb using sulfur oxidizing Archaea.* University of Ottawa (Canada), 1999.

[100] P. Stanley and W.K. Chan, « The application of thermoelastic stress analysis techniques to composite materials », *in*: *The Journal of Strain Analysis for Engineering Design* 23.*3* (1988), pp. 137–143.

[101] D. Steiner Petrovič et al., « Differential scanning calorimetry study of the solidification sequence of austenitic stainless steel », *in*: *Journal of thermal analysis and calorimetry* 105.*1* (2011), pp. 251–257.

[102] Y. Takahashi and T. Kumano, « Crystal structure of natural rubber », *in*: *Macromolecules* 37.*13* (2004), pp. 4860–4864.

[103] Y. Tanaka, « Structural characterization of natural polyisoprenes: solve the mystery of natural rubber based on structural study », *in*: *Rubber chemistry and technology* 74.*3* (2001), pp. 355–375.

[104] S. Toki, T. Fujimaki, and M. Okuyama, « Strain-induced crystallization of natural rubber as detected real-time by wide-angle X-ray diffraction technique », *in*: *Polymer* 41.*14* (2000), pp. 5423–5429.

[105] S. Toki et al., « Strain-induced molecular orientation and crystallization in natural and synthetic rubbers under uniaxial deformation by in-situ synchrotron X-ray study », *in*: *Rubber chemistry and technology* 77.*2* (2004), pp. 317–335.

[106] M. Tosaka et al., « Effect of network-chain length on strain-induced crystallization of NR and IR vulcanizates », *in*: *Rubber chemistry and technology* 77.*4* (2004), pp. 711–723.

[107] M.i Tosaka et al., « Crystallization and stress relaxation in highly stretched samples of natural rubber and its synthetic analogue », *in*: *Macromolecules* 39.*15* (2006), pp. 5100–5105.

[108] E. Toussaint et al., « Combining displacement, strain, temperature and heat source fields to investigate the thermomechanical response of an elastomeric specimen subjected to large deformations », *in*: *Polymer testing* 31.*7* (2012), pp. 916–925.

[109] S. Trabelsi, « Etude statique et dynamique de la cristallisation des élastomères sous tension », 2002PA112193, PhD thesis, 2002, 174 p. URL: `http://www.theses.fr/2002PA112193`.

[110] S. Trabelsi, P.-A. Albouy, and J. Rault, « Crystallization and melting processes in vulcanized stretched natural rubber », *in*: *Macromolecules* 36.*20* (2003), pp. 7624–7639.

[111] S. Trabelsi, P.-A. Albouy, and J. Rault, « Effective local deformation in stretched filled rubber », *in*: *Macromolecules* 36.*24* (2003), pp. 9093–9099.

[112] L. R. G. Treloar, « Stress-strain data for vulcanised rubber under various types of deformation », *in*: *Transactions of the Faraday Society* 40 (1944), pp. 59–70.

[113] L.R.G. Treloar, « Crystallisation phenomena in raw rubber », *in*: *Transactions of the Faraday Society* 37 (1941), pp. 84–97.

[114] L.R.G. Treloar, « The elasticity of a network of long-chain molecules », *in*: *Transactions of the Faraday Society* 39 (1943), pp. 36–64, 241–246.

[115] P. Vacher et al., « Bidimensional strain measurement using digital images », *in*: *Proceedings of the Institution of Mechanical Engineers, Part C: Journal of Mechanical Engineering Science* 213.*8* (1999), pp. 811–817.

[116] V. Vitkovskii, V.G. Gorshenev, and Y.F. Potapov, « Measurement of spectral directional emissivity of materials and coatings in the infrared region of spectrum », *in*: *Thermal engineering* 56.*3* (2009), pp. 245–248.

[117] W.W. Vogt, « Chapter X The Physics of Vulcanized Rubber », *in*: *The Chemistry and Technology of Rubber* 74 (1937), p. 332.

[118] B. Wang and B. Pan, « Subset-based local vs. finite element-based global digital image correlation: A comparison study », *in*: *Theoretical and Applied Mechanics Letters* 6.*5* (2016), pp. 200–208.

[119] O. H. Yeoh and P.D. Fleming, « A new attempt to reconcile the statistical and phenomenological theories of rubber elasticity », *in*: *Journal of Polymer Science Part B: Polymer Physics* 35.*12* (1997), pp. 1919–1931.

DOCTORAT MATIERE
BRETAGNE MOLECULES
LOIRE ET MATERIAUX

UNIVERSITÉ DE RENNES 1

Titre : Contribution de l'imagerie quantitative pour la caractérisation mécanique, thermique et calorifique du caoutchouc

Mot clés : Cristallisation sous tension, Thermographie infrarouge, Corrélation d'images numériques, Élastomères

Résumé : La dépendance du comportement mécanique à la température, couplée aux nombreux couplages thermomecaniques présents dans les élastomères, implique que l'utilisation conjointe de méthodes de champs pour caractériser la thermomécanique des élastomères offre d'innombrables informations sur les phénomènes physiques apparaissant dans le matériau. L'objet de cet thèse est de développer une méthode utilisant à la fois la thermographie infrarouge et la corrélation d'images numériques pour tirer le maximum d'informations possible lors d'essai mécaniques hétérogènes sur des matériaux élastomères.

Title: Contribution of quantitative imaging to the mechanical, thermal and calorific characterization of rubber

Keywords: Strain-induced crystallization, Infrared thermography, Digital image correlation, Elastomers

Abstract: The thermal dependence of the mechanical behavior, coupled with the numerous thermomechanical couplings present in elastomers, implies that the use of field methods to investigate the thermomechanical response of elastomers gives lot of information on physical phenomena which occurs in the material. The aim of this PhD thesis is to develop a method using both infrared thermography and digital image correlation to extract all information possible during mechanical testing of elastomeric materials.